



**OPTIMIZATION OF A LOW HEAT LOAD
TURBINE NOZZLE GUIDE VANE**

THESIS

Jamie J. Johnson, First Lieutenant, USAF
AFIT/GAE/ENY/06-M19

**DEPARTMENT OF THE AIR FORCE
AIR UNIVERSITY**

AIR FORCE INSTITUTE OF TECHNOLOGY

Wright-Patterson Air Force Base, Ohio

APPROVED FOR PUBLIC RELEASE; DISTRIBUTION UNLIMITED

The views expressed in this thesis are those of the author and do not reflect the official policy or position of the United States Air Force, Department of Defense, or the United States Government.

AFIT/GAE/ENY/06-M19

OPTIMIZATION OF A LOW HEAT LOAD TURBINE NOZZLE GUIDE VANE

THESIS

Presented to the Faculty

Department of Aeronautical and Astronautical Engineering

Graduate School of Engineering and Management

Air Force Institute of Technology

Air University

Air Education and Training Command

In Partial Fulfillment of the Requirements for the
Degree of Master of Science in Aeronautical Engineering

Jamie J. Johnson, BS

First Lieutenant, USAF

March 2006

APPROVED FOR PUBLIC RELEASE; DISTRIBUTION UNLIMITED.

OPTIMIZATION OF A LOW HEAT LOAD TURBINE NOZZLE GUIDE VANE

Jamie J. Johnson, BS

First Lieutenant, USAF

Approved:

Dr. Paul I. King, (Chairman)

Date

Dr. Ralph Anthenien, (Member)

Date

Dr. Milton Franke, (Member)

Date

Acknowledgments

This thesis effort would not have been possible without a certain special group of people. First, I am indebted to my faculty advisor, Dr. Paul I. King, for approving this thesis idea and his guidance and support throughout my time as a student. The insight and experience pertaining to my study area was very helpful. Next, I would like to give many thanks to my thesis sponsor, Dr. John P. Clark, from the Air Force Research Laboratory's Propulsion Directorate (AFRL/PR), for his vast amount of persistent technical advice, design knowledge, and assistance during the execution of the thesis work. Thank you both for keeping the critical thinking going in my head with respect to all aspects of this project.

I would also like to thank the following people: Mr. Charles Stevens, my former AFRL branch chief, for allowing me to do my thesis work and take up office space in his branch, Dr. Richard Anthony and Lt Ryan Lemaire of AFRL/PR for their help in the design and fabrication of thin film heat flux gauges used in my experiments, Mrs. Emilee Brown and Mrs. Dayna Martin for their help with document presentation, Mr. Rob Free for precise soldering of wires to the heat flux gauges, Mr. Jay Anderson, the AFIT lab supervisor, and his staff including Mr. Randy Miller for the prompt and accurate fabrication of the scaled turbine vanes to be used in the experiment, Mr. Jan LeValley and Mr. Bob Jaruseiwic of the AFIT Machine Shop for their outstanding work in fabricating numerous critical parts for the experimental test section, Mr. Bob Wirrig, Test Cell 21 technician, for his support in ensuring proper shock tube operation, AFRL co-op students Mike Ooten and James Dagg for their programming assistance in the optimization phase of this work, Dr. Mike Flanagan for his expertise in proper instrumentation of the experimental rig, and Dr. Richard Rivir (ST) for allowing the use of the shock tube as an experimental apparatus. Finally, I thank the student body and other AFIT faculty for their friendliness and support during my time at AFIT.

Jamie J. Johnson

Table of Contents

	Page
Acknowledgements.....	v
List of Figures.....	viii
List of Tables.....	xi
List of Symbols.....	xii
Abstract.....	xiv
 I. Introduction.....	 1
Background.....	1
Turbine Airfoil Heat Transfer.....	5
Goals and Expectations of the Present Effort.....	6
Structure of the Thesis.....	8
 II. Literature Survey.....	 10
Experimental Turbine Heat Transfer Measurements.....	10
Heat Transfer Experiments and Attempts to Validate Prediction Methods.....	12
Turbomachinery Optimization.....	18
 III. Code Validation and Airfoil Optimization Methodology.....	 21
CFD Code Validation.....	21
Airfoil Re-Design and Optimization.....	30
 IV. Experimental Apparatus and Design.....	 42
Shock Tube Theory.....	42
Experimental Hardware.....	47
Shock Tube Facility.....	47
Flange Piece.....	50
Turbulence Grid.....	53
Linear Cascade Test Section.....	55
Thin Film Heat Flux Gauges.....	62
Instrumentation Summary.....	70
Data Acquisition System.....	73
Experimental Apparatus Summary.....	74

V.	Discussion of Thesis Results.....	77
	Code Validation Results.....	77
	VKI Airfoil Pressure Loading Predictions.....	77
	VKI Airfoil Heat Transfer Predictions.....	80
	VKI vs. LHL Airfoil.....	89
	Experimental Procedure, Data Reduction, and Results.....	108
	Procedure.....	108
	Test Time.....	110
	Turbulence Measurements.....	116
	Experimental Comparison of VKI and LHL Vanes.....	120
	Comparison of Heat Transfer to Prediction.....	132
VI.	Conclusions and Recommendations.....	145
	Conclusions.....	145
	Error and Uncertainty.....	147
	Recommendations for Future Work.....	147
Appendix A.	Supplemental MATLAB Codes.....	150
Appendix B.	Essential Shock Tube Relations.....	159
Appendix C.	Test Section Secondary Flow Analysis.....	161
Appendix D.	Fundamentals of Thin Film Heat Flux Gauge Operation.....	167
Appendix E.	Thin Film Heat Flux Gauge Production Process.....	171
Appendix F.	Calibration of Thin Film Heat Flux Gauges.....	173
Appendix G.	Heat Flux Gauge Coordinates for VKI and LHL Vanes.....	177
Appendix H.	CAD Drawings of Designed Parts with Dimensions.....	178
Appendix I.	Additional Airfoil CFD Data.....	183
Appendix J.	Determination of Turbulence Intensity from an Uncalibrated Hot-wire.....	193
Appendix K.	Equipment Used.....	195
	References.....	196
	Vita.....	202

List of Figures

Figure 1	Engine State-of-the-Art as a function of turbine inlet temperature.....	2
Figure 2	Traditional turbofan engine and stator vane location (from Ref [1]).	4
Figure 3	VKI vane cross-section shape.	24
Figure 4	VKI vane O- and H-grid structures.	24
Figure 5	Near-wall grid thickness Reynolds number plotted on the pressure and suction surface of the VKI vane.	25
Figure 6	VKI vane aerodynamic parameters.	26
Figure 7	WILDCAT code flow-solver setup parameters.....	29
Figure 8	Interface windows for changing airfoil parameters by hand.	33
Figure 9	Airfoil design system loading plot for the Drive to Target Loading function...	35
Figure 10	Interactive optimization iteration design log.....	37
Figure 11	Genetic algorithm setup and process methodology.....	40
Figure 12	Shock tube regions before rupture of diaphragm.	42
Figure 13	Flow phenomena in a shock tube after diaphragm is broken.	43
Figure 14	Shock tube flow regions after first shock wave reflection.	44
Figure 15	Shock tube temporal wave phenomena.	46
Figure 16	AFRL 16-foot shock tube and transonic vane cascade.	49
Figure 17	Image of hydraulic clamp and diaphragm-rupturing spike at shock tube section interface.....	50
Figure 18	CAD drawing of shock tube flange piece without turbulence grid.	52
Figure 19	Image of flange piece that connects test section to shock tube.	52
Figure 20	Drawing and image of turbulence grid used to generate approximately 6% Tu.	54
Figure 21	Typical variation of first vane isentropic exit Mach number with reaction for a modern High-Impact Technology (HIT) turbine rig.....	57
Figure 22	Schematic of shock tube linear 7-vane cascade test section (shown here with VKI vanes installed).	61
Figure 23	Image of the cascade test section without data instrumentation.....	62
Figure 24	Design drawing of platinum thin-film heat flux gauge array with expanded view of a single gauge area.	68
Figure 25	Images of the thin-film heat flux gauges installed on surface of VKI vane....	69
Figure 26	Image of an uninstalled heat flux gauge array with relative size shown.....	69
Figure 27	Image of instrumented cascade test section as viewed from heat flux gauge lead-wire side.	72
Figure 28	Image of shock tube test section as viewed from static pressure tap side.....	72
Figure 29	Image of shock tube data acquisition system.	74
Figure 30	Shock tube cascade experimental setup.	76
Figure 31	WILDCAT pressure loading prediction for two VKI runs at $M_2 = 0.84$	79
Figure 32	WILDCAT pressure loading prediction for two VKI runs at $M_2 = 0.875$	79
Figure 33	WILDCAT pressure loading prediction for three VKI runs at $M_2 = 1.02$	80
Figure 34	WILDCAT heat flux prediction for VKI run MUR228 ($M_2=0.932$, $Re_2=596000$, $Tu=1\%$).	85
Figure 35	WILDCAT heat flux prediction for VKI vane run MUR247 ($M_2=0.922$, $Re_2=2120000$, $Tu=1\%$).	85

Figure 36 WILDCAT heat flux prediction for VKI run MUR237 ($M_2=0.775$, $Re_2=1010000$, $Tu=6\%$).	86
Figure 37 WILDCAT heat flux prediction for VKI vane run MUR218 ($M_2=0.76$, $Re_2=1010000$, $Tu=4\%$).	86
Figure 38 WILDCAT heat flux prediction for VKI run MUR129 ($M_2=0.84$, $Re_2=1140000$, $Tu=0.8\%$).	87
Figure 39 Convergence history for a sample WILDCAT run of 10,000 iterations.	88
Figure 40 LHL vane aerodynamic parameters.....	90
Figure 41 LHL vane cross-section geometry.....	91
Figure 42 Relative shape, loading, and heat flux distribution of VKI and LHL vanes for a sample laminar viscous WILDCAT calculation.	92
Figure 43 Fractional surface distance pressure loading comparison of VKI and LHL vanes using AGS model.....	96
Figure 44 Heat flux distribution on surfaces of VKI and LHL vanes for AGS modeled transition.	97
Figure 45 2-D Isentropic Mach number flow-fields for VKI (a) and LHL (b) vanes. ..	102
Figure 46 2-D absolute velocity (ft/s) flow-fields for VKI (a) and LHL (b) vanes.....	103
Figure 47 2-D static pressure (psia) flow-fields for VKI (a) and LHL (b) vanes.....	104
Figure 48 2-D vorticity ($s^{-1} \times 10^5$) for VKI (a) and LHL (b) vanes.	105
Figure 49 2-D Static temperature ($^{\circ}R$) for VKI (a) and LHL (b) vanes.....	106
Figure 50 Pseudo-Schlieren (slug/ft) comparison of VKI (a) and LHL (b) vanes.	107
Figure 51 Pressure histories during a sample shock tube run.....	112
Figure 52 Inlet (top) and exit (bottom) static pressure voltage traces for a nominal experimental run.	112
Figure 53 Raw and converted (heat flux) voltage signals for a LE heat flux gauge during a sample shock tube run.....	114
Figure 54 Expanded view of the experimental test time for the converted heat flux signal. Correcting for independent channel gain response increased the heat flux signal slightly.	115
Figure 55 Single-film hot-wire output with turbulence grid installed at $P_4 = 60$ psia. .	118
Figure 56 X-wire turbulence level measurement data.	120
Figure 57 VKI vane experimental heat flux for different Tu	124
Figure 58 LHL vane experimental heat flux for different Tu	126
Figure 59 Grid-in ($Tu=5\%$) experimental heat flux comparison of VKI and LHL vanes.	128
Figure 60 Root-mean-square calculation of heat flux for Run 10 & 16.	129
Figure 61 Grid-out ($Tu=2\%$) experimental heat flux comparison of VKI and LHL vanes.	130
Figure 62 Experimental repeatability of heat flux data for reflected shock tube linear vane cascade trials.....	132
Figure 63 AFRL TRF sample data (Ref [60]) showing increased inlet total temperature at test start.	136
Figure 64 VKI vane midspan heat flux with WILDCAT laminar and turbulent predictions.....	138
Figure 65 LHL vane midspan heat flux with WILDCAT laminar and turbulent predictions.....	138

Figure 66 Turbulent boundary layer momentum and thermal diffusion time surface distribution for LHL vane run 16 experimental conditions.	142
---	-----

Appendix Figures

Figure C.1 Secondary flow over the surface of an airfoil.....	163
Figure C.2 Static pressure prediction of nominal cascade condition using 3-D CORSAIR code.....	164
Figure C.3 Loss profile for test section vane aspect ratio showing stable midspan.....	165
Figure C.4 Comparison of 2-D and 3-D code predictions at vane midspan.....	166
Figure C.5 Total pressure contour at the 50% chord downstream i-plane for 3-D flow prediction.....	166
Figure D.1 Thin film gauge on semi-infinite layer.....	167
Figure D.2 Penetration depth of thermal wave for 100 micron insulator thickness.....	170
Figure F.1 Calibration curves to find α for VKI vane thin film gauges.....	176
Figure F.2 Calibration curves to find α for LHL vane thin film gauges.....	176
Figure H.1 Flange piece used to bolt cascade test section to shock tube, house the turbulence grid, and provide flow area reduction into cascade inlet.....	178
Figure H.2 Turbulence grid sandwiched between tow thin border plates for producing 6% theoretical freestream turbulence intensity.....	179
Figure H.3 Plexiglass side wall designed to interchangeably house both vane geometries in the 7-vane cascade test section using metal pins.....	180
Figure H.4 Cascade test section with VKI vanes shown installed.....	181
Figure H.5 VKI vane geometry with pin hole locations.....	182
Figure H.6 LHL vane geometry with pin hole locations.....	182
Figure I.1 Predicted Stanton number comparison for VKI and LHL vane geometries using the Abu-Ghannam and Shaw (AGS) transition model.....	183
Figure I.2 Predicted skin friction coefficient comparison for VKI and LHL vane geometries using the AGS transition model.....	184
Figure I.3 Predicted shape factor comparison for VKI and LHL vane geometries using the AGS transition model.....	184
Figure I.4 Predicted boundary layer thickness comparison for VKI and LHL vane geometries using the AGS transition model.....	185
Figure I.5 Suction surface curvature, area, and thickness distributions for the VKI (a) and LHL (b) vanes.....	186
Figure I.6 Laminar prediction of pressure loading comparing the VKI and LHL vanes. The LHL geometry causes less loss than VKI.....	187
Figure I.7 Laminar prediction of heat flux distribution comparison of VKI and LHL vanes. The LHL geometry clearly has lower LE heat flux.....	188
Figure I.8 Turbulent prediction of pressure loading comparing the VKI and LHL vanes. The LHL geometry causes less loss than VKI.....	189
Figure I.9 Turbulent prediction of heat flux distribution comparing the VKI and LHL vanes. The LHL geometry exhibits lower LE heat flux.....	190
Figure I.10 Laminar and turbulent predictions of velocity and temperature profiles at maximum height of the vanes in the suction side for (a) the VKI vane and (b) the LHL vane using WILDCAT run at the MUR237 design conditions.....	192

List of Tables

Table 1	Comparison of VKI and LHL vane details with modern nozzle guide vanes. ...	58
Table 2	Temperature Coefficients of Resistance for the VKI and LHL gauges.....	65
Table 3	Selected VKI heat transfer runs and flow conditions for purposes of code validation.....	81
Table 4	Relative surface lengths of VKI and LHL vanes.....	92
Table 5	Final candidate airfoils from optimization process compared to VKI vane.	94
Table 6	Shock tube flow conditions for $P_4 = 60$ psia.....	110
Table 7	Shock tube experimental run conditions for vane heat transfer measurement.	122
Table 8	Summary of experimental heat transfer characteristics for the VKI and LHL vanes.	132
Table 9	Temperature boundary conditions for WILDCAT code consideration.	134

Appendix Tables

Table F.1	VKI vane thin film heat flux gauge calibration data.....	172
Table F.2	LHL vane thin film heat flux gauge calibration data.....	173
Appendix G	VKI and LHL vane heat flux gauge coordinates.....	175
Table I.1	LHL vane manufacturing coordinates.....	189

List of Symbols

Alphabetical

a	= local speed of sound
b_x	= airfoil axial chord
c_p	= specific heat capacity
C	= airfoil true chord
CR	= convergence ratio
d	= turbulence grid wire diameter
D	= thermocouple bead diameter
E	= no-flow voltage
F_t	= tangential loading coefficient
h	= coefficient of heat transfer, vane span or height, enthalpy
H	= shape factor, airfoil cross-section height
I	= current
k	= thermal conductivity
L	= airfoil midspan wetted length, axial chord
LE	= leading edge
m	= lumped capacitance time constant
M	= Mach number
Nu	= Nusselt number
P, p	= pressure
PS	= pressure side [of vane]
\dot{q}''	= heat flux
R	= resistance, universal gas constant
Re	= Reynolds number
s	= pitch, vane surface distance
s/s_x	= fraction of surface distance
St	= Stanton Number
SS	= suction side [of vane]
T	= temperature
t	= time
Tu	= turbulence intensity
TE	= trailing edge
u_τ	= wall friction velocity
U	= freestream flow velocity
V	= voltage
W	= wave velocity
x	= axial length, thermal wave penetration depth
x/b_x	= fraction of axial distance
y	= vertical coordinate
y^+	= near-wall grid thickness Reynolds number
Z_{TE}	= trailing edge secondary flow penetration depth

Greek

α	= thermal conductivity, temperature coefficient of resistance, air flow angle
γ	= ratio of specific heats, transition intermittency factor
δ^*	= inlet endwall boundary layer thickness
ε	= turbulent eddy viscosity
Δ	= denotes a change in a property
Λ	= turbulent eddy length scales
π	= mathematical constant, 3.1415926
ρ	= density
ν	= kinematic viscosity

Subscripts

0	= total, pertaining to original state
1	= inlet condition
2	= exit condition
b_x	= based on axial chord
ex	= exit condition
i	= pertaining to current state
in	= inlet condition
m	= mean or average
R	= reflected [shock]
s	= static, surface
S	= shock (pertaining to)
t	= total, thermal
tR	= total reflected
w	= wall
x	= axial
θ	= boundary layer momentum thickness property
∞	= freestream flow property

Abstract

Often turbomachinery airfoils are designed with aerodynamic performance foremost in mind rather than component durability. However, future aircraft systems require ever increasing levels of gas-turbine inlet temperature causing the durability and reliability of turbine components to be an ever more important design concern. As a result, the need to provide improved heat transfer prediction and optimization methods presents itself. Here, an effort to design an airfoil with minimized heat load is reported. First, a Reynolds-Averaged Navier-Stokes (RANS) flow solver was validated over different flow regimes as well as varying boundary conditions against extensive data available in literature published by the Von Karman Institute (VKI). Next, a nominal turbine inlet vane was tested experimentally for unsteady heat load measurements in a shock tube linear cascade with special attention paid to leading edge and suction side characteristics and used to validate the flow solver further at the experimental conditions. The nominal airfoil geometry was then redesigned for minimum heat load by means of both design practice and two types of optimization algorithms. Finally, the new airfoil was tested experimentally and unsteady heat load trends were compared to design levels as well as the nominal vane counterpart. Results indicate an appreciable reduction in heat load relative to the original vane computationally and experimentally providing credible evidence to further bolster the practice of preliminary design of turbine components solely with respect to heat transfer using computational models and methods traditionally employed purely by aerodynamicists.

AFIT/GAE/ENY/06-M19

*To Sheana, Owen,
and Family*

OPTIMIZATION OF A LOW HEAT LOAD TURBINE NOZZLE GUIDE VANE

I. Introduction

Background

Historically, the design of turbine components specifically for reduced heat transfer has been done to a rather limited extent, perhaps due to the extensive complexities of accurately modeling heat transfer in realistic turbine environments which often contain three-dimensional, unsteady, secondary, transonic, and turbulent flows. In addition, efforts focused on understanding turbine airfoil heat transfer have been commonly overshadowed by work done on the associated aerodynamics. Current standards in aircraft engines and research engines of the future demand affordable, efficient, light weight, and increasingly durable technologies, suggesting that further exploration of heat transfer issues relating to turbine component failure is in order. Turbine entry-temperatures are commonly well above the allowable metal temperatures of its components. Since aircraft engines of the future demand ever-increasing performance levels, higher turbine inlet temperatures, and higher thrust-to-weight ratios, and maximum thermal efficiencies, turbine-related heat transfer issues and its accuracy of prediction are becoming more critical to gas-turbine research and design. Figure 1 below is a plot of the advancement trend of gas-turbine engine performance in the form of specific core power versus turbine inlet temperature. Clearly, increased performance characteristics relate to higher temperatures. Therefore, as turbine designers pave the way to future gas-turbine technologies, the primary concern should pertain to designing

components that perform well under increasing heat loads and thus have superior durability with respect to previous engine designs.

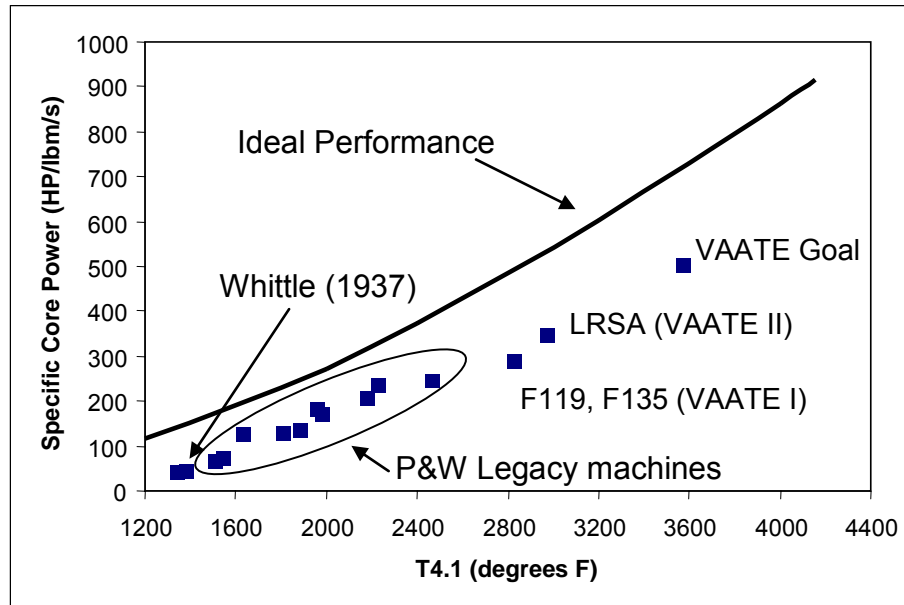


Figure 1 Engine State-of-the-Art as a function of turbine inlet temperature.

Gas-turbine engine components are renowned for being designed for optimum aerodynamic performance for high pressure loading and minimized loss. However, turbine component durability issues are becoming the focus of more turbine design programs as many engine test failures are ultimately traceable to a problem of heat transfer. Therefore, a lucid picture of thermodynamic properties in turbine components should ideally precede primarily designing for aerodynamic performance. For example, supporting a turbine that has traded-off some aerodynamic qualities in favor of good thermal performance and yields a relatively long life is indisputably better than nurturing a turbine with optimum aerodynamic qualities and a shortened operating life due to a sub-par thermal design. Turbine components subject to significant thermal stresses and high

temperatures are constantly susceptible to failure mechanisms such as cracking, hot corrosion, high-temperature oxidation, and thermal fatigue. Concepts including internal cooling passages, external film cooling, high-tech ceramic materials, and thermal barrier coatings, to name a few, have all been implemented by industry in an effort to combat the unfavorable effects of excessive surface heat transfer. Yet these technologies have been most often used on vanes and blades with geometries designed primarily for aerodynamic performance rather than thermodynamic performance. This effort suggests that heat transfer optimization of turbine airfoils become an additional standard concept in increasing component durability and improving thermal efficiency. If turbine engine designers take steps to have complete knowledge of the overall unsteady heat loads to be experienced by an engine, then this performance capability shortage can be fulfilled.

As advances are being made in computing power, numerical prediction methods, and measurement and detection technology, there is no better era than the present to study heat transfer issues. This study focuses on the aerodynamic issues commonly associated with increased heat transfer including transition, free-stream turbulence, and pressure gradients all by means of manipulation of airfoil cross-section geometry. The logical place to begin this effort is in the hottest part of the turbine where extremely high turbine inlet temperatures exist, just downstream of the combustor, at what is commonly known as engine station four [1], at the leading edge of the nozzle guide vane. From here on, a nozzle guide vane in a gas-turbine engine will be referred to as a vane, stator, or nozzle. Figure 2 shows where to find a turbine stage and the non-rotating stator vanes within a cross-section of a classical two-spool turbofan engine which has an inlet,

compressor, combustor, turbine, augmentor, and exit nozzle. Rotating components are black and stationary components are gray.

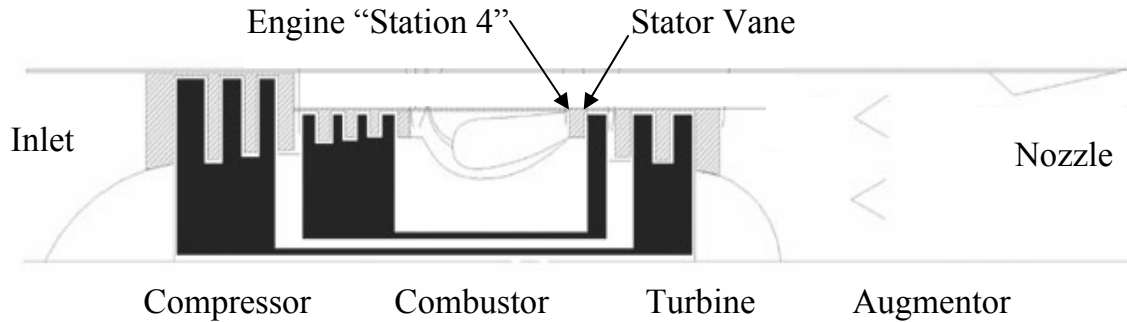


Figure 2 Traditional turbofan engine and stator vane location (from Ref [1]).

The first step to ensuring turbine components do not fail under their harsh operating environment is the accurate prediction of the different causes and attributes of heat transfer on a turbine airfoil stator vane. Accurate local heat transfer predictions are required to improve vane service life and to reduce cooling requirements. A need for a means to predict local heat transfer coefficients with accuracy has been a primary concern of researchers for years and a well-established design practice for predicting heat load can be a figure of merit for the design of future systems. Thus increased familiarity and prediction of the intricacies of the boundary layer on the airfoil surface is necessary. The transport properties of laminar and turbulent flows are very different, therefore proper prediction of overall heat transfer to turbine vanes and blades is critically dependent on the knowledge of the location and duration of the transition between these two regimes. As flow field property prediction methods have evolved to be a widely accepted science as will be discussed in the literature survey, the forthcoming techniques

will offer an innovative and modern approach to designing and testing a 2-D turbine stator vane airfoil geometry explicitly for reduced surface heat transfer.

Turbine Airfoil Heat Transfer

The problem of heat transfer starts in the properties of the air flow going through an engine. The extremely hot combustion products carry vast amounts of heat energy which are transferred through the surface of turbine components via the natural boundary layers created by the flow. Understanding boundary layer development characteristics is essential to understanding the surface heat transfer on turbine airfoils. A boundary layer can be defined as the thin layer between the freestream flow and the surface over which it travels where there is a velocity and temperature gradient normal to the surface depending on the inherent flow conditions.

Controlling the aspects of a boundary layer that contribute to heat transfer by manipulating the shape of an airfoil cross-section is at the heart of this effort. While a thick laminar boundary layer may insulate a surface, the same thickness boundary layer that has experienced transition to a fully-turbulent flow regime will cause higher heat transfer due to a number of contributing factors. In turbulent boundary layers, there is increased mixing (compared to laminar boundary layers where there is essentially no mixing) and thus more communication of thermal transport normal to a surface from an air flow to that surface. There is also increased skin friction and shear stresses with turbulence, thus a higher magnitude of heat transfer. Generally, heat transfer and early transition has not been major concern on the pressure side of an airfoil, where favorable pressure gradients exist. While the gas temperatures on the pressure (concave) side of an

airfoil can be high, rarely does the flow, especially on a turbine stator vane, become fully-turbulent. Pressure side boundary layers can see small areas of turbulence followed by a “relaminarization” as seen by Nicholson et al. [2], which will be discussed later in the paper. On the other hand, since transition to turbulence on the suction side is much more prevalent due to the adverse pressure gradient experienced by the flow, this will be an area of focus for this project. The challenge is to create an airfoil geometry that keeps the boundary layer laminar and smoothly accelerate the flow over the suction side thereby staving off transition to turbulence for as long as possible towards the trailing edge. However, there is a trade-off here. As a laminar boundary layer is accelerated ($dP/dx \ll 0$), the boundary layer thins causing higher surface temperature gradients and thus higher heat flux, but then it has not tripped into turbulence which causes mixing and increased skin friction. And while a thicker boundary layer insulates better, a turbulent boundary layer almost always causes higher heat transfer. Achieving delayed transition reduces the amount of surface over which turbulence occurs, thus decreasing heat transfer. As a result of changing the suction side, the pressure side curvature may change to keep overall airfoil heat load down and the aerodynamic qualities healthy. These methods will be discussed in more detail in the code validation and airfoil design optimization sections of this thesis. Out of these initial principles, objectives for a complete study of turbine airfoil heat transfer can be composed.

Goals and Expectations of the Present Effort

This project is first and foremost a design effort. The primary goal is to attempt to design a 2-D turbine vane airfoil that has a reduced heat transfer “load” at midspan

(half-way between the hub and tip on the vane) solely due to its geometry. The term “heat load” will be used many times in this paper and can be assumed to define the cumulative heat transfer on both the pressure and suction sides of the airfoil. The primary hypothesis of this problem is that through design, a vane airfoil geometry can be generated that exhibits reduced heat transfer. In order to efficiently attack this problem, tools will be necessary to design the airfoil and ensure that the theoretical heat transfer is accurate by validating existing computational codes, a nominal airfoil (not optimized for heat transfer) with extensive known experimental data concerning its heat transfer and pressure loadings will need to be elected, and finally the new airfoil designed for reduced heat transfer will need to be compared to the nominal airfoil through suitable experimentation. Consequently, out of the primary goal are born other more specific goals:

1. To validate a RANS flow-solver by comparison of the experimental data from the nominal airfoil to the results of the code for the same boundary conditions.
2. To use a novel turbomachinery design system (TDAAS) [3] used by the Air Force Research Laboratory (AFRL) in concert with the validated code to optimize the nominal 2-D vane airfoil and transform it to a geometry with reduced theoretical heat transfer as seen by the code while having good aerodynamic qualities as well.
3. To compare two turbine stator vanes and observe a lower heat load in the optimized vane by means of a linear cascade uncooled heat transfer experiments in which the turbine-like flow conditions are created in a proven shock tube facility used in the past for Air Force Institute of Technology (AFIT) and AFRL experimental purposes.

The details and methodology of each goal in this study will be elaborated in later portions of this report. These goals may now present a logical structure and order to this effort. It is anticipated that the following report will be a step towards a modern solution to an old and pervasive problem in the turbomachinery design industry and contribute to a more accurate prediction of heat transfer on turbine stators and increased confidence in numerical heat transfer prediction and optimization methods for reduced heat load.

Structure of the Thesis

The remainder of this thesis will be divided into the following five main sections denoted by a roman numeral and starting with the next section:

- II. A review of literature pertaining to: the study of gas-turbine heat transfer in experiments, numerical heat transfer prediction and development efforts, and modern airfoil optimization techniques.
- III. The computational methodology executed as it pertains to the validation of the 2-D flow solver code and the re-design and optimization of the “Low Heat Load” (LHL) airfoil.
- IV. The methodology of the experimental design and setup of the linear cascade shock tube tests for observed heat transfer assessments.
- V. A discussion of the results and solutions of each part of the thesis pertaining to the validation, optimization, and experimentation efforts as well as how it compares with past research efforts in the respective areas.
- VI. A summary of conclusions to be taken away from this large volume of work, a discussion of possible sources of error in the entire work, and

logical suggestions and recommendations for appropriate follow-on work to be done as a result of this cumulative effort.

Through this structure it can be seen that this thesis effort has three primary phases: a code “validation phase”, an “optimization phase”, and an “experimental phase”. While the validation phase also includes the choice of a nominal airfoil with accompanying flow regime tests, and the optimization phase may be considered to have more re-design rather than true optimization, these main parts of the thesis work will be referred to as the phases listed above for convenience and brevity. In addition, the methodology section is split into two parts: a computational part with the first two phases and an experimental part with the third phase.

II. Literature Survey

In this section, previous work on turbine heat transfer is reviewed. First, efforts that examine experimental gas-turbine component heat transfer in representative flow environments along with their respective flow facilities and heat transfer measurement devices is discussed. Then, different types of turbine heat transfer prediction methods are reviewed along with their relative accuracy and application to past experimental works. Finally, a basic history of optimization design methods for aerodynamic and thermal purposes is given.

Experimental Turbine Heat Transfer Measurements

The work pioneered by Dunn and Stoddard [4] resulted in some of the first significant experimental transient spatially resolved heat transfer data recorded in turbine-representative flows. Working with a state-of-the-art 176 degree stator vane annulus sector, demonstrating a reputable short flow duration shock tunnel facility, and pyrex-platinum heat flux gauge technology which was difficult at the time to fabricate and install, they were able to discover trends in the heat transfer in a turbine environment not seen before and identify heat transfer problem areas, such as towards the trailing edge of the vane suction side (SS), on the hub wall and end wall near the SS, and near the leading edge on the vane pressure side (PS). Some of the first experimental evidence of SS transition to turbulence was concluded from these experiments. Dunn and Hause [5] later converted the shock-tunnel facility to accommodate a full annulus complete Garrett TFE-731-2 turbine stage with stator and rotor to take heat flux and pressure data and compared

results to Ref [4] and rig design estimates. The spatially resolved heat transfer results showed an increasing Stanton number (St) with increasing chord Reynolds number on the SS indicating the existence of boundary layer transition. Comparisons to the work done in Ref [4] suggested the rotor may cause upstream influence on the nozzle guide vane boundary layer development. Also, this work was some of the first to map heat flux in the form of St over the PS and SS, as will also be done in this paper. York et al. [6] used a linear 5-vane cascade to conduct extensive endwall heat transfer experiments over a range of isentropic exit Mach number (M_2), exit Reynolds number (Re_2), gas-to-wall temperature ratio (T_0/T_w), and more to provide a detailed database to identify 3-D flow trends and to aid the development of correlations. Their work would become the definitive endwall heat transfer reference for many future cascade research efforts.

Frye [7] was one of the first to use the experimental apparatus used in this thesis to record heat transfer measurements. In 1966, he used it to validate that heat flux gauges were a viable experimental tool. Much later, Gochenaur [8] and Elrod [9] used flush-mounted Germanium thermocouples and a transient finite differencing scheme to obtain heat transfer rates on a flat plate with a shock induced boundary layer and on five midspan points (leading edge and $1/4$, $1/2$ chord points on the PS and SS) on a vane in an eight-passage cascade. Comparing reflected shock temperature ratio (T_5/T_1) to calculated heat transfer over a range of shock Mach numbers, they recognized increases from the leading edge (LE) to the $1/4$ chord point on the SS and attributed this to transition. A steady decrease in heat transfer from the LE to $1/2$ chord point on the PS of the instrumented vane was also seen. The flat plate analysis indicated a need for knowledge of freestream turbulence levels for more accurate calculations, which is done for the

present work with hot-wire measurements obtained downstream of a turbulence grid and without a turbulence grid. Fillingim [10] took the above work a step further by increasing heat flux resolution and using three CALSPAN [11] heat flux gauges on each side of a cascade vane and a thermocouple at the $\frac{1}{4}$ chord point on the SS. He also observed increased heat transfer at the LE stagnation point and on the SS due to transition in which the start of transition appeared to move towards the leading edge for increasing test section inlet Mach numbers.

Heat Transfer Experiments and Attempts to Validate Prediction Methods

One of the main goals behind obtaining experimental data is to gain enough to compare to theoretical and numerical or computational models being produced, so that the models, which can be easier to execute than experimentation, can be validated and proven in predicting flow characteristics. While some of the researchers noted above performed studies on blades instead of vanes, many of the heat transfer characteristics discovered are still valid for this work, especially since much of the earlier blade cascade work did not take into account effects of rotation or the flow obstruction of an upstream guide vane like in many of the works of Dunn. Perhaps better known for experimental heat transfer measurements, Graziani et al. [12] conducted some of the earliest endwall and blade surface measurements using a large number of thermocouples on a 4-blade large-scale cascade in a low-speed wind tunnel. Stanton number contours were realized for a thin and thick inlet boundary layer, in which thinner boundary layers resulted in higher heat transfer. Regions of high vane heat transfer were noticed at the leading edge and past about half of the SS, especially near the endwalls, while low heat transfer levels

were seen on the blade PS. This work showed some of the first indications of the complexity and 3-D nature of SS flows. Comparing the data to the 2-D finite difference calculation by Kays and Crawford (STAN-5) showed reasonable agreement for varying inlet boundary layer thickness, perhaps due to the large scale of the blades and relatively low speed flow in the tunnel. Wistanley et al. [13] compared the stator heat transfer work of Dunn [4] to predictions using flat plate correlations, a 2-D parabolic boundary layer code (STAN-5), and a 3-D viscous code (NANCY). He found that turbulent flat-plate correlations and post-transition boundary layer codes generally over-predict surface heat transfer, especially on the nozzle guide vane (NGV) SS, leading to the fact that more work was necessary to explore SS heat flux. Consigny and Richards [14] performed heat transfer measurements on a rotor blade using the VKI light piston tunnel (LPT) for varying inlet Mach numbers, inlet Re , and inlet flow angles. The rotor was instrumented with 40 painted-on platinum thin films in a 6-blade cascade. They found that transition onset on both airfoil surfaces occurred earlier for increasing Re and turbulence level with higher Tu increasing the SS heat load. Comparing these runs at four different Tu to the 2-D two-equation kinetic energy dissipation model, or k - ϵ turbulence model, showed an under-prediction of SS heat transfer coefficient and a common lack of prediction of SS transition onset. Simoneau et al. [15] also noted this trend in their summary of flow prediction models, in which this type of model at least gives good insight to 2-D type flows, such as at midspan. While the work of Consigny and Richards was for a turbine static rotor cascade, little change in heat transfer was found due to subtle changes in inlet flow angle.

Soon after, Dunn et al. [16], [17] used their own shock tunnel full stage heat transfer rig data from Ref [5] and data for three different T_0/T_w to compare to the STAN-5 code and an Air Force Research Laboratory (AFRL) Turbine Design System code (TDS). It was found that there was very little effect on NGV St due to changes in T_0/T_w . The TDS code predicted NGV and the non-rotating rotor PS St reasonably well, in which there was early transition to turbulence on the NGV SS. With a rotor in motion, vane and blade boundary layers reportedly appeared turbulent. These turbulent behavior and early transition characteristics augment turbine component heat transfer, and are at the root of the investigation of this thesis, especially for the optimization portion. Still using the TFE rig, Dunn [18] then took rotor blade heat transfer measurements at hub, midspan, and tip location of a blade downstream of an NGV that injected air out of the PS into the flow for two different cooling air-to-gas temperature ratios and compared the data to a flat-plate technique and the STAN-5 code. Results indicated another case of turbine component SS heat transfer unpredictability, as the flow at all three span locations transitioned at about 20% of the wetted suction surface and neither the laminar or turbulent flat plate correlation was effective, while the turbulent STAN-5 prediction only matched after 50% of the suction surface. PS heat transfer, however, was more predictable, even with the basic turbulent flat plate theory. Historically, PS characteristics have been easily simulated, perhaps because in favorable pressure gradients, the acceleration acts to stabilize the boundary layer and counteract effect of free-stream turbulence as seen in the work by Blair [19].

Still using a shock tube to create short-duration turbine-representative inlet flows, Dunn [20] took on the Garrett low-aspect-ratio ($AR = 1.5$) turbine stage (LART) taking

midspan NGV and blade heat transfer measurements and comparing them to local flat-plate prediction methods. This low aspect ratio nature of the turbine component geometry is similar to that seen in the shock tube cascade experiments of this thesis. The vane Stanton number data unexpectedly well-exceeded the turbulent flat plate prediction, contrary to the trend seen in Ref [13], with transition occurring at 6% of the SS distance. The rotor data showed good prediction once again for the turbulent PS, while the SS data lie between the laminar and turbulent predictions, transitioning at about 30% of the surface distance. This augmented SS St compared to prediction, possibly due to unsteady boundary layer heat transfer phenomena, leaves much to be explored.

This trend is also seen when Rae et al. [21] compares two inviscid NASA codes named MERIDL and TSONIC and the STAN-5 code to two different rig heat transfer data sets, both recorded by Dunn using the LART and the TFE rigs. Comparison of the LART data to the NASA codes for transitional and turbulent values of Re_θ shows midspan SS St magnitudes exceeding the predictions by a ratio of 2:1. However, the PS rotor comparison fared well. Comparisons of the LART data to the $k-\epsilon$ model were done at two levels of Tu (5 and 10%). Even still, the models did not come close to predicting the vane SS and PS data which was again twice the magnitude of the prediction of the $k-\epsilon$ model. Also, in line with the history of the comparisons outlined above, the rotor data was relatively well matched with prediction, perhaps because the rotor is insulated from any eccentric inlet flow characteristics seen by the NGV. More recently, Haldemann et al. [22] conducted heat transfer measurements at 20, 50, and 80% span using the shock-tunnel of Dunn on an inlet vane and compared the data to a KEP boundary layer prediction technique of Suo and Louunsbury in which St at 50% and 80% span was

mostly under-predicted, except at the LE. The predictions were quoted as being “not particularly good at any of the spanwise locations [of the vane]”. This and the examples above may lead one to think that this short-duration shock tunnel vane data may never be properly predicted.

Concerning turbulence effects on heat transfer, the works of Galassi et al. and Blair et al. both produced profound results towards this end. Blair et al. [23] studied midspan heat transfer for a turbine inlet stator, rotor, and second stator using the UTRC large, low-speed steady flow stage-and-a-half turbine at 0.5% and 10% Tu. The first vane row showed a dramatic effect of inlet Tu on increased heat transfer, with transition occurring very early on the SS, while the rotor and second stator saw little heat transfer magnitude dependence on Tu, which also lends to the fact that flow regulated by the vane diminishes the probability of downstream components seeing wildly 3-D unsteady effects and resultant heat transfer augmentation. In comparison to a finite-difference boundary layer code for laminar and turbulent predictions, both the first and second stator Stanton number were greatly under-predicted by the turbulent model on both the vanes’ PS and SS surfaces.

Galassi et al. [24] used a 4-blade cascade and jet-grid with three injection orientations and two upstream locations to examine intensity and length scale effects on St. Heat transfer was measured using 20 thermocouples on one of the middle blades. They compared measured St in grid-out runs with a laminar equation for St from Kays and Crawford [25], while the grid-in runs were compared to the method of Ambrock for turbulent flow St. Data correlated well with the laminar and turbulent predictions. With the jet-grid installed, SS transition onset moved from 70% of the surface distance for no

grid to 10% for the near-station grid and 20% for the far-station grid. A proportional relationship between Tu and St was witnessed along with an inverse relationship for length scale size and Nusselt number (Nu). This was yet another case of augmented SS heat transfer due to early transition. Lastly, Giel et al. [26] also performed studies measuring heat flux using liquid crystals for a stationary 12-blade cascade for two inlet Re , two M_2 , and turbulence grid in ($Tu = 7\%$) and out ($Tu = 0.25\%$) cases. Here, high Re and high Tu (grid in) both contributed to early SS transition, almost near the LE stagnation point. This complies with the detailed boundary layer measurements of Radomsky et al. [27], which stated that for very high (i.e. combustor level) Tu , the integral parameters on the SS moved upstream compared to low Tu levels, thus effecting skin friction and heat transfer. Comparing the experimental results of Giel to the 3-D Navier-Stokes code (RVC3D), transition onset was fairly predicted but the following was determined: LE heat transfer was under-predicted for low Tu and Re cases, PS values were under-predicted for all high Tu cases, and for all high Re cases (regardless of Tu) the SS heat transfer was under-predicted over the whole surface distance. Boyle et al. [34] performed perhaps the definitive prediction method breakdown comparing four models for predicting Stanton number due to varied Tu with sets of vane data compiled by Ames et al., Radomsky and Thole, and Arts [29] from a wide range of flow conditions. While other models exhibited interesting trends, the prediction results of the Abu-Ghannam and Shaw (AGS) transition length model is of primary interest as it was a critical part of the flow-solver code used in this thesis. Boyle concluded that in general the AGS model: predicted vane PS heat transfer well, is preferred for higher Re flows, uses a conservative length model with transition duration being predicted as often too

long, and on some occasions under-predicted SS heat transfer. The trends in all of these cases indicated early transition from higher Tu and inlet Re and an under-prediction of SS heat transfer when compared to various prediction codes.

The preceding case studies present an outstanding case for the need to further understand turbine nozzle guide vane leading edge and suction side heat transfer characteristics and create a vane with acceptably lowered heat load qualities, which can be validated by both modern predictive and experimental methods.

Turbomachinery Optimization

Very little overall has been accomplished in the way of optimizing turbine components specifically for reduced heat transfer. One would be challenged to find extensive information concerning this narrow subject in open literature; however, there are a large number of researchers who have used optimization techniques in similar areas of study. Nicholson et al. [30] conducted some of the original studies of this nature, stating that predicting the heat transfer through the boundary layer to the surface of engine components was critical to minimizing the loss of efficiency created by film cooling. The study compared pressure profiles and heat transfer on the pressure and suction surfaces of two different rotor blades of different stagger angles in a linear 2-D cascade row at the end of an isentropic light piston tunnel which ran at varying conditions. This work was purely done with pressure side optimized geometries. The low and high stagger airfoils were analyzed for the effects of transition, Re , M , and Tu on heat transfer. They found that SS transition was very common and moved forward with increasing Re and that increased Tu causes augmented mean heat transfer rates. Similar

trends will be seen in the predictions of this work. The study effectively built on the prospect of minimizing heat transfer via boundary layer control methods and it was concluded that aerodynamic efficiency is not compromised by a heat-transfer-optimized design.

On the aerodynamic side, algorithms have been used quite extensively since the mid-1990s to solve optimization problems using objective functions. CFD was used by Durbin et al. [31] to define optimally contoured endwalls for a one-blade, two-pass infinite cascade for turbulence modeling studies. Obayashi and Tsukhara [32] used three different types of optimization algorithms for aerodynamic shape design. Specifically, the purpose was to determine upper and lower surface contours for a wing airfoil in order to maximize the lift coefficient. Gradient-based, simulated annealing (SA), and genetic algorithms (GAs) were compared. While the GA may have used the most computational time, the GA far out-performed the other algorithms creating a coefficient of lift 25% higher than the next best result. Thus, it was declared that a GA, which is used in the heat transfer optimization of a turbine vane airfoil in this work, is the best option for aerodynamic optimization. Anguita et al. [33] used GAs as part of a Support Vector Machine (SVM) artificial intelligence concept to design a turbine blade with low loss and high loading. Similar concepts are used here, in which the GA is a critical part of an elaborate design scheme. Demeulenaere et al. [28] effectively used multipoint optimization techniques with genetic algorithms, custom fitness functions, an artificial neural network (ANN) to improve the efficiency of a rotor blade by almost 1% and the pressure ratio by over 2%. Arnone et al. [35] successfully used 3-D CFD analyses and genetic algorithms with geometric parameterization and complex fitness functions to

reduce profile loss on a high-lift blade while keeping other design specifications constant, resulting in a higher performance airfoil geometry. These and many other works since then support the use of GAs, which will be utilized in the re-design and optimization of the nominal turbine vane in this work.

III. Code Validation and Airfoil Optimization Methodology

CFD Code Validation

Accurately predicting heat transfer rate distributions on various turbine engine components in the design process is critical to achieving the goal of increased turbine inlet temperatures and thus improved cycle efficiencies. Through validation of a computational fluid dynamics (CFD) flow-solver that uses initial and boundary conditions, theoretical equations (RANS), and computes flow field properties, it is very important to know that what the code is conveying about heat transfer is as correct as possible. To begin this effort, a code needed to be validated and an airfoil to validate the code had to be chosen. The code used in this effort, currently used by NASA Marshall, is a quasi-three dimensional viscous fluid dynamics analysis tool for axial flow turbomachinery vane and blade rows named WILDCAT by Dorney [36]. The studies here will be restricted primarily to 2-D as it only deals with an airfoil geometry of a cross-section (at midspan) as mentioned before. The WILDCAT code has the ability to predict steady or unsteady flow fields for single or multiple blade rows and generate grids for the calculations using another code called WILDGRD. From here on, for simplicity, the code will be referred to as WILDCAT. The analysis is performed mathematically using the numerical solution of the Navier-Stokes equations. The numerical technique used in the solution is a time marching, implicit, upwind finite-difference scheme with a zonal, mixed grid topology. It is second order in time and third order in space. The more explicit details of this Navier-Stokes numerical scheme can be reviewed in Ref [37], which showed that overall turbomachinery vane row performance can be predicted to

within 2% using 900,000 full span computational grid points with the Baldwin-Lomax algebraic turbulence model. The code grid zones included two overset grids, an O and an H grid. The grids are used to make the sequential temporal numerical calculations. The O grid zones are generated using an elliptic equation solution procedure, encircle the airfoil to accurately resolve blunt leading edge and trailing edge regions, and can easily be made essentially orthogonal in the viscous-dominated near-wall region. The H grid simplifies grid construction and handles flow boundary conditions in passages between the airfoil, and areas upstream and downstream. Lee and Knight [38] performed computational studies and determined that this grid topology and the computational grid density both have an effect on predicted heat transfer solutions.

Next, an airfoil with an extensive pressure loading and heat transfer database at a wide range of conditions was selected to be run through the code to validate it. This baseline airfoil, which will be referred to from here on as the VKI vane (or airfoil), is a highly loaded transonic turbine nozzle guide vane that experienced extensive aerothermal cascade testing in the von Karman Institute (VKI) short duration Isentropic Light Piston Compression Tube facility. The measurements taken on the vane were compiled and documented by Arts [29] in which tests were performed for several combinations of freestream flow parameters, primarily Reynolds number (Re), turbulence intensity (Tu), and Mach number (M), in order to assess aerodynamic performance and convective heat transfer characteristics. The VKI vane was a logical choice since the original intent of this experimental database was to use the data for validation of both inviscid and viscous calculation methods. VKI compared their heat transfer results to predictions by a 2-D boundary layer code called TEXSTAN, which was generally an adequate model for

laminar and fully turbulent flow for the ranges of Re_2 , M_2 , and Tu . The VKI test program consisted of 7 blade velocity distribution (pressure loading) runs and 21 convective heat transfer runs with varied freestream conditions according to the following ranges: $T_0 = 420$ K, $M_2 = 0.7$ to 1.1 , $Re_2 = 5 \times 10^5$ to 2×10^6 and $Tu = 1.0$ to 6.0% . M_2 is the cascade exit Mach number, Re_2 is the cascade exit Re, and T_0 is inlet total temperature.

The VKI vane shape was originally optimized for a downstream Mach number equal to 0.9 by means of an inverse method developed at VKI. Figure 3 shows the VKI vane geometry plotted on fractional axial chord coordinates with the position of the flow passage throat located. Figure 4 shows the O and H grids and how they appear as applied to the VKI vane. Seven different pre-defined, generic grids were available for the execution of the code for the VKI vane including a standard grid for routine calculations in the transonic regime, supersonic grid with a very fine grid element structure, and a heat transfer grid which was defined explicitly for the purposes of heat transfer calculations. It has a near-wall grid thickness Reynolds number, $y^+ = (\Delta y u_\tau)/\nu \leq 1.0$ all around the airfoil. Commonly, $y^+ < 1$ is acceptable for two-equation turbulence models and $y^+ < 3.0$ is acceptable for the Baldwin-Lomax turbulence model [39] which is used in this case by the WILDCAT code. Figure 5 plots y^+ over both the PS and SS of the VKI vane. While the other grids were experimented with, it was found that the heat transfer grid gave the most accurate results for the code validation. It has an O grid structure that radiates normal to the vane surface and the grid element normal component becomes finer closer to the surface. The size in (i, j) coordinates of the O grid is $i = 121$ by $j = 23$ while the size of the H grid is $i = 60$ by $j = 30$. The O grid has a near-wall grid element height, $\Delta y = 1.27 \mu\text{m}$. Figure 4 also shows a blow-up of this heat transfer grid structure.

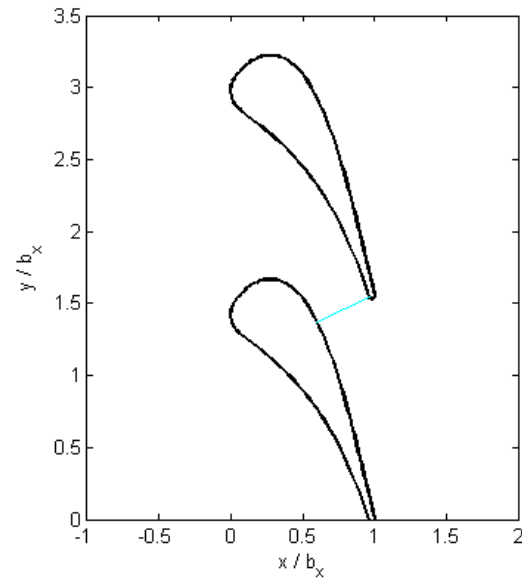


Figure 3 VKI vane cross-section shape.

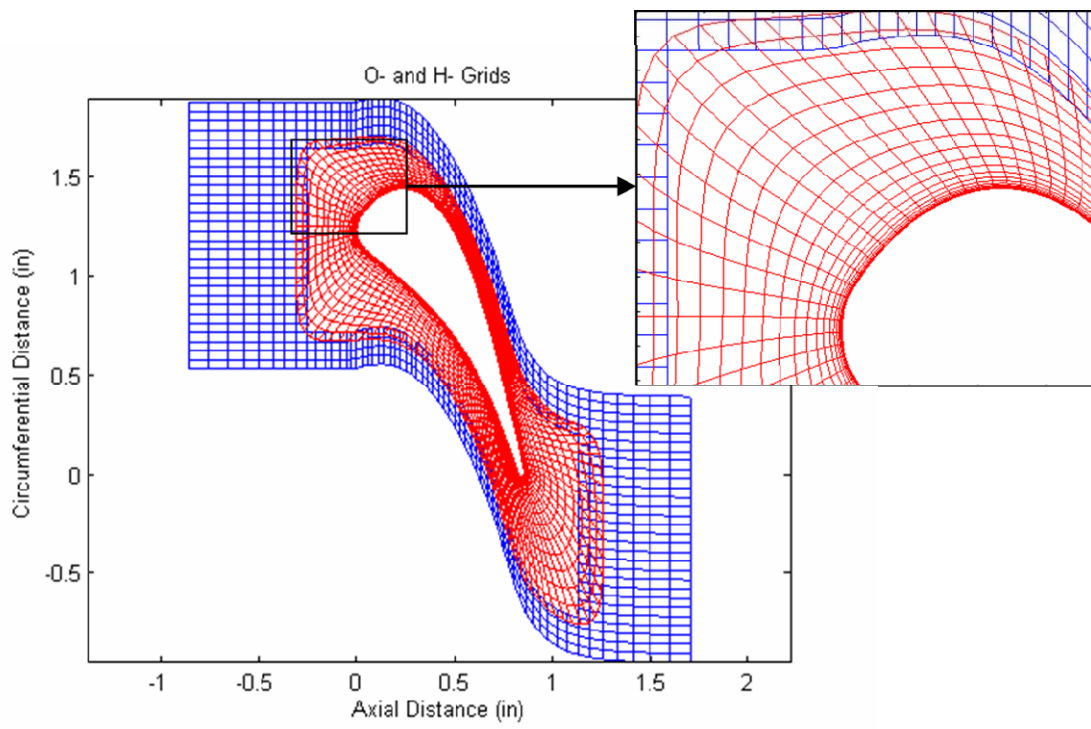


Figure 4 VKI vane O- and H-grid structures.

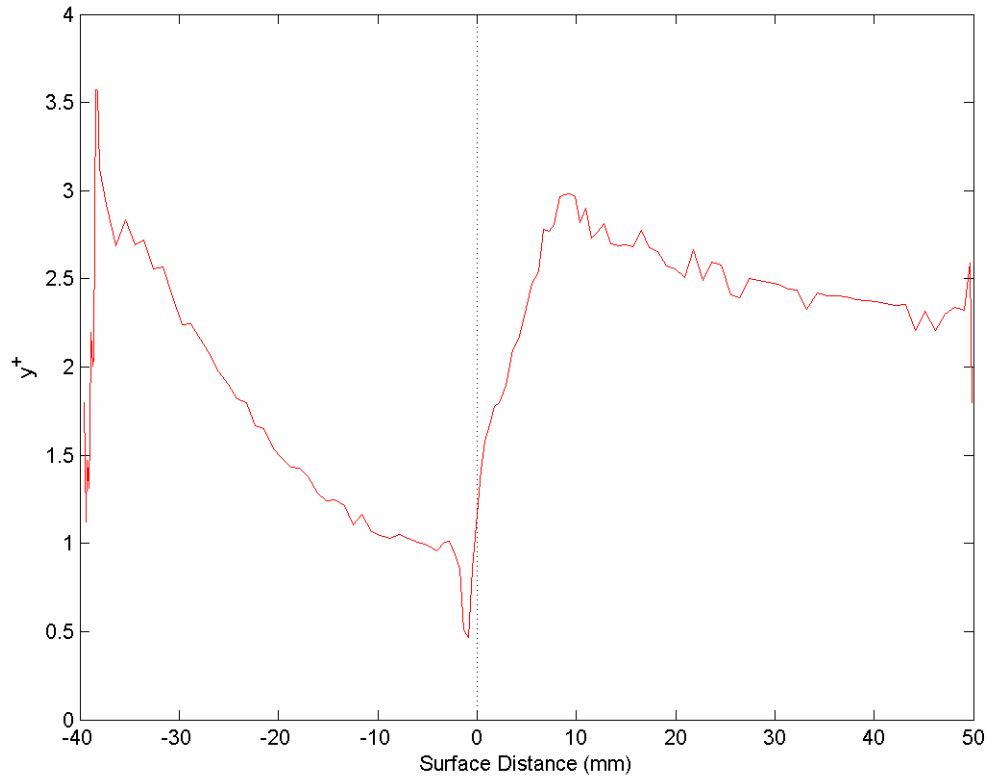


Figure 5 Near-wall grid thickness Reynolds number plotted on the pressure and suction surface of the VKI vane.

Figure 6 is a list of parameters pertaining to the VKI vane as it appears when the geometry is loaded into WILDCAT. It includes the vane's height-to-length ratio, axial chord length, leading edge diameter, relative air angles, and all geometric parameters. Most of these parameters will play an active role in the optimization of the vane when desired ranges are specified for the automated algorithms to define the design space. This vane shape was loaded into the WILDCAT code using the 405-coordinate list provided by VKI and converted, or splined, down to 199 points for ease of calculation by the code. It was then verified that the same shape and pressure loadings were created between the original coordinates and the 199-point representation.

Airfoil Design Parameters

Case Title :
"VKI 1V, Midspan"

General parameters : NF, Bx (in), rad (in), H/L, betagage (deg) :
470 0.8574 99.7371 1.2843 74.9907

Leading-edge parameters - LED (in), leer, Bet1 (deg), LEW (deg), LEWF :
0.35547 1.4696 0 91.149 0.59489

Trailing-edge parameters - TED (in), Bet2 (deg), TEW (deg), TEWF, uncvtrn (deg) :
0.03408 72.6456 4.7656 0.81581 12.6682

Bezier curve control handles : L1, L3F, L3R, L4, L5, L7 :
0.23324 0.4541 0.32906 0.74237 0.73434 0.55848

Flowfield parameters - M1 (rel), M2,is (rel), Ttin (deg R), Ptin (psia) :
0.15 0.775 751.1 25.43

Streamtube-height ratios - HleH1, HteHle, H2Hte :
1 1 1

Relative air angles - Bet1g (deg), Bet2g (deg) :
0 72.6456

Gas parameters : Rgas (ft lbf / lbfm / deg R), gama (1) :
53.35 1.4

Structural parameters: MomX (in lb), MomY (in lb) :
1e-005 0

OK Cancel

Figure 6 VKI vane aerodynamic parameters.

The WILDCAT code was then embedded in an easy-to-use MATLAB turbine design and analysis system (TDAAS) used by turbine component designers at AFRL and created by Clark [3]. The design system, which will be discussed in more detail in the optimization portion of the thesis, allowed the user to have a graphical user interface (GUI) for efficient operation of the grid generator and flow solver code using simple menus to input information. Using the WILDCAT code in the design system, once an airfoil coordinate geometry was read into the code, a grid of the desired type was

generated, all the necessary flow condition parameters and desired number of iterations were entered, and the code was executed. The code could ultimately compute the resulting flow field properties as they apply to heat transfer, pressures, Mach numbers, boundary layer characteristics, and more. The WILDCAT code was used to input the appropriate unique flow conditions for each run and simulate all 7 of the pressure loading and all 21 of the convective heat transfer trials performed experimentally by VKI and compare the code output with the actual data produced by the VKI vane in their cascade. A significant amount of programming went into ensuring the code was working correctly in the user-friendly GUI environment and to obtain all the code outputs for every VKI run. These MATLAB codes, composed as a supplement to the original to the work by Clark [3] on the design system, can be found in Appendix A. The results of these code validation runs will be discussed later in the paper for all of the velocity distribution runs by VKI and a subset of the heat transfer run population for which there was a good variation of the freestream conditions and a concrete conclusion about the accuracy of the code could be made.

To give the reader an idea of the information necessary for each run and a basic familiarity with the WILDCAT code, Figure 7 shows a sample input screen including all the necessary flow conditions to run the code. This screen would appear after an airfoil geometry was loaded and a grid chosen. Each parameter is assigned a variable name such as ITER for the number of iterations desired. During one iteration, the WILDCAT code solves the Navier-Stokes equations for continuity, momentum, and energy over all grid elements for both the O and H grids. Generally, the larger number of iterations, the better the solution because of the higher probability of having reached an acceptable level

of convergence. Convergence plots will be provided with the validation results later in the paper. For the most part, using the heat transfer grid, all pressure loading and heat transfer predictions were run for at least 10,000 iterations. Other key variables that were entered in the window to setup each run include the following: $M_{2,is}$, the isentropic exit Mach number, $T_{t,in}$, the total temperature upstream of the vane, $P_{t,in}$, the total pressure upstream of the vane, FTUR, the freestream turbulence level entered in decimal form, and IHEATS, the vane wall boundary condition. When IHEATS = 1, a Dirichlet condition is used and the wall temperature (in deg Rankine) on the boundary is specified. When IHEATS = 2, a Neumann condition is used and the heat flux is specified. As VKI provided the wall temperature for each of the heat transfer runs, only the Dirichlet condition was used for validation purposes. The variables ILAM and ITRAN were also critical for each run. When ILAM = 0, the code assumed fully turbulent flow and calculated using turbulent viscous equations. When ILAM = 1, the laminar viscous equations were solved. In the near-wall region, the flow is governed by the 2-D laminar boundary layer momentum equation used by WILDCAT and is given below in (1):

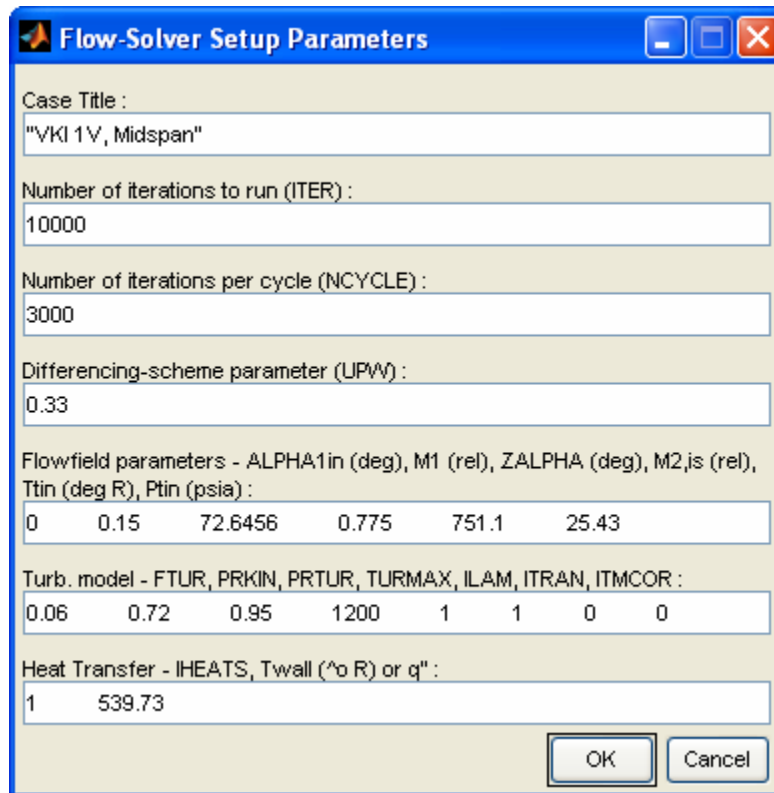
$$\rho u \frac{\partial u}{\partial x} + \rho v \frac{\partial u}{\partial y} = -\frac{dP}{dx} + \frac{\partial}{\partial y} \left(\mu \frac{\partial u}{\partial y} \right) \quad (1)$$

To transform into the 2-D turbulent momentum equations, the velocity is given a mean and fluctuating component by letting $u = \bar{u} + u'$ and the higher order terms are removed giving equation 2:

$$\bar{\rho} \bar{u} \frac{\partial \bar{u}}{\partial x} + \bar{\rho} \bar{v} \frac{\partial \bar{u}}{\partial y} = -\frac{d\bar{P}}{dx} + \frac{\partial}{\partial y} \left(\mu \frac{\partial \bar{u}}{\partial y} \right) - \overline{\rho u' v'} \quad (2)$$

where the last term is the Reynolds shear stress that is a function of an eddy viscosity, μ_t . This turbulent eddy viscosity is the basis of the two-layer turbulence model used by

WILDCAT, produced by Baldwin and Lomax [39]. The WILDCAT assumed transition onset as defined by a number of models. ITRAN could be varied in order to specify the transition model desired in which the user could choose from those of Dunham, Seyb-Singh, Mayle, Baldwin-Lomax, Abu-Ghannam/Shaw (AGS), and others. For validation purposes, as will be seen in the results section, only the AGS transition model [40] was chosen to be studied against the VKI data. All other variables such as the inlet flow angle ($\text{ALPHA}_{1\text{in}}$), inlet Mach number (M_1) and vane air flow turning angle ($Z\text{ALPHA}$) were kept constant for all runs.



The image shows a Windows-style dialog box titled "Flow-Solver Setup Parameters". It contains several input fields and a table for parameters. The "Case Title" is "VKI 1V, Midspan". The "Number of iterations to run (ITER)" is 10000. The "Number of iterations per cycle (NCYCLE)" is 3000. The "Differencing-scheme parameter (UPVW)" is 0.33. The "Flowfield parameters" table has columns for ALPHA1in (deg), M1 (rel), ZALPHA (deg), M2,is (rel), Ttin (deg R), and Ptin (psia), with values 0, 0.15, 72.6456, 0.775, 751.1, and 25.43 respectively. The "Turb. model" table has columns for FTUR, PRKIN, PRTUR, TURMAX, ILAM, ITRAN, and ITMCOR, with values 0.06, 0.72, 0.95, 1200, 1, 1, 0, and 0 respectively. The "Heat Transfer" field is set to 1 and 539.73. There are "OK" and "Cancel" buttons at the bottom right.

Flowfield parameters - ALPHA1in (deg), M1 (rel), ZALPHA (deg), M2,is (rel), Ttin (deg R), Ptin (psia) :					
0	0.15	72.6456	0.775	751.1	25.43

Turb. model - FTUR, PRKIN, PRTUR, TURMAX, ILAM, ITRAN, ITMCOR :						
0.06	0.72	0.95	1200	1	1	0 0

Figure 7 WILDCAT code flow-solver setup parameters.

These WILDCAT runs were repeated until a wide enough set of flow conditions were covered to deem the code validation complete for the experimental data of the VKI vane and the relative WILDCAT results. For future reference, the pressure loadings will

be displayed with fractional axial chord (x/b_x) on the x-axis with static-to-total pressure ratio ($P/P_{t,in}$) on the y-axis. Meanwhile the heat transfer will be mapped with fractional surface distance (s/s_x) on the horizontal axis (pressure surface spans from -1 to 0 and the suction surface from 0 to 1) and heat flux on the vertical axis. This convention for plotting heat transfer has been used traditionally by Arts [29], Dunn [18], Nicholson [30], and many more, and will be used when displaying the results in the code validation and experimental results sections of the thesis. Now that the code validation methodology has been articulated, the methodology of the vane optimization will be described (skip ahead to section V to see the validation results).

Airfoil Re-design and Optimization

Optimization of the VKI vane for reduced heat transfer was a rigorous, iterative design and computation process. The MATLAB design and analysis system for turbine airfoils recently implemented at the Air Force Research Laboratory by Clark [3] was critical to the optimization task. Complete details of the system are not releasable in open forum at present, but the basic methodology as it applies to the current study is given here. The system employs an industry-standard airfoil shape-generation algorithm developed by Huber [41] to define turbine blade and vane shapes. The grid generator and flow solver of Dorney and Davis [37] are used to determine the aerothermodynamic behavior of the design shapes. The shape and grid generators and the flow solver are then combined with GUI-based flow-field-interrogation and design-optimization techniques to allow a designer to realize new and/or improved airfoils in short order. The optimization can proceed via either gradient based (sequential quadratic programming

(SQP)) or genetic algorithms (GA), and a wide range of objective functions are specifiable by the user. For example it can be used to reduce loss, manipulate the pressure loading characteristics of an airfoil, or minimize heat flux at specified areas for an airfoil surface, as is the focus of this study. Among other advantages, this design system allows reverse-engineering in which the user can specify the desired flow characteristics and generate a new airfoil shape based on these.

Knowing that a true optimization of a complex problem such as this involves a plethora of variables and would take a very long to perform all the calculations necessary, the optimization objectives for the airfoil geometry had to be clear, prioritized, and limited to a few main ideas. At first, as the thesis title explains, the idea was to reduce the overall heat load on the optimized vane relative to the baseline VKI vane. This objective may be ambiguous since the optimized airfoil may have a lower integrated heat load over both the pressure and suction surfaces compared to the VKI vane, but have one or more hot spots that would cause failure of surface material integrity in an actual engine test. This is only one of many possible adverse results linked to this unclear objective. In addition, the attributes of heat transfer on the airfoil, just like the aerodynamics, have to have some aesthetic qualities to them as well as they pertain to good design practice, experience, and other heuristics known by designers historically in turbine component design. Ideally, the new airfoil must also perform well aerodynamically (low loss, high loading) and have reduced surface heat transfer characteristics when tested either computationally or experimentally. Thus, the re-design and optimization process is a balance of both art and science. Both good judgment (art) and extensive parameter analysis (science) went into the formation of the optimized airfoil. To quell the issue of

needing concrete objectives for this task, it was ultimately decided that the goal of the optimization was to (1) reduce leading edge (LE) heat transfer and (2) drive back transition on the suction side as far possible towards the trailing edge (TE).

The design system specified earlier was very flexible in that it allowed the user to attack the problem from many angles. After the VKI airfoil geometry was loaded into the design system and the appropriate flow conditions were entered as if a WILDCAT run was being executed, an optimization case could be launched in which a window appeared and ranges of key airfoil design parameters could be specified. The airfoil parameters can be categorized into four categories: main airfoil parameters such as axial chord and height-to-length ratio, LE parameters, TE parameters, and Bezier curve parameters for the PS and SS curves. These parameters can all be incrementally varied using slider bars and the real-time changes in the airfoil shape, area distribution, SS curvature distribution, and thickness distribution can be seen in an accompanying window and be evaluated in almost real-time, which is a major advantage of the design system. Figure 8 shows the GUI windows for changing the airfoil parameters and seeing the real-time changes to the shape. Following the science aspect of the airfoil optimization, the optimization suite allows the user to perform repetitive runs of the WILDCAT code for the specified number of iterations given the variable ranges (problem space) from which to find the best solution. For example, WILDCAT could be run for 10,000 flow-solving iterations 1,000 times, or for 1,000 optimization iterations. Each new WILDCAT result outputs new flow characteristics and the optimization code decides whether to explore a different shape based on the prescribed user desirability of the results. Pertaining to the “art” aspects of the optimization, the user may decide to run WILDCAT, observe the resulting

flow characteristics of the airfoil (heat transfer and pressure loading), alter the airfoil parameters as desired using slider bars, and run WILDCAT again. This is in effect was hand-iterations of the optimization with human design judgment incorporated between each WILDCAT run. Finally, it would turn out that airfoil pressure loading plots and surface heat transfer plots were two primary tools used in this process to assess whether desired characteristics had been met.

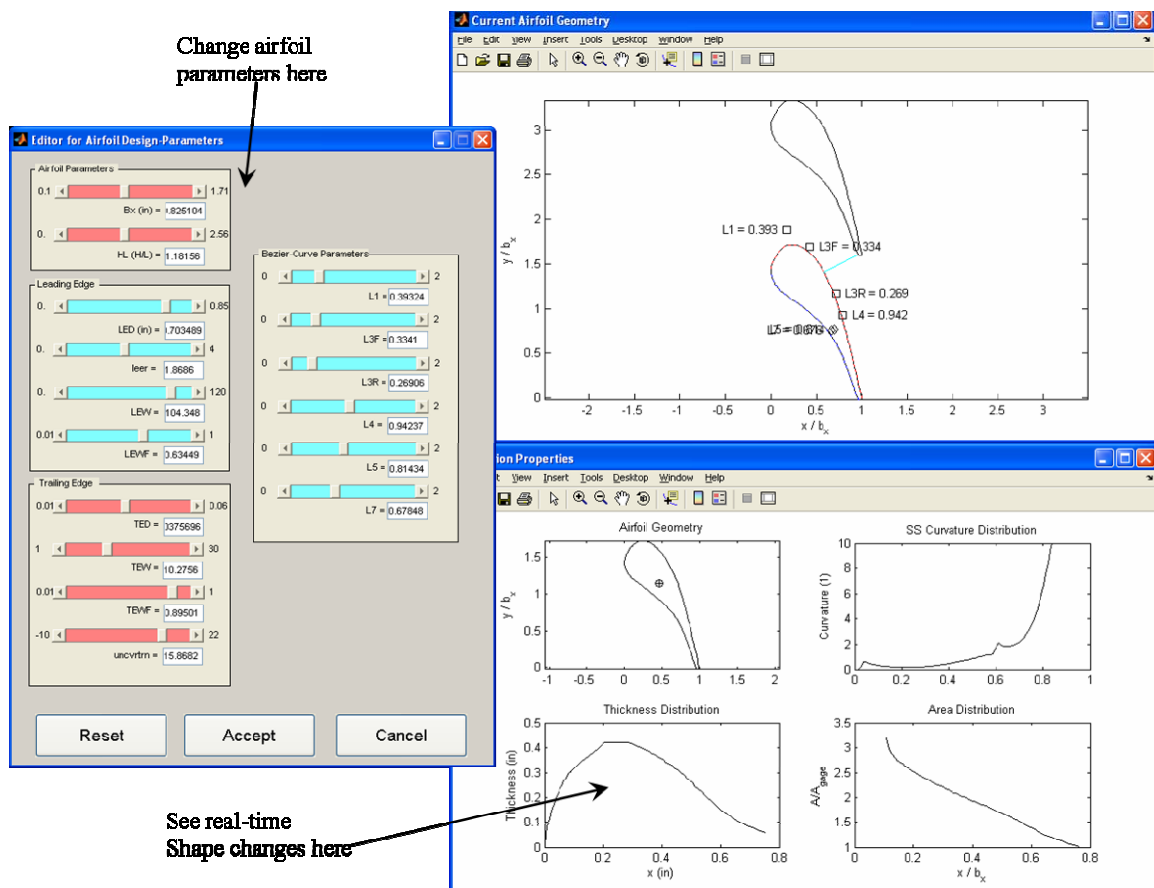


Figure 8 Interface windows for changing airfoil parameters by hand.

The optimization suite could perform a selection of different operations. One of the optimization operations is called *Drive to Target Loading* and allowed the designer to reverse-engineer an airfoil. During the re-design of the VKI vane it was determined from

the AGS transition model [40] that derived the start of transition from turbulence level and a pressure-gradient parameter, and from design practice with the interactive GUI, that driving the minimum SS $P/P_{t,in}$ back towards the TE of the airfoil generally resulted in delayed transition. This assumes the minimum was arrived at with as little oscillation in pressure gradient as possible. The airfoil pressure loading results from a WILDCAT run could be examined and the *Drive to Target Loading* function allowed the actual graph of the SS pressure ratio to be manipulated by the user with the mouse pointer and submitted to the sequential quadratic programming (SQP) optimizer algorithm. Then, the airfoil shape would be changed in order to get as close to the desired loading as possible—hence the reverse engineering aspect of the design system. Briefly, the SQP algorithm is a generalization of Newton’s method for unconstrained optimization in that it finds a step away from the current point by minimizing a quadratic model of the problem. It replaces the objective function with a quadratic approximation and replaces constraint functions with linear approximations. Figure 9 shows the plot of the loading along with the desired loading line which could be dragged into place using the mouse pointer. This method was successful in arriving at the delayed theoretical transition characteristics of the final optimized vane selected.

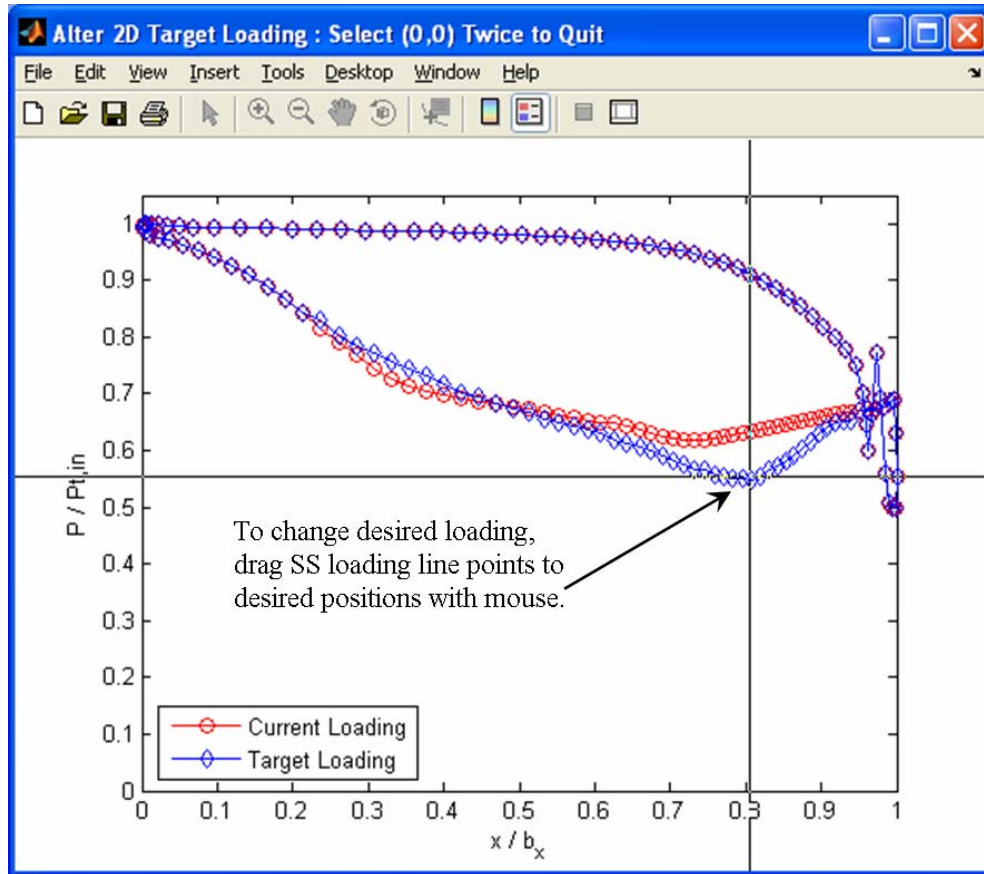


Figure 9 Airfoil design system loading plot for the Drive to Target Loading function.

Knowing that heat flux is heat transfer per unit area, if the area is increased, then the heat flux must decrease. Also, the larger the radius of curvature, the lower the level of heat flux [25]. To achieve the goal of reduced LE heat transfer, it was postulated that increasing the leading edge diameter (LED) parameter of the airfoil would help provide a solution. A great amount of attention was given to this objective in hand-iterations, or the art, of the optimization process. Of course, changing the LED meant other parameters would change as well in order to keep pressure loading and SS heat transfer acceptable. These hand-iterations, or any other automated optimization iterations performed, were saved in a design log file which could be reviewed at any time. The user could scroll through all optimization iterations completed so far with the respective

airfoil shape, fractional surface distance pressure loading, and heat transfer plots. This invaluable tool gave good indication as to whether the optimization was headed in the right direction as it pertains to the design objectives. Figure 10 shows the MATLAB window of the design log with the slider bar for scrolling through the cumulative airfoil optimization iterations. The dotted blue line represents the airfoil to which the user has chosen to compare all optimization iteration results; here the VKI airfoil is shown. The solid red lines represent the current airfoil design. This guaranteed efficient design progression as the current best airfoil could be accepted and run in WILDCAT with slight changes in parameters and then immediately compared to the previous design using the design log windows.

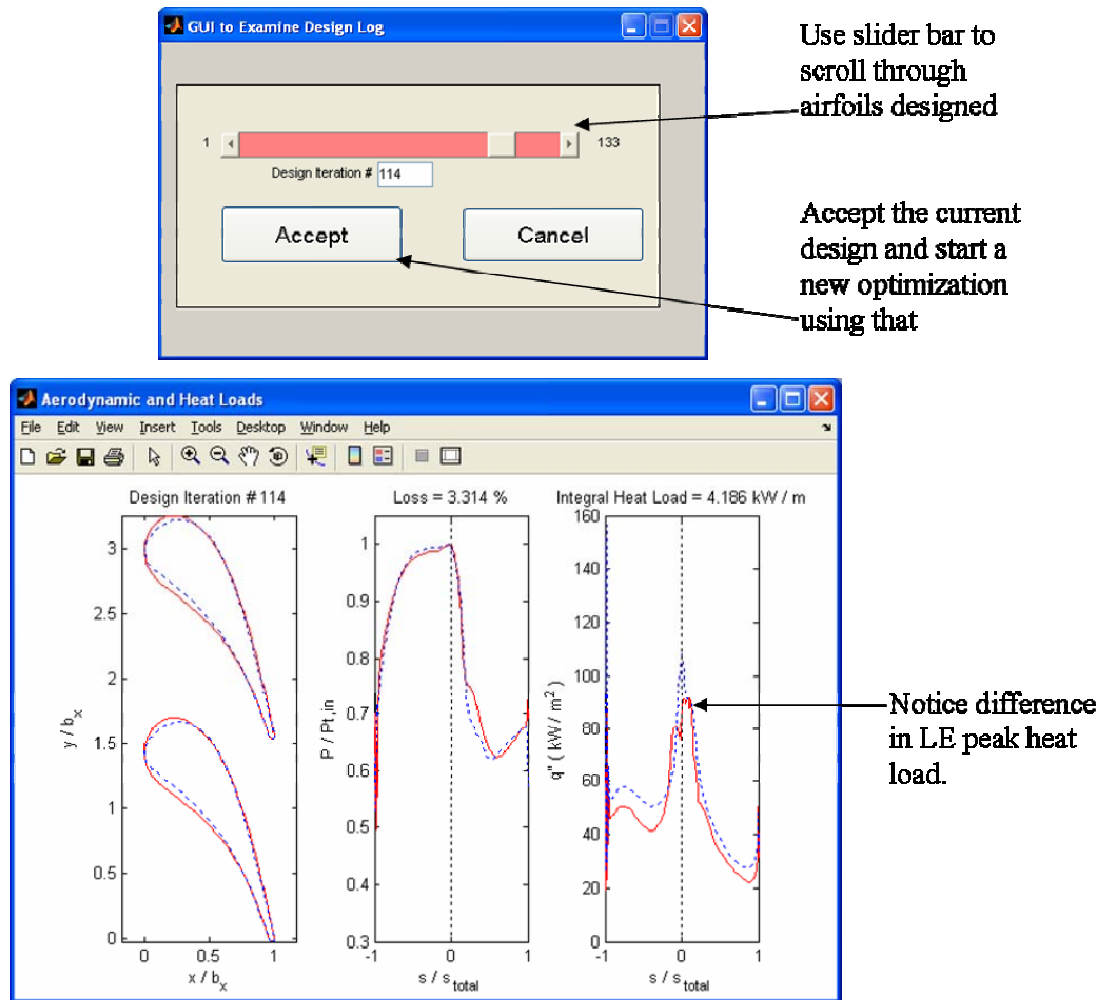


Figure 10 Interactive optimization iteration design log.

The final tool used in the airfoil optimization process was a genetic algorithm, or GA. GAs, which are sometimes called multi-objective genetic algorithms (MOGAs), have been used frequently in recent aerodynamic design practice for optimization purposes [33], [32]. They can readily locate an optimal point in a problem space of theoretically infinite dimensions. In other words, much like the SQP algorithm, the turbine designer can vary several parameters and input desired ranges of these parameters related to the quantity optimized. Genetic algorithms are a process for function optimization that mimics the genetic reproduction process experienced by biological

organisms [42]. The GA uses fitness functions prescribed by the user to determine the best option available. Fitness functions were used that best represented the priority of the airfoil parameters that were being optimized, such as heat transfer, which was a result of multiple other parameters. Careful implementation of a fitness function, which is subjective to the designer, will result in a significantly improved airfoil in minimum time by using the process of natural selection to improve the set of parameters, or genes, that describe the airfoil. The GA is not perfect, however, as it is susceptible to mutations and elitism, which makes the structure of the fitness function critical to the success of the GA. Here the nature of the fitness functions, or objective functions, stayed close to the two main goals for the optimization for reducing LE heat load, and manipulating the SS curves to delay transition towards the vane TE.

Technically, the GA is started with a set of parameter ranges specified by the user which were assigned 6 bits per range. This creates one long binary bit string that defines an airfoil shape: if there were 9 parameter ranges, then an airfoil would be defined by a 54-digit bit string. Since it is a binary logic, two to power of the number of bits specified becomes the number of slices into which the parameter range is split (here it would be $2^6 = 64$). Next the user chooses the initial population size to be explored—the larger the number the better chance of finding an optimum in the problem space. In this case a population size of 40 was chosen. Hence, there were a random set of 40 54-digit bit strings to begin the optimization. The number of generations is chosen next, which for this case was 38. This means the best airfoil from each generation was chosen to breed and recalculate the population for 40 generations of airfoils (could be called a 40 x 40 GA). Finally, a fitness function, which for this case followed the desired objective

outlined above, is selected and the GA is executed. Generating and coding a fitness function is a complex process and has the greatest impact on the final results of the GA. The initial code structure, variables used, and methodology which laid the groundwork for commanding the desired objectives in the fitness functions relating to reduced heat transfer design was accomplished by Dagg [43]. The intricacies of composing a proper fitness function may be examined in that reference. The approximate average computation time for the genetic algorithm operations alone to find a heat transfer optimized airfoil was approximately 5 days. Figure 11 is a flow chart with the basic steps of the algorithm and screen shots of the MATLAB GA optimization suite windows that were used to execute the runs.

Finally, to outline the constraints of the optimization of the VKI vane, it was decided that the axial chord be kept constant (at 0.8575 in) for simplicity and interchangeability when it came time to test each vane cascade using the shock tube. In addition the optimization iterations (whether by hand or by automated SQP or GAs) were constrained to optimizing for a single set of flow conditions for every time the WILDCAT code was executed. The flow conditions used were for the VKI's MUR237 cascade heat transfer experimental run, whose conditions are given in Table 3 of the code validation results section of the thesis. These flow conditions were chosen for their applicability to a realistic modern turbine inlet environment and because they would match the conditions for a turbulence grid-installed shock tube run when it came time to record experimental heat transfer for both vanes.

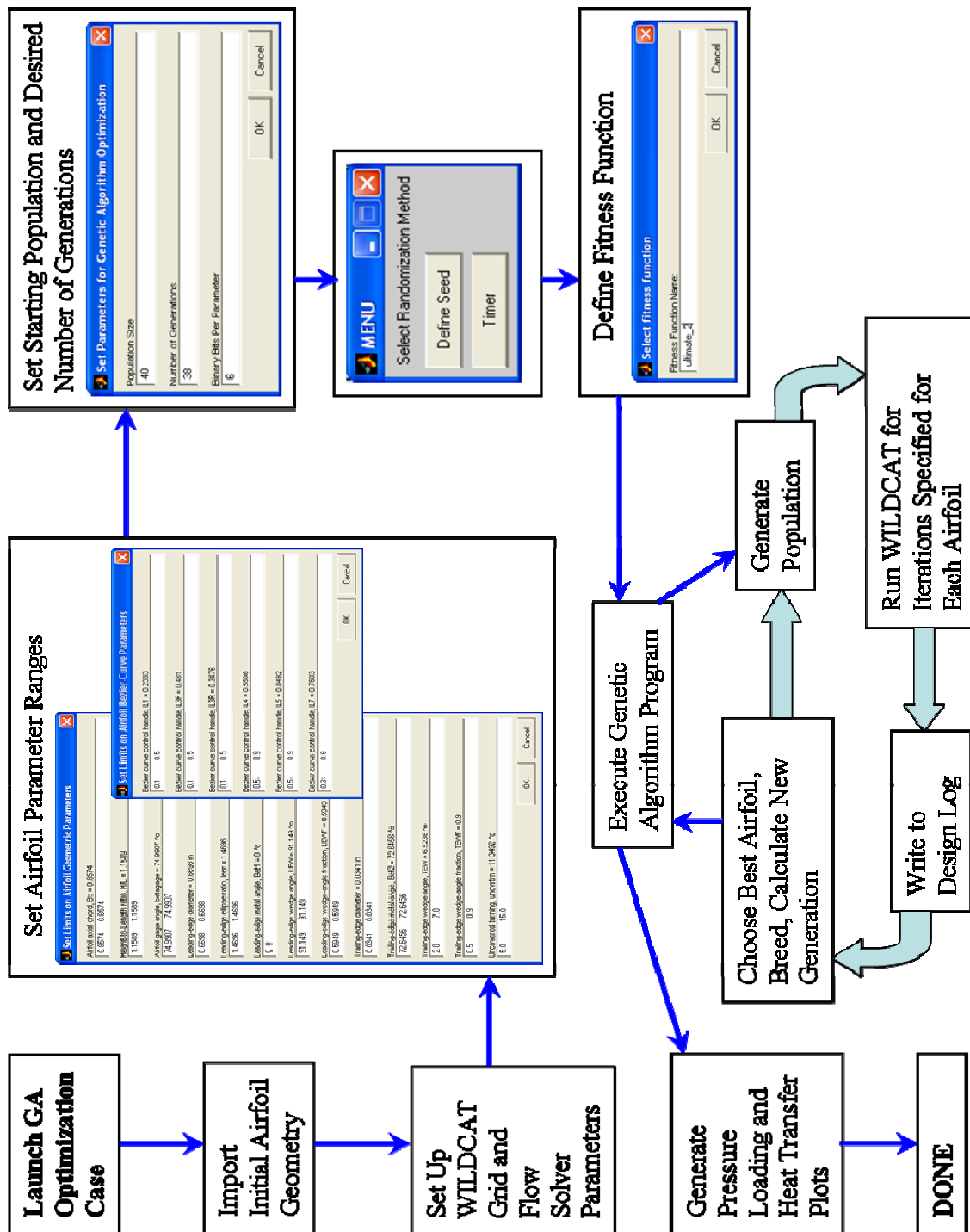


Figure 11 Genetic Algorithm Setup and Process Methodology

In summary, the VKI airfoil was transformed and redesigned to the desired lowered heat transfer specifications following the general steps described below:

- 1) The airfoil was run through numerous automated SQP optimization iterations to reduce overall heat load.
- 2) Knowing the objective of step 1 was too ambiguous and unsatisfied with the results in that step, the two main objectives stated above were enforced.
- 3) The *Drive to Target Loading* function with SQP optimization was used to attempt to delay transition.
- 4) Hand-iterations and good design judgment were used to aid in reducing LE heat load by examining airfoils with large LEDs. This also supplied a favorable starting position for the GA process which cut down on computing time.
- 5) The best airfoil obtained from the process above was entered into a 40 object by 38 generation GA which further explored the problem space reiterating the objectives illustrated above and the final airfoil calculated was selected.

As a result, suitable airfoil geometry had been created that met the two main objectives pertaining to reduced surface heat load. Hereafter, the new geometry will be referred to as the low-heat-load vane, or LHL. Once a solution was found, the two airfoils could be compared in a real turbine-representative flow environment.

IV. Experimental Apparatus and Design

Shock Tube Theory

Shock tubes have been used ad nauseam in the past by experimentalists interested in studying thermodynamic and chemical properties of gases. A shock tube is a laboratory device made up of a driver and driven section separated by a diaphragm and is used to create the high temperatures and pressures required in this study. The end of the shock tube driven section is connected to a linear cascade test section used to test the airfoils for midspan heat load. The dimensional and structural specifics of the shock tube and test section will be discussed in the next section. The following will summarize the physics of shock tube operation as described by Anderson [44], in order to set up the appropriate flow conditions for analysis of heat transfer in the cascade. The driver section will be referred to as region 4 and the driven section is region 1 as seen in Figure 12 below showing the shock tube before the diaphragm is broken. The shock pressure ratio is defined as the driver pressure divided by the driven pressure (P_4/P_1).

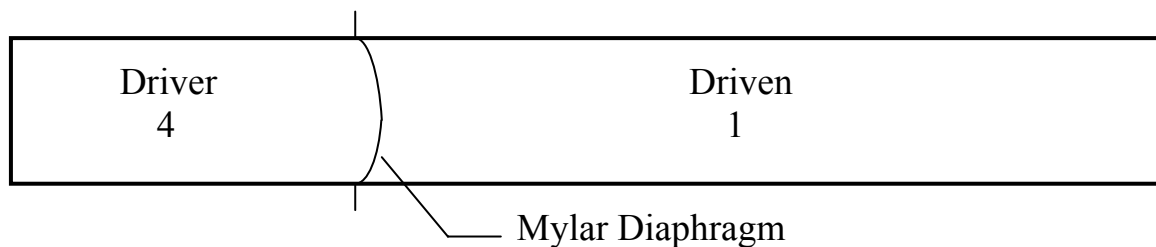


Figure 12 Shock tube regions before rupture of diaphragm.

In general terms, when the diaphragm dividing the sections is broken, a shock wave propagates down the tube through the driven section and is reflected at the end of

this section due to the constricted flow passage in the test section. Meanwhile, an expansion wave (or rarefaction wave) simultaneously travels up the driver side and reflects at the closed end as well. These waves continue to reflect back and forth passing each other over the length of the shock tube until the equilibrium atmospheric pressure is reached throughout the internal volume of the tube.

In more depth, after the diaphragm is ruptured, a strong shock wave (in hypersonic compressible flow terms, a translating normal shock) is generated inside the tube bringing behind it high temperature and high pressure gas and imparting a mass motion velocity as prescribed by normal shock relations [44]. Figure 13 below shows the shock tube sections and gas regions after the diaphragm is broken. As the shock wave travels into the driven section the expansion wave moves into the driver section at the local sonic velocity, which depends on the properties of the desired gas.

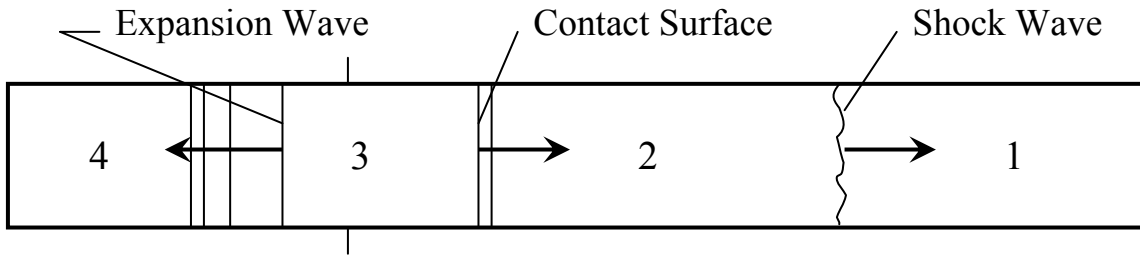


Figure 13 Flow phenomena in a shock tube after diaphragm is broken.

Assuming more time has passed, after reflection of the incident shock wave at the far end of region 1 where the test section connects, the wave moves back into region 2 as shown Figure 14. This causes an even further increase in pressure and temperature behind the reflected shock wave creating a region 5 as shown in Figure 13 below. It is this region that sets up to form the inlet test conditions for the linear cascade test section for vane

heat transfer experimentation. The resulting pressure difference in this region compared to the ambient pressure outside causes the flow to move through the cascade. Thus the flow properties in the test section inlet will be somewhat close to the conditions generated behind the reflected shock wave. Note that regions 2 and 3 have the same pressure and velocity in which region 3 is created via isentropic expansion and region 2 is created by way of a highly viscous shock event. They are separated by a contact surface which is the interface between the driver and driven gases which moves at the velocity of the gas behind the shock wave. This, however, is not important since both the driver gas and driven gas are atmospheric air for the purposes of this study. Finally, a sixth region is generated behind the reflected expansion wave which will not be of significance for these testing purposes.

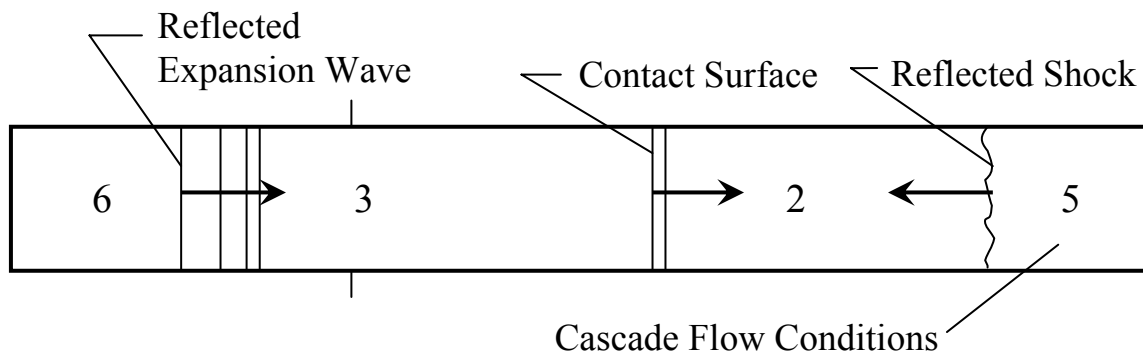


Figure 14 Shock tube flow regions after first shock wave reflection.

Shock tubes can create flow conditions which are easily and highly repeatable and use very little power or resources, but one disadvantage is the exceptionally short duration of desired flow conditions due to the extremely fast nature of equalization of shock and expansion waves in the tube. Typically, test times from a shock tube can vary from 5 to 30 ms, depending on the length of the tube, which will be seen later in this

paper for this case, and which also agrees with experiments done in the past using shock tubes to generate test conditions such as the work completed by Dunn in the late 1970s and all of the 1980s in his turbine heat transfer experiments. Therefore, the pressure and temperature boundary conditions for this experiment can be described as quasi-steady state, since viewing test data with a broad resolution flow characteristics would look unsteady, but with high enough time resolution of data acquisition, the flow conditions actually achieve steady conditions for times on the order of the test times given above. However, as will be seen in following discussions, the heat transfer assessed is undoubtedly unsteady. The physical reason for the short test times is explained with reference to Figure 15 which shows the temporal nature of each wave, or disturbance, in the shock tube plotted against distance traveled, x . Assuming the test section is located at the end of the driven section as it is for this experiment, it can be seen that the test time available is the interval between reflection of the incident shock wave off the test section inlet and the next subsequent disturbance. Depending on the initial conditions of the shock tube, this second disturbance could either be the reflected expansion wave from the driver end or a reflection off the contact surface of the shock wave that had traveled back into region 2 [10]. Proper detection of the actual shock tube run times requires appropriate instrumentation and data acquisition frequencies as will be explained later in the experimental results discussion of this paper.

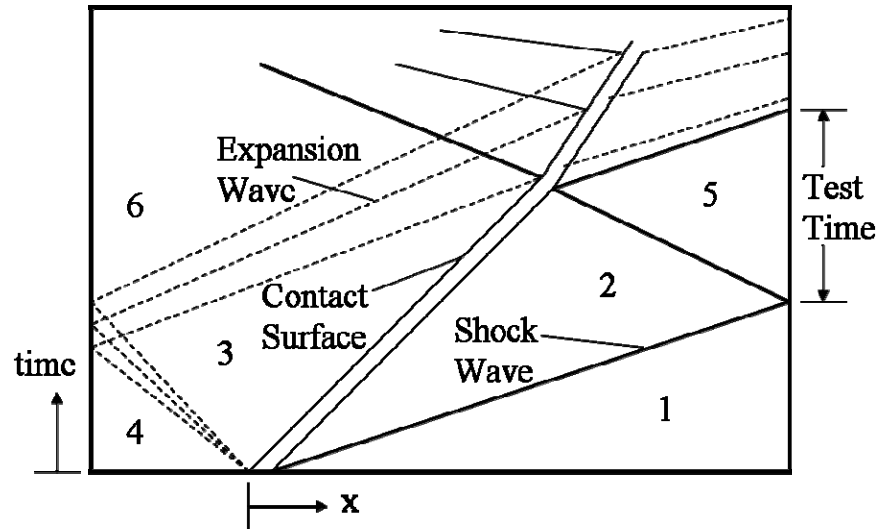


Figure 15 Shock tube temporal wave phenomena.

Subsequently, out of this theory originated a set of equations found in Anderson [44] for unsteady wave motion which can be used to predict the conditions of the flow entering the test section based on the given initial pressures in the driver and driven sections and the properties of the working gas. This detailed sequence of shock tube equations can be found in Appendix B of this document which can be used for hand calculation or programmed into applicable software. A MATLAB code was created for just such a purpose and became useful in setting up the experimental run condition matrix, which helped identify the test section inlet temperatures and Re based on vane chord resulting from varying driver pressures, and will be explained in the procedural section of the experimentation portion of the thesis.

Experimental Hardware

Shock Tube Facility

Many different facilities have been used in the past to perform turbine related heat transfer studies. They essentially fall into two main categories, long run-time (i.e. steady state) facilities and those that have short run durations. Notable long run-time facilities include those used by Blair [23], Graziani [12] and York [6] which tend to be more common in industry. Short run-time facilities of distinction include the shock tunnel facility used extensively by Dunn et al. and the isentropic light piston tunnel (ILPT) established by Jones, Schultz, Oldfield et al. [30]. The apparatus used here falls into the latter category, along the lines of the facilities used by Dunn et al. [4], as short-duration methods use much less power, are less expensive to operate, and are regularly much more convenient and repeatable than long run-time flow facilities. In addition, as seen by the above works, short run-time facilities have long been established as a validated technique for performing aerodynamic and heat transfer measurements.

For the experiment at hand, a rectangular cross-section, low shock pressure ratio shock tube used in past AFIT theses experiments by Frye [7], Gochenaur [8] and Fillingim [10] was used to model the high temperature, high pressure environment of a turbine inlet in order to measure heat transfer on the nominal and optimized vanes in a turbine-representative environment. The shock tube, currently in use by AFRL, consists of a high pressure driver section and a relatively low pressure driven section separated by a diaphragm. The driver section can be pumped up to a desired pressure while the driven side can be evacuated to a desired pressure to increase the magnitude of shock pressure ratio. In the current experiment, only the driver side pressure is increased and the driven

side is kept at atmospheric pressure. Using well established transient test techniques, the shock tube can be used to obtain spatially resolved heat transfer rates on different gas turbine components. The facility provides a clean, uniform, and accurately-known gas-dynamic condition at the test section inlet. Figure 15 is an image of the shock tube setup.

The shock tube is a total of 16 ft in length with a 4 ft long (1.22 m) driver section and a 12 ft (3.66 m) driven section and a uniform rectangular internal cross section 4 in (10.15 cm) by 8 in (20.32 cm). The shock tube itself is described in greater detail in Frye [7]. A 120 psi compressor air supply system was used to increase and control the driver side pressure. The driver section lies on a 2-axis mobile platform for ease of repeatability of experimental runs in replacing diaphragms and removing used diaphragm fragments. Once a proper diaphragm is installed, the driver and driven sections are held together with a hydraulic clamp built on to the driven section and operated using a hand-pump. Mylar sheets of varying thickness are available for use in the shock tube as diaphragms to separate the two sections. For the purposes of this effort, the diaphragms used were 7 mils (0.007 in) thick and installed with thin rubber gaskets on both sides between the clamped sections to help prevent air leakage. This diaphragm thickness, as will be explained in the experimental procedure, was exclusively used as a result of the limitations of other thicknesses. Figure 17 shows the diaphragm interface. The diaphragm was ruptured and the shock initiated using a non-intrusive hand-trigger-operated pneumatic spike built into the center of the driver section. The driver section pressure was monitored by a Kulite pressure transducer rated to 100 psia linked to a computer, which will be elaborated when the shock tube instrumentation is addressed. The shock tube was connected to the vane cascade test section at the end of the driven section.

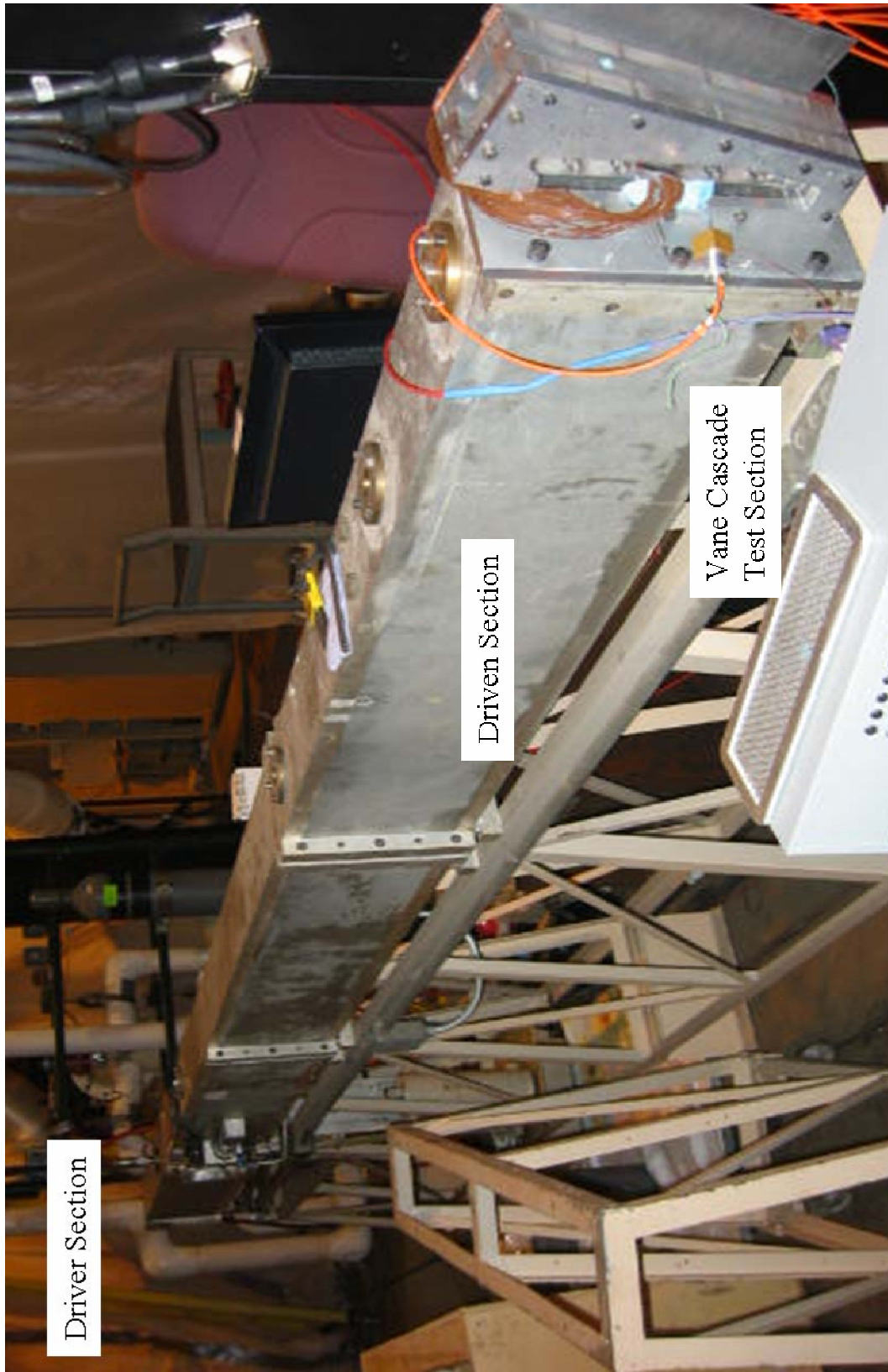


Figure 16 AFRL 16-foot Shock Tube and Transonic Vane Cascade

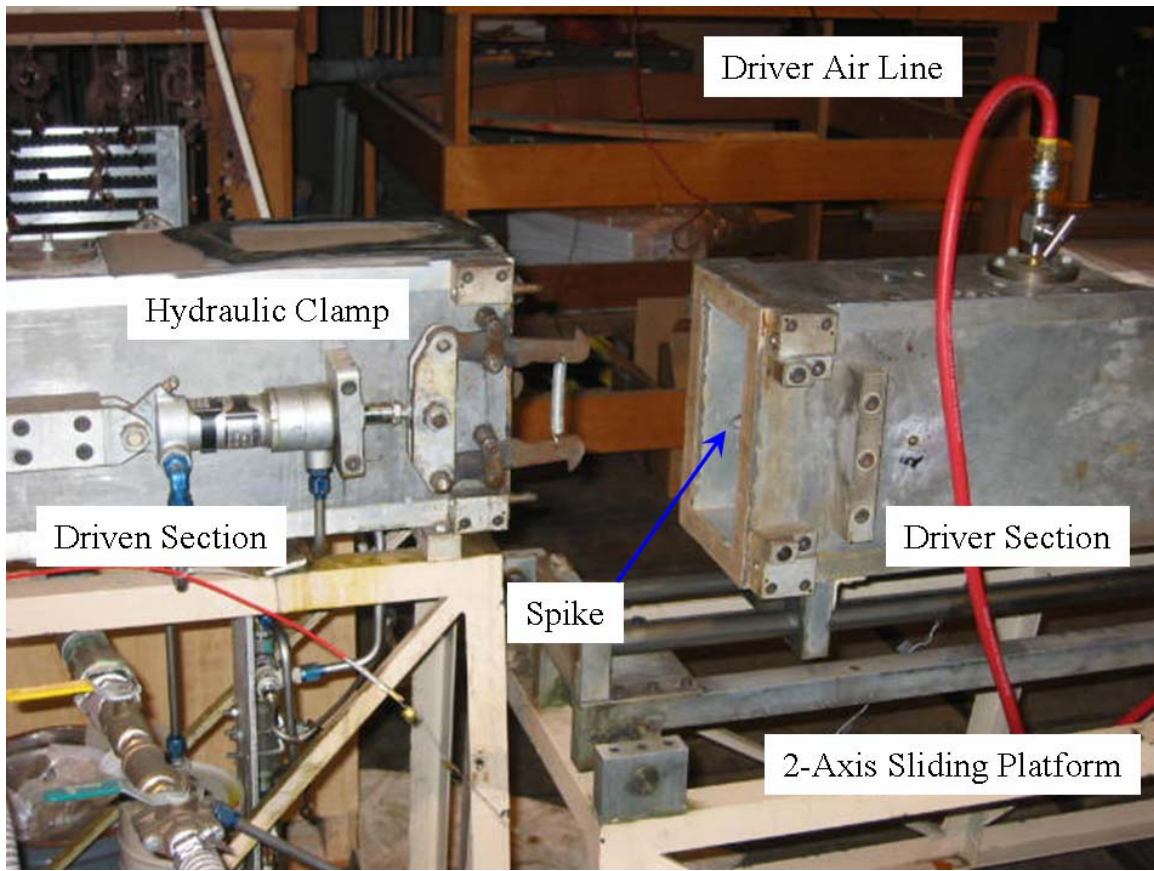


Figure 17 Image of hydraulic clamp and diaphragm-rupturing spike at shock tube section interface.

Flange Piece

A piece of hardware was designed and fabricated to serve the purpose of connecting the shock tube to the test section, providing a somewhat smooth transition for the flow to the test section, and housing the turbulence grid. This flange piece replaces the shock reflection section used by Gochenaur [8] and Fillingim [10] in their experiments which protected the test section and delicate instrumentation from mylar shrapnel (which could be produced when the diaphragm is broken) and ensured appropriate shock reflection. From their work it was discovered that since the flow is choked downstream in the test section the flow undergoes a significant area reduction, the shock reflection section was not necessary. This was seen in the similarity of

Gochenaour's data with and without use of the reflection section. In the present experiments, the flange piece provides a smooth but sudden area reduction to ensure reflection of the shock back into the tube. Rarely did mylar pieces from a broken diaphragm travel downstream into the test section. If there was shrapnel, the test section was detached and the shrapnel removed from the end of the driven section and the run was repeated to ensure the heat flux gauges did not make errant measurements due to pieces covering the instrumented vane. During routine operation, the diaphragms would break cleanly in a diagonal pattern resulting in no fragmented pieces.

The flange piece provided a smooth transition for the flow between the internal rectangular tube cross section (4 x 8 inches) and the smaller (1 x 8 inches) rectangular cross section of the test section inlet by having a 0.25 in radius fillet on the edge of the inlet opening. The flange piece had to take up as little axial space as possible, so as to not provide more end-wall surface for boundary layers to grow, since the shock tube rig did not have a boundary layer bleed plenum like much of the work of Dunn [5] did. The flange piece also had an inlay so the turbulence grid could be sandwiched between the screwed-on test section and shock tube when necessary for the flow conditions and easily be removed or replaced. The opening to the test section also lies in this inlay, so the flow encountered the grid at the appropriate distance upstream of the vanes and then proceeded to undergo an area reduction into the cascade. Figure 18 below shows a drawing with dimensions while Figure 19 is an image of the flange piece designed for the experiment. The flange piece was bolted to the test section in the inlay section and bolted back to the shock tube using the larger bolt holes on the outer part of the piece. The thickness of the piece was $\frac{1}{2}$ in and $\frac{1}{4}$ in at the inlay.

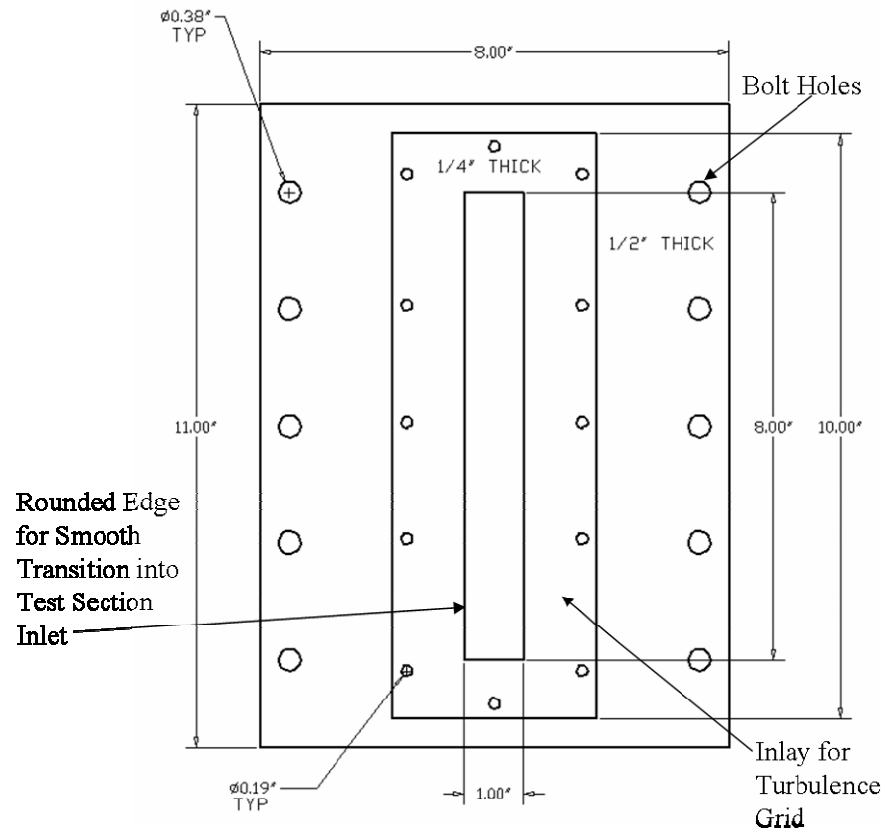


Figure 18 CAD drawing of shock tube flange piece without turbulence grid.



Figure 19 Image of flange piece that connects test section to shock tube.

Turbulence Grid

A turbulence grid was necessary for experimentation for providing the appropriate freestream turbulence intensity, Tu , for each run. The term freestream is used here to describe any undisturbed flow not inside a boundary layer. Since the VKI test with $Tu = 6\%$, and exit Mach number of 0.8, and $Re = 10^6$ was chosen to simulate experimentally with the shock tube as explained before, a grid needed to be designed to generate the prescribed Tu . While Arts [29] tested the VKI vane at multiple intensities, only the 6% Tu condition is simulated here experimentally for simplicity and reduction of variables, and hence only one grid was used for this project. With no grid in, the natural freestream turbulence of the shock tube of approximately 2% can be simulated. However, with the fabrication of more grids, it may be possible to further test the vanes at other values of Tu . Figure 20 below shows a CAD drawing with dimensions and an image of the turbulence-generating grid used in the shock tube experiments.

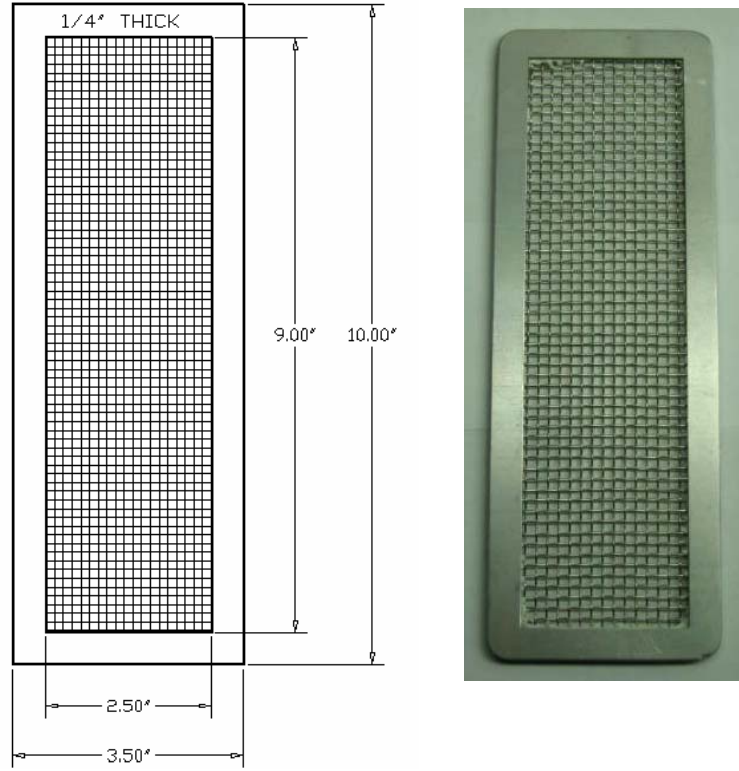


Figure 20 Drawing and image of turbulence grid used to generate approximately 6% Tu.

The grid was designed first by reviewing the work of Roach [45], who composed a database of varying grids that generate a unique value of Tu, depending on the mesh type, grid wire diameter, wire spacing, and distance upstream from the desired location of freestream turbulence measurement. The measurement point for this experiment would be the location of the leading edge of the vane cascade. Roach used the following correlations below, 3 and 4, to describe turbulence intensity and axial integral length scale, respectively,

$$Tu = C \left(\frac{x}{d} \right)^{-\frac{5}{7}} \quad (3)$$

$$\frac{\Lambda_x}{d} = I \left(\frac{x}{d} \right)^{\frac{1}{2}} \quad (4)$$

where $C = 0.8$ and $I = 0.2$ are constants derived for square meshes with round wire cross sections, x is the axial distance from the grid wires to the location of theoretical measurement of Tu , and d is the wire diameter. Reviewing the grids used by Roach to achieve the necessary Tu , an appropriate wire diameter value was known and the grid upstream distance, x , could be calculated. This distance turned out to be 1.375 in, which governed the design thickness of the flange piece discussed earlier at $\frac{1}{2}$ in. Thus, the grid used for these tests was a $\frac{1}{4}$ in thick plate with a square mesh and a wire diameter of 0.035 in (0.889 mm) and spacing between wire centers of 0.132 in (3.353 mm). These values gave an actual theoretical value of Tu according to Roach of 5.82%, which was deemed close enough to the 6% necessary. This also creates integral axial length scales, Λ_x , of 0.044 in at the vane leading edge, which was found by Roach to have no Re dependence. Since the theoretical values of Tu and Λ_x in equations 3 and 4 were found in experiments using steady flow wind tunnels, the freestream turbulence levels will be measured experimentally for the abruptly established unsteady flow of the shock tube apparatus to ensure that the actual values of Tu are close to the expected values of Tu . The results of these measurements are given in the results section of the paper.

Linear Cascade Test Section

The test section used in the current experiment made it possible to take valuable data concerning the heat transfer at midspan for both the VKI and LHL vanes. The vanes were lined up in a row, or a cascade, to represent the orientation of the vanes as they are in an actual turbine engine. A cascade takes a portion of the annulus of blades or vanes in a turbine and straightens them out into a linear row to create a 2-D physical

representation. Enough vanes were used to create good periodicity (a repetition of flow properties due to the vane row from passage to passage) in the proximity of the vane that data will be taken on and to limit any secondary flow effects caused by the physical limits of the test section. In addition, it should be noted that while the pressure and temperature entering the cascade test section provide realistic non-dimensional flow parameters, the flow in the experiment is atmospheric air and not combustion products from a combustor as in the real environment of a turbine engine inlet.

The vanes were separated by a pitch, s , of 1.33 in creating six passages between vanes to provide for good flow periodicity. This resulted in a solidity (b_x/s) of 0.64 and hence a pitch-to-chord ratio, s/b_x of about 1.56. The original nozzle guide vane tested by VKI had an axial chord, b_x , of 1.645 in. The vanes tested in the shock tube cascade are approximately half scale (52%), having an axial chord of 0.8575 in, which results in a relatively low aspect ratio (AR) of 1.166. This is the value used in the numerical portion of the thesis for both the VKI and LHL vane, which was kept constant as a main control to simplify the optimization of the vane and reduce complexities due to the necessity of different turbine stage axial dimensions caused by larger or smaller axial chord lengths. Finally, as these are nozzle guide vanes, the inlet flow angle to the cascade, α_1 , is 0 deg.

The cascade vanes were chosen to be comparable with typical turbine engine flow conditions. Figure 21 plots first vane (1V) exit Mach number against reaction (which is the ratio of rotor static pressure change to the stage change in static pressure) for a modern High-Impact Technology (HIT) turbine rig for a constant AN^2 value, where AN^2 equals the vane annulus area times the rotor speed in RPM squared. Generally, an increase in AN^2 indicates an increase in the state-of-the-art of turbomachinery. Table 1

shows that both vanes being tested experimentally have exit Mach numbers consistent with modern high reaction turbines. In addition, their pitch-to-chord ratios and Zweifel coefficients are larger than state-of-the-art military turbines (e.g. the F119 and F120). So, since the vanes happen to show evidence of healthy aerodynamic qualities they are a suitable step in the direction of the HIT turbine rig, which is itself a representative turbine for long-range strike aircraft. The term Zweifel coefficient is defined by the ratio of tangential force per unit depth to the maximum tangential force that can be achieved efficiently [46], and is common in determining loading in turbine stator and rotor design.

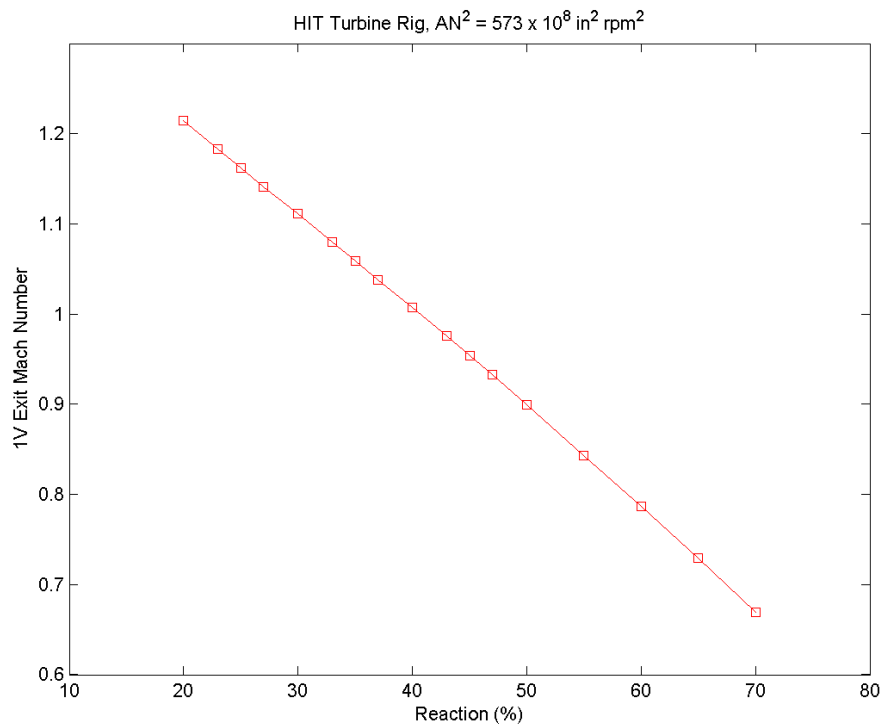


Figure 21 Typical variation of first vane isentropic exit Mach number with reaction for a modern High-Impact Technology (HIT) turbine rig.

Table 1 Comparison of VKI and LHL vane details with modern nozzle guide vanes.

Vane Details	F119	F120	HIT TR	VKI	LHL
Exit Mach Number	0.82	0.67	0.89	0.80	0.80
Pitch / Axial Chord	1.39	1.46	1.91	1.56	1.56
Zwiefel Coefficient	0.73	0.74	0.85	0.79	0.77
Turning (degrees)	75	74	78	75	75

The framework for the test section is the same used by Gochenaur and Fillingim in their work. Seven identical, smooth ABS (Acrylonitrile Butadiene Styrene) plastic vanes fabricated in the AFIT 3-D printer plated with a very thin layer of copper 15 mils thick made up the linear cascade which sat between two $\frac{3}{4}$ in clear plexiglass walls which were screwed together by the metal framework on the outside. The copper layer was added to make the vane surfaces smoother than if they were just the rough plastic from the 3-D printer. It was decided that since the layer of copper was so thin relative to the thickness of the vanes, that the plastic vane thicknesses did not have to be reduced to accommodate the copper thickness. Also, it was verified that the test times using the shock tube are so short that conduction effects to the copper through the thin film gauge substrate are negligible (see Appendix Figure D.2). The area ratio of the test section is 4 with the inlet and outlet having areas of 8 and 2 in², respectively. Thus the throat of the test section is at its exit. The cascade lies 1 inch downstream of the test section inlet. Both sets of vanes had the same value of flow turning, about 75°, just as they did for their CFD analyses. The inlet Mach number upstream of the cascade row can be estimated from the known test section area ratio, $A/A^* = 4$. From isentropic relation tables for air (assuming $\gamma = 1.4$) this critical area ratio corresponds to an inlet Mach number, M , of about 0.15 and an inlet static to total pressure ratio, P_t/P_0 , of 0.9844. From this P_t can be

found and knowing that the exit static to total pressure ratio is found by $P_{ex}/P_0 = P_{ex}/P_i * P_i/P_0$, the exit isentropic Mach numbers are found to be between about 0.80 and 0.85 for most runs. This value is comparable with the vane exit Mach numbers seen in Table 1 by designers of a future research turbine [47], and by Gochenaur [8], Fillingim [10], Dunn [17], and Arts [29].

The test section plexiglass walls held the vanes in place by compression using metal pins, three per vane, and these lie in a pattern such that both the VKI or LHL vanes could be installed for testing at any time. The most upstream pin holes were used as a reference point to ensure the same space between that pin and the forward-most point on the vanes were the same between the VKI and LHL versions when planning the locations of the pin holes to be drilled in the vanes. When the metal framework was unscrewed, the test section could be pulled apart and the vane sets easily exchanged. Only the middle vane, the fourth, was instrumented at midspan for heat transfer measurements with state-of-the-art thin film heat flux gauges which will be explored in detail shortly.

The cascade vanes each had a span, h , of 1 in. Since this is a relatively short vane span (thus a small aspect ratio), there is good reason to believe secondary flow effects could hinder quality heat flux data at midspan. Appendix C gives a detailed analysis of the 3-D vane flow-field in the test section using CFD tools and recent empirical prediction techniques from open literature to find that the 1 inch flow width is rather worthy for making midspan measurements here. With the combination of turbulence and secondary flow effects due to short span or too much turning, the midspan heat transfer measurements may be severely augmented or distorted, which would not compare well with past runs in other facilities with the same conditions, or compare well to the

WILDCAT predictions. Khalatov et al. [48] used a 5-vane cascade to find that midspan heat transfer actually decreases while endwall heat transfer increases as the pitch decreases and that higher levels of freestream turbulence had significant effects on laminar-to-turbulent transition and the resulting heat transfer. Assuming this is true, increasing pitch to compare to modern turbines as discussed above may be risky. The quick study in Appendix C reveals that horseshoe vortices generated due to end wall secondary flow only propagates to 15% span on each end of the vane at the trailing edge, suggesting it is safe to monitor flow properties such as heat flux at 50% span.

Figure 22 below shows the shock tube linear cascade test section and its main features with the air flow going from right to left. The static pressure tap arrays upstream and downstream of the vane row in the plexiglass end wall were essential in calculating Mach numbers for each run. The two other instrumentation ports positioned on the opposite plexiglass end wall were used for probes to record total temperature (T_t) and total pressure (P_t). These same ports would later be used to measure T_u and length scales using a hot-wire anemometer probe to test the grid and make comparisons with theoretical T_u . An upcoming summary of instrumentation for the entire shock tube experiment will paint a better picture of all flow aspects recorded. Figure 23 is a photograph of the cascade without instrumentation from the side of the airfoil-shaped endwall hole that the thin film instrumented vane would go into and pin to the other endwall. Finally, no dump tank was attached to the end of the test section as in previous works using the shock tube. There was no need to add one, except to subdue the noise of each shock tube run, in which case adding a large dump tank would be more trouble than necessary. Thus, the flow through the shock tube exited out to atmospheric pressure and

the extremely short-lived noise of each run was not considered a problem when wearing hearing protection.

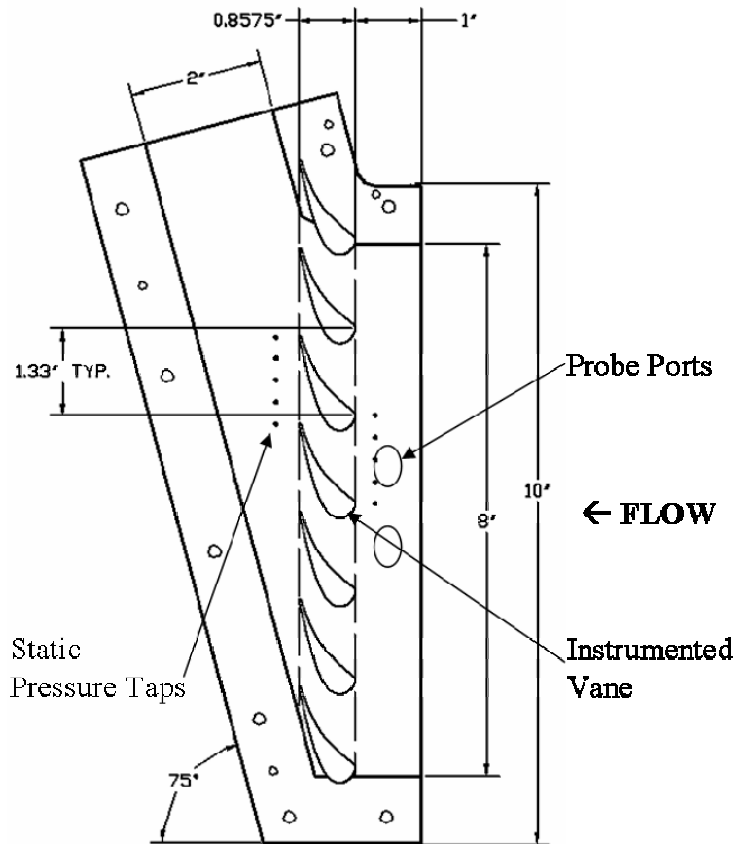


Figure 22 Schematic of shock tube linear 7-vane cascade test section (shown here with VKI vanes installed).

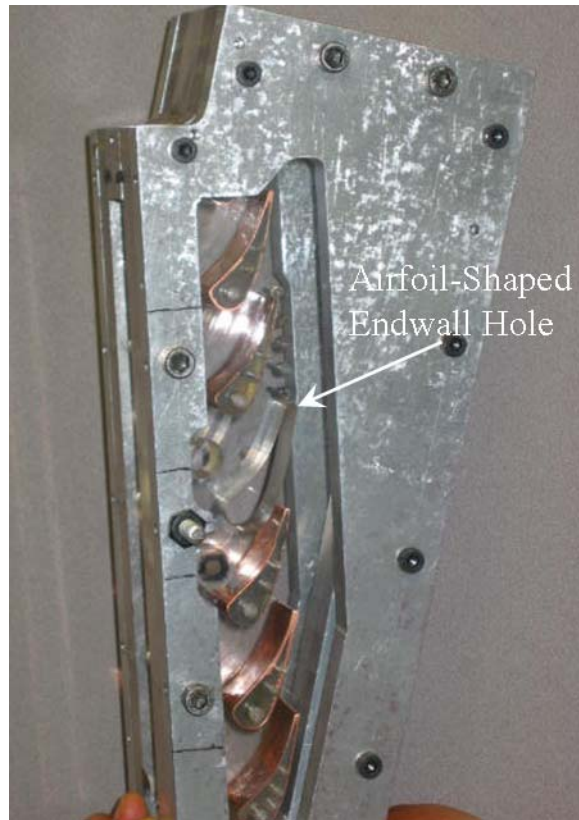


Figure 23 Image of the cascade test section without data instrumentation.

Thin Film Heat Flux Gauges

Gauges similar to those used in this experiment have been used a great amount in the past in multiple works and validated for short-duration heat transfer measurements by researchers such as Dunn [49], Fillingim [10], and Oldfield [50]. Heat transfer rates are inferred from the temperature distribution data gathered by the short response-time thin film resistance gauges. Modern high-density thin film heat flux gauges fabricated and designed at AFRL were used to obtain heat transfer data at the midspan of each vane in order to compare the VKI to the LHL vane in the turbine-representative shock tube test section environment. The gauges designed specifically for this experiment are fundamentally similar to those used by Dunn [49] and others in the past in that voltage

changes are measured across a thin film resistance under constant current. However, the high density array gauges used here follow the design methods of Anthony [51] and that they have many advantages over older technology gauges. The newer gauges can be aligned directly next to each other end to end as will be seen in this experiment. These flexible films are virtually non-intrusive to the flow lying flush on the curved surface of the vanes. Voltage leads may be as thin as possible which takes up significantly less surface space; their resistances are not critical as no current is passed over the leads. The compilation of gauges and leads can be all one material, instead of having leads of a lower resistance material such as copper, which greatly improves manufacturing efficiency. Finally, only one constant current supply is necessary to power all the gauges on a film array in which the current may be monitored with a low temperature coefficient resistor located in series with the current wires. As a result, these heat flux films can be used to take revolutionary heat transfer measurements in complex locations in turbomachinery such as hub platforms, shrouds, cooling flow locations, and more.

The gauges are composed of a thin flexible Kapton insulating substrate layer 50 microns thick with known thermal properties underneath a thin layer of conducting platinum metal 500 Angstroms thick sputtered on top. They were carefully adhered to the VKI and LHL vanes to be positioned in the middle of their respective cascades using an adhesive 50 microns thick with a release liner to expose the adhesive when ready to be applied to a surface. The platinum thin films with substrate are designed very thin so they may be applied to any surface to make measurements, thus the instrumented vane in the middle of the test section vane row was not reduced or undercut to accommodate the miniscule thickness of the films.

The platinum thin film gauges traditionally work assuming the semi-infinite slab heat transfer principle for the substrate layer. Using the known properties of the gauge, the vane surface temperature may be determined from voltage differences detected by a data acquisition system with a high sample frequency. A constant current is passed through the gauges and changes in voltage across the gauge are proportional to changes in the surface temperature. This theory for these types of gauges has been laid out in detail in numerous works including Fillingim [10], Oldfield [50] and Doorly [52]. A detailed summary of physical heat flux gauge operation and the applied theory is given in Appendix D, where it can be seen how raw voltages are converted to values of surface heat flux. A great amount of tedious work goes into the proper fabrication of the thin film heat flux gauges used in this experiment as well. A step-by-step summary of the AFRL photolithography process in producing the thin films is found in Appendix E.

In order to obtain detailed midspan spatial heat transfer resolution, a higher resistance gauge density was used here than in the work of Gochenaur [8], Fillingim [10], Oldfield [30], and for the earlier works of Dunn [5]. The VKI and LHL vanes had a total of 27 and 28 midspan thin film gauges, respectively, since the LHL vane had a slightly larger surface distance. The VKI vane had 10 gauges on the PS and 17 on the SS, while the LHL vane had 10 gauges on the PS and 18 on the SS. Table 2 shows the gauge sizes and temperature coefficients of resistance (α) in terms of $1/(^{\circ}\text{C})$ that were a result of instrumented vane calibrations. These coefficients were found by taking measurements in an oven at four different temperature steps. They would later be used in the calculation of heat flux from raw voltage data from the shock tube experiment. Due to time constraints for the availability of data processing equipment, the calibration had to

be done after the actual cascade experiments. By the time the calibration was performed, the VKI thin film had lost function in 5 of 27 gauges while the LHL film had lost function in 8 of 28 gauges. Therefore, the broken gauges were assigned the α of the closest neighboring gauge of the same size (small or large). These assumed values of α are shown in italics in Table 2. Details on the calibration of the heat flux gauges can be found in Appendix F.

Table 2 Temperature Coefficients of Resistance for the VKI and LHL gauges.

Gauge No.	Gauge size	α [°C ⁻¹]	
		VKI	LHL
1	L	0.001604	0.001587
2	L	<i>0.001604</i>	0.001676
3	L	<i>0.001568</i>	<i>0.001676</i>
4	L	0.001568	<i>0.001547</i>
5	L	0.001574	0.001547
6	S	0.001594	0.001564
7	S	0.001569	<i>0.001564</i>
8	S	0.001594	0.001495
9	S	0.001577	0.001532
10	S	<i>0.001577</i>	<i>0.001532</i>
11	S	0.001478	<i>0.001532</i>
12	S	<i>0.001478</i>	<i>0.001527</i>
13	S	0.001521	<i>0.001527</i>
14	S	0.001578	0.001527
15	L	0.00163	0.001575
16	L	0.001612	0.001494
17	L	0.001605	0.001598
18	S	0.001576	0.001609
19	S	0.001528	0.001572
20	S	0.00154	0.001609
21	S	<i>0.00154</i>	<i>0.001609</i>
22	S	0.001537	0.001608
23	S	0.001496	0.001582
24	S	0.001497	0.001563
25	S	0.00149	0.001556
26	S	0.0015	0.001541
27	S	0.001492	0.00153
28	S		0.001528

Approximate Gauge sizes:

Small (S): 0.2 mm x 2.0 mm

Large (L): 0.4 mm x 4.0 mm

The thin film gauges used in these experiments required a great amount of design considerations before they could be fabricated. The sizes of each gauge as seen in Table 2 are consistent with good design practice meeting the minimum 10:1 length-to-width ratio recommended for good data collection [51]. The next design consideration had to do with the leads that connected the gauges to the lead wires. Good heat transfer resolution required gauges that were as small as possible and as close together as possible. However, they could not be too close, since they had to accommodate the minimum soldering width for attaching lead wires. The design of the gauges also took into consideration how the gauge leads and lead wires were to exit out of the cascade test section. This was resolved by making the middle instrumented vane with a 2 in span, twice as long as the other vanes, and having a perfectly positioned airfoil-shaped hole in the plexiglass end wall 1/16 in thicker than the airfoil all around so that the delicate film leads, their fragile solder points, and the lead wires could easily be led out of the test section to the data acquisition components uninhibited. As an aside, this thin opening all around the instrumented airfoil was kept open to protect the thin film and in the worst case bled the boundary layer a bit to possibly reduce end wall secondary flow, aiding in good midspan measurements. This required two different plexiglass pieces, one for each airfoil shape, which had to be switched when switching the vane cascade between the VKI and LHL geometries. Finally, to properly investigate the heat transfer around the airfoil, as the focus areas for this study as described before were reduced LE heat load and delayed transition, the gauge densities were increased (and the gauge sizes were decreased to the minimum possible size) near the leading edge and past approximately 50% of the suction surface for each vane. This provided increased data resolution around

the surface in the areas of interest. Thus, there were two different gauge sizes on the thin films, which will be termed small and large. Small gauges measured 0.2 mm by 2.0 mm while large gauges were 0.4 mm by 4.0 mm with room temperature resistances of approximately 50 and 170 ohms, respectively. As a result, large gauges had 4 times the area of the small gauges, and as a fundamental design requirement, the aspect ratio for all gauges were subsequently kept constant. All gauges were spaced 0.2 mm apart. The actual coordinate locations of the heat transfer gauges with respect to the leading edge for both vanes are listed in Appendix G. Figure 24 shows the heat flux gauge design for VKI as it is ready to be printed (drawn using Corel Draw) with a blow-up of the actual gauge area from where heat flux is inferred (shaded green). The image appears backwards because of the nature of the production process in printing the gauge design and eventually having it exposed, developed, and sputtered with platinum. The white areas represent the actual platinum pattern on the film. The current, shown in red, runs through the first and last leads in the gauge and a voltage difference is read through the leads for each individual gauge area. It can be seen where the SS, PS, and LE of the VKI vane are located along with the concentration of smaller gauges near the LE and on the SS where transition tends to occur. Finally, Figures 25 and 26 are images of the produced platinum thin films as installed on the vane and lying flat off the vane, respectively. In the instrumented vane picture, it can be seen that the wires (2 wires per lead to get a voltage difference) are soldered on to each lead on the gauge and then covered with an epoxy substance to help firm up the connection.

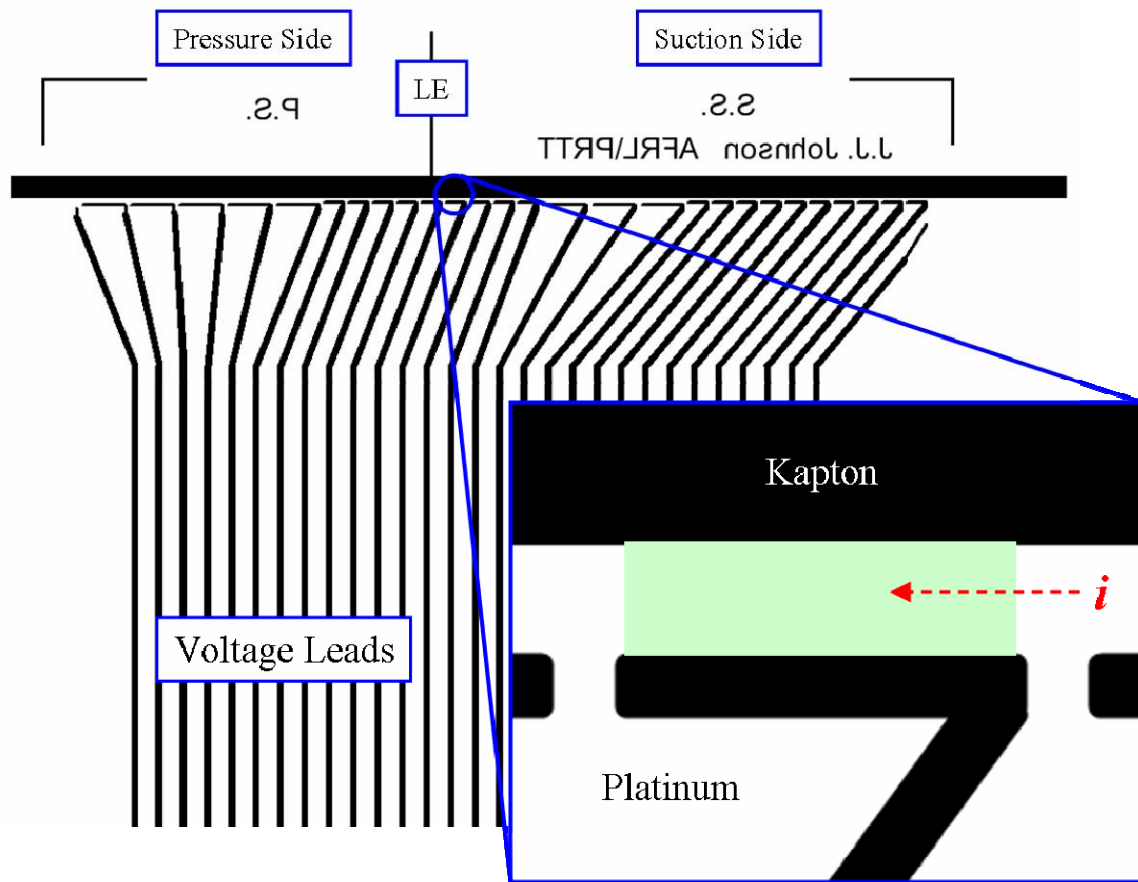


Figure 24 Design drawing of platinum thin-film heat flux gauge array with expanded view of a single gauge area.

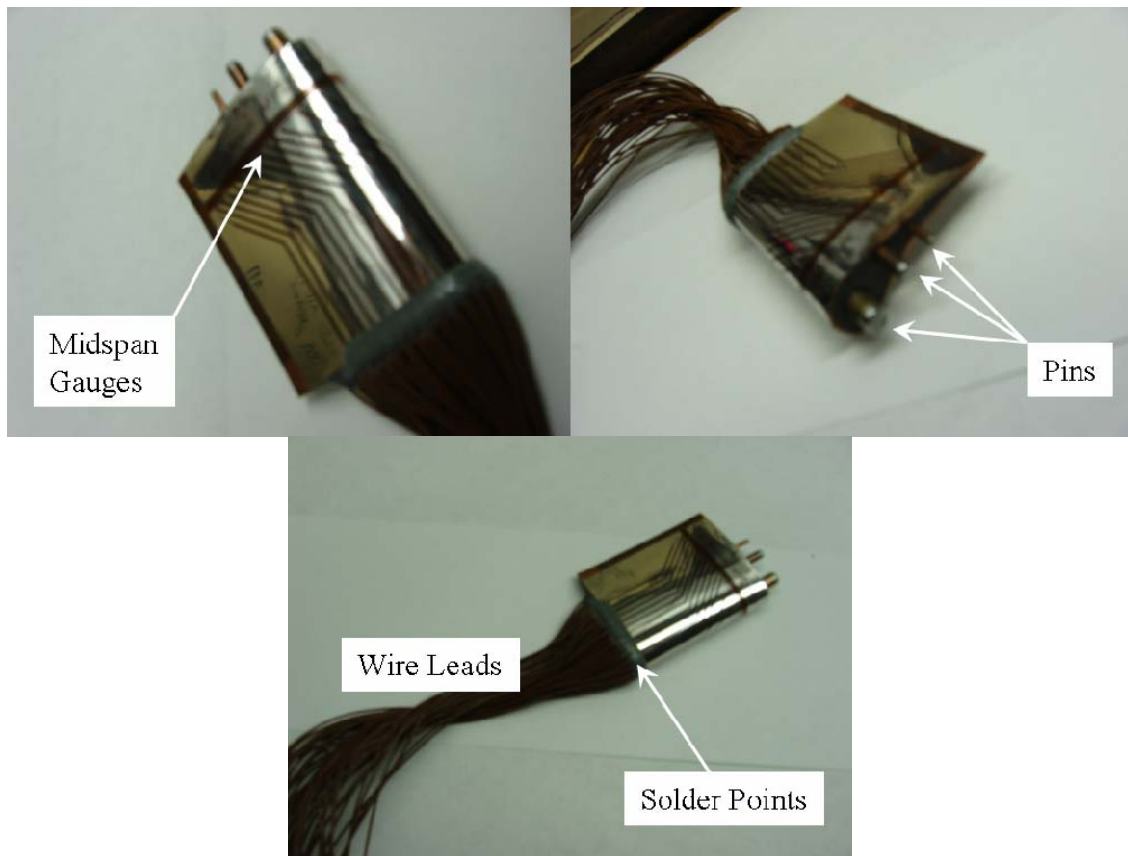


Figure 25 Images of the thin-film heat flux gauges installed on surface of VKI vane.



Figure 26 Image of an uninstalled heat flux gauge array with relative size shown.

Instrumentation Summary

Pressure data were necessary in both the shock tube and the cascade test section. Two high sensitivity, fast-response, model XCS-062 Kulite pressure transducers with 0.062 in diameters rated to 150 psia were used in the shock tube sections to record absolute pressure. One was located 12 inches from the diaphragm in the driver section of the shock tube and the other was located 140 inches from the diaphragm towards the end of the driven section. The pressure transducer in the driver section gave real time readings so it was known when the desired driver pressure was reached before the diaphragm was broken. The driven section transducer was close to the test section and recorded wave disturbance histories and pressures to help determine wave reflection times and local flow properties.

Static pressures were recorded in the test section in the form of two 5-hole arrays in the plexiglass end wall that spanned one pitch length (1.33 in), with one $\frac{1}{4}$ in upstream and one $\frac{1}{4}$ in downstream that were centered on the flow path between the instrumented vane and the vane above it in the cascade. Each static pressure tap hole in the plexiglass had a diameter of 0.05 in which extended out to a metal tube receiver of the same inner diameter. Hollow clear flexible pressure lines fit around the metal tube receivers and led to nearby model PDCR-22 Druck differential pressure transducers rated to 150 psid. Static pressure data was taken using a total of eight Drucks, three upstream of the cascade row and five downstream. Due to a lack of Drucks rated to the appropriate pressures, the 5-hole pressure tap array could not be filled to capacity upstream of the cascade. From these, flow properties including Mach number could be calculated upstream and downstream of the vanes using the total pressure measurement, the averaged upstream

and downstream static measurements, and standard isentropic flow relations. The total pressure was taken in one of the probe ports using a pitot tube connected to a short pressure line that in turn was linked to another Druck pressure transducer. Special care was taken in keeping the length of all pressure lines as short as possible to minimize pressure-reading lag; none of the lines were more than about four inches.

Two probe ports in the plexiglass end wall as mentioned before allowed access for total pressure, total temperature, and freestream turbulence measurements using a hot-wire anemometer. The ports were centered on the flow passages just above and below the middle instrumented vane, $\frac{1}{2}$ in upstream of the cascade row, as seen in before in Figure 22. All probes used in these test section ports were firmly held in place with custom made plugs that kept air from leaking out and ensured accurate data collection with the delicate probes. Lastly, the total temperature readings were taken using a 3 mil type E thermocouple wired to a powered cold reference junction and in turn wired to a data sampling card to read the transient voltages on the computer. The fully instrumented cascade test section from the heat flux gauge lead wire side is shown in Figure 27. The other side of the test section is then shown in Figure 28.

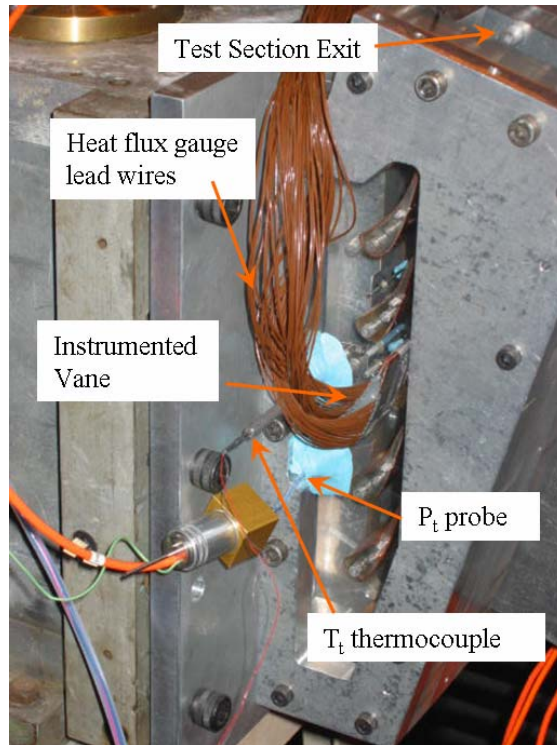


Figure 27 Image of instrumented cascade test section as viewed from heat flux gauge lead-wire side.

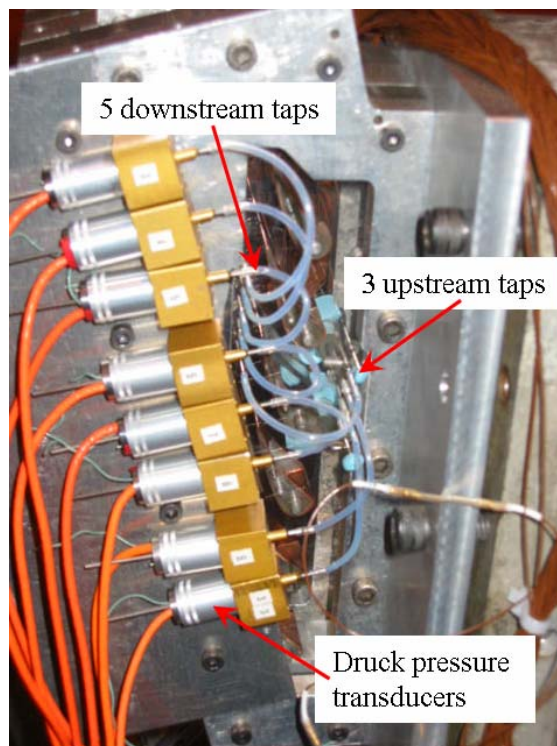


Figure 28 Image of shock tube test section as viewed from static pressure tap side.

Data Acquisition System

The data was obtained from all the instruments linked to the shock tube and its cascade test section using National Instruments SCXI data sampling cards and a state-of-the-art model PXI-1045 data processing computer. These cards also provided the excitation voltage for the pressure readings. Knowing the transient nature of the heat transfer data was of key importance for the thesis, 32 channels of high-frequency data sampling on eight four-channel cards was provided for the thin film heat flux gauges. 12 channels of lower frequency data sampling was provided for all other data measurements including static pressure and total pressure and temperature. The processor featured a simultaneous sample-and-hold capability allowing both the low and high frequency data to be stored as it was received and be recorded on the same time interval, which was beneficial in examining the heat flux response with respect to the timing of the wave disturbances in the shock tube. Staying in accordance with good signal processing practice, the Nyquist sampling theorem was followed when obtaining heat flux data. The theory states that if a signal is to be sampled at regular intervals in time, the sampling frequency must exceed some minimum value in order to reconstruct the original signal unambiguously from the samples [53]. This Nyquist frequency must be at least twice the frequency of the signal detected. Thus, as the signal bandwidth was approximately 89 kHz for the thin films, the relatively high sampling frequency when obtaining all heat flux data was 200 kHz per channel. This compares to all low frequency pressure and temperature data that was sampled at 10 kHz. Figure 29 is an image of the low and high frequency data processors used in the shock tube experiment. The heat transfer films were connected to two custom-made 15-channel current source and signal-amplifier

boxes, as designed by Anthony [51], which are also shown in Figure 29. These selectively amplified high frequency signal components and provided a useful current display. Finally, the two current source boxes were powered by a Tektronix model PS-280 DC ± 15 V power supply.

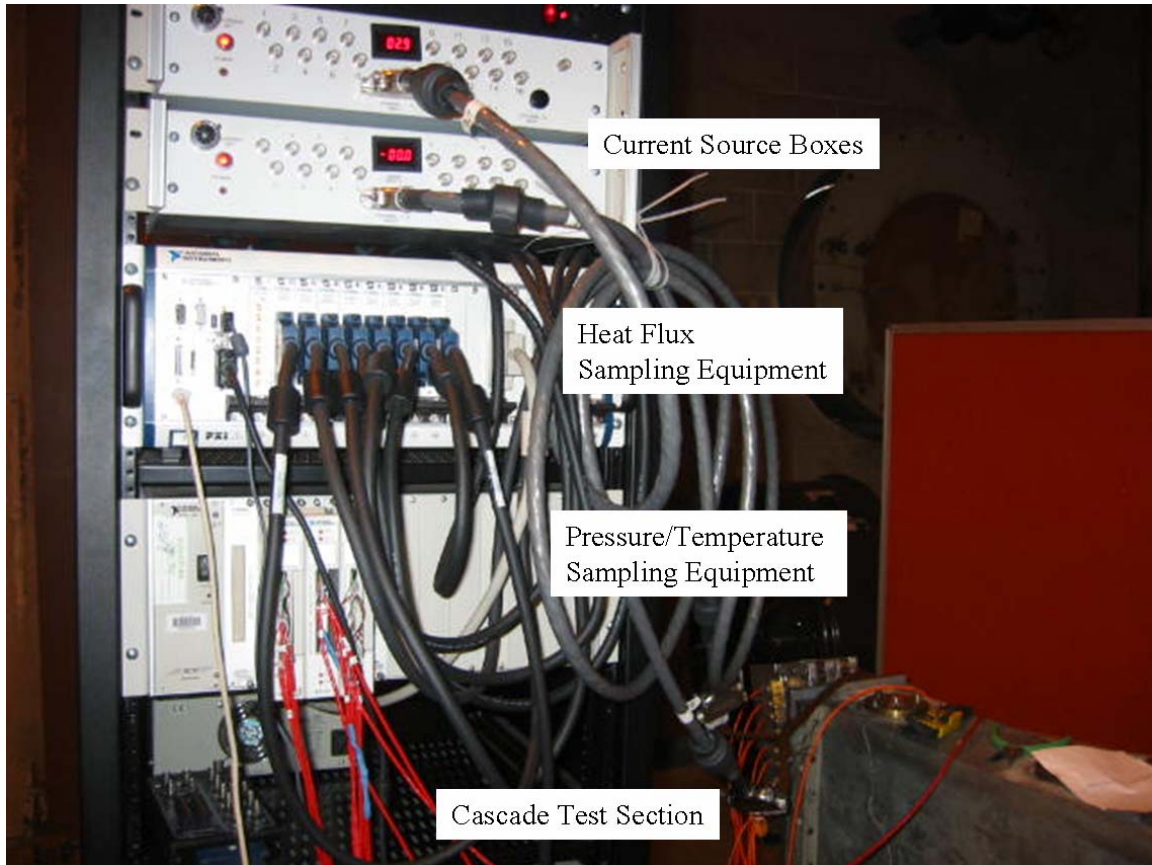


Figure 29 Image of shock tube data acquisition system.

Experimental Apparatus Summary

A large compressor was used to increase the pressure in the driver section of the shock tube once a diaphragm was installed and clamp between sections. The vane cascade test section was connected at the end of the driven section with a flange piece that could house a turbulence grid if necessary. A total of 9 Druck's, 2 Kulites, 1

thermocouple, and 27 (VKI vane) or 28 (LHL vane) platinum thin films were used to obtain the essential data for each run. All the data was processed through a sophisticated high-frequency data acquisition system that allowed easy observation of measurements using MATLAB scripts for each run. Figure 30 shows the basic experimental setup for the shock tube experiment to investigate midspan heat transfer on both the VKI and LHL vane. Also, for reference, CAD drawings of designed parts of the cascade test section with are given with dimensions in Appendix H.

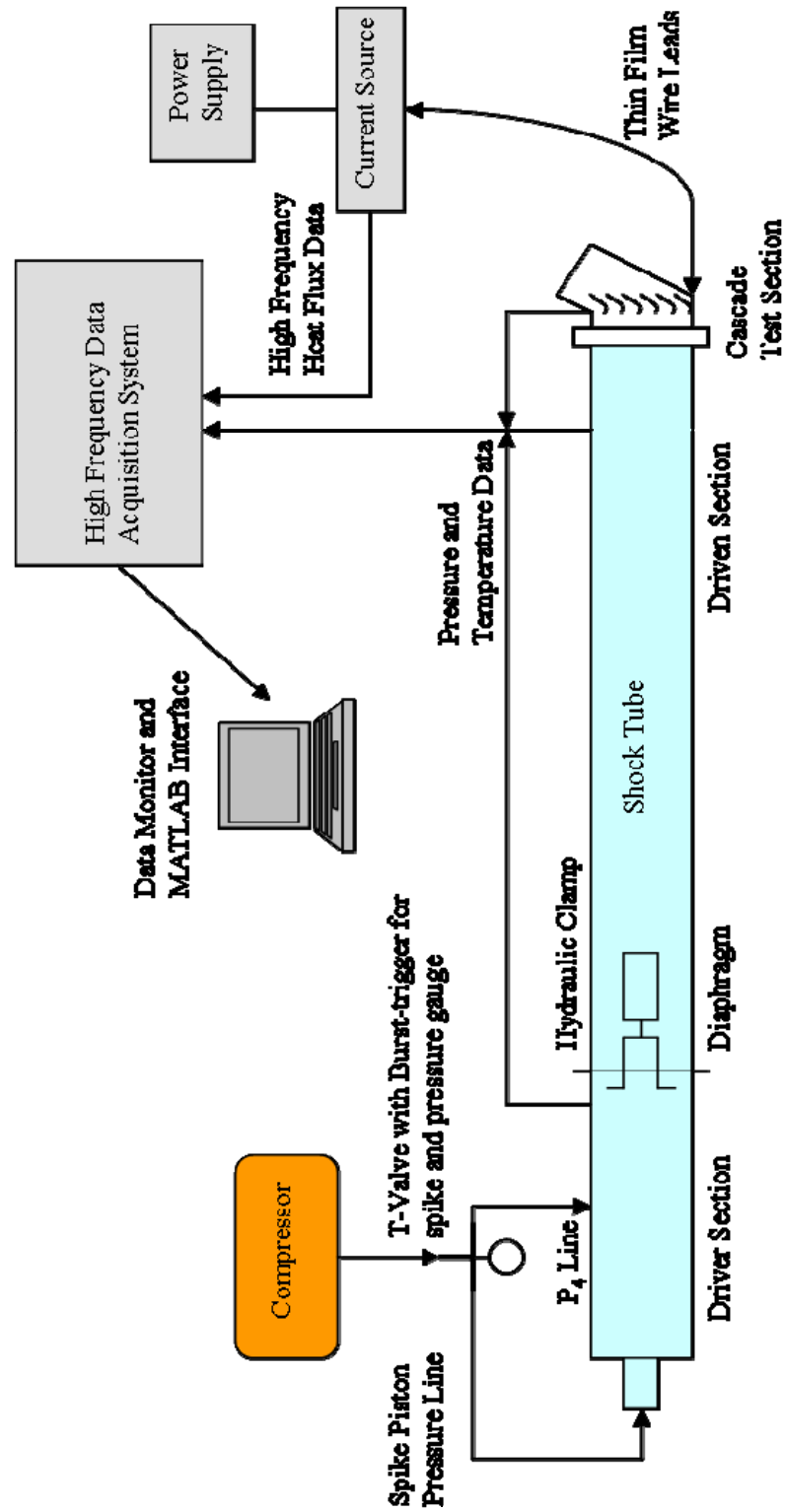


Figure 30 Shock tube cascade experimental setup.

V. Discussion of Thesis Results

Code Validation Results

VKI Airfoil Pressure Loading Predictions

Historically, older 2-D heat transfer prediction methods have commonly over-predicted heat transfer rates on both surfaces of an airfoil since non-transitioning turbulence models are used [54]. This agrees with the common industry practice of using a fully turbulent prediction in designing turbine components and cooling systems in order to be conservative with respect to durability. On the other hand, as seen in the literature survey, many more recent 3-D codes severely under-predict heat transfer and predict poorly the onset of transition. Using more realistic heat transfer predictions would assuredly result in better airfoils, leading to turbine energy savings and improved thermal efficiencies. The WILDCAT code uses various viscous flow models (e.g. laminar, turbulent, and transition) to predict flow characteristics and ultimately predict heat transfer. The goal here was to ensure the WILDCAT code gave realistic predictions when compared to data with varying aerodynamic parameters.

Since the pressure loading, or velocity distribution, results from WILDCAT were relied on so heavily for the heat load optimization of the VKI vane, the 2-D pressure loading cases for the VKI data will be reviewed first and compared using the same flow conditions to the WILDCAT flow solver output. The heat transfer grid in WILDCAT was used for these cases. A total of seven experiments were run to analyze the VKI vane at three discrete transonic isentropic exit Mach numbers (M_2). To get the data, 27 static pressure tapings on the surface of the vane were used, with one each at the leading edge

(LE) and trailing edge (TE) stagnation point, 7 on the pressure side (PS), and 18 on the suction side (SS). The VKI airfoil cross section coordinates and exact initial flow parameters were entered into the WILDCAT code for runs of 10,000 iterations. Figures 31, 32, and 33 display the VKI experimental results and the numerical prediction for pressure loading plotted against fraction of axial chord by the WILDCAT code for $M_2=0.84$, $M_2=0.875$, and $M_2=1.02$, respectively. Total inlet pressures for the three increasing Mach number runs were 20.8, 21.4, and 23.2 psia, respectively. Also shown to the right of the loadings are local isentropic Mach number plots, showing the acceleration of the flow around the airfoil. Given on the top of the plots are the exit static pressure distortion, which is used to study possible levels of downstream unsteadiness, and the total percentage pressure loss. Both tend to increase with increasing M_2 . The results clearly show that the code predicts the pressure loading profile very well over both the PS and SS of the VKI vane for the range of transonic isentropic exit Mach number. The prediction even fares well for the obvious supersonic shock regions of the SS for the $M_2 = 1.02$ case. There is only a very small disparity between the data and the prediction on the SS for lower M_2 runs—probably due to complexities of the SS boundary layer change from a favorable to adverse pressure gradient. Now that the predicted pressure loadings are satisfactory in the transonic range, the range for which the VKI and optimized airfoils are designed to perform, the heat transfer predictions can be addressed.

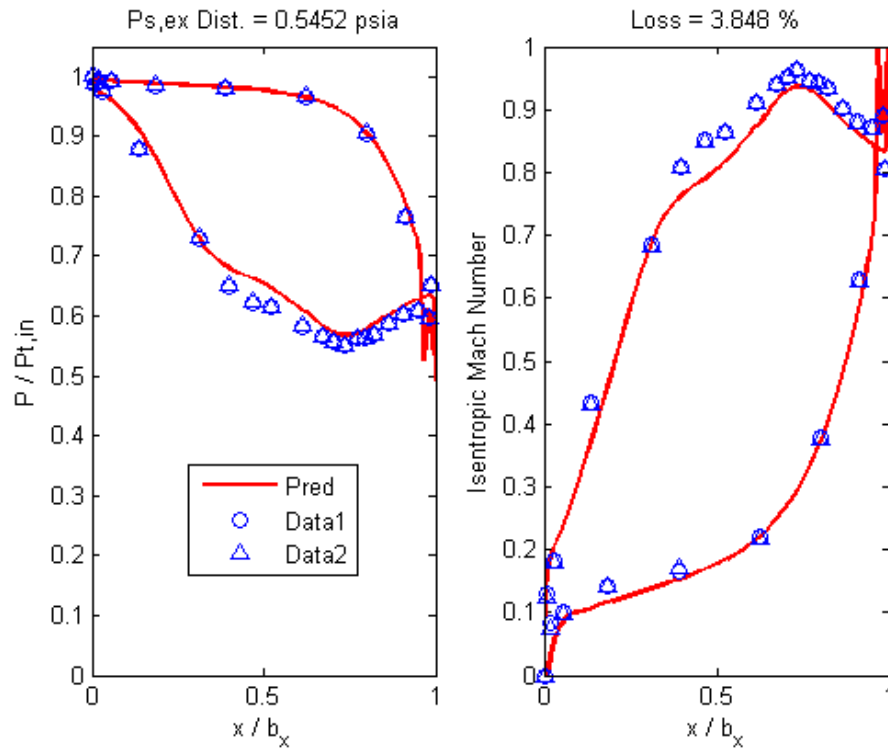


Figure 31 WILDCAT pressure loading prediction for two VKI runs at $M_2 = 0.84$.

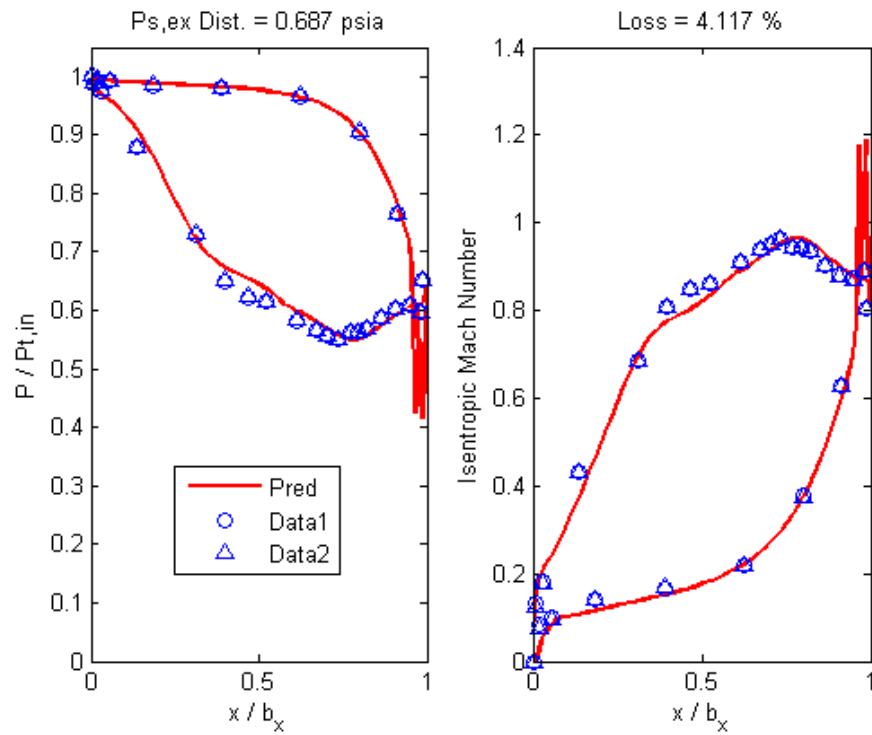


Figure 32 WILDCAT pressure loading prediction for two VKI runs at $M_2 = 0.875$.

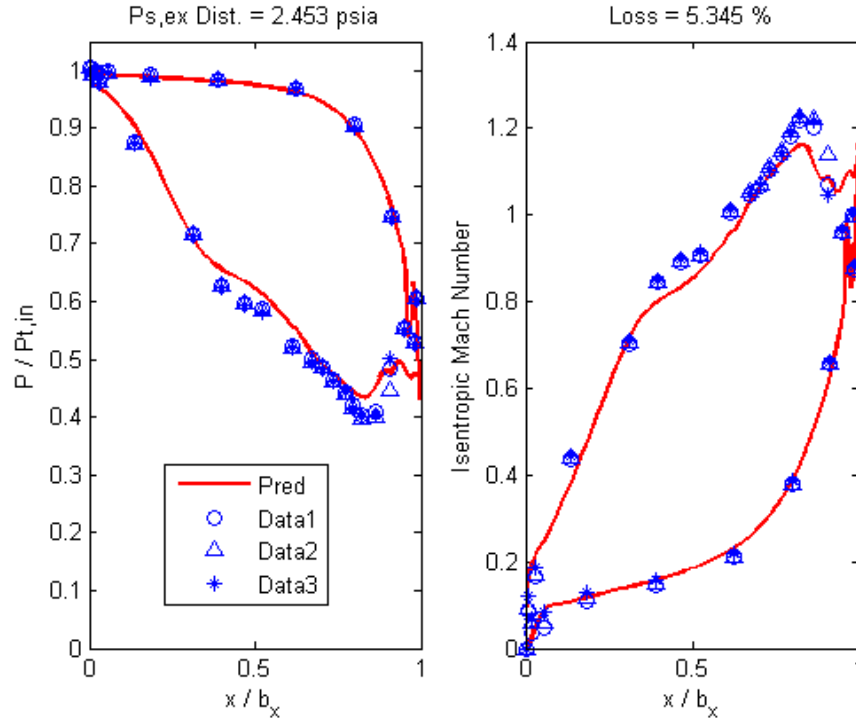


Figure 33 WILDCAT pressure loading prediction for three VKI runs at $M_2 = 1.02$.

VKI Airfoil Heat Transfer Predictions

The collection of heat transfer runs performed by VKI was narrowed down to five cases for the purpose of comparison of the VKI experimental results and the WILDCAT RANS prediction. The cases selected span a range of three discrete values of exit Reynolds number (Re_2) and turbulence intensity level (Tu) for an approximate $M_2 = 0.80$, which matches the values to be seen in the cascade shock tube experimental comparison of the VKI and LHL vanes. Table 3 below gives the original names of the five runs and their respective key parameters including total temperature and total pressure. The numbers in the table are more precise, but the Re values are essentially 5×10^5 , 10^6 , and 2×10^6 , while Tu is basically 1%, 4%, and 6%. The exact parameter values shown, except for Re , were entered into the WILDCAT code as flow solver setup parameters to simulate

each of these runs with the VKI vane geometry. The VKI experiments used a total of 45 platinum thin film gauges over the surface of the airfoil to obtain the heat flux data.

Table 3 Selected VKI heat transfer runs and flow conditions for purposes of code validation.

Test Name	M ₂	Re ₂	Tu [%]	T ₀ [K]	P ₀ [psia]
MUR228	0.932	595,500	1.0	403.30	13.27
MUR247	0.922	2,117,000	1.0	416.20	49.24
MUR237	0.775	1,011,000	6.0	417.30	25.43
MUR218	0.760	1,007,000	4.0	413.50	25.29
MUR129	0.840	1,135,000	0.8	409.20	26.82

WILDCAT calculates heat flux for a Dirichlet, or isothermal boundary condition (since the wall temperature is specified at the flow-solver parameter screen when solving for heat transfer on either vane) via the following sequence: \dot{q}'' is found by equation (5):

$$\dot{q}'' = -k_f \frac{dT}{dy} \quad (5)$$

where the normal static temperature gradient, $\frac{dT}{dy}$, is solved using the proper Navier-Stokes equations for the specified type of boundary layer and $k_f = f(T_f)$ is the fluid (in this case air) thermal conductivity at the temperature of the fluid. Only the Dirichlet type boundary condition was used for the work in this thesis. To calculate the integral heat load, WILDCAT uses the \dot{q}'' found before and applies Newton's law of cooling in equation (6) to solve for the fluid heat transfer coefficient, h:

$$\dot{q}'' = h_f (T_{aw} - T_w) \quad (6)$$

where T_{aw} is replaced with the specified $T_{t,in}$ at the setup screen and T_w is the wall temperature listed in the work by Arts [29] for each MUR- heat transfer run and specified as well. Then, in order to get the integrated, or total, heat load over the vane surface, the following integral in equation (7) is used to get an average heat flux, $\overline{\dot{q}''}$:

$$\overline{\dot{q}''} = \frac{1}{L} \int_0^L \dot{q}''(x) dx \quad (7)$$

where L is the total surface distance around the airfoil. For the VKI vane, $L = 3.5217$ in. From here, non-dimensional Stanton and Nusselt numbers may be plotted if desired. Now heat flux can be predicted by the flow-solver and compared to the extensive range of data.

Figures 34 through 38 shows heat flux distributions on the complete fractional surface distance (PS from -1 to 0, SS from 0 to 1 on the x-axis) of the VKI vane for the VKI data, the WILDCAT laminar viscous prediction, turbulent viscous prediction, the natural Abu-Ghannam and Shaw (AGS) transition model prediction, and a triggered start of transition using the AGS model to compare to VKI data transition onset locations, for the five runs shown in Table 3. In the figures, the pressure side distribution is on the left and the suction side is on the right half of the plots. In this sense, the flow goes from the center of the plots away towards the trailing edge (pressure side flow goes from right to left). By entering the fractional surface distance value for which the slope of the line first becomes positive in the VKI data on the SS of the VKI vane, the WILDCAT could perform predictions with a forced transition onset at that point which was termed *hardtrip* in the plots. The hardtrip function caused the laminar viscous equations to be evaluated

up until the specified point of transition. In this way an apples-to-apples comparison of the SS transition could be observed between data and prediction and it could be shown that by delaying transition, the overall heat load of the vane will decrease since the integral heat flux for the hardtrip is obviously less than for AGS. The hardtrip function helps assess key boundary layer parameters at the realistic transition point for many different cases. The AGS model depends on skin friction coefficient C_f , momentum thickness Reynolds number Re_θ , and boundary layer shape factor H . This line shows an earlier transition to turbulence than does the hardtrip function for all five heat flux plots. It can be seen that both transition predictions are somewhat sudden. This is because AGS [40] is only a transition start model in WILDCAT, and not a transition length model, as can be seen in the disparity between the hardtrip AGS line and the VKI data. In addition, the AGS model was derived from experiment solely performed on a flat plate, not on a turbine vane. Some WILDCAT and other open-literature transition models are gleaned from the Narasimha [55] universal intermittency concept, γ , which have been shown to be flawed by Clark et al. [56]. The AGS model tends to be more widely used than most models. Also, more modern transition models for attached flows have yet to be integrated into the WILDCAT flow solver.

Many trends can be seen in the predictions. The predicted vane peak heat load at the leading edge and at the beginning of SS turbulence onset has a strong and relatively proportional Re_2 dependence. SS transition is obviously prevalent even at lower Re runs, so the heat flux predictions provide good motivation for attempting to delay transition to reduce airfoil heat load in the optimization effort. All figures also present a heavy transition onset location dependence on Tu . As Tu increases, transition tends to occur

earlier on the SS, which agrees with the work of Blair [19]. This trend was also observed for increasing Re_2 . For constant $Tu = 1\%$ as Re_2 grew from 5×10^5 to 2×10^6 , AGS and hardtrip transition onset locations on the SS moved back towards the stagnation point dramatically and the LE peak heat flux nearly tripled. Concerning the natural AGS and turbulent viscous predictions, there appears to be transition to turbulence at about the -0.1 location for all five runs, which accounts for the overprediction of heat transfer on the PS. For the most part, SS laminar predictions are very accurate. On the PS, however, for the high Re case, the laminar boundary layer heat transfer is over-predicted. In contrast, for the high Tu case the PS laminar heat flux is under-predicted, which tends to be in accordance with past studies that have experienced freestream turbulence heat transfer augmentation [56] due to possible secondary or unsteady flow effects [26]. In addition, the laminar viscous prediction only accounts for shear in the boundary layer and has no inherent way to account for unsteady heat and mass transport due to higher levels of Tu . Overall, it appears that for transitional to typical turbine levels of Re_2 , the WILDCAT code prediction performs very well, especially for SS characteristics. This contrasts many of the prediction comparisons mentioned earlier in the literature survey (see Refs [13], [20], [21]) and is a step in the right direction. For high Tu , PS laminar heat transfer is under-predicted. For high Re_2 , PS laminar heat transfer is over-predicted; however, the SS heat flux is captured well.

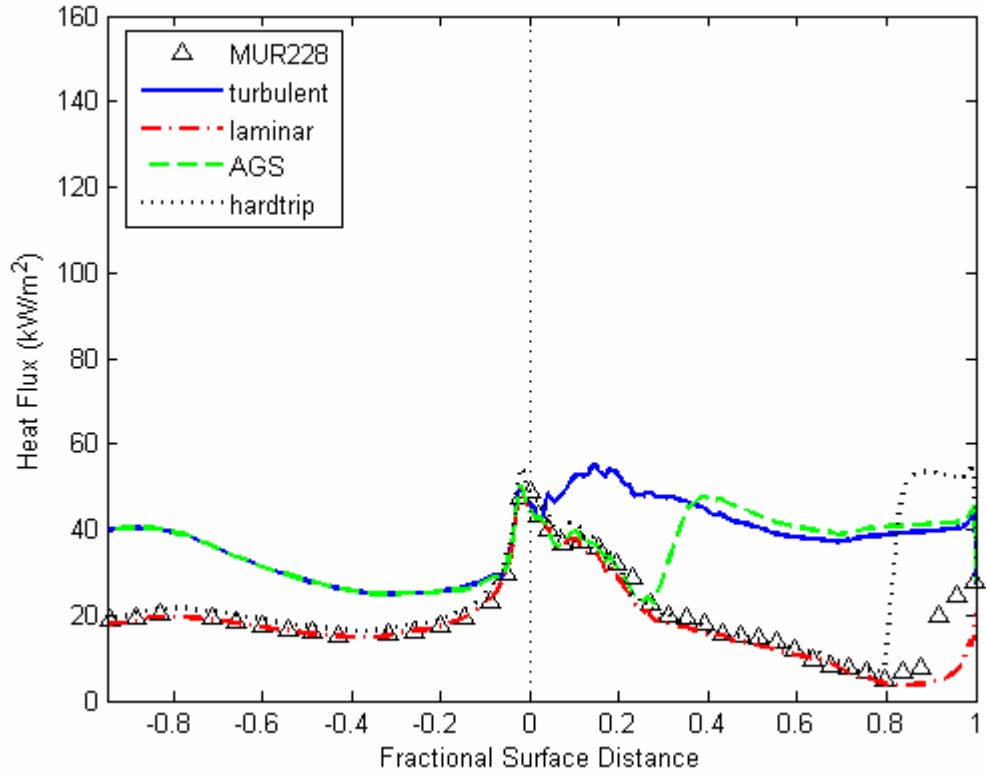


Figure 34 WILDCAT heat flux prediction for VKI run MUR228 ($M_2=0.932$, $Re_2=596000$, $Tu=1\%$).

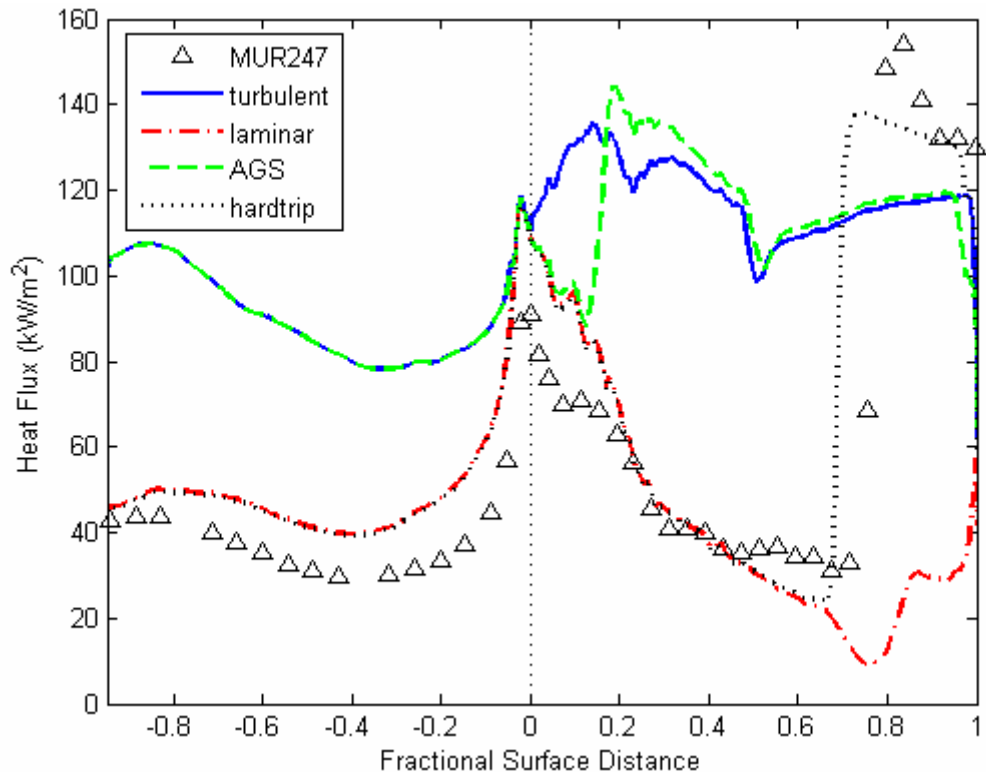


Figure 35 WILDCAT heat flux prediction for VKI vane run MUR247 ($M_2=0.922$, $Re_2=2120000$, $Tu=1\%$).

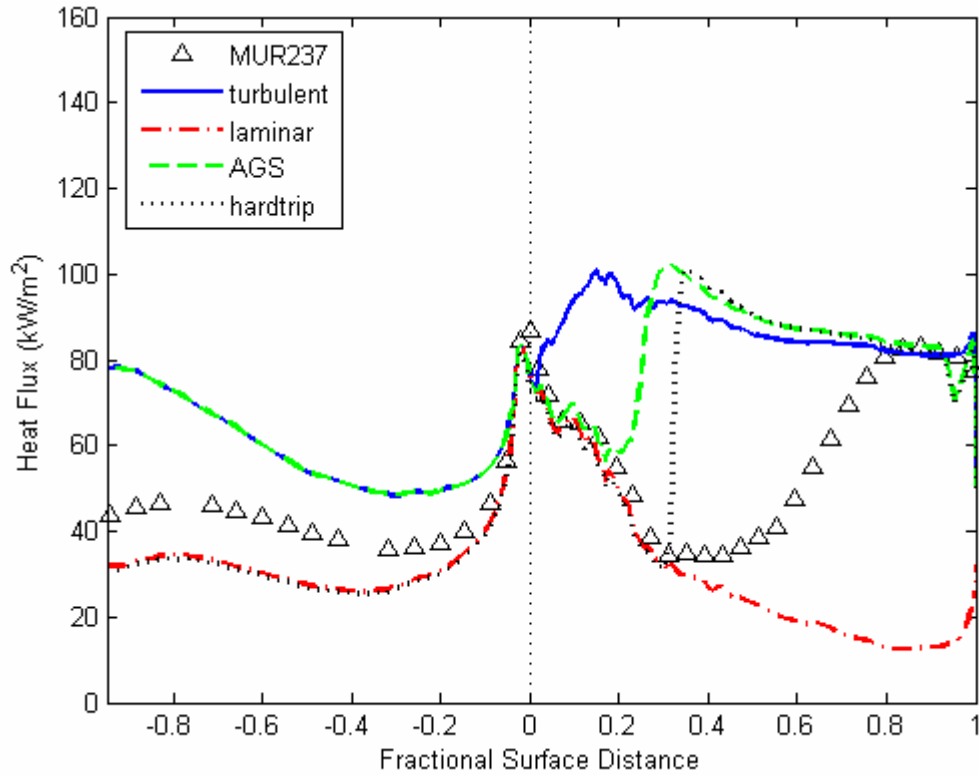


Figure 36 WILDCAT heat flux prediction for VKI run MUR237 ($M_2=0.775$, $Re_2=1010000$, $Tu=6\%$).

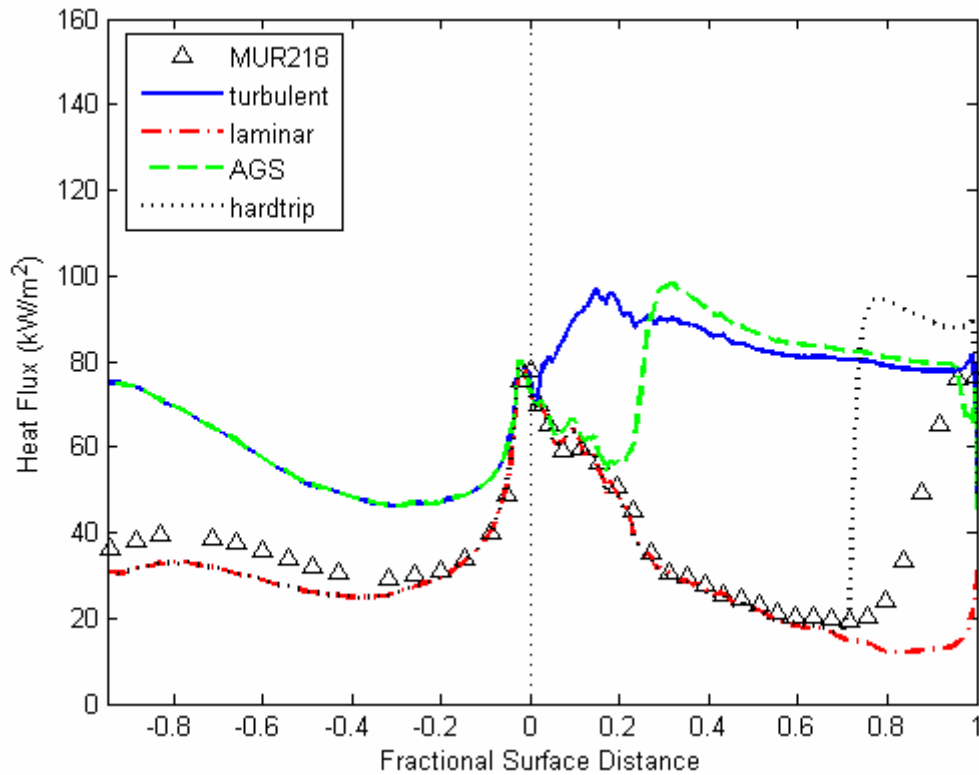


Figure 37 WILDCAT heat flux prediction for VKI vane run MUR218 ($M_2=0.76$, $Re_2=1010000$, $Tu=4\%$).

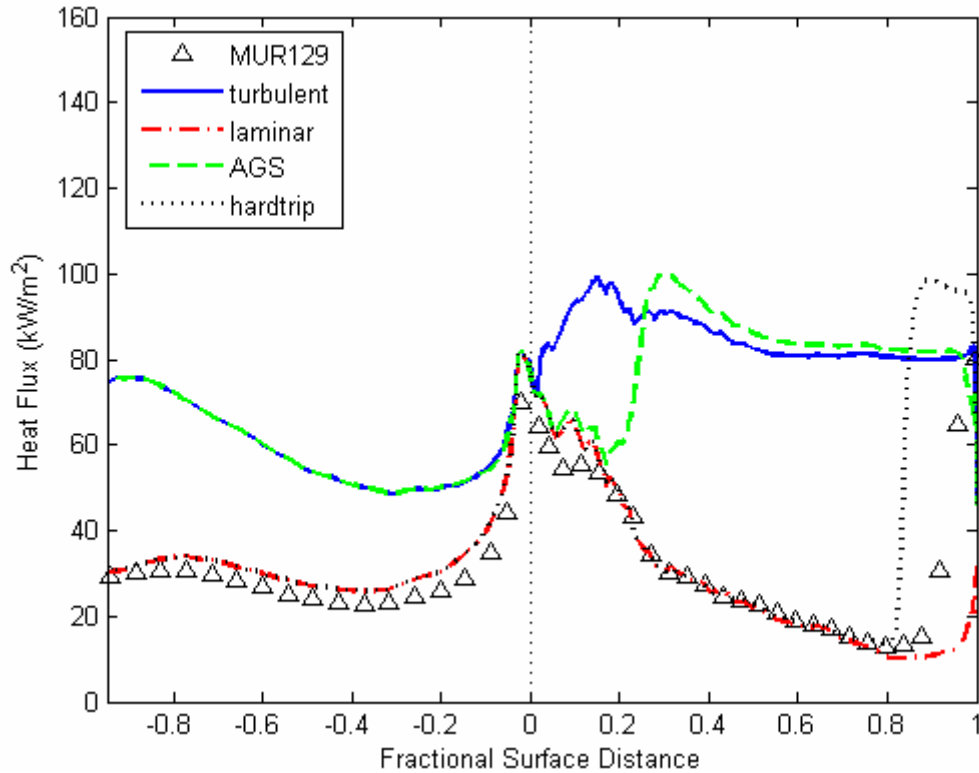


Figure 38 WILDCAT heat flux prediction for VKI run MUR129 ($M_2=0.84$, $Re_2=1140000$, $Tu=0.8\%$).

A reliable RANS flow solver such as WILDCAT should always be checked to ensure that an appreciable convergence of the parameters being solved for has occurred. Figure 39 below shows an example convergence plot for a calculation done with the heat transfer grid for 10,000 iterations. It is easy to see that total pressure, total temperature, and loss percentage all converge rather quickly. Inlet parameters are shown as constant variables because they are specified by the user and used by the code to calculate the values downstream of the airfoil. For most of the calculations that were performed in the design system using the results of WILDCAT, parameters were taken from converged and final values. To ensure no unconverged values adversely affected any flow-field calculations, all runs for code validation and optimization added 1,000 iterations to the

standard 10,000 iterations from which to get average solved parameters for aerodynamic and thermodynamic consideration.

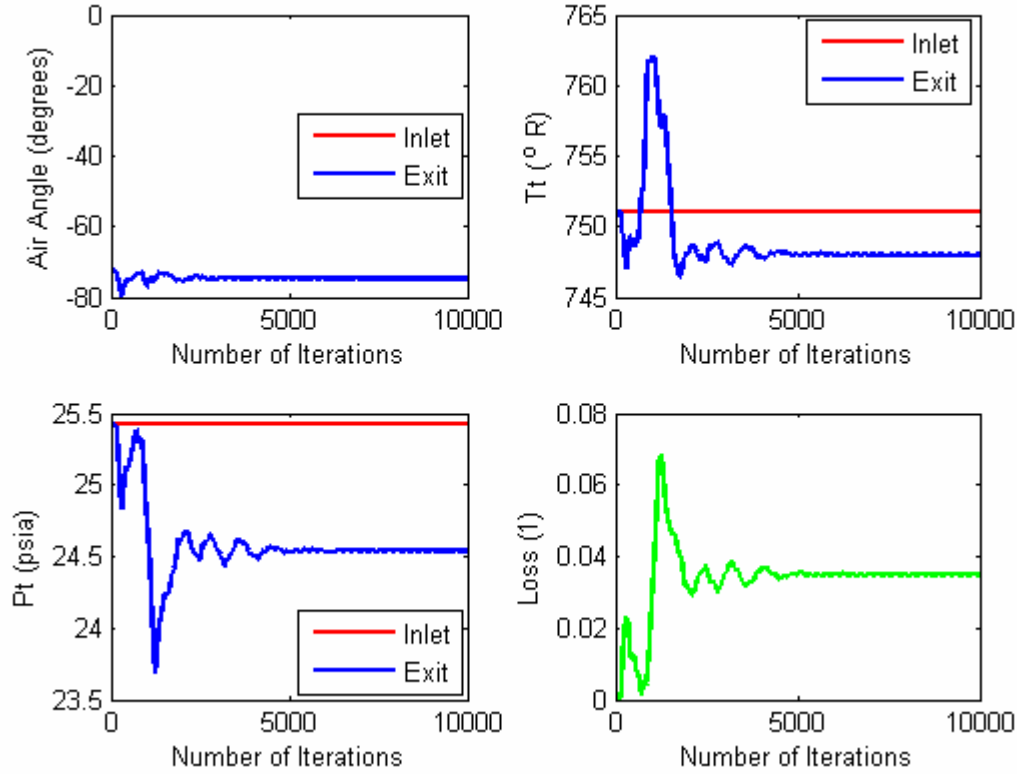


Figure 39 Convergence history for a sample WILDCAT run of 10,000 iterations.

Now that a reputable 2-D Navier-Stokes code has been properly validated against a good range of accurately obtained turbine-representative data, and the results have shown relatively successful prediction compared to an abundance of past numerical and computational techniques, the WILDCAT code can be used for a vast variety of turbine component design and optimization tasks that assess surface heat transfer as the primary focus. Here, the WILDCAT code will be used exhaustively, for literally millions of iterations, to re-design a turbine nozzle guide vane geometry to have an optimum thermal loading performance. The comparison of the VKI data for constant M_2 and range of T_u

and Re_2 show that the WILDCAT code is a viable tool for predicting pressure and heat transfer distributions on turbomachinery components in turbine inlet flow environments. The predictive method outlined above may be used as a critical component to the aerodynamic and thermal design of modern turbine vane and blade airfoils.

VKI vs. LHL Airfoil

After the lengthy and iterative process previously outlined was executed, the re-design and optimization of the VKI tested vane for the objectives of reduced leading edge heat transfer and delayed suction side transition yielded impressive results, especially considering limited practical history an innovation of this turbine component design technique. A direct comparison of the two vanes is given in this section to cover a wide range of aero-thermodynamic flow characteristics and considerations. The reduced heat transfer airfoil that was consecrated as a solution for the reduced heat load design will be referred to from here on as the low-heat-load airfoil, or LHL. Using the methodology and constraints described earlier, a solution was finally found after thousands of optimization iterations and weeks of cumulative computing time.

The new LHL vane is different from the VKI vane in that it has a slightly larger leading edge diameter (LED), resulting in a rounder, more even LE structure which will serve to spread out the LE heat load. The LHL vane also has a thicker mid-chord and slimmer TE section for enhanced flow acceleration. Figure 40 is the set of main aerodynamic parameters as the LHL vane is defined in the WILDCAT code window. These may be compared to the VKI parameters listed in the code validation section of the thesis. Notice that the leading edge diameter (LED) almost doubled, the increase in TE

wedge angle, and the reduction in height-to-length ratio (H/L) and uncovered turning. Other parameters listed are merely for reference and documentation for future work.

Airfoil Design Parameters					
Case Title :					
LHL 1V					
General parameters : NF, Bx (in), rad (in), H/L, betagage (deg) :					
470	0.8574	99.7371	1.1589	74.9907	
Leading-edge parameters - LED (in), leer, Bet1 (deg), LEW (deg), LEWF :					
0.6698	1.4696	0	91.149	0.5949	
Trailing-edge parameters - TED (in), Bet2 (deg), TEW (deg), TEWF, uncvrtrn (deg) :					
0.0341	72.6456	6.5238	0.9	11.3492	
Bezier curve control handles : L1, L3F, L3R, L4, L5, L7 :					
0.2333	0.481	0.3476	0.5508	0.8492	0.7603
Flowfield parameters - M1 (rel), M2 is (rel), Ttin (deg R), Ptin (psia) :					
0.15	0.775	751.1	25.43		
Streamtube-height ratios - HleH1, HteHle, H2Hte :					
1	1	1			
Relative air angles - Bet1g (deg), Bet2g (deg) :					
0	72.6456				
Gas parameters : Rgas (ft lbf / lbm / deg R), gama (1) :					
53.35	1.4				
Structural parameters: MomX (in lb), MomY (in lb) :					
0	0				
					OK Cancel

Figure 40 LHL vane aerodynamic parameters.

Figure 41 is a first view of the reduced heat transfer optimized solution showing the midspan cross-section airfoil geometry for the LHL vane. The axial chord and air turning angle are the same as for the VKI vane, as they were constraints to help simplify the optimization process.

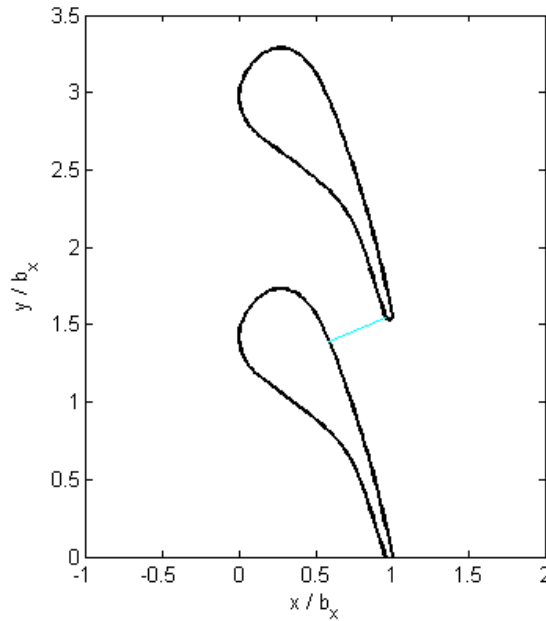


Figure 41 LHL vane cross-section geometry.

Figure 42 shows a relative comparison of the two vane geometries as they appear in the design log plots with sample laminar pressure loading and heat flux distribution assessments for the design flow conditions defined by the MUR237 VKI experimental heat transfer run as mentioned before. The red line corresponds to the LHL vane while the blue dotted line is the original VKI vane. As a refresher, this design log could be scrolled through to see past results of WILDCAT runs after a change in airfoil parameters is made. The broader LE shape and slimmer TE section is easily emphasized by the figure. Notice the differences in the pressure loading and heat transfer distributions—the LHL vane LE heat load is significantly less. Also,

Table 4 gives the relative midspan surface lengths of the two vanes. The quantitative process for arriving at the LHL vane geometry will be discussed next.

Table 4 Relative surface lengths of VKI and LHL vanes.

Vane	Suction side (in)	Pressure side (in)	Total surface length (in)
VKI	1.9799	1.5418	3.5217
LHL	2.0514	1.5779	3.6292

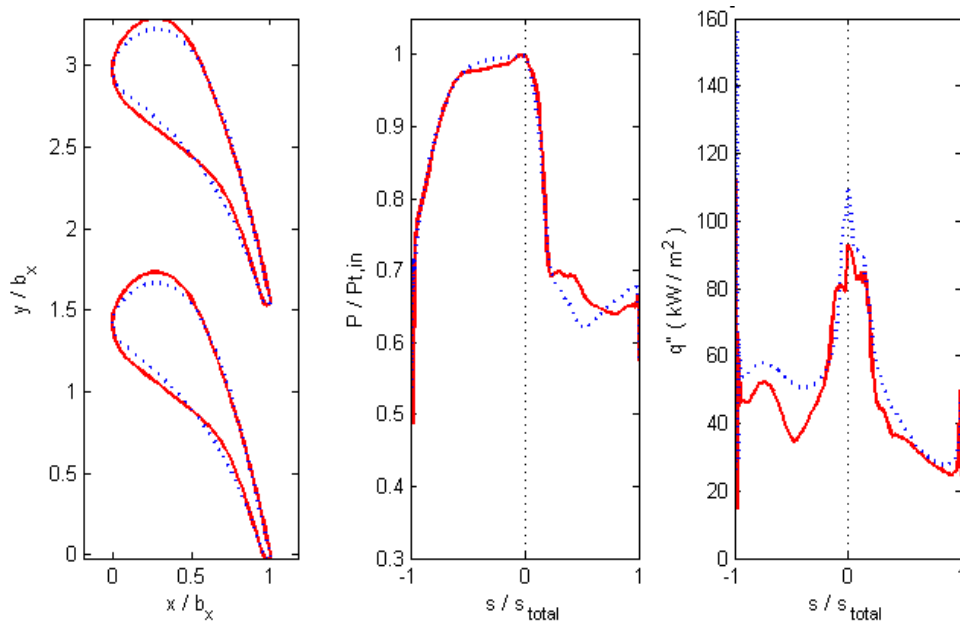


Figure 42 Relative shape, loading, and heat flux distribution of VKI and LHL vanes for a sample laminar viscous WILDCAT calculation.

As seen in Figure 42, the pressure loading and heat flux distribution plots were relied on rather heavily in assessing the most desirable airfoil geometry. To reiterate, the two main goals of the re-design process were to lower the LE peak heat load and delay the onset of transition on the SS as far as possible by driving the minimum static-to-total pressure ratio, $P/P_{t,in}$, or maximum Mach number, back as far as possible towards the TE.

Many different airfoil shapes were observed during the process of the optimization. At first, when the objective was to simply reduce the airfoil integral heat load (which of course turned out to be an ambiguous goal) with the sequential quadratic programming (SQP) algorithm, the code was churning out vanes that did have a low integral heat load, however, many had poor aerodynamic characteristics with shocks near the TE and areas of very high heat flux on the design log plots. These airfoils were not aesthetically pleasing either, ranging from large LE lamb-chop shapes to extremely thin shapes with high values of H/L . There needed to be assurance that the SS flow would not transition or have strong shocks and that the heat flux distribution looked reasonable in relation to historical design practice. In other words, in the eyes of an experienced turbine component designer, these plots needed to have aesthetic qualities with smooth SS loading lines and classical heat flux distribution aspects such as smooth gradient buckets on either side of the LE for a laminar prediction. Thus, the need for the reconsideration of optimization objectives.

Following the path of the more specific working objectives, after many weeks of computing, the results were narrowed down to a healthy group of airfoil geometry candidates. Table 5 compares the properties most relating to the goal of the reduced heat transfer optimization for the original VKI vane, the best airfoil that could be created by hand-iterations (changing parameters by hand and re-running WILDCAT over and over again), and two good candidates that resulted from the genetic algorithm (GA). Listed are the fractional axial chord coordinates of minimum $P/P_{t,in}$, aerodynamic loss, integral heat load, and LE peak heat load for each vane. The coordinates, x/b_x and $P_s/P_{t,in}$, in the second column are of the point of minimum static-to-inlet-total pressure ratio on the

suction side plot as in the middle graph in Figure 42. A higher value in x increased the probability of delayed transition while a lower value in y showed a greater overall acceleration of SS flow in keeping the boundary layer laminar. The GA airfoils given are the 987th and 1,508th optimization iteration that resulted when the two objectives, which were translated into proper fitness functions, were enforced. The values were taken from WILDCAT runs of the midspan geometries using a heat transfer grid at 10,000 iterations and the laminar viscous assumption.

Table 5 Final candidate airfoils from optimization process compared to VKI vane.

Airfoil	Minimum SS P/P_{t,in} coordinate (x/b_x, P_s/P_{t,in})	Loss (%)	Integral Heat Load (kW/m²)	LE Peak Heat Load (kW/m)
VKI	(0.51, 0.61)	3.521	4.170	112.5
Best hand-iterated	(0.56, 0.63)	3.359	4.265	95.4
GA (987)	(0.70, 0.63)	3.118	4.248	96.0
GA (1508)	(0.75, 0.63)	3.198	4.271	96.1

Observing the values in Table 5 it is clear that the GA was very successful in realizing the two main optimization objectives. The 987 and 1508 airfoils had GA fitness scores of 44 and 51, respectively, while the next best airfoil created by the GA had a score of only 30. Naturally, these two stood out and were suitable as a final choice. From here, one airfoil had to be chosen to progress further in the study to be tested experimentally for reduced heat transfer. The aerodynamic losses, integral heat loads and LE peak loads of the two GA airfoil solutions are essentially the same. While the 987 has slightly better numbers for these three categories, it was eliminated in favor of the 1508 airfoil. Knowing the two main objectives of the optimization, and that the peak loads

were the same, the fact that the 1508 airfoil moved the minimum pressure ratio point towards the TE a whole 5% of the surface distance over the 987 airfoil, this made it the definitive option. This is a significant design improvement for delaying transition with an x-coordinate of minimum pressure ratio 24% closer to the TE of the wetted suction surface distance compared to the VKI vane.

The decision process was not quite this simple, as the loading plots had to be inspected thoroughly to ensure no significant SS pressure bumps were observed. There had to be a smooth acceleration of the flow with no fluctuation of $P/P_{t,in}$ that would cause the laminar boundary layer to trip into a turbulent layer and subsequently cause higher heat transfer. Vane 1508 from the genetic algorithm, known in this work as the low heat load (LHL) vane, had two small fluctuations of this nature, but they were allowed knowing they were not profound enough to cause transition onset applying the AGS model. The pressure loading for the LHL vane is shown in Figure 43 where it can be seen that existence of these fluctuations likely allowed the minimum pressure ratio point to move to the 0.75 x-coordinate of fractional SS surface distance. While the minimum $P/P_{t,in}$ for the VKI vane has a lower y-coordinate and thus tends to accelerate the flow more gradually, the position of the x-coordinate and took precedence in determining the best solution. Also shown in Figure 43 is a direct comparison to the VKI loading. The loadings were determined by running the WILDCAT code at the design conditions of MUR237 ($Re_2 = 10^6$, $M_2 = 0.8$, and $Tu = 4\%$). The VKI curves are visually much smoother than those of the LHL, but the LHL vane would prove to be a much better performing vane concerning all aspects of turbine vane performance. It can be seen that the LHL vane even has a slightly lower percentage pressure loss. Concerning separation,

neither of the vane loading profiles indicate that separation is an issue for this set of conditions.

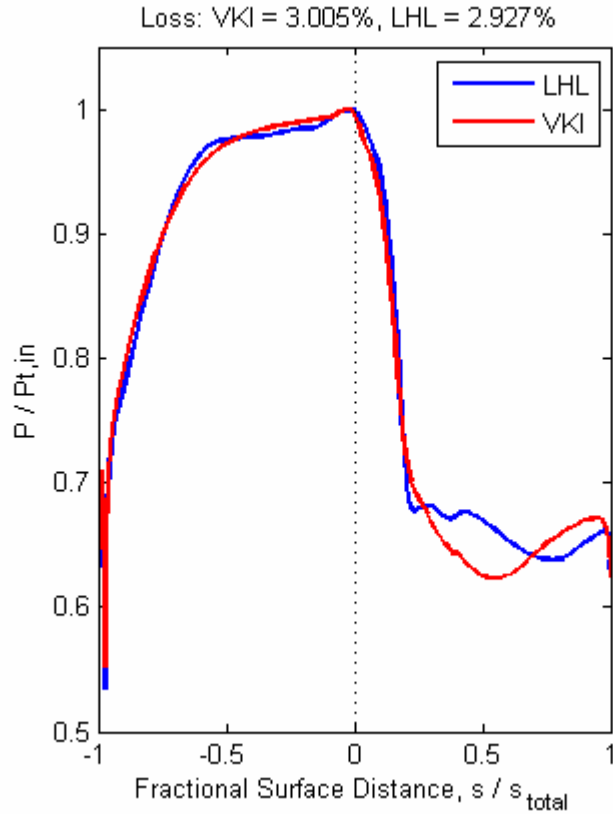


Figure 43 Fractional surface distance pressure loading comparison of VKI and LHL vanes using AGS model.

Naturally, as it is at the heart of this thesis, the LHL vane is expected to have reduced theoretical heat transfer characteristics, according to the design system and prediction methods used. Figure 44 below shows the heat flux distributions as a function of fractional surface distance for both the VKI and LHL vanes using a heat transfer grid and the AGS transition model. The LHL vane clearly has a much lower leading edge heat load, delayed transition by as much as 20% of the SS distance over VKI, lower integrated heat load, and better aerodynamic qualities with lower loss. Concerning downstream unsteady wakes, the LHL vane also reduced vane exit static pressure ratio distortion 3.3%. It is clear that the larger leading edge of the LHL vane worked well at

evening out and lowering the peak heat load at the geometric stagnation point. Instead of spiking like VKI and creating a local hot spot, the heat flux stays low and fluctuates slightly, resulting in a 15% reduction in LE heat load. While the PS heat flux is higher, the SS heat transfer curve behaves stupendously, indicating that the SS curvature was engineered perfectly. These factors all indicate that the computational optimization of the VKI vane to the LHL vane with much more desirable heat transfer qualities was a success. Figure 44 could be considered the definitive result of the thesis, but this is only a computational result. A proper test would be to evaluate relative performance in an experimental forum. Both of the main re-design and optimization objectives were realized and a worthy candidate has been chosen which can in be tested experimentally to observe if the same heat transfer trends occur in a realistic environment.

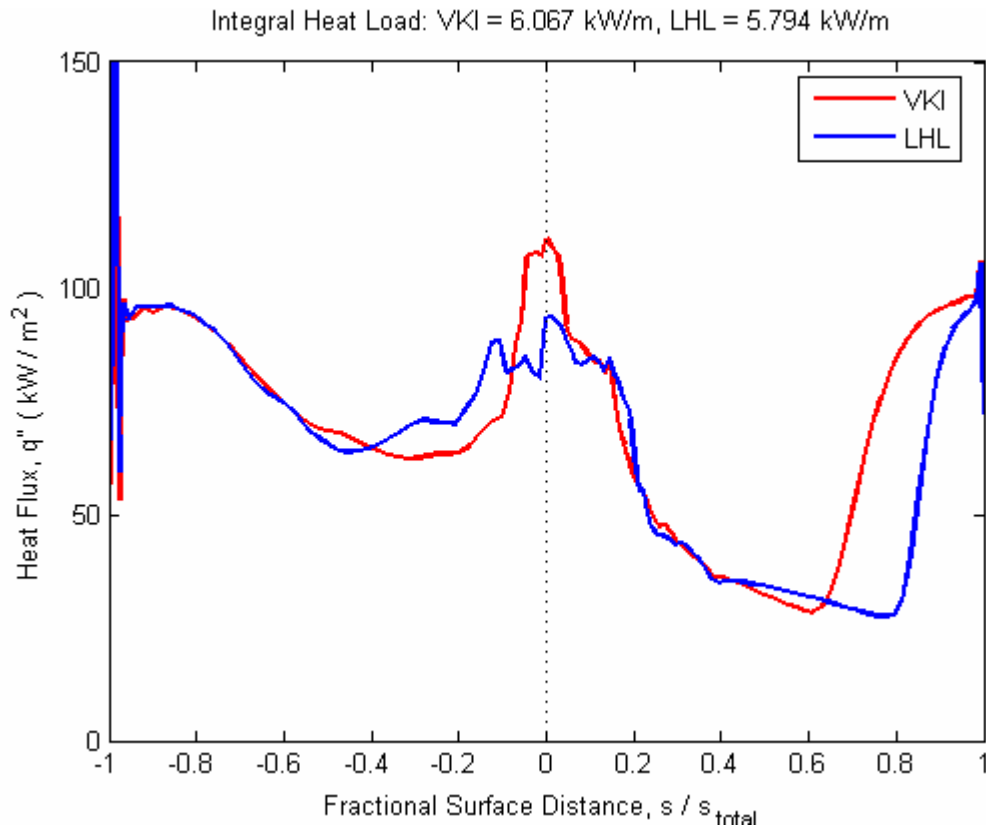


Figure 44 Heat flux distribution on surfaces of VKI and LHL vanes for AGS modeled transition.

While the LHL vane was optimized for the flow conditions of the VKI experimental heat transfer run MUR237, it is not appropriate to assume the LHL vane will perform with such reduced heat transfer for any other flow condition or combination of Tu , Re_2 , and M_2 . However, the stationary nozzle guide vane in a turbine works to guide the flow into a desirable orientation to do work on the rotor blades, turn the rotor shaft and ultimately produce thrust. While the exact axial point of choke can vary in the nozzle, depending on the area distribution and boundary conditions, the flow in vane passages is categorically designed to have transonic exit properties and choke the flow from the combustor. It does the same amount of flow-turning no matter what the flow conditions are, and observing the pressure loadings for the vane, very little changes would be seen over the course of a typical engine throttle transient (this, of course, is not the case for a rotating blade downstream). For the appropriate spectrum of turbine inlet conditions, the LHL vane would assuredly perform with similar reduced heat transfer characteristics relative to the VKI vane. Thus, the optimized LHL vane will certainly have improved thermal performance for a wide range of prescribed off-design conditions.

As the flow over a turbine nozzle guide vane normally has laminar and turbulent regions with transition in between on both the pressure and suction surfaces for most operating conditions, the focus of the heat transfer comparison stayed with the AGS prediction. It showed that the SS, and in consequence the integral, heat load could be reduced by delaying transition as a result of moving the minimum SS pressure ratio point back towards the TE as far as possible. To view the pressure loading and heat flux distribution comparisons of the VKI and LHL vanes at the design conditions applying the laminar and turbulent WILDCAT predictions, the reader may refer to Appendix I. Also

included for reference in the appendix are boundary layer property comparisons of the two vanes for the AGS model prediction, vane area and curvature distributions, the airfoil coordinates of the LHL vane, and boundary layer temperature and velocity profiles of the two vanes.

The WILDCAT code, which finds the flow properties for each of the vanes, in conjunction with the novel design system, provides outstanding tools for the turbine designer. One of these tools is the plotting of color contours for any of the properties that can be calculated by the flow-solver. Interesting comparisons can be made between the VKI and heat load optimized LHL vanes. To further summarize and compare the flow properties for the two vanes, Figures 45 through 50 give side-by-side comparisons of the 2-D midspan shaded flow-field for (in this order) isentropic Mach number, absolute velocity, static pressure, vorticity, static temperature, and a pseudo-Schlieren image. All plots were generated using a supersonic (high detail) grid and a laminar viscous assumption. The top plots are the VKI vane and the bottom plots are the LHL vane for each flow-field property illustrated. The most prominent trends can be seen in the gradients of flow properties.

Figure 45, showing the isentropic Mach number, a dramatic difference between the two vanes can be seen. A slightly higher inlet and exit Mach number is seen for the LHL vane. In addition it can be seen that the flow is more gradually accelerated through the vane passages of the LHL vane than for the VKI vane, most likely attributable to the redesigned SS curvature.

In Figure 46 for the flow-field absolute velocity, this less severe vane passage gradient can again be seen for the LHL vane. Another interesting trait of the velocity plot

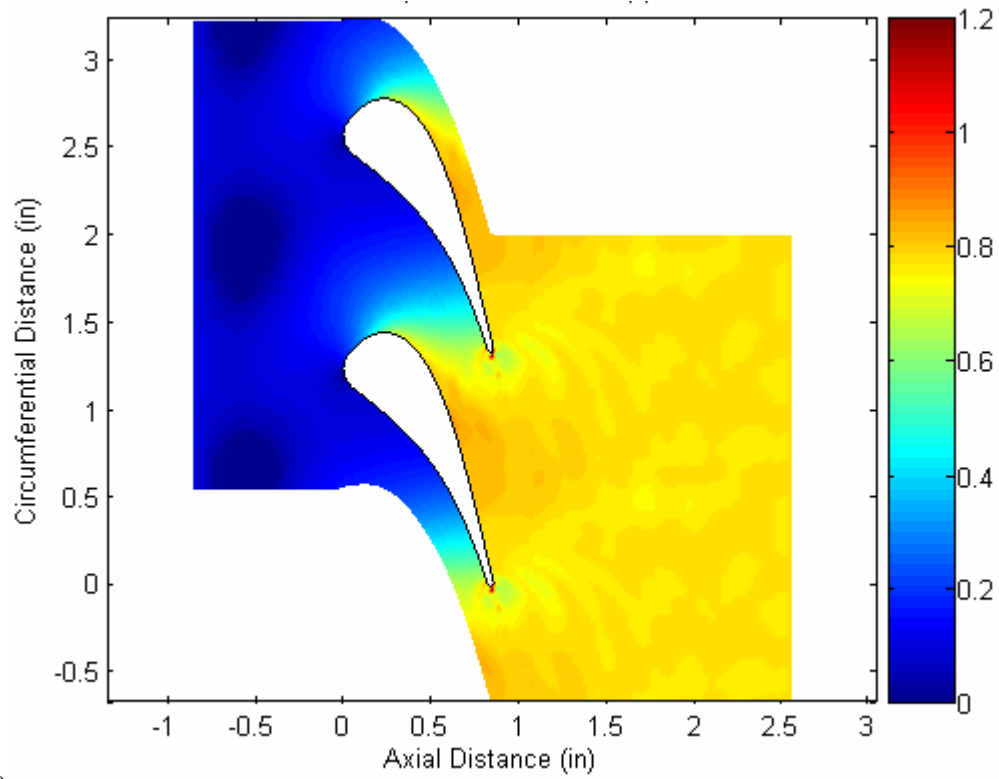
is the way in which trailing edge vortices are produced by each vane due to the low pressure stagnation of flow at this point. As far as velocity gradients are concerned, the TE vortices for the LHL vane are less pronounced, which could in turn cause less wakes and slightly less unsteadiness for a downstream rotor blade compared to the VKI vane. Comparing the SS velocity gradients, it appears that the VKI vane has a small (possibly shock-inducing) gradient at about 60% surface distance, while the LHL vane has an even smaller gradient at the same location.

The static pressure fields seen in Figure 47 show that any TE shocks that may occur from the accelerated exit flow may be more evident for the LHL vane. The pressure waves radiating from the TE of the vane for LHL appears to be stronger than for VKI. Supporting the suggestion given in the absolute velocity field discussion, the next figure, Figure 48, shows that the magnitude of vorticity off the TE may be a bit greater for the VKI vane as the gradients are more apparent.

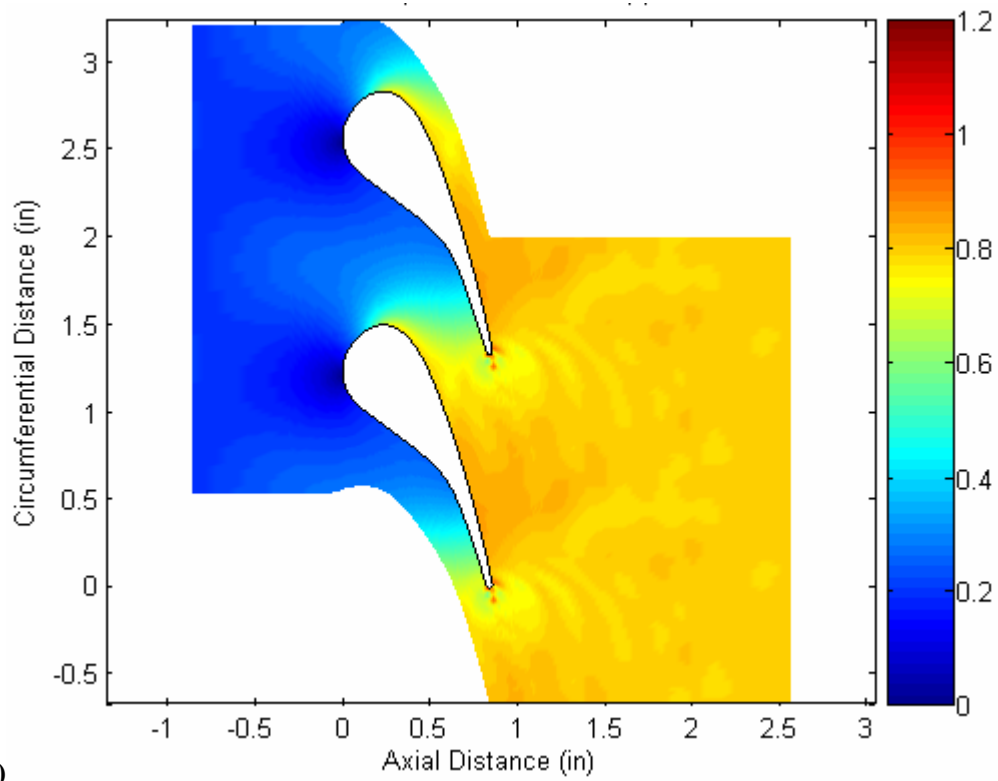
Finally, the static temperature flow for the vanes in Figure 49 seem to be quite similar, while the pseudo-Schlieren plot of Figure 50 illustrating the density gradients around the airfoils also show that the TE shocks for the LHL vane may be a bit stronger than for the VKI vane. The white areas on the SS may be ignored because they are false calculations of the flow due to the way the gradients are determined, hence the term pseudo-Schlieren. Only further experimental study would be appropriate to study this issue.

When it comes to the challenge of reduced airfoil surface heat load, and the contenders are VKI versus LHL, LHL wins rather decisively. Aerodynamically, while the LHL vane has shown that it has lower loss and very desirable pressure loading

characteristics, the mounting evidence pointing to shock structures possibly forming on the suction side is suspect. Nevertheless, a full summary and comparison of two worthy turbine nozzle guide vanes for heat transfer and aerodynamic qualities has been given. The study can now progress further and it can be seen how the two might perform in a linear cascade shock-tunnel experiment.

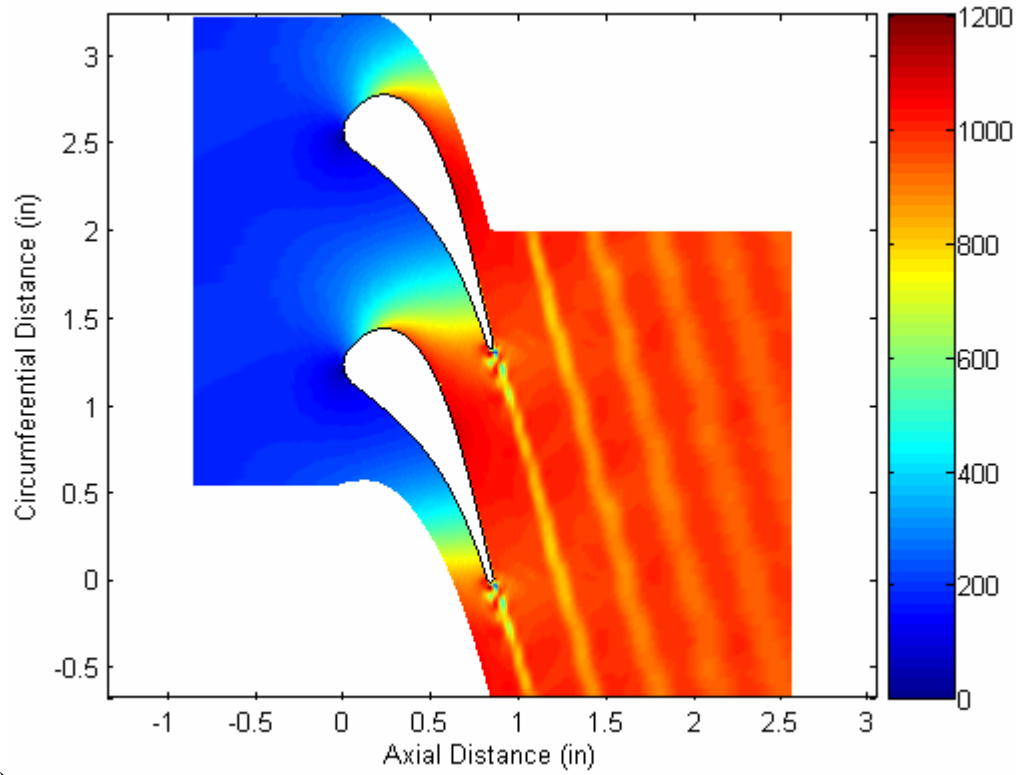


(a)

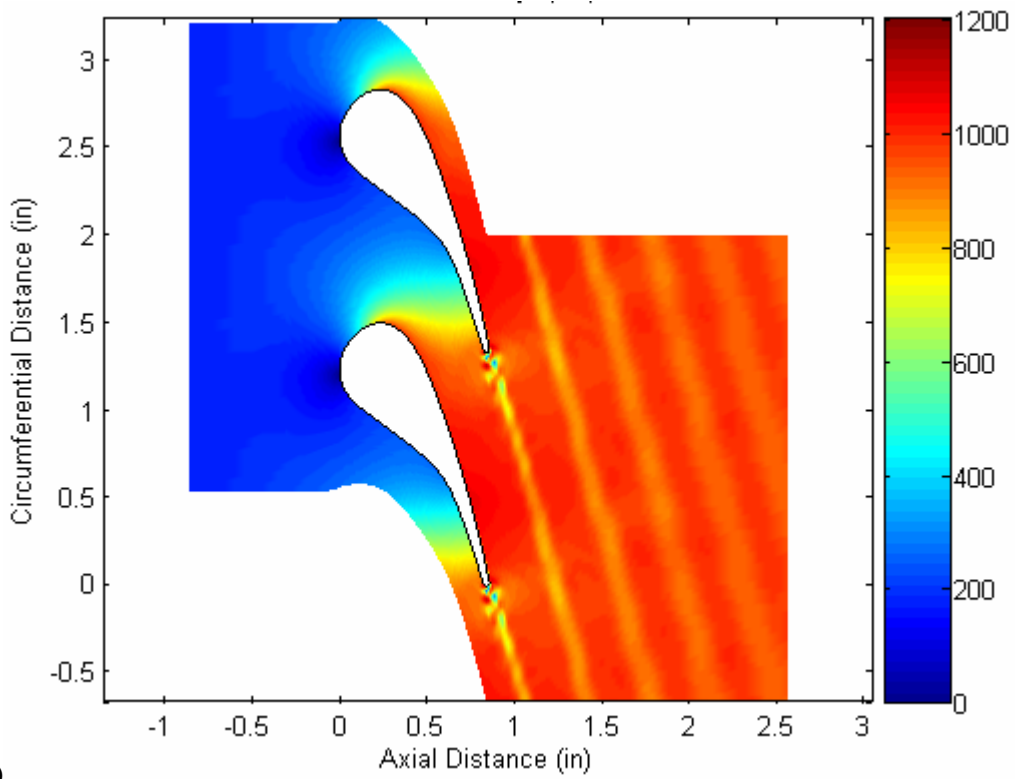


(b)

Figure 45 2-D Isentropic Mach number flow-fields for VKI (a) and LHL (b) vanes.

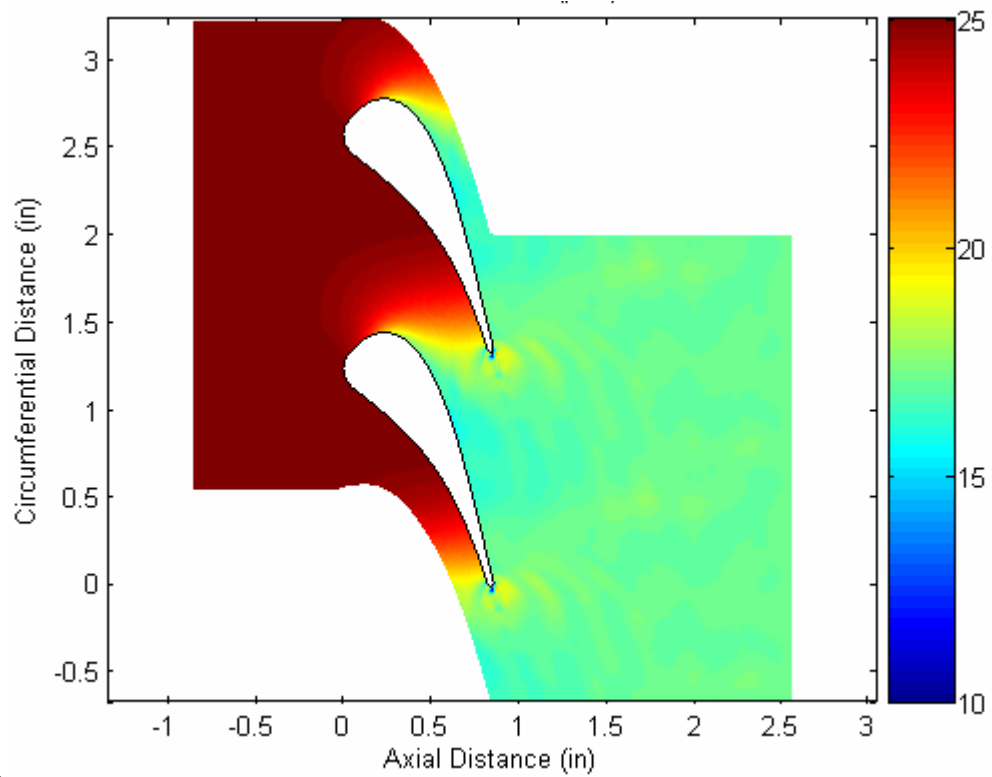


(a)

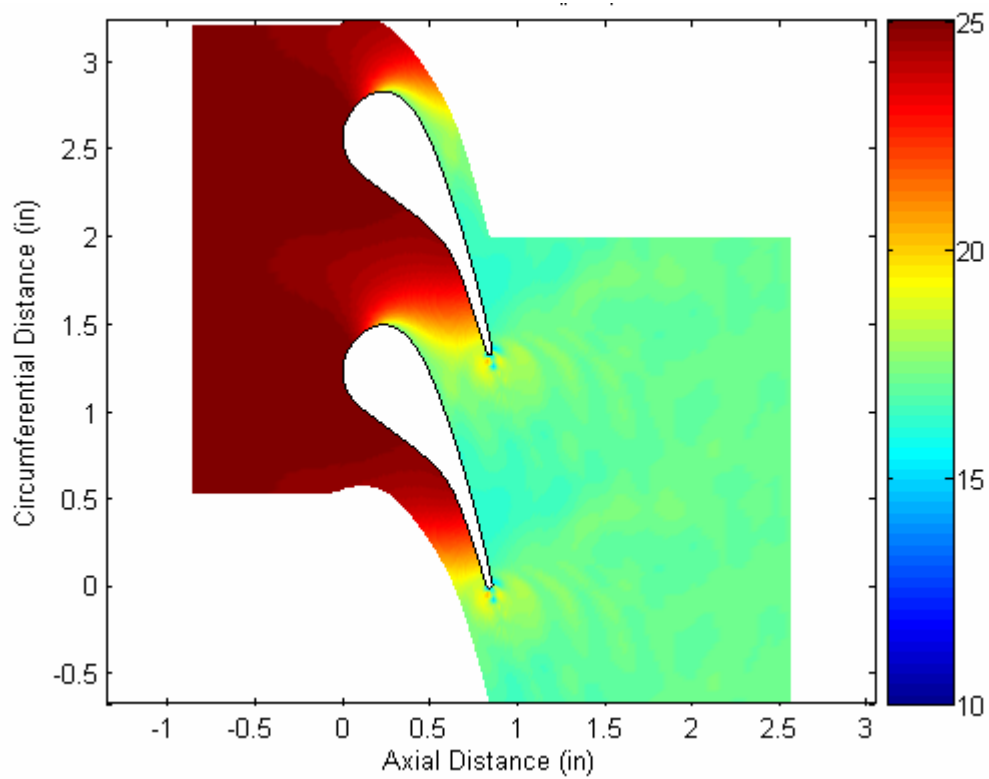


(b)

Figure 46 2-D absolute velocity (ft/s) flow-fields for VKI (a) and LHL (b) vanes.

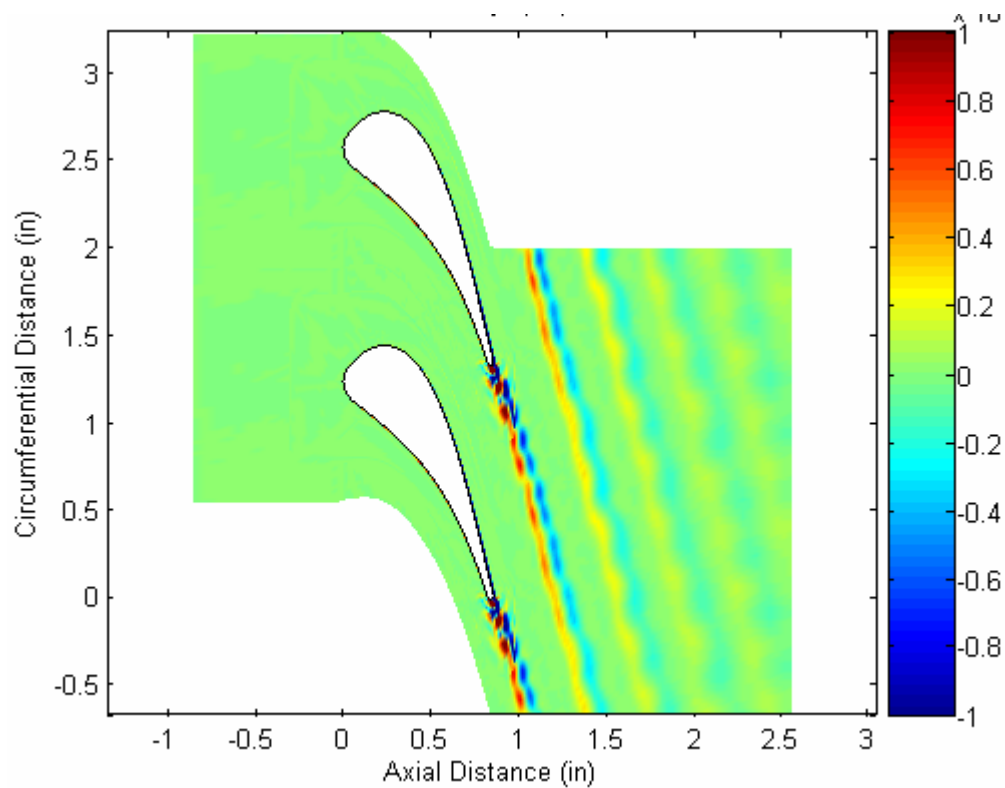


(a)

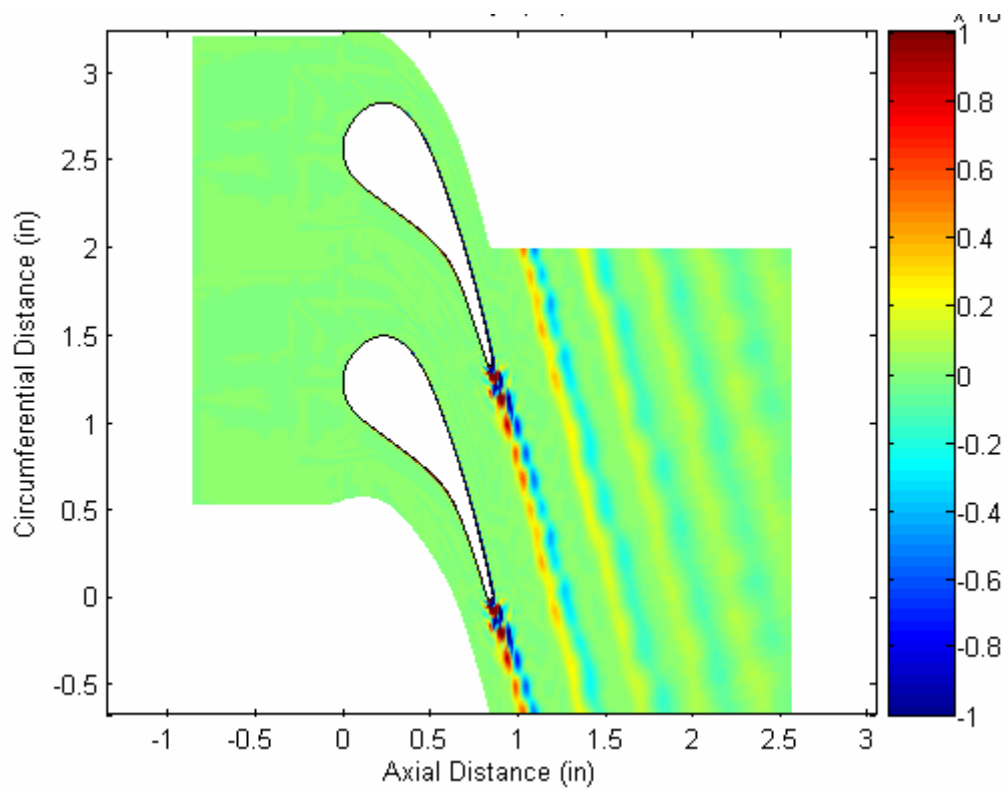


(b)

Figure 47 2-D static pressure (psia) flow-fields for VKI (a) and LHL (b) vanes.

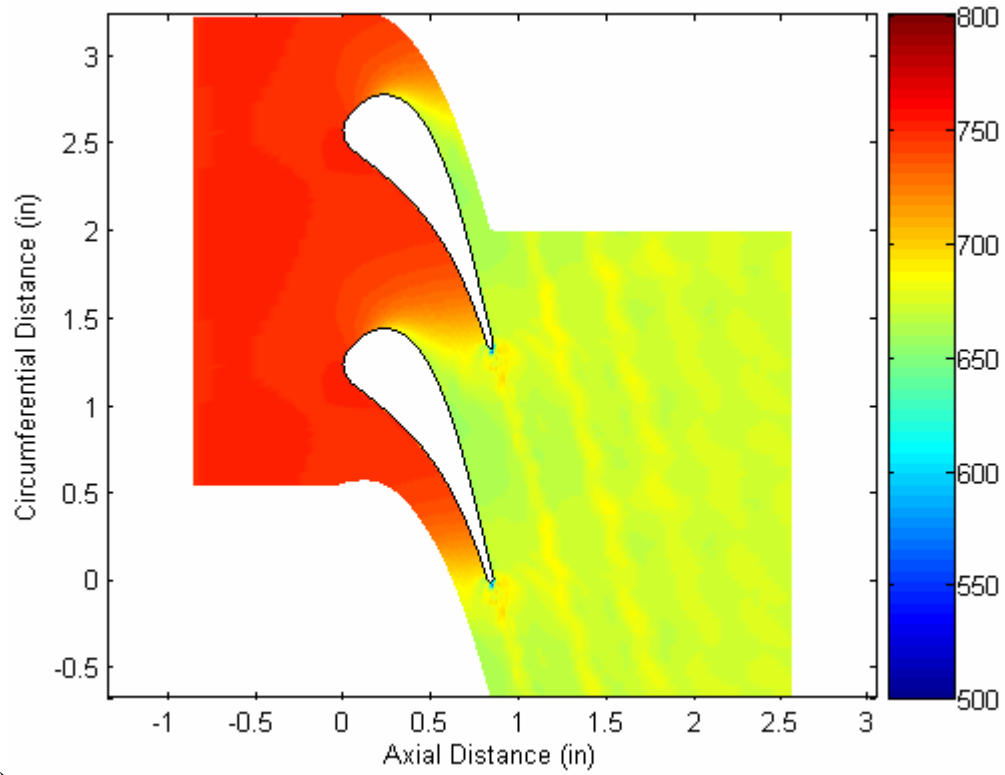


(a)

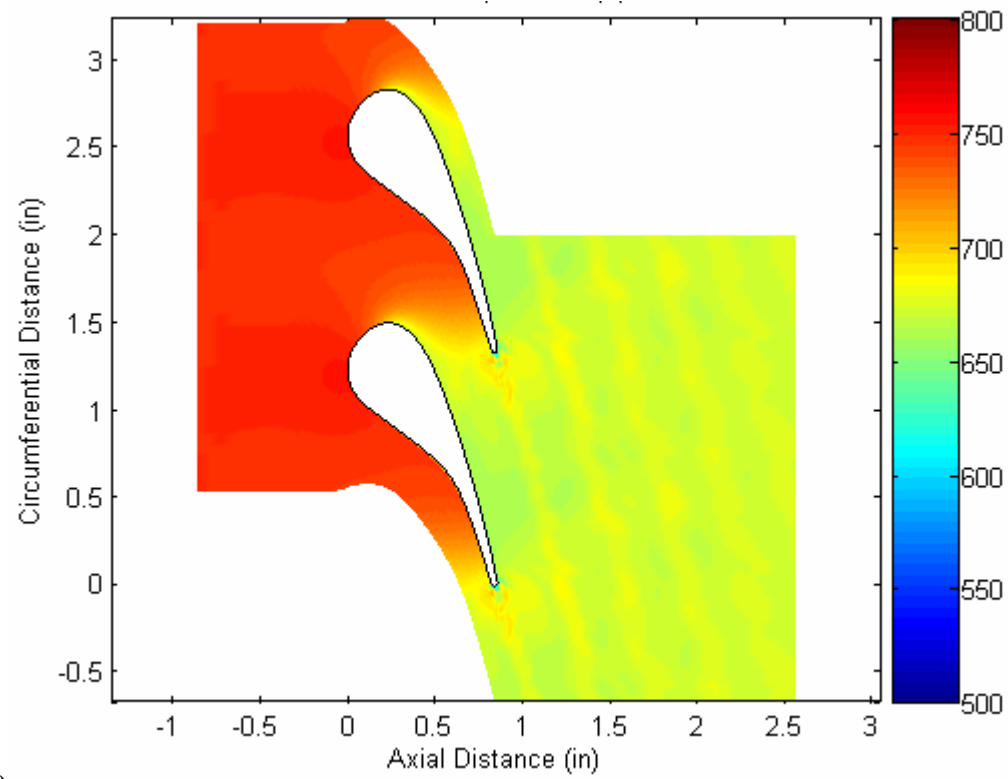


(b)

Figure 48 2-D vorticity ($s^{-1} \times 10^5$) for VKI (a) and LHL (b) vanes.

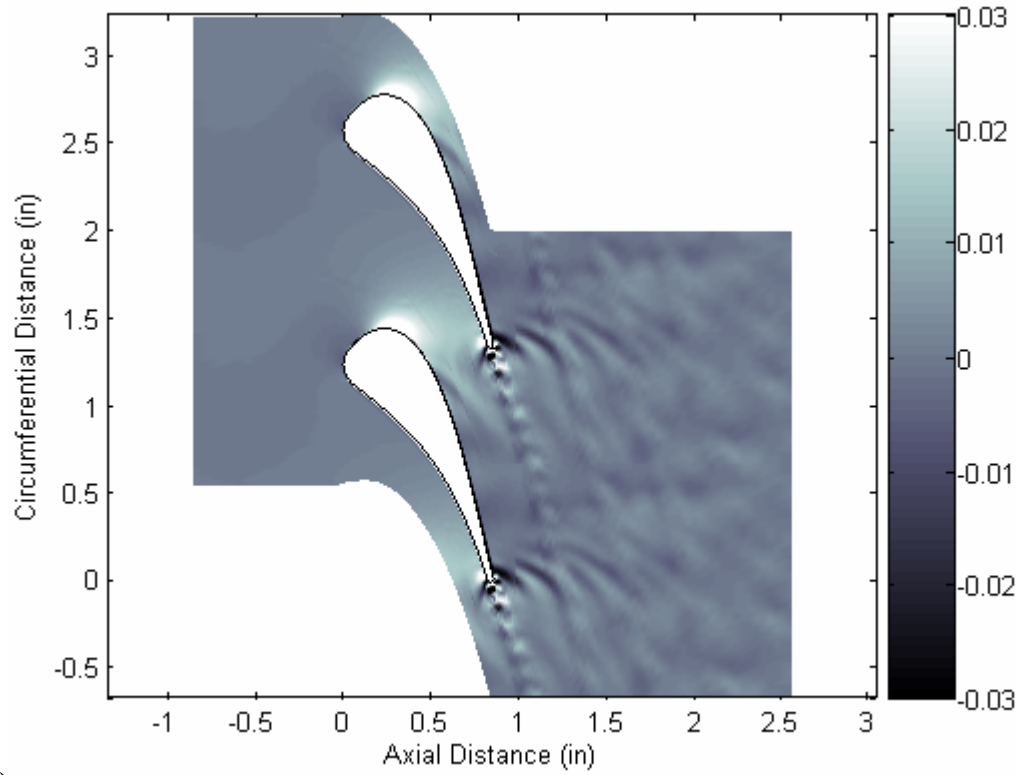


(a)

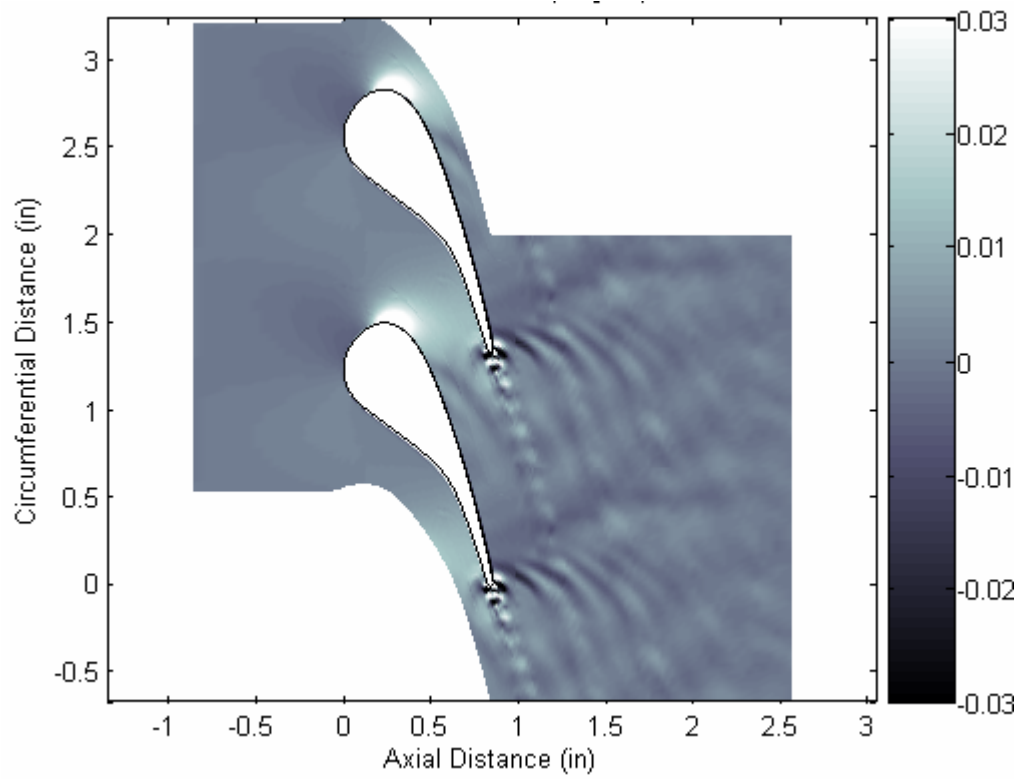


(b)

Figure 49 2-D Static temperature ($^{\circ}\text{R}$) for VKI (a) and LHL (b) vanes.



(a)



(b)

Figure 50 Pseudo-Schlieren (slug/ft) comparison of VKI (a) and LHL (b) vanes.

Experimental Procedure, Data Reduction, and Results

Procedure

Prior to each shock tube run the current source boxes were given time to achieve a steady thermal state. A mylar diaphragm was installed and hydraulically clamped between the shock tube driver and driven sections. Care was taken to ensure the mylar as well as the rubber gaskets on each side of the Mylar were centered in the interface to prevent any possible problems with driver pressure leakage. A constant current of 4 mA was passed through the gauges. The resulting ohmic (i^2R) heating of the gauge subsequently produced a negligible part of the gauge temperature difference experienced during experimentation. Using a large compressor, the driver section of the tube was pumped to the desired pressure using the real-time read-out of the driver side Kulite transducer. A valve was used to seal off the driver section and another valve was opened to release high pressure air into the line for the spike piston. Ambient temperature and pressure were recorded. Using LabView software, driver pressure could be monitored, and the sampling frequency and data buffer values could be entered along with the desired test time. When the desired driver pressure was reached and the software was ready to sample data, a verbal command was given to depress the trigger which activated the spike to break the mylar diaphragm and ultimately send a normal shock wave propagating down the tube. Data was collected for 2.5 s and written to a MATLAB file for all runs. As the pressure in the shock tube equalized with atmospheric pressure and all disturbances had dissipated in a mere 200 ms, the raw data was reduced appropriately to save future computing time when converting the voltages to more useful forms. To

repeat the process, the old mylar diaphragm was taken out and discarded, the inside of the tube was inspected for shrapnel, and a new diaphragm was installed.

Diaphragm thicknesses of 2, 5, 7, and 10 mil were available for this work. Only the 7 mil diaphragm thickness was used knowing the range of desired driver pressures of 50 to 80 psia and because of complications with other thicknesses. The 5 mil diaphragms would stretch like a balloon at the desired driver pressure so much so that the internal spike when deployed would not reach far enough to break the stretched diaphragm. The 10 mil diaphragms were found to be too thick for this work since when the spike broke through the diaphragm in the necessary driver pressure range, the diaphragm would not rupture violently enough to create a shock wave. The spike would merely poke a hole in the center of the mylar, merely creating a fast leak out of the driver section.

As the tests only used one turbulence grid, the cascade experiments in the shock tube only examined two different values of T_u . In addition, since the thicker diaphragms which could bear more driver pressure (P_4) did not break appropriately in order to create a good moving normal shock, and since lower P_4 runs did not stimulate the thin films enough to create significant changes in raw voltage (thus heat flux), nor are they representative of typical turbine inlet conditions, only a single P_4 of approximately 60 psia was used for all runs. Thus the best four runs of the VKI and LHL vanes with the grid in and out are available for heat transfer analysis. Table 6 gives the flow condition values to be expected in the shock tube according to the shock tube equations compiled by Anderson [44] for this experimental driver pressure. The value for axial vane chord Re can be assumed to be the isentropic exit value, or Re_2 , for comparison to past experiments.

Table 6 Shock tube flow conditions for $P_4 = 60$ psia.

Shock pressure ratio, P_4/P_1	4.20
Shock Mach number, M_s	1.346
Shock Wave Velocity, W	461.38 m/s
Total Pressure after reflected shock, P_5	51.29 psia
Total Temperature after reflected shock, T_5	427.9 K
$P_{s,in}/P_{s,ex}$	1.947
Re based on vane axial chord, Re_{bx} (based on $M_{ex}=0.8$)	676,720

Test Time

As the shock tube is a short-duration flow facility, the test time for all shock tube runs was approximately 5 ms. This is of about the same magnitude as the test times seen by Fillingim [10] in his thesis work with the same shock tube, but significantly less than the 80 ms of Dunn [54] in his full stage turbine work. The test time was resolved by observing the total pressure pitot tube transducer voltage trace from the test section inlet and the raw voltage trace from the thin film heat flux gauge located nearest the LE of the test vanes. The short duration flow test time could be observed where the raw signal flow characteristics were roughly constant. Figure 51 is an expanded view of the absolute total pressure read by the driver section and driven section Kulite transducers and the pitot probe positioned in the center of the cascade test section inlet for a sample shock tube run. The translation of the shock wave created in the tube can be seen quite clearly. At the beginning of the plotted time span, the driver pressure drop indicates the point in time when the diaphragm is ruptured and the shock is created in the tube. Eventually, yet rather quickly, the shock reaches the end of the driven section and the test section inlet probe, as the driven Kulite and pitot probe (divided by the flange piece that reduced the

area of the flow and reflected the shock) were only 5 inches apart. At this point (about 540 ms global time) the shock has reflected back into the shock tube and the high pressure reflected flow region, region 5 defined by Anderson, causes flow to move through the test section. This is also where the test time can be seen. This rough signal plateau appears to last for approximately 5 ms. The driver section then receives the reflected shock which phases through the reflected expansion wave from the driver section for a short time as seen by the reduction in pressure, and another step-rise in pressure is seen by the driver section as the shock wave moves down towards the test section again. This wave phenomena repeats while waning in strength as the pressure in the tube decreases down to ambient levels. This repetition explains the periodic, diminishing-amplitude nature of the pressure and heat flux voltages obtained from the experiment. The reader may refer back to the shock tube theory section of the thesis to gain more insight on the unsteady wave characteristics seen in a typical shock tube.

The two graphs displayed in Figure 52 show cascade inlet and exit pressures from the combined read-out of the 3 upstream static pressure taps (top) and the 5 downstream static pressure taps (bottom). Similar patterns as for the total pressure measurements can be observed here as well. Again, as the wave disturbances reflect back and forth internally between the ends of the tube, the effect is multiple occurrences of test section flow generated behind a reflected shock inside the tube that decreases in amplitude with time.

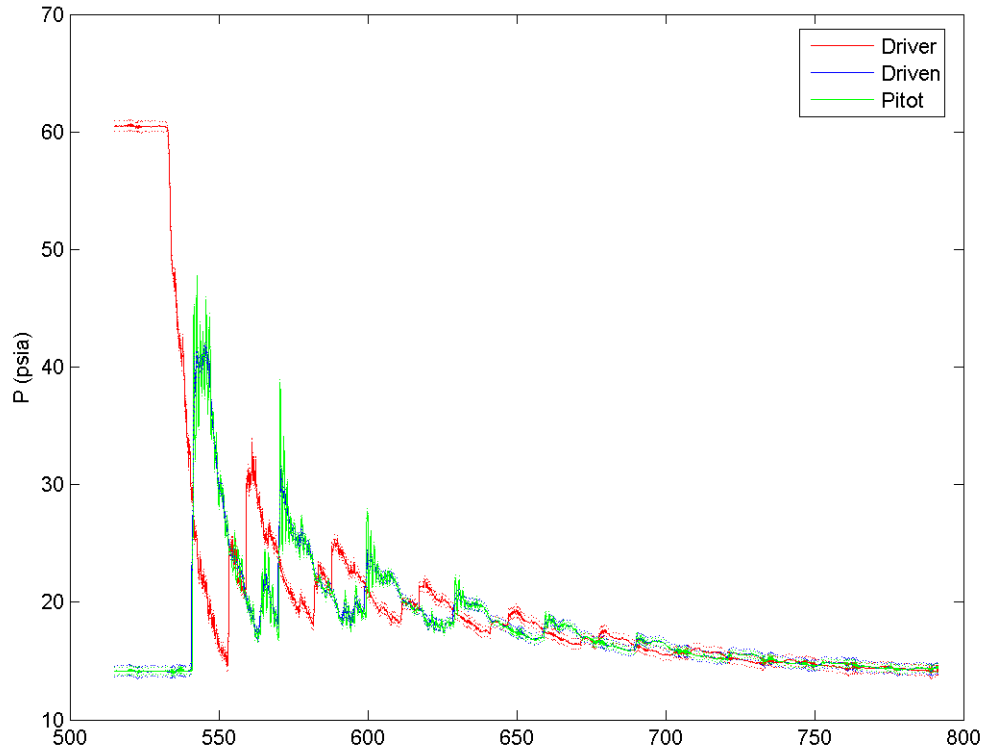


Figure 51 Pressure histories during a sample shock tube run. The apparent line thickness denotes measurement uncertainties.

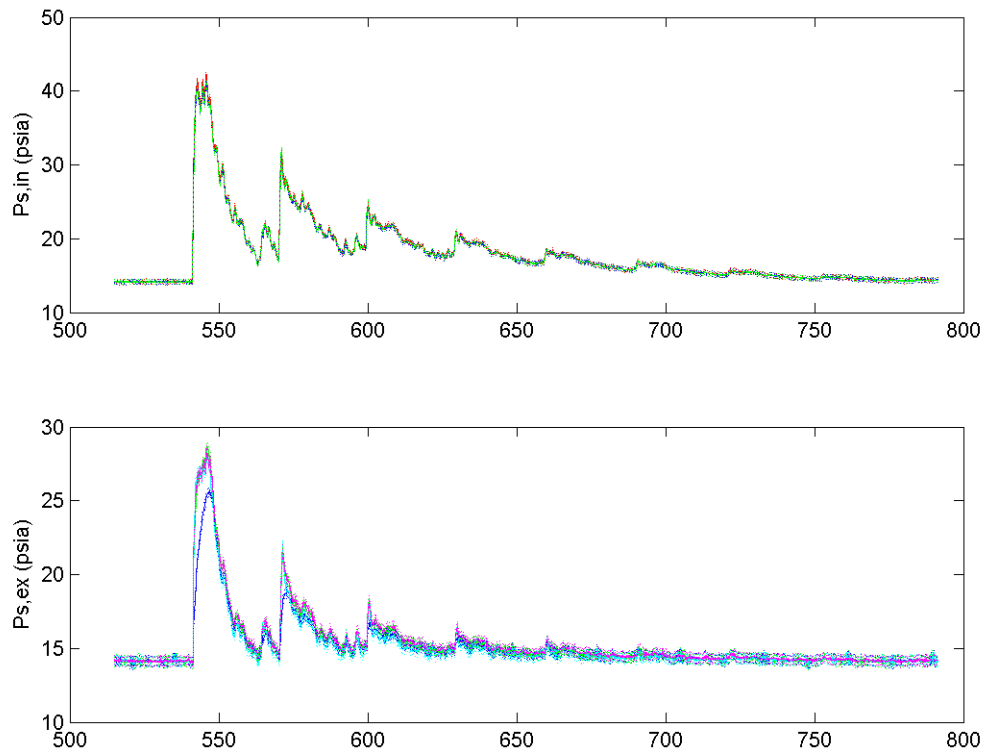


Figure 52 Inlet (top) and exit (bottom) static pressure voltage traces for a nominal experimental run. The apparent line thickness denotes measurement uncertainties.

Figure 53 below shows voltages and converted heat flux histories for a given shock tube experimental run. All three plots in the figure are signals recorded from a single leading edge thin film heat flux gauge. The top two graphs show the raw voltage and time derivative of raw voltage (dV/dt), respectively. The second plot gives the slopes of the raw voltage to help wring out exactly where in time voltage spikes due to the interaction of unsteady wave disturbances are occurring. An initial high amplitude spike was evident for essentially every run. Care was taken to ensure the test time did not include this spike. The two black vertical lines therefore define the actual test time. From the third plot in Figure 53, the average heat flux for a given gauge on the vane for a given run within the test time was used as the unsteady maximum value to be used for plotting against fractional surface distance of the vane to analyze experimental surface heat transfer distributions.

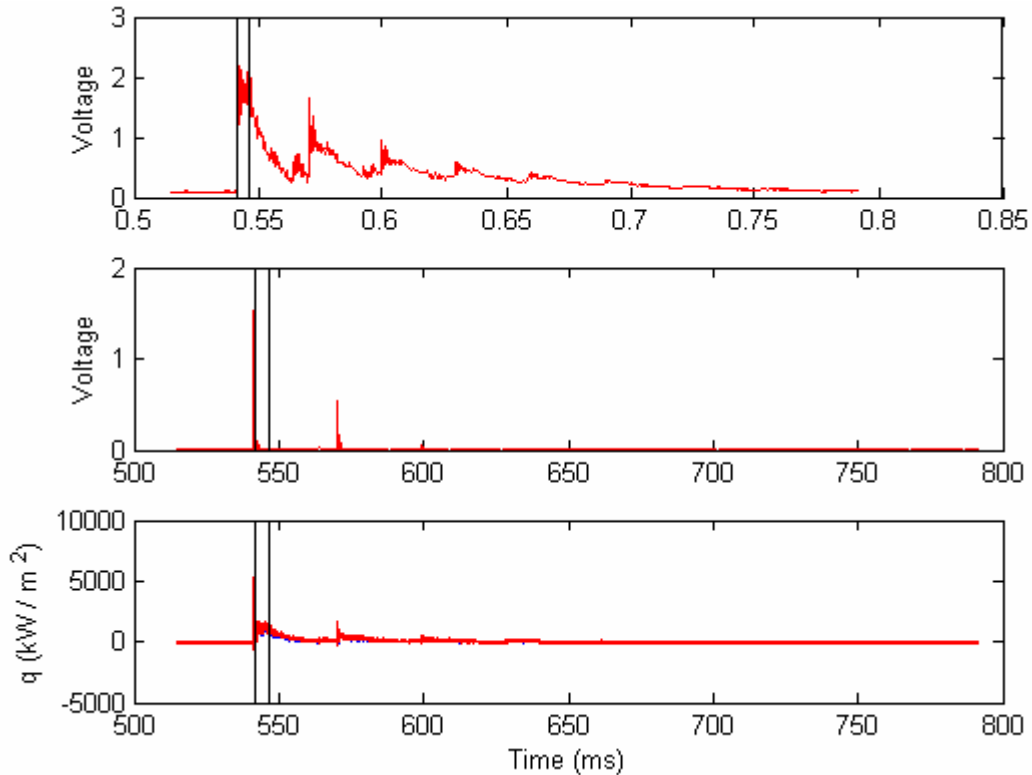


Figure 53 Raw and converted (heat flux) voltage signals for a LE heat flux gauge during a sample shock tube run.

It was discovered during the data reduction process that each of the total of 30 channels in the pre-emphasis filter and current source boxes (15 channels per box) used to process heat transfer data had a unique gain response over a range of measured frequencies. This makes sense knowing that no two complex circuits are truly alike. Since the test time was approximated at 5 ms, the minimum signal frequency is 1.0 divided by this amount, or 200 Hz. Originally, all the channel gains were measured using a nominal gain from one of the 30 channels at 200 Hz, which is not entirely thorough. To correct this and obtain the right time-average, the time-mean from the ratio of nominal gain to actual gain at that frequency was scaled using an optimizing function in MATLAB. Consequently, optimum boost-filters that best fit the measured response for each channel were designed to ultimately get a more accurate heat flux signal. Figure 54

shows a magnified view of the converted heat flux signal in the bottom plot of Figure 53 from which an average was calculated using MATLAB codes with the start at end times indicated. It also illustrates the effect of the correction for channel gain response uniqueness. The corrected signal is more enhanced resulting in higher heat flux values, at least for the current channel depicting the signal from the LE heat flux gauge. In general for most gauges, a slight increase in heat flux was noticed for the optimized signal.

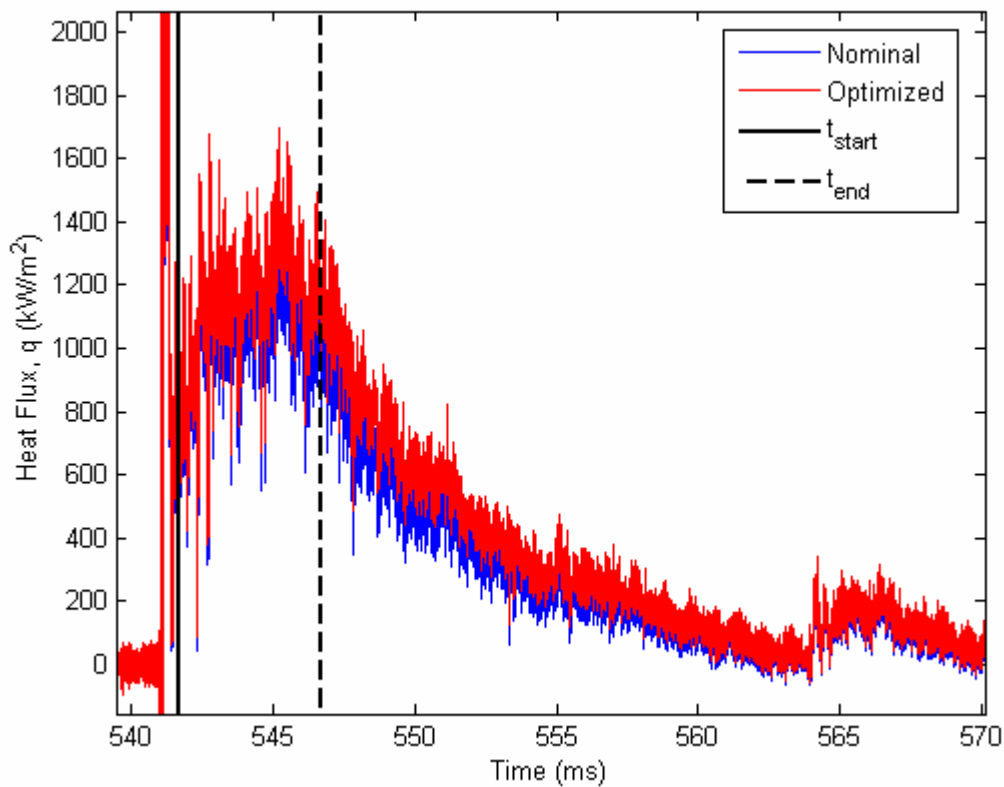


Figure 54 Expanded view of the experimental test time for the converted heat flux signal. Correcting for independent channel gain response increased the heat flux signal slightly.

All reduced heat transfer data was realized using the methods of Oldfield [50], which is standard for this type of semi-infinite substrate thin film heat flux gauge. This means the heat conduction was modeled using the semi-infinite solid assumption, as it is described by Ref [57]. MATLAB codes created by Oldfield were used to perform an

infinite impulse response (IIR) technique to deboost, filter, and convert raw voltage data to heat flux. Details pertaining to heat flux gauge operation and conversion of voltage to heat flux is outlined in Appendix D.

Turbulence Measurements

To ensure the freestream turbulence intensities (Tu) experienced by the thin-film-instrumented vanes in the shock tube cascade were close to the expected values from grid design, a single-film TSI model 1210 T1.5 hot-wire probe with 0.06 in sensing length mounted perpendicular to the flow direction and a TSI model IFA-300 constant temperature anemometer were used to take measurements in the test section. The same probe ports used to obtain inlet total temperature and pressure measurements were used to measure turbulence levels. Data was taken for shock tube runs at approximate driver pressures of 60 psia (the same pressures used in the actual experimental runs) with and without the turbulence grid installed. Equation 8 gives the definition of Tu ,

$$Tu = \frac{\sqrt{u'^2}}{U_\infty} \quad (8)$$

which assumes isotropic turbulence [47]. Isotropy occurs when the root-mean-square (rms) of the fluctuating velocity ($\sqrt{u'^2}$) is the same in all three coordinate directions. U_∞ is the freestream velocity of the flow. Without the grid, a background level of Tu between 1% and 2% is expected, which has been observed by experimentalists for unobstructed flows such as Roach [45]. Of course, as the turbulence grid used was designed to generate 6% turbulence intensity, approximately that value was expected to be measured by the hotwire.

After processing the data by way of the methods outlined in Appendix J for determining Tu from an uncalibrated hot-wire such as that used here, it was found that the experimental turbulence intensities were very close to the expected theoretical values. Without the grid, the measured Tu was $2 \pm 0.3\%$. With the grid installed, the experimental Tu was $5 \pm 1.0\%$. The measured values include a margin of error as determined by Mee and Dickens [58]. In addition, these values were measured 0.5 in upstream of the instrumented cascade vane and are a good estimate of what the vane actually experienced at the leading edge, considering the measurement error. Figure 55 shows the grid-installed raw voltage flow measurement along with the high-pass filtered version of the data on the top graph and the autocorrelation coefficient (ACF) as calculated in Appendix J in the bottom graph. The corresponding eddy length scales are estimated to be slightly larger than the turbulence grid wire diameter ($d = 0.035$ in compared to the theoretical $\Lambda_x = 0.044$).

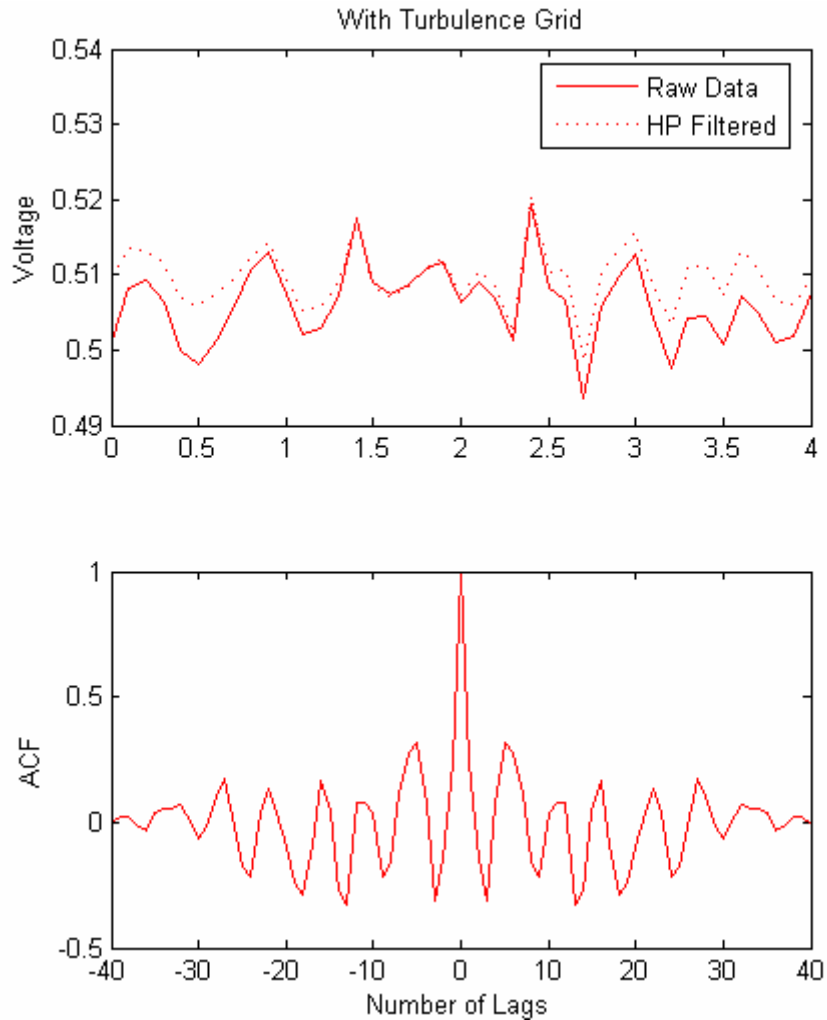


Figure 55 Single-film hot-wire output with turbulence grid installed at $P4 = 60$ psia.

Originally, the turbulence levels were measured using a model TSI-1250 two-component (X-wire) hot-wire probe with 0.08 in sensing lengths. One of the two channels on the X-wire was obviously showing errant readings after performing a few good grid-in measurements, giving a grid-out turbulence level of over 13%. The wire may have been disturbed upon the removal of the grid. In addition, the ACF for the X-wire did not reach any sort of periodicity over the shock tube test time which also indicated a flawed measurement. The X-wire did however provide one good channel for measuring Tu after grid removal, which turned out to be 5.4% with the grid in and 2.1%

without, which agrees very well with the measurements of the single-film. In addition, this one good channel in the X-wire displayed an interesting mean-flow variation characteristic, perhaps suggesting the passing of an unsteady wave from the shock tube over the test time. The idea of filtering out the lower frequency signals to reduce the effects of mean flow variation was considered, but since most of the turbulent kinetic energy (TKE) from the grid occurs at low frequencies, it was decided that only unfiltered data was reliable. Figure 56 gives the raw voltage, high-pass signals, and ACF of the X-wire for reference. The increased voltage of the faulty channel that gave augmented Tu levels can be seen in the second plot.

Concerning measurement of turbulent eddy length scales utilizing either the single-film or X-wire, it was found that the test time of 4 to 5 ms may be too short to get an accurate estimate experimentally. To estimate the spectrum of turbulence, multiple averages of the spectrum are needed to resolve the fluctuation characteristics. Since an autocorrelation is the value of the power spectrum at zero frequency, it follows that it might not be able to be estimated properly over the extremely short test duration. Now that a proper procedure, along with test time resolution and experimental turbulence measurements have been laid out, the heat flux data recorded in the shock tube experiments may be examined for the VKI and LHL vanes.

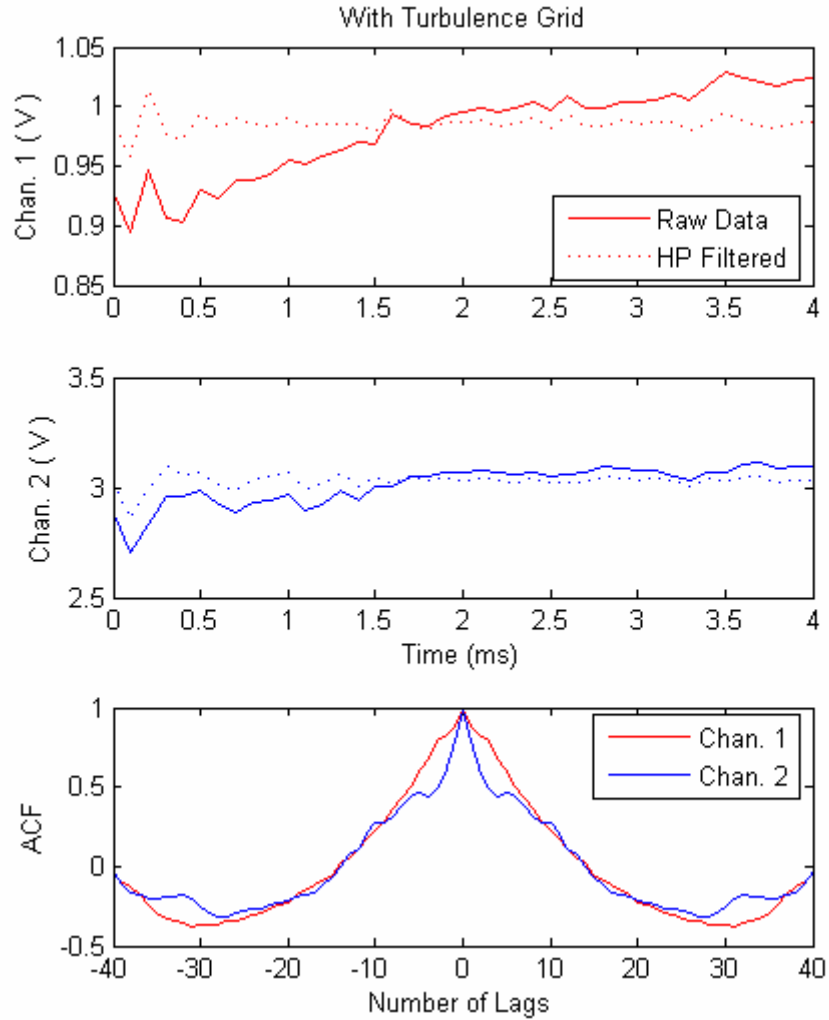


Figure 56 X-wire turbulence level measurement data.

Experimental Comparison of VKI and LHL Vanes

To recap, a low pressure ratio rectangular shock tube was used with a 2-D linear vane cascade test section to record midspan heat transfer measurements for the VKI vane and the computationally heat-load-optimized LHL vane geometry. All runs were performed with a driver pressure of approximately 60 psia whereas data was taken with ($Tu \approx 5\%$) and without ($Tu \approx 2\%$) a turbulence grid installed upstream of the test section for each of the two vanes. This resulted in a total of four unique experimental runs. Table 7 gives all run conditions and measured flow properties such as pressures and

Mach numbers from the four runs for which heat transfer data will be analyzed. Properties with the subscript “in” are for the test section inlet and properties with the subscript “ex” are for the test section exit ($M_2 = M_{ex}$).

First, the grid in versus grid out heat transfer measurements will be analyzed for each vane. In order to get the experimental heat flux distributions correctly represented as functions of fractional surface distance, the locations of the heat flux gauges around the vane had to be charted as film distances from the LE and then converted to fractional distance by multiplying by the respective vane total midspan wetted length. The Kapton arrays were designed to be 1/16 inches shorter than this wetted length so the films did not hang off the TE of the vanes. Ideally, the edges of the entire gauge would have been spaced the appropriate distance from the TE when being centered on the LE and wrapped around the vanes. Unfortunately, the gauges of the LHL were slightly off-center when the gauges were adhered to the vane surface. However, these factors were taken into account when converting to fractional distance coordinates, which ensures that the heat flux measured in the subsequent plots have the appropriate data point locations. The coordinates of the gauge locations for the VKI and LHL vane are listed in Appendix G.

Table 7 Shock Tube experimental run conditions for vane heat transfer measurements.

Run No.	Vane	Grid in?	P ₄ (psia)	P ₅ (psia)	P _{t,in} (psia)	P _{s,in} (psia)	P _{s,ex} (psia)	P _{amb} (psia)	M _{in}	M _{ex}
10	VKI	Yes	60.23	39.21	39.04	37.79	24.65	14.22	0.216	0.838
11	VKI	No	59.61	40.46	40.36	39.17	25.39	14.22	0.208	0.842
16	LHL	Yes	60.51	40.33	40.12	39.15	25.93	14.16	0.188	0.815
17	LHL	No	59.72	39.38	39.62	38.41	25.51	14.16	0.211	0.819
18	LHL	No	60.39	40.96	41.03	39.86	26.27	14.16	0.203	0.824

Figure 57 compares run numbers 10 and 11 for the VKI vane with grid in and grid out. The physical concentration of gauges as designed near the LE and past about 40% of the SS can be seen in the relative proximity of the data points. This increased the data resolution in the areas of interest on the vane surface. It is expected that this plot would show lower heat transfer for a case with no grid relative to a case with the turbulence grid for the same vane, which for the most part is seen, primarily for the high magnitude heat flux characteristics. Near the LE, there appears to be early transition followed by relaminarization. Near the TE, seeing a PS transition to such high heat flux is a surprise knowing the typical historical data in open literature for similar run conditions of M_2 and Re_2 . The source of the high heat flux is unknown at this point, or the data is spurious.

In general, the pattern of the heat flux distribution measured in the shock for this and essentially all runs had unconventional characteristics compared to what a prediction might show. Normally, the LE heat flux would indicate an obvious local maximum with a definitive decrease in magnitude on either side making it easy to pick out where the LE is located. In Figure 57, it may be difficult to believe that the LE heat transfer occurs at the $x = 0$ location. Additional calculations (to make certain the values in Appendix G are correct) were done to ensure that the LE heat transfer was what it was and CFD trials were performed to ensure that unsteady wave motion could not move the LE flow stagnation point through a change in the inlet flow angle. It may appear that the LE heat transfer lies at 20% of the suction surface distance, but if this were true the flow stagnation would have to move towards the suction side with a resultant inlet flow angle, α_1 , of 40° , which is impossible.

Consequently, both surfaces appear to show rather sudden increase transition to turbulence after passing the LE and an area of extremely high heat transfer relative to the rest of the surface, especially on the SS, which may be attributable to formation of shocks near the vane passage exit. However, the SS may instead be indicating early transition, relaminarization, and then transition again at about 60% of the fractional distance. If that were the case, the grid out (lower Tu) run appears to transition later, which agrees with theory. Gauge number 16 on the VKI vane SS turned out to be a dead gauge as seen by its reading of zero heat flux. While the magnitude of heat transfer is much higher than expected, the heat flux gauges are clearly giving probable heat flux readings with a reduction in heat transfer for the case of experimental $Tu = 2\%$ as opposed to the $Tu = 5\%$ case, which agrees with theory and trends in past experiments in Refs [24], [26], and [27]. Error bars in Figure 57 and subsequent plots show heat flux uncertainty.

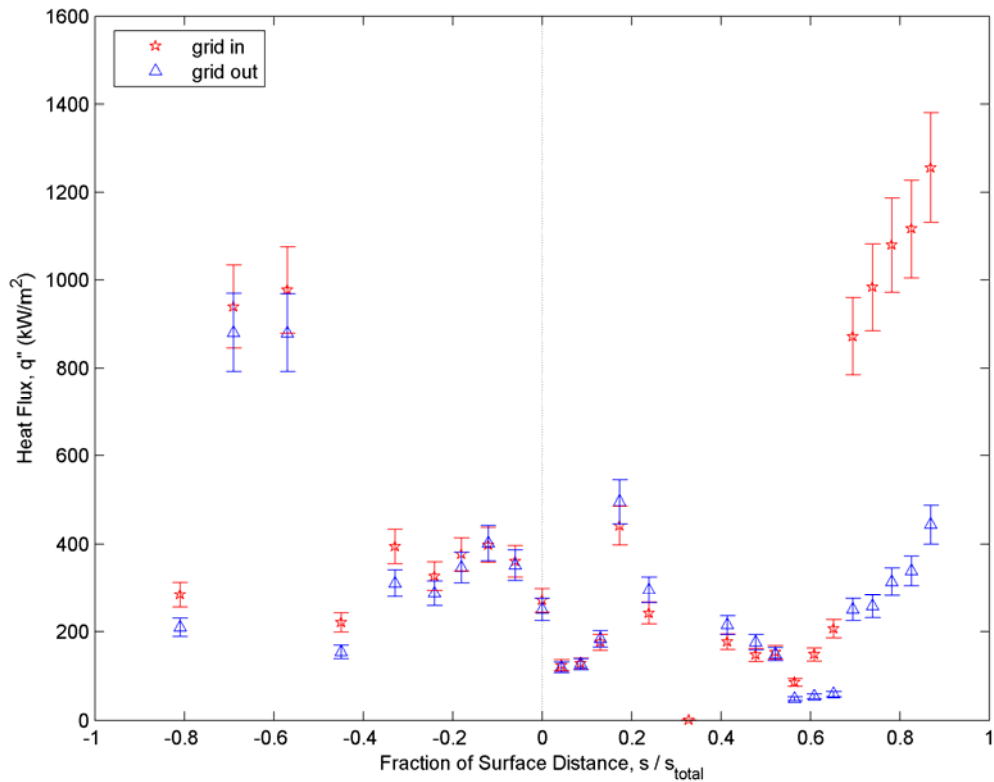


Figure 57 VKI vane experimental heat flux for different Tu .

The heat flux from the LHL vane grid-in and grid-out runs is illustrated in Figure 58. Here the heat flux is much better-behaved, as compared to the data for the VKI vane, especially on the PS. The distribution is smooth with possible transition from a laminar boundary layer to a turbulent one at about 30% of the PS, although the entire PS may be laminar. Immediate transition occurs on the SS at about 4% of the SS. Interestingly, each vane experienced early SS transition at the same fraction of surface distance, regardless of the level of Tu . More investigation may be necessary to explain this phenomenon, as historically in numerous experiments, increasing Tu had caused earlier transition onset. The heat transfer from transition to turbulence on the SS is much more pronounced than that of the PS. The experimental SS boundary layer follows theory as the heat transfer is high at first and decreases as the boundary layer grows. The SS heat transfer decreases so much as to possibly suspect relaminarization of the boundary layer, which may be possible as the LHL vane was designed to hold off transition as long as possible. The change in loading in Figure 43 supports this. Again, this second transition event occurs closer to the TE for the grid-out lower Tu case, as it should. One must keep in mind the scale of the heat flux—while the values appear low on the SS after transition, at least for the grid in case, the heat flux is still on the order of 100 kW/m^2 . Lastly, the SS shock peak heat transfer is much higher than that for the VKI with and without the grid in.

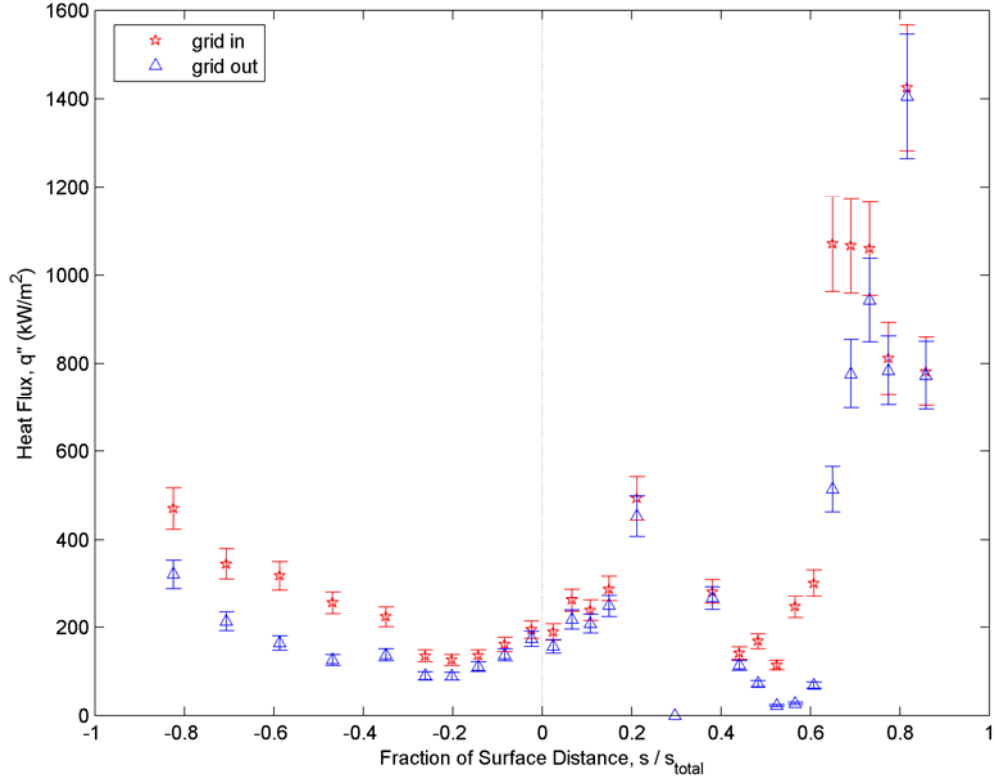


Figure 58 LHL vane experimental heat flux for different Tu .

Grid-in and grid-out comparisons have been made for each individual vane showing heat transfer trends that agree with theory and literature. Now the heat transfer comparison of the VKI and LHL vanes can be addressed. In the optimization effort of this thesis, it was shown that the LHL vane had commandingly more desirable heat transfer heat transfer qualities over the VKI vane. Figure 59 compares shock tube experimental runs 10 and 16 which both had the grid installed upstream of the test section. The LHL vane clearly exhibits significantly lower PS and lower LE heat transfer by almost 30% of the VKI vane magnitude. This shows that the WILDCAT code successfully predicted that the LHL vane would have lower LE heat transfer relative to VKI. In addition the heat transfer is generally much higher than in the prediction as seen by the levels and the heat flux scale on the y-axis. Generally, the LHL vane is mostly

laminar, with high heat transfer due to thinned-out boundary layers. The immense difference in heat transfer compared to what is expected will be addressed in the next section. Using MATLAB to inspect the data, it turns out that transition occurred at 11% of the SS distance for the LHL vane and 4% for the VKI vane. It appears for the LHL vane the SS there is short-lived laminar boundary layer followed by an immediate transition to turbulence, while the VKI SS appears to rise right up to turbulent levels of heat transfer, slightly lower than that for the LHL vane. This supports the prediction of the LHL vane delaying SS transition (and PS as well) longer than the VKI vane. However, this may not be a significant finding knowing the fact that the levels of heat transfer are so high in the first place—up to $1,600 \text{ kW/m}^2$ for the experimental data compared to only 120 kW/m^2 for the prediction suggests that something currently unexplainable is causing unrealistic heat transfer levels in the shock tube cascade test section. In addition, since both vanes essentially have immediate transition to turbulence, and with the positions of transition onset being so close with this unexplainably augmented heat transfer, it may not be appropriate to compare SS transition with this particular data. To further investigate the transition point on the suction side, the root-mean-square (rms) of the measured heat flux was calculated to exaggerate the dominant features in the midspan spatial distribution, which was a method initially employed by Owen [59].

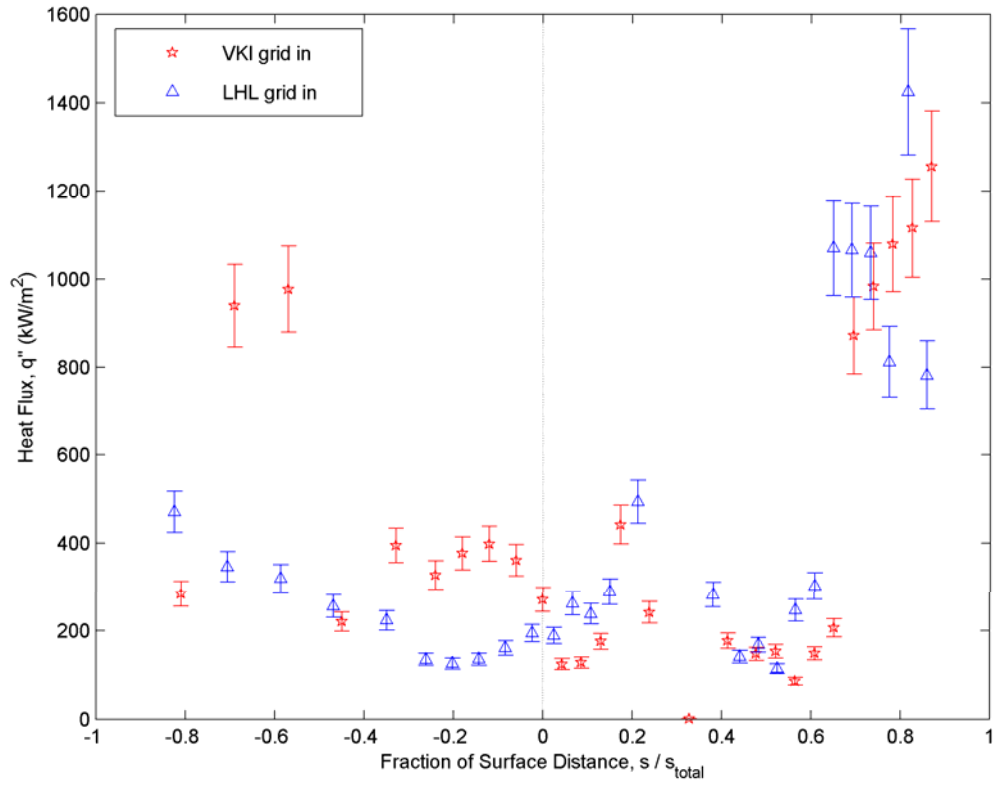


Figure 59 Grid-in (Tu=5%) experimental heat flux comparison of VKI and LHL vanes.

Figure 60 shows a sample of this calculation for the runs recently examined, runs 10 and 16. The SS transition onset locations still appear to be where they were originally reported. While the SS shock heat transfer is not necessarily clearer, the PS transition on the LHL vane is very plainly indicated using the rms plot at about 35% of the surface compared to the VKI vane at 10%. Referring back to Figure 58, experimental heat transfer for the LHL vane with the turbulence grid in is generally lower, especially on the pressure side. SS heat transfer appears to be about the same since both vanes see early transition followed by relaminarization and similar strong shocks near the TE.

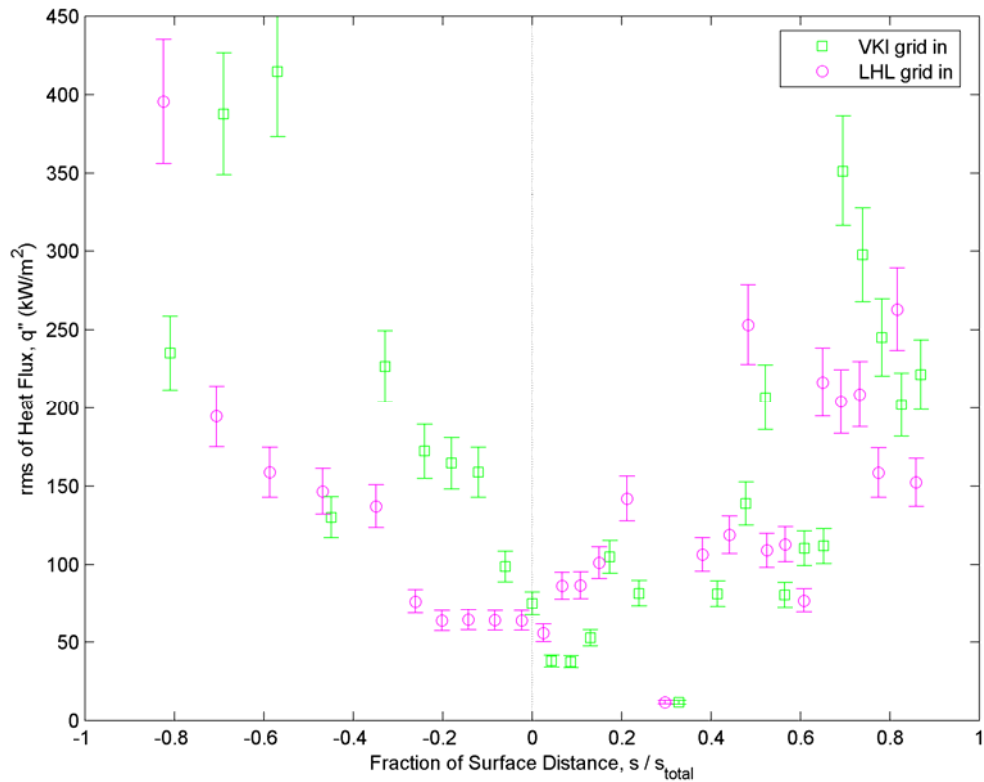


Figure 60 Root-mean-square calculation of heat flux for Run 10 & 16.

For the grid-out cases with experimental Tu of approximately 2% in Figure 61, the LHL vane shows more favorable traits than in the case for higher freestream level. On both surfaces, the LHL has generally lower heat transfer, with an apparent reduction

in LE heat flux of over 30% compared to the VKI vane, which is a larger reduction than the design plots which showed a 15% reduction. The only exception is the heat transfer near the TE, which is obviously more pronounced on the LHL vane SS. The reason for this occurrence may suggest more experimental investigation is necessary. However, the pressure loading plots and predicted heat transfer for both vanes at these conditions gave no indication of shocks that would originate so far back from the TE, so again it may be more likely that there is relaminarization followed by transition (to higher heat transfer).

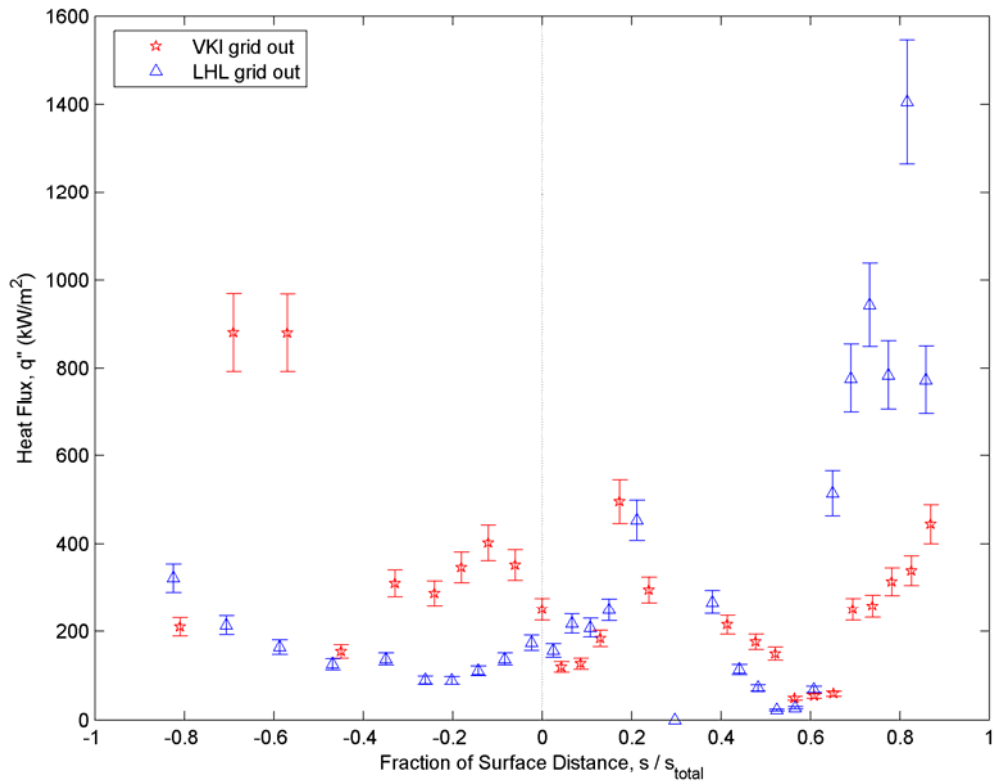


Figure 61 Grid-out ($Tu=2\%$) experimental heat flux comparison of VKI and LHL vanes.

To demonstrate the repeatability of the shock tube runs, run numbers 17 and 18 are plotted together in Figure 62. These two runs, both the LHL vane without the grid installed, were executed back-to-back within the full series of 22 shock tube runs performed. The repeatability of the heat transfer data is very good, especially for lower

levels of heat flux. The disparity between run data tends to increase with increasing heat transfer magnitude. This disparity could also be because the driver pressures for the two runs are slightly different. The shock tube proved to be an inexpensive and highly repeatable rig for examining heat transfer on the VKI and LHL vanes to find that the LHL vane exhibited generally lower heat flux, especially at the leading edge. One of the two goals that were established for obtaining a heat load optimized vane were reached when it came to the experimental data. An additional benefit may be seen in the lower PS heat flux due to delayed transition due to the loading. More investigation may be necessary to study the suction surface heat transfer experienced in the cascade. Table 8 is given to review the experimental heat transfer attributes pertaining to the LE and SS transition. In summary, a vane that was successfully optimized computationally for reduced heat transfer has fared rather well in an initial experimental study with inlet flow conditions similar to a turbine.

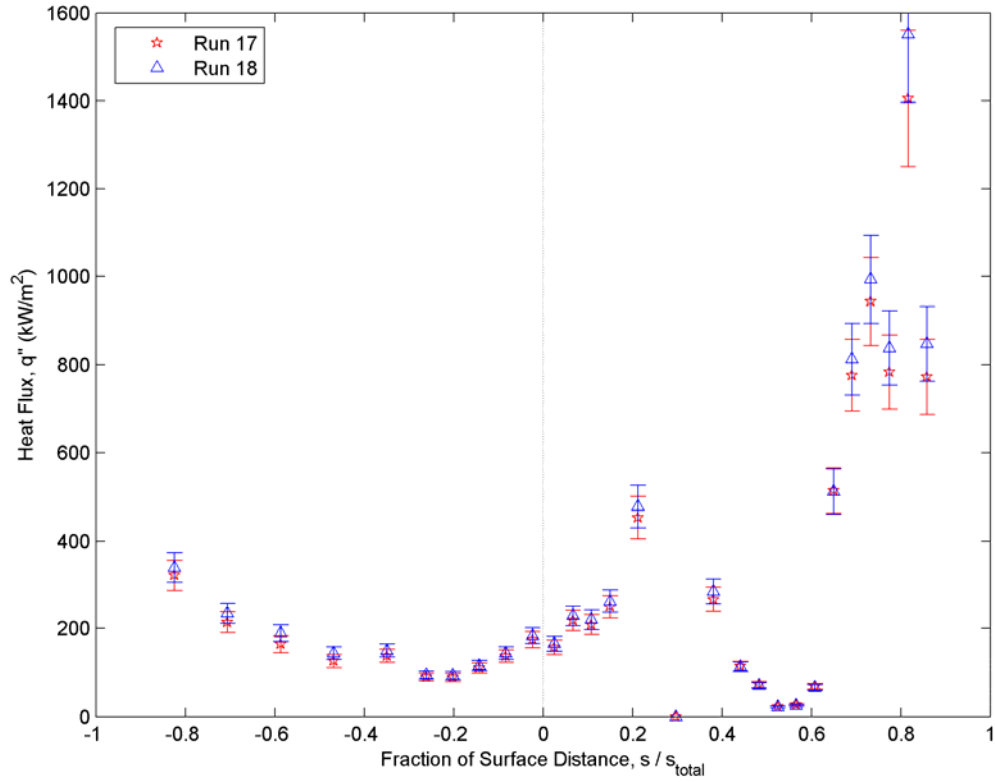


Figure 62 Experimental repeatability of heat flux data for reflected shock tube linear vane cascade trials.

Table 8 Summary of experimental heat transfer characteristics for the VKI and LHL vanes.

Vane geometry	Approximate Tu (%)	LE Heat Flux (kW/m ²)	SS transition onset (% SS)	2 nd transition location (% SS)	PS transition onset (%)
VKI	2.0	270.93	4	57	45
VKI	5.0	250.33	4	57	10
LHL	2.0	194.21	11	53	None
LHL	5.0	173.87	11	53	35

Comparison of Heat Transfer Data to Prediction

The shock tube provided a means for obtaining and comparing unsteady, transient, spatially resolved midspan heat flux for both the VKI and LHL vane. While the shock tube has been used in many previous applications, the experimental technique

used here is not intended to simulate every possible parameter pertinent to turbine heat transfer studies. However, the flow similarity conditions are sufficiently attained so measured heat flux data may be used to validate or improve confidence in the accuracy of flow prediction techniques under development. In this section, an attempt is made to compare the widely used RANS WILDCAT code by Dorney [36], which was previously been validated against the VKI isentropic light piston tube [29] that creates more steady, relatively longer duration turbine-representative flows. In order to further investigate the measured heat flux, WILDCAT was run with the same flow conditions as the shock tube tests to compare the heat transfer prediction to the data taken using the thin films. As stated by Simoneau et al. [15], matching the flow physics in a turbine inlet is the first requirement for making a good heat transfer comparison to current predictive capabilities. In much of the work by Dunn, his shock-tunnel test sections saw unsteady pressure (and possibly heat transfer) measurements like those obtained here for the AFRL shock tube.

In order to obtain predictions, the appropriate boundary conditions are necessary, such as total pressure, total temperature, inlet and exit isentropic Mach number, inlet turbulence intensity level, and the vane surface wall temperature prior to the run. Difficulties were experienced with the total temperature thermocouple instrument. Since the size of the bead and lead wires was too large for accurate measurement, over the extremely short test duration good data could not be obtained without correction. The temperature only increased to a fraction of the theoretical shock-tunnel level, T_{t5} . However, knowing the characteristic response time of a 1 mil thermocouple of the same materials (type E) and by using a lumped capacitance analysis, it can be determined to what temperature level, $T_{t,in}$, the thermocouple bead would have reached, had it had

enough test time to properly respond. The time constant of the 1 mil thermocouple, m , had an inverse relationship with the bead diameter, D , so for three times the diameter, the response time increased accordingly to a value of 120 ms, which is much larger than the typical 5 ms test time. While the total pressures and Mach numbers can be used from Table 7, Table 9 gives the appropriate (i.e. corrected) total inlet temperatures and wall temperatures to go into the WILDCAT code as boundary conditions.

Table 9 Temperature boundary conditions for WILDCAT code consideration.

Run	Compensated $T_{t,in}$ (K)	ΔT (K)	Augmented $T_{t,in}$ (K)	T_{wall} (K)
10	443.23	+ 76.49	519.72	962.68
11	463.78	+ 81.93	545.72	961.15
16	439.01	+ 78.16	517.18	967.32
17	443.14	+ 77.53	520.67	968.11
18	466.03	+ 83.46	549.49	967.27

The ΔT term in Table 9 is necessary due to the increase in enthalpy of initially stagnant ambient air occupying the test section that is pushed through the cascade from the driven section after initial shock wave reflection. To elaborate, the theoretical T_5 found from shock tube equations as in Appendix B is not exactly the same at the cascade inlet temperature, $T_{t,in}$, that would have been experienced by a thermocouple with a short enough response time. With a brief calculation, the resulting total temperature rise can be found. From Anderson [44], finding ΔT begins with the unsteady energy equation (9), which states that for unsteady flow ($\partial p / \partial t \neq 0$) the total enthalpy is not constant,

$$\rho \frac{Dh_0}{Dt} = \frac{\partial p}{\partial t} \quad (9)$$

Letting the derivative of pressure with respect to time be a discrete step change, the expression evolves to that of equation 10,

$$\frac{Dh_0}{Dt} = \frac{\Delta p}{\Delta t} \left(\frac{1}{\rho} \right) \quad (10)$$

Allowing the changes in time to cancel out due to a discrete change in time, the equation becomes

$$\Delta h_0 = \frac{\Delta p}{\rho} \quad (11)$$

where Δh_0 in equation 11 equals $c_p \Delta T_0$. Solving for the change total temperature after the reflected shock, you get equation 12:

$$\Delta T_s = \Delta T_{tR} = \frac{\Delta p}{\rho c_p} \quad (12)$$

where $\Delta T_{tR} = (T_{t,in}(measured) - T_{t,in}(compensated))$ and the compensated total inlet temperature is that found above using the response time for a 3 mil thermocouple. This is the temperature seen in the second column of Table 9. Even longer flow duration blow-down facilities like the Air Force Research Laboratory Turbine Research Facility (AFRL TRF) experience this change in enthalpy at test start-up. Figure 63 shows a sample TRF data trace from the study of Clark et al. [60] with supply and inlet total pressures and temperatures along with heat flux depicting this initial increase in enthalpy. Notice how the heat flux and inlet total temperature traces show evidence of this while the pressure plots do not. Again, this is because the time variation of total enthalpy arises due to the time-varying pressure as given by (9). Now all ingredients are gathered for making proper predictions of the vane heat transfer distributions using the correct boundary conditions.

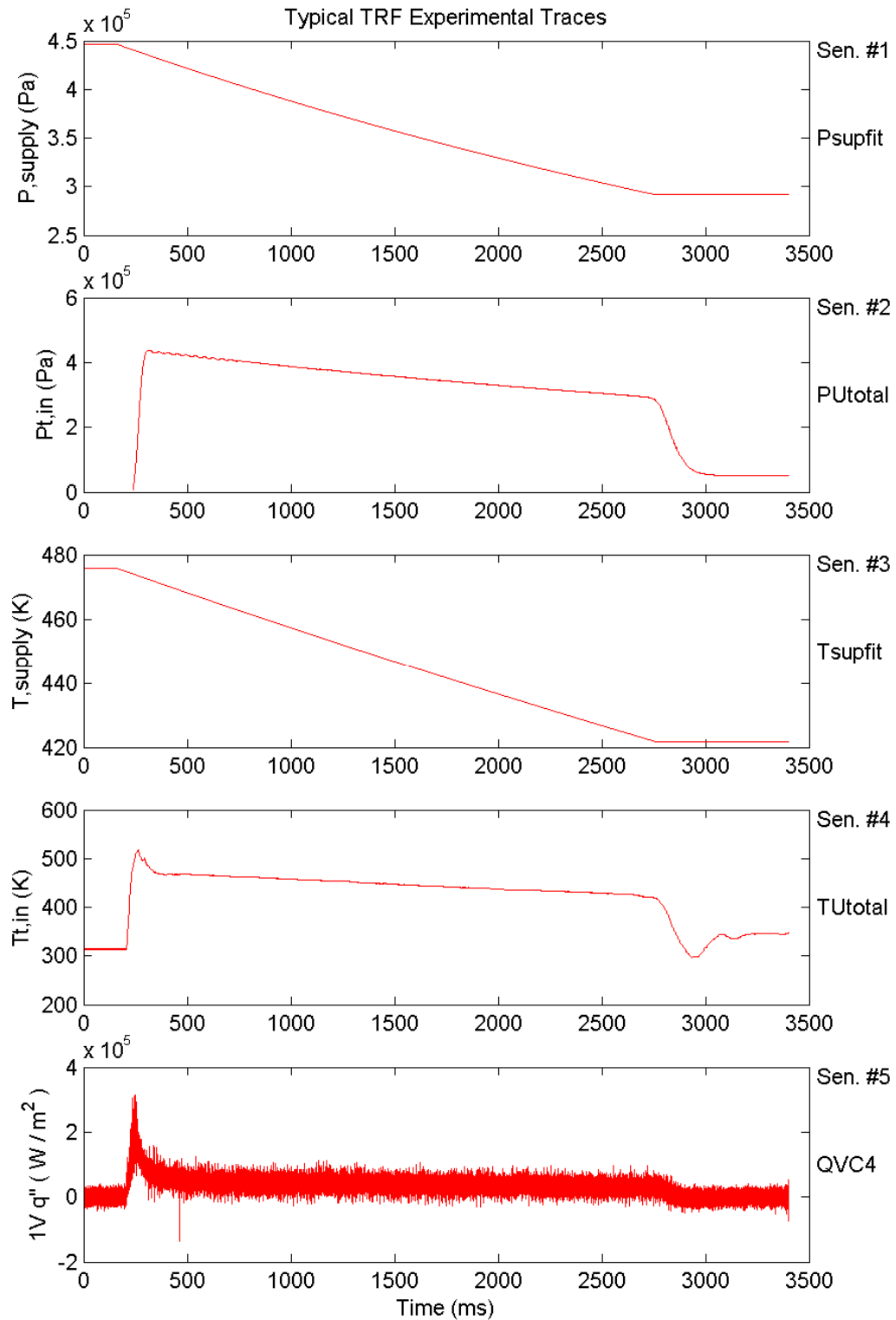


Figure 63 AFRL TRF sample data (Ref [60]) showing increased inlet total temperature at test start.

Even though the priority of this thesis has already been accomplished, (designing a low heat load vane and verifying the benefit), a final investigation of heat flux for the reflected-shock experimental runs is in order, especially as the measured heat flux is so high. In addition, as so many predictions of heat transfer data in open literature in the past have disregarded heat flux in favor of predicting Stanton number, it is desirable to meet the challenge of predicting heat flux, \dot{q}'' , since it is the primary driver for turbine engine cooling flow requirements [54]. The WILDCAT code was run with the boundary conditions of experimental grid-in run 10 in Figure 59 to compare laminar and turbulent predictions of heat flux for the VKI vane geometry. Only the experimental grid-in data is given for plotting against predictions knowing the primary effect of turbulence in WILDCAT prediction pertains to the AGS transition model. Thus no appreciable effect between $Tu = 2\%$ and $Tu = 5\%$ would be expected for the predictions. Thus, attempting a prediction of the high Tu (grid-in) experimental data is appropriate. For the VKI vane in Figure 64, it appears that the LE heat flux is predicted very well, and as the flow gets closer to the TE, the prediction becomes less accurate. Overall, the turbulent prediction tends to be closer to the data on both vane surfaces, but even the fully turbulent simulation under-predicts the measurement. Figure 65 shows the laminar and turbulent heat flux predictions plotted against cascade experimental data from run 16 for the LHL optimized heat load geometry vane. The LE heat flux is again predicted very well (it appears that the stagnation point is moved slightly towards the PS) whereas on most of the PS and SS of the LHL vane, the data is extremely under-predicted. The laminar prediction is fairly accurate on the PS near the LE while the turbulent prediction is too low for the subsequent transition to turbulence in the data.

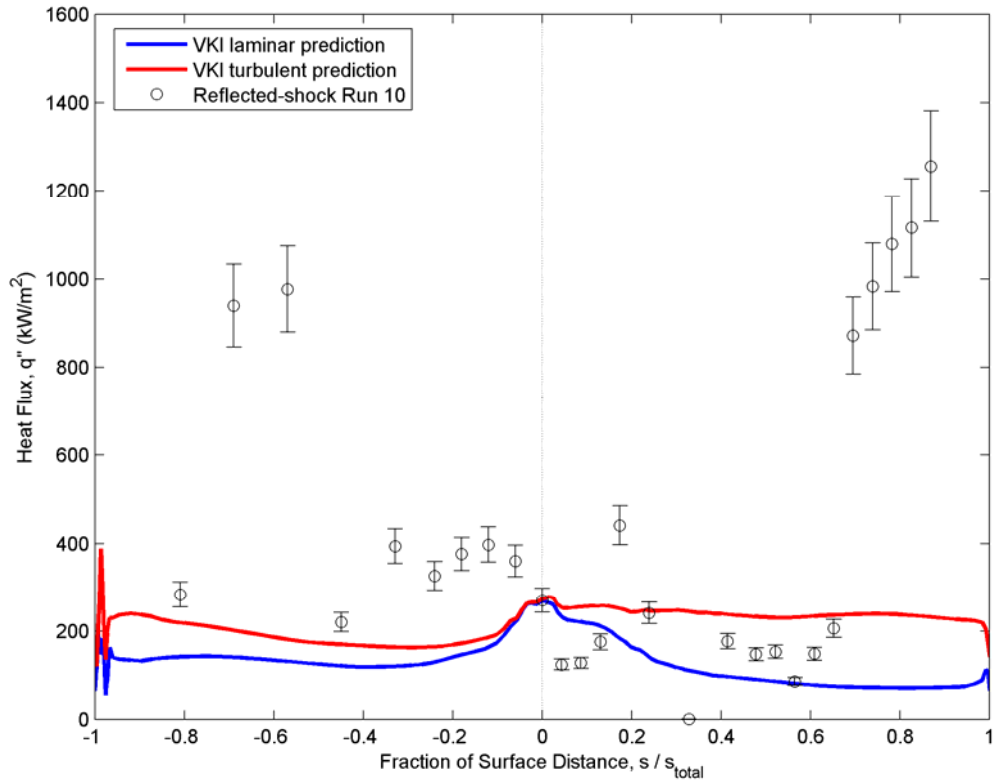


Figure 64 VKI vane midspan heat flux with WILDCAT laminar and turbulent predictions.

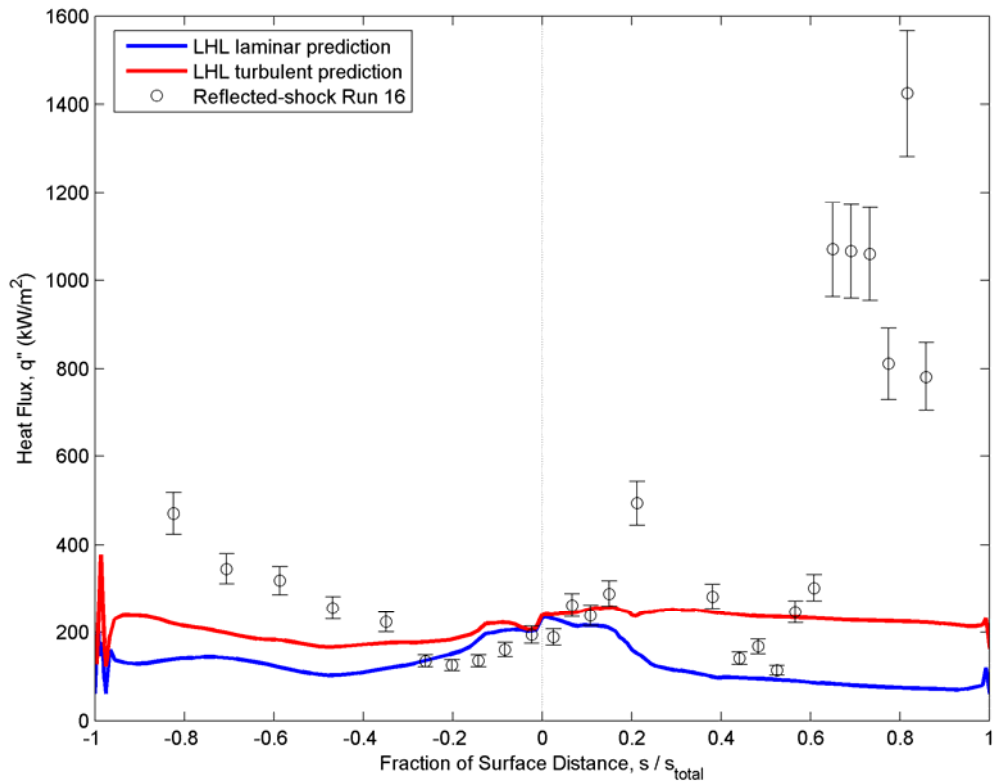


Figure 65 LHL vane midspan heat flux with WILDCAT laminar and turbulent predictions.

This primary trend of under-prediction of data demands further investigation. There may be strong, unsteady shocks near the TE for both vanes (on top of the turbulent freestream flow) that cannot be precisely modeled with a constant inlet and back pressure with a subsonic exit flow. Presuming that the predictions are closer to what the vanes would experience in a steady, more turbine-representative environment than the shock-tunnel, a range of possible phenomena could account for the heat transfer augmentation in the experiments. Such gross under-prediction of experimental data is not entirely uncommon in open literature concerning similar vane and blade heat transfer studies (see Refs [14], [18], [20], [21], [26], [22]). Some of the historical under-prediction may be a consequence of modeling inaccuracies with respect to transitional and turbulent suction side flow. However, there may be instances in which the heat flux measured experimentally was higher than what is to be expected in a turbine environment, given the differences between the operation of reflected shock tunnels and working turbines. For example, consider the work of Finke et al. [61]. The authors compared multiple 2-D and 3-D Navier-Stokes and multi-stage Euler codes to midspan heat transfer data from a low aspect ratio turbine vane cascade test section obtained in the CALSPAN reflected-shock tunnel (See Dunn [20]). The augmented heat transfer relative to the code predictions was at the time attributed to vane surface roughness. However, it seems doubtful that the surface roughness of rig-quality hardware would result in heat transfer augmentation of turbulent flow by as much as 50% on both the PS and SS of the vane. There is a plethora of pertinent data collected in the CALSPAN shock tunnel, but there are few instances of accurate prediction of turbine vane heat transfer as compared to the measurements.

Here, it is postulated that test time of the AFRL shock tunnel (which is substantially smaller than that obtained in the CALSPAN facility) is not long enough to create an appropriate flow-field to take turbine-representative heat transfer measurements. The flow entering the cascade test section is unsteady as evidenced by inspection, but for the unsteady pressure field the flow is quasi-steady over the run time of 5 ms, as seen in Figure 54. Thus proper pressure and in turn inlet and exit Mach numbers can be measured. On the other hand, this is likely not enough time for the heat transfer to be realistically measured. The flaw does not lie with the capability of the thin film gauges used to measure heat flux as seen in the high frequency voltage traces of Figure 53. Instead, it is an artifact of the unsteady flow itself.

The time it takes a particle to pass through the test section under steady state conditions can be calculated from the conditions seen in the test section for the VKI and LHL cascade experiment. Analyzing a WILDCAT prediction gives this particle transit time to be about 0.75 ms for the vane design conditions of MUR237. From Anderson [44], the pressure field, otherwise known as the potential flow-field, sets up on a time-scale that is significantly less than the particle transit time since finite pressure waves propagate at the local flow speed plus the local sonic speed. For this example, a finite pressure wave would propagate through the test section in about 0.2 ms. Hence, flow in the test section is set up sufficiently for assessment of total and static pressures at about 1 ms after flow start. This is one reason why there has been little difficulty historically in predicting pressure loadings using computational methods and comparing the results to reflected shock data. However, viscous disturbances are well known to propagate at a fraction of the local flow speed, so consequently, over the same time scale, boundary

layers are significantly less developed relative to the potential flow field. One would not expect this in a longer run time facility such as the isentropic light piston tube (ILPT) used by Oldfield [30] or facilities with even longer run times such as the AFRL TRF (on order of 3 s). Thus, boundary layers formed over the surfaces of VKI and LHL vanes in the reflected shock tunnel test section in the current experiment may be significantly underdeveloped and thinner than that seen over a longer run time. This means exceptionally high levels of heat transfer (and shear stress), which was observed in the experimental data of this study. This would explain the accurate prediction of LE heat transfer with the prediction becoming worse farther downstream towards the TE as is exhibited in Figures 64 and 65 for the VKI and LHL data. According to the premise above, at any given time, the boundary layer nearer the LE on either surface would be more developed than the boundary layer nearer the TE of the vane. The TRF data of Figure 63 supports this reasoning. One notes a 6X augmentation of heat flux over the more steady level attained after the tunnel start-up transient (>100 ms duration).

A quick analysis of momentum and thermal diffusion times defined by δ^2/ν and δ_t^2/α , respectively, is as follows. δ is the velocity boundary layer thickness and δ_t is the thermal boundary layer thickness. ν is the kinematic viscosity and α is the thermal diffusivity of the flow. The vane surface distribution of these characteristic time scales for the conditions of LHL run 16 (grid in, $T_u = 5\%$) is given in Figure 66, assuming a turbulent boundary layer. It shows that near the trailing edge (where extremely high heat transfer was experienced in the cascade experiment), the appropriate boundary layer momentum diffusion time is of order 30 to 35 ms—much longer than the 5 ms run time. Past about 40% of the SS distance, the shock-reflected test times may become too short

for the boundary layer to be fully established. Thus, the limited insulation from freestream flow and augmented heat transfer. Concerning the thermal diffusion time, past about 70% of the SS distance the plot begins to exceed the typical test time, further suggesting underdevelopment of the turbulent boundary layer on the SS. The oscillation in the prediction near the TE can be attributed to the discrete nature of the O-grid in integrating the boundary layer normal the surface. The δ is calculated by integration from the wall until the local vorticity is less than 1% of its maximum value near the wall. Since this value may vary (e.g. 0.8 or 0.99 percent) to fulfill the $< 1\%$ criteria, some oscillation occurs. While the previous finite pressure wave vs. viscous disturbance transit time argument likely better proves the existence of an inchoate boundary layer, both vanes in the experiment exhibit augmented SS heat transfer where the large diffusion times relative to the test times occur, and this suggests a need for future investigation.

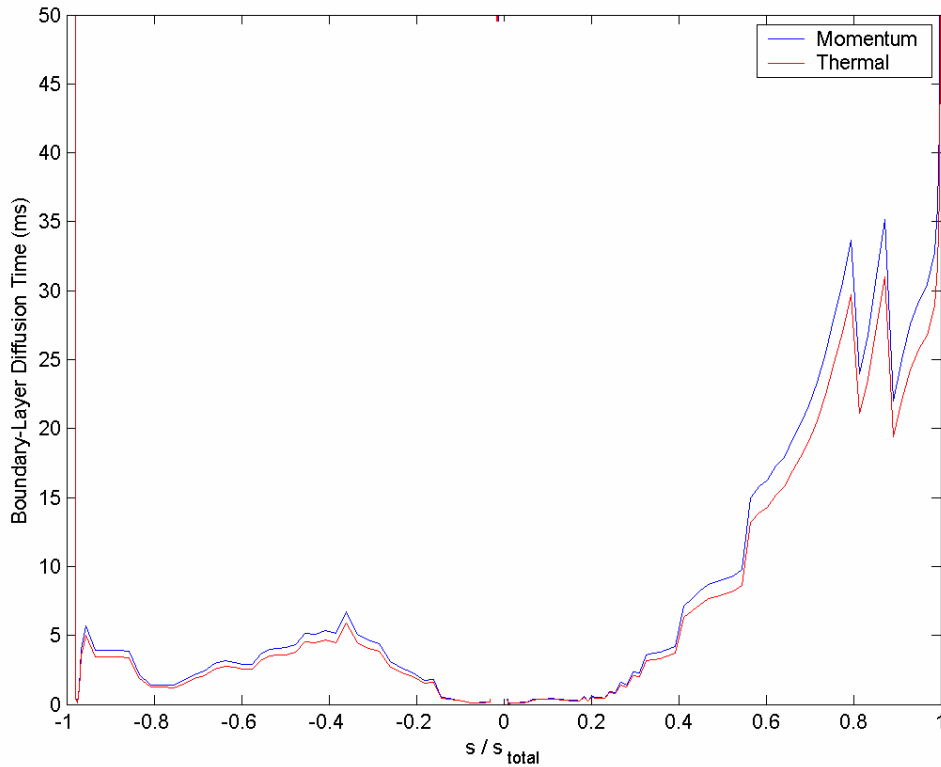


Figure 66 Turbulent boundary layer momentum and thermal diffusion time surface distribution calculation for LHL vane run 16 experimental conditions.

The characteristic response time of the heat flux gauges layers based on the total gauge thickness and thermal properties of the materials (platinum and kapton) were calculated to be on the order of 5 μ s. This suggests that for the 5 ms test times, while the heat flux is apparently unsteady, the magnitude assessments are sufficiently accurate.

The suggestion outlined above may have implications in the real world today concerning future propulsion technology. While the unsteadiness resulting from the shock tube has fundamentally repetitive, decreasing amplitude waves due to ambient pressure equalization, other more high-tech devices provide consistent, high amplitude, high velocity, unsteady wave phenomena. It has been suggested to use pulse-detonation combustors instead of steady flow (i.e. deflagration) combustion turbine engines due to the increased thrust-specific fuel consumption. Following the lessons learned in these experiments, one can surmise that at full operating conditions a pulse-detonation combustor positioned upstream of a conventional turbine may cause a periodic variation in boundary layer thickness on the turbine inlet vanes. This in turn may result in significantly increased heat transfer relative to levels seen in conventional motors, which themselves are life limited. Successful design of a pulse detonation combustor with an integrated turbine may be critically dependent upon keeping heat flux magnitudes under control. In addition, remember that in this experiment, no valve was required to achieve the reflected shock conditions. It is unlikely that detonation waves would be swallowed by a downstream vane row, which by definition presents a decreasing area to the wave. The inlet vane annulus and multiple turbine stages would act as obstructions to the pulse detonation combustor, and multiple shock reflections would occur inside as a result.

As a final point, the capability of prediction of the heat transfer in the 2-D linear vane cascade in shock-tunnel flow has proven to be better than expected for the elevated heat transfer levels of the experiments, especially for leading edge heat transfer, indicating that the RANS WILDCAT code is a satisfactory tool for assessment of the entire spectrum of flow-field properties. Further investigation concerning prediction of heat flux in short duration, reflected-shock flows is necessary for PS and SS heat transfer towards the TE. However, the prediction of shock tube data was not the priority of this work. The point of this effort was to show that a validated code could be used to optimize a vane geometry that has lower heat load qualities relative to the nominal design. Both the code and the experiments have shown that the heat-load optimized LHL vane exhibits lower heat transfer distributions in general compared to the VKI vane, with both design objectives having been met: reducing the leading edge heat load and delaying transition on the suction side. In addition, delayed transition on the pressure side was found. Although this was not an explicit design objective, it was expected from the altered pressure side loading. From here, it is plausible that the WILDCAT code could be used in a variety of further turbine design and optimization projects including the reduction of turbine nozzle guide vane heat transfer. This has important implications as AFRL/PRTT proceeds to the design of the HIT turbine rig, which is representative of the USAF Long-Range Strike mission.

VI. Conclusions and Recommendations

Conclusions

A number of significant findings were made as a result of this complete study concerning both numerical prediction and experimental assessment of turbine component heat transfer. The followings conclusions were drawn from this thesis:

- 1) The WILDCAT Reynolds-Averaged Navier-Stokes flow solver was validated over a wide range of turbine inlet conditions (Re_2 , M_2 , and Tu) giving accurate predictions of vane midspan heat transfer and pressure loading against an extensive database of light piston compression tube facility experiments at the von Karman Institute.
- 2) The now validated WILDCAT code in union with the AFRL turbine design and analysis system (TDAAS) was used (with two types of optimization algorithms) to generate an optimized turbine nozzle guide vane midspan geometry (LHL vane). The design successfully reduced leading edge peak heat transfer by 15% and delayed suction side transition 24% closer to the trailing edge compared to the nominal VKI vane. In addition, for the Abu-Ghannam and Shaw transition model, the LHL vane showed lower integral heat load as well as lower loss, suggesting that the optimized vane had more desirable aerodynamic qualities as well.
- 3) Reflected shock short duration tests in a linear cascade experiment allowed turbine-inlet experimental comparisons of the VKI and LHL vanes with and without a turbulence grid installed at similarity conditions consistent with a turbine inlet. Transient, spatially resolved, unsteady heat flux was measured at midspan. The Low

Heat Load (LHL) vane exhibited LE heat transfer levels 28% lower than the VKI vane for estimated freestream turbulence of 5% and 31% lower for freestream turbulence of 2%. The LHL vane delayed PS transition 25% relative to the VKI vane. However, early transition, followed by relaminarization was experienced on the SS of the vanes. Also, subsequent transition to turbulence took place in shocks formed near the trailing edge causing any conclusions as to whether the LHL vane significantly delayed transition on the suction side to be too ambiguous at this time.

4) Further investigation of heat transfer due to unsteady wave phenomena is called for as excessive heat flux levels for both vanes were measured near the TE. It was postulated that the short duration experimental runs (5 ms) of the shock tube were inadequate for the viscous flow field to establish itself. So the boundary layers that formed on the vane surfaces were correspondingly thinner, and this caused higher than expected heat flux measurements. Nevertheless, there was undoubtedly a decrease in relative heat transfer for the LHL vane compared to the VKI vane.

5) A further attempt to validate the WILDCAT code was made by comparing laminar viscous and turbulent viscous predictions to the experimental heat flux data collected using the shock tube. Leading edge heat flux was well-predicted, but a significant under-prediction of the data was experienced for most of the pressure and suction surfaces of both the VKI and LHL vane geometries. Again, this was consistent with thin, underdeveloped boundary layers. This is suitable since the experimental heat transfer (at least towards the TE of the vanes) was for the most part unsteady while the WILDCAT prediction was a steady flow prediction.

Error and Uncertainty

Most of the possible error occurring in this thesis is tied to the experimental heat transfer study of the two turbine inlet vanes. Heat transfer gauges like those used in this experiment have been employed successfully for decades. Uncertainties in the measurement of the midspan heat flux using the platinum thin film gauges is expected to be of order $\pm 10\%$, as shown in multiple previous studies of heat flux uncertainty using the same instruments (see Refs [60], [62], and [66]). Concerning pressure data error, the Kulite transducer error in the shock tube was $\pm 0.45\%$ of full scale. The Druck transducers used in the test section had uncertainties of approximately $\pm 0.2\%$ of full scale. Error in the experiments would have certainly decreased if not for the calibration of heat flux gauges occurring after experimentation, the loss of function of multiple heat flux gauges before calibration, the use of an oven to calibrate heat flux gauges instead of a more well controlled method involving a water or oil bath to increase accuracy of calibration (due to the higher heat transfer coefficient in the calibrating medium).

Recommendations for Future Work

A wide variety of different follow-on studies can be performed as a result of the findings of this broad yet cohesive study of turbine vane heat transfer. The following improvements and suggestions for further work are encouraged:

- Repeat the experimental heat transfer measurements using an isentropic light piston tunnel (perhaps by converting the current shock tube), resulting in relatively longer run times and compare results. Using more grids and varied boundary conditions, a larger

database of experimental data can be created for a wide range of turbulence intensity and Reynolds number.

- Repeat the entire optimization study instead for a low heat load optimized 2-D turbine rotor blade geometry using linear cascade experimental tests. Generate fitness functions for the optimization that take into account the upstream vane geometry to in effect create a full turbine stage that is optimized for reduced heat transfer.
- Perform an end-to-end calibration of fast-response thin film heat flux gauges, including the electronics used to pre-emphasize the signals prior to digitization.
- Perform follow-on work on the same turbine inlet vane or with a new 3-D version of the optimized vane to study ID and OD predicted (using the CORSAIR code) and experimental heat flux by installing gauges at 20% and 80% span, and on endwalls.
- Perform film-cooled experimental studies of the same heat load optimized vane by pumping cooling air through the endwalls of the test section and through the heat flux gauge instrumented vane.
- Conduct flow visualization studies for both vane geometries using particle image velocimetry (PIV), Schlieren imaging, or the AFRL/PRTT water table to further examine the fundamental mechanisms causing shock structures and transition to turbulence.
- Perform the same experimental studies with different gases with different boundary conditions to simulate combustor exit flow conditions as seen in reality by a turbine inlet (i.e. match values of ratio of specific heats, γ , seen in gas-turbine engines).
- Conduct detailed fundamental studies of heat transfer and boundary layer development due to unsteady waves in a linear cascade test section to realize the heat loads experienced by a turbine inlet downstream of a pulse-detonation combustor.

- Add the transition modeling capability of the Praisner and Clark model [56] to the design system to perform further computational studies of current and future vane and blade geometries.
- Add the 2-D large eddy simulation (LES) capability under development in the AFRL/PRTT HIT program with Prof. Roger Davis to TDAAS to make predictions of pressure loadings and heat transfer.

Appendix A: Supplemental MATLAB Codes

Numerous codes were generated to make the turbine design and analysis system (TDAAS) run more efficiently and to generate the numerical predictions and process experimental heat flux data presented in this thesis. In particular, two codes were instrumental in obtaining the majority of the findings of this study. The attached MATLAB codes include:

Code 1) Compile the data for the validation of the WILDCAT code against the VKI experiments.

Code 2) Convert and process raw voltage data from the cascade experiment for all pertinent run conditions discussed herein. Included are 3 additional coded functions called out by this code.

Code 1:

```
% vki_data_harvester.m

% M-file to compile necessary data from the results of run_vki_wildcat
program.
% Saves pertinent data in arrays for later ease of manipulation.

% Jamie J. Johnson
% 28 February 2005

load_vki_case_matrix;

load ('C:\Documents and Settings\johnsojj1\My
Documents\VKI_matrix\wallheatflux.txt');

exp_data_col = [241 239 245 243 116 247 232 235 237 213 217 218 210 129
132 222 224 221 226 230 228];

%
for loop = 1:length(vki.MUR),
    legend_count=1;
    legend_str{legend_count}=[ 'MUR',num2str(vki.MUR(loop))];
```

```

%
dir_name = ['MUR',num2str(vki.MUR(loop))];
command_str = ['cd ',dir_name];
eval(command_str);

% Turbulent:
cd turbulent;
file_path = [pwd,'\']
file_extension = '.dat_1001';
if ~isempty(dir([file_path,'xyz2',file_extension])),
    plot_vki_quantities_ds;
    q_turbulent{loop} = q_local_DD;
    legend_count = legend_count+1;
    legend_str{legend_count}='turbulent';
else
    q_turbulent{loop}=[];
end;

% Laminar:
cd ../laminar;
file_path = [pwd,'\']
if ~isempty(dir([file_path,'xyz2',file_extension])),
    plot_vki_quantities_ds;
    q_laminar{loop} = q_local_DD;
    legend_count = legend_count+1;
    legend_str{legend_count}='laminar';
else
    q_laminar{loop}=[];
end;

% Abu-Ghannam & Shaw:
cd ../AGS;
file_path = [pwd,'\']
if ~isempty(dir([file_path,'xyz2',file_extension])),
    plot_vki_quantities_ds;
    q_ags{loop} = q_local_DD;
    legend_count = legend_count+1;
    legend_str{legend_count}='AGS';
else
    q_ags{loop}=[];
end;

% "Hard-trip":
cd ../hardtrip;
file_path = [pwd,'\']
if ~isempty(dir([file_path,'xyz2',file_extension])),
    plot_vki_quantities_ds;
    q_hardtrip{loop} = q_local_DD;
    legend_count = legend_count+1;
    legend_str{legend_count}='hardtrip';
else
    q_hardtrip{loop}=[];
end;

cd ../../;

```

```

index = find(exp_data_col == vki.MUR(loop))+2;

figure(loop);
set(loop, 'Color', [1 1 1]);
ind_non_zero=find(wallheatflux(:,index)>0);

plot(wallheatflux(ind_non_zero,2),wallheatflux(ind_non_zero,index), 'k^'
);
    hold on;
    xtemp=[-s_ps{1}(length(s_ps{1}):-
1:1)'/max(s_ps{1}),s_ss{1}']/max(s_ss{1})];

    %

    if ~isempty(q_turbulent{loop}),
        ytemp=[q_turbulent{loop}(ind_ps(length(ind_ps):-
1:1))',q_turbulent{loop}(ind_ss)']/1000;
    end;
    plot(xtemp,ytemp, 'b-');

    %

    if ~isempty(q_laminar{loop}),
        ytemp=[q_laminar{loop}(ind_ps(length(ind_ps):-
1:1))',q_laminar{loop}(ind_ss)']/1000;
    end;
    plot(xtemp,ytemp, 'r-');

    %

    if ~isempty(q_ags{loop}),
        ytemp=[q_ags{loop}(ind_ps(length(ind_ps):-
1:1))',q_ags{loop}(ind_ss)']/1000;
    end;
    plot(xtemp,ytemp, 'g-');

    %

    if ~isempty(q_hardtrip{loop}),
        ytemp=[q_hardtrip{loop}(ind_ps(length(ind_ps):-
1:1))',q_hardtrip{loop}(ind_ss)']/1000;
    end;
    plot(xtemp,ytemp, 'k-');

    legend(legend_str,2);
    title(['MUR',num2str(vki.MUR(loop)),' : M_{exit} = ',num2str(vki.M_outlet(loop)),' , Re_{exit} = ',num2str(vki.Re_outlet(loop))...
        ', Tu_{inlet} = ',num2str(vki.Tu_intensity(loop)),'%']);
    xlabel('Fractional Surface Distance');
    ylabel('Heat Flux ( kW / m^{ 2 } )');
    axis([-0.95 1 0 160]);
    hold off;

end;

```

```
%
```

Code 2:

```
% q_data_harvester.m
%
% M-file to perform all calculations of experimental flow conditions
and heat flux.
%
% J. J. Johnson
% 4 February 2006

clear all;
%
% Calculate filter coefficients :
[bz_T2q,az_T2q] =desT2qsiIIR1(0.01,200000,6,431.0,0);
[bz_boost,az_boost] =debfilt1(-464.2139,-
4.5455e+04,458.0306,0.01,200000);
[bz_deboost,az_deboost]=debfilt1(-4.5455e+04,-
464.2139,1/458.0306,0.01,200000);
%
load level_multipliers_200Hz.mat;
%
% Load desired shock tube run:
good_to_go =0;
while ~good_to_go,
    [sfile1,spath1]=uigetfile('Run*.mat','What run? ');
    if ischar(spath1(1,1)) & ischar(sfile1(1,1)),
        file_name=strcat(spath1,sfile1);
        file_path =spath1;
        ind_dot =find(file_name=='.' );

file_extension=file_name(ind_dot(length(ind_dot)):length(file_name));
        else
            file_name='';
        end;
        if isempty(file_name),
            flowfield='';
            return;
        elseif ~isempty(findstr(file_extension, '.MAT')) |
~isempty(findstr(file_extension, '.mat')),
            good_to_go=1;
        else
            h=msgbox('No, select a shock tube run, Jackass.','Invalid File
Type','warn');
            waitfor(h);
            good_to_go=0;
        end;
    end;
end;
%
load(file_name);
%
ind_R =find(file_name=='R');
run_number =str2num(file_name(ind_R+3:ind_R+4));
%
if run_number<=11 | run_number>=19,
```



```

        airfoil_geometry_str='VKI'
else
    airfoil_geometry_str='1508'
end;
%
% Convert measured voltage to heat flux using Oldfield's methods:
convert_to_q;
% Gathers pertinent timespan of heat flux creating average for gauge:
get_avg_q;
% Mach number calculations from "lo" freq data:
get_flowfield_data;

% convert_to_q.m
%
% M-file to convert measured voltage to heat flux via MLGO's methods.
%
% J.P. Clark and J.J. Johnson
% revised 4 February 2006
%
gain=1;           % True for all heat-flux channels (MJF).
sqrt_rho_c_k=431; % J/(m s^0.5 K)
%
if strcmp(airfoil_geometry_str,'VKI'),
    load('VKIalpha.txt');
    alpha_gauge= [VKIalpha(:,2)];
    loop_max    = 27;
    R1          = [VKIalpha(:,7)];
    T1          = [VKIalpha(:,8)];
    s_fraction  = [VKIalpha(:,9)];
elseif strcmp(airfoil_geometry_str,'1508'),
    load('alpha1508.txt');
    alpha_gauge= [alpha1508(:,2)];
    loop_max    = 28;
    R1          = [alpha1508(:,7)];
    T1          = [alpha1508(:,8)];
    s_fraction  = [alpha1508(:,9)];
end;
%
ind_1k_lo=max(find(time_lo<=time_hi(1000)));
T_initial=mean(raw_V_lo(1:ind_1k_lo,8))-273.15;
I_actual = 0.004036;% [Amps]
%
load optimum_boost_filters;
%
for gauge=1:loop_max,
%for gauge=11:11,
    % get initial DC voltage :
    R_initial(gauge)      =(1+alpha_gauge(gauge))*(T_initial-
T1(gauge)))*R1(gauge);
    Vo(gauge)             =I_actual*R_initial(gauge);
    %
    V_time0(gauge)        =mean(raw_V_hi(1:1000,gauge));
    V_signal(:,gauge)     =(raw_V_hi(:,gauge)-V_time0(gauge))/gain;
    %

```

```

V_deboost_nom(:,gauge)=filter(bz_deboost,az_deboost,V_signal(:,gauge));
% nominal filters
    T_signal_nom(:,gauge)
=V_deboost_nom(:,gauge)/(Vo(gauge)*alpha_gauge(gauge));
    q_signal_nom(:,gauge)
=filtcas(bz_T2q,az_T2q,T_signal_nom(:,gauge));
    %
    [bz,az]
=design_deboost_filter(optimum_config(gauge,:)); % optimal filters
    V_deboost_opt(:,gauge)=filter(bz,az,V_signal(:,gauge));
    T_signal_opt(:,gauge)
=V_deboost_opt(:,gauge)/(Vo(gauge)*alpha_gauge(gauge));
    q_signal_opt(:,gauge)
=filtcas(bz_T2q,az_T2q,T_signal_opt(:,gauge));
    %
    figure(gauge);
    title(['Converted Heat Flux vs. Time, Gauge # ',num2str(gauge)]);
    subplot(2,1,1);
    plot(1000*time_hi,raw_V_hi(:,gauge));
    hold on;
    plot(1000*[time_hi(1) time_hi(length(time_hi))],[V_time0(gauge)
V_time0(gauge)], 'r-');
    plot(1000*[time_hi(1) time_hi(length(time_hi))],[V_time0(gauge)
V_time0(gauge)], 'y:');
    hold off;
    ylabel('Voltage');
    subplot(2,1,2);
    plot(1000*time_hi,q_signal_nom(:,gauge)/1000, 'b-');
    hold on;
    plot(1000*time_hi,q_signal_opt(:,gauge)/1000, 'r:');
    xlabel('Time (ms)');
    ylabel('q" (kW / m^{ 2})');
    hold off;
end;

% get_avg_q.m
%
% Presumes convert_to_q.m has been run. Finds time-mean heat flux from
% converted voltage traces.
%
% J. P. Clark and J. J. Johnson
% revised 4 February 2006

pitot_dVdt_squared=diff(raw_V_lo(:,5)).^2; % square of first
derivative of

                                % pitot voltage trace
ind_time_start_for_avg=find(pitot_dVdt_squared==max(pitot_dVdt_squared)
);
time_start_for_avg      =time_lo(ind_time_start_for_avg+1)+0.0004
time_end_for_avg        =time_start_for_avg+0.005; % average over 5ms of
data
%
figure(101);
set(101,'Color',[1 1 1]);
subplot(3,1,1);

```

```

plot(time_lo(2:length(time_lo)),raw_V_lo(2:length(time_lo),5),'r-');
hold on;
temp_axis=axis;
plot([time_start_for_avg time_start_for_avg],[temp_axis(3)
temp_axis(4)],'k-');
plot([time_end_for_avg time_end_for_avg],[temp_axis(3)
temp_axis(4)],'k-');
ylabel('Voltage');
hold off;
%
subplot(3,1,2);
plot(1000*time_lo(2:length(time_lo)),diff(raw_V_lo(:,5)).^2,'r-');
hold on;
temp_axis=axis;
plot(1000*[time_start_for_avg time_start_for_avg],[temp_axis(3)
temp_axis(4)],'k-');
plot(1000*[time_end_for_avg time_end_for_avg],[temp_axis(3)
temp_axis(4)],'k-');
ylabel('Voltage');
hold off;
%
subplot(3,1,3);
plot(1000*time_hi,q_signal_nom(:,23)/1000,'b-');
hold on;
plot(1000*time_hi,q_signal_opt(:,23)/1000,'r-');
temp_axis=axis;
plot(1000*[time_start_for_avg time_start_for_avg],[temp_axis(3)
temp_axis(4)],'k-');
plot(1000*[time_end_for_avg time_end_for_avg],[temp_axis(3)
temp_axis(4)],'k-');
xlabel('Time (ms)');
ylabel('q (kW / m2)');
hold off;
%
ind_min_lo=max(find(time_lo<=time_start_for_avg));
ind_max_lo=max(find(time_lo<=time_end_for_avg));
%
ind_min_hi=max(find(time_hi<=time_start_for_avg));
ind_max_hi=max(find(time_hi<=time_end_for_avg));
%
q_mean_nom=mean(q_signal_nom(ind_min_hi:ind_max_hi,:),1);
%
q_std_opt =std(q_signal_opt(ind_min_hi:ind_max_hi,:),1,1);
%
exp_trace=q_signal_opt(ind_min_hi:ind_max_hi,23);
del_t_exp=1/rawfs_hi;
%
% Calculate experimental DFT results :
%
%fft_window=hanning(length(exp_trace))';
fft_window=boxcar(length(exp_trace));
%fdom =fft((exp_trace-mean(exp_trace)).*fft_window,length(exp_trace));
fdom =fft(exp_trace.*fft_window,length(exp_trace));
fnorm=abs(fdom)*2/length(exp_trace);
fnorm=fnorm(1:floor(length(fnorm)/2));
freq =([1:fix(length(exp_trace)/2)]-
1)*((1/del_t_exp)/(length(exp_trace)));

```

```

%
fnorm_exp=fnorm;
freq_exp =freq;
%
figure(105);
set(105,'Color',[1 1 1]);
loglog(freq_exp/1000,fnorm_exp,'r-');
xlabel('Frequency (kHz)');
ylabel(['DFT Mag.']);
%
figure(102);
set(102,'Color',[1 1 1]);
plot(s_fraction,q_mean_nom.*factor_200Hz_nom(1:length(q_mean_nom))/1000
,'b^');
%plot(s_fraction,q_mean_nom/1000,'kv');
xlabel('Fraction of Surface Distance');
ylabel('Time-Mean Heat Flux, (kW / m^{ 2} )');
hold on;
%
figure(103);
set(103,'Color',[1 1 1]);
plot(s_fraction,q_std_opt/1000,'ro');
xlabel('Fraction of Surface Distance');
ylabel('rms of Heat Flux, (kW / m^{ 2} )');
hold on;

% get_flowfield_data
%
% Finds static pressures, total pressures, total temperatures, and Mach
% numbers for a prescribed experimental run.
%
% J. J. Johnson and J. P. Clark
% revised 19 January 2006
%
druck_calibrations;
ind_patm_run=find(p_atm(1,:)==run_number);
%
ind_up    =[10 11 12];
if strcmp(airfoil_geometry_str,'VKI'),
    ind_down =[1 2 3 4 9];
elseif strcmp(airfoil_geometry_str,'1508'),
    ind_down =[9 2 3 4 9];
end;
ind_driver=7;
ind_driven=6;
ind_Tt    =8;
ind_Pitot =5;
%
for i = 1:size(raw_V_lo,2),
    if i~=ind_Tt & i~=ind_driver,
        V_initial =mean(raw_V_lo(1:ind_1k_lo,i));
        P_signal(:,i)=(m_sensors(i)*(raw_V_lo(:,i)-
V_initial))+p_atm(2,ind_patm_run);
        P_mean(i) =mean(P_signal(ind_min_lo:ind_max_lo,i));
    elseif i==ind_Tt,
        Tt_signal =raw_V_lo(:,i);
        Tt_mean =mean(Tt_signal(ind_min_lo:ind_max_lo));
    end;
end;

```

```

        Tt_max_time =Tt_signal(ind_max_lo);
    elseif i==ind_driver,
        V_final      =mean(raw_V_lo(length(raw_V_lo)-
ind_1k_lo:length(raw_V_lo),i));
        P_signal(:,i)=(m_sensors(i)*(raw_V_lo(:,i)-
V_final))+p_atm(2,ind_patm_run);
        P_mean(i)     =mean(P_signal(1:ind_1k_lo,i));
    end;
end;
%
P_driver  =P_mean(ind_driver)
P_driven  =P_mean(ind_driven)
%
Ptin      =P_mean(ind_Pitot)
Psin      =mean(P_mean(ind_up))
Psex      =mean(P_mean(ind_down))
%
Min        =m_prat(1.4,Ptin/Psin)
Mex        =m_prat(1.4,Ptin/Psex)
%
% Compensate for thermocouple time response:
Ttin      =get_best_Tt(time_lo(ind_max_lo)-
time_lo(ind_min_lo),Tt_max_time,Min,T_initial)
%
figure(104);
set(104,'Color',[1 1 1]);
subplot(4,1,1);
plot(1000*time_lo,P_signal(:,ind_driver),'r-');
hold on;
plot(1000*time_lo,P_signal(:,ind_driven),'b-');
plot(1000*time_lo,P_signal(:,ind_Pitot),'g-');
hold off;
ylabel('P (psia)');
legend('Driver','Driven','Pitot');
%
subplot(4,1,2);
plot(1000*time_lo,P_signal(:,10),'r-');
hold on;
plot(1000*time_lo,P_signal(:,11),'b-');
plot(1000*time_lo,P_signal(:,12),'g-');
hold off;
ylabel('Ps,in (psia)');
%
subplot(4,1,3);
plot(1000*time_lo,P_signal(:,1),'r-');
hold on;
plot(1000*time_lo,P_signal(:,2),'b-');
plot(1000*time_lo,P_signal(:,3),'g-');
plot(1000*time_lo,P_signal(:,4),'c-');
plot(1000*time_lo,P_signal(:,9),'m-');
hold off;
ylabel('Ps,ex (psia)');
%
subplot(4,1,4);
plot(1000*time_lo,Tt_signal,'r-');
ylabel('Tt (K)');
xlabel('Time (ms)');

```

Appendix B: Essential Shock Tube Relations

The following equations for moving normal shock waves (unsteady wave motion) derived by Anderson [44] were used to find the theoretical conditions that occur for varying shock tube driver pressures. The equations below are the minimum necessary for finding the total temperature behind a reflected shock (T_5) to ultimately find test section inlet conditions due to a given driver pressure (shock pressure ratio). The reader is encouraged to refer back to the shock tube theory section of this thesis to recall what subscript numbers pertain to which region of flow within the shock tube. Some simplifications to equations are made for the conditions of the current experiment. Equation B.1 starts with finding P_2 by iteration knowing the initial shock pressure ratio across the diaphragm:

$$\frac{P_4}{P_1} = \frac{P_2}{P_1} \left\{ 1 - \frac{(\gamma - 1) \left(\frac{P_2}{P_1} - 1 \right)}{\sqrt{2\gamma \left[2\gamma + (\gamma + 1) \left(\frac{P_2}{P_1} - 1 \right) \right]}} \right\}^{\frac{-2\gamma}{(\gamma - 1)}}$$

(B.1)

Now P_2 can be used to find T_2 with equation B.2 in which γ is the ratio of specific heats for air:

$$\frac{T_2}{T_1} = \frac{P_2}{P_1} \left[\frac{\frac{(\gamma + 1)}{(\gamma - 1)} + \frac{P_2}{P_1}}{1 + \frac{(\gamma + 1)}{(\gamma - 1)} \left(\frac{P_2}{P_1} \right)} \right] \quad (B.2)$$

The wave velocity, W , is found with equation B.3 in which “a” is the local speed of sound:

$$W = a \sqrt{\frac{(\gamma+1)}{2\gamma} \left(\frac{P_2}{P_1} - 1 \right) + 1} \quad (\text{B.3})$$

Next, the shock Mach number is found by $M_S = W/a$. Now the mass-motion velocity, u_p , is found using equation B.4:

$$u_p = \frac{a}{\gamma} \left(\frac{P_2}{P_1} - 1 \right) \left(\frac{\frac{2\gamma}{(\gamma+1)}}{\frac{P_2}{P_1} + \frac{(\gamma-1)}{(\gamma+1)}} \right) \quad (\text{B.4})$$

From here, with equation B.5, the reflected wave Mach number, M_R , is found by iteration knowing the shock Mach number found above:

$$\frac{M_R}{M_R^2 - 1} = \frac{M_S}{M_S^2 - 1} \sqrt{1 + \frac{2(\gamma-1)}{(\gamma+1)^2} (M_S^2 - 1) \left(\gamma + \frac{1}{M_S^2} \right)} \quad (\text{B.5})$$

Now the reflected wave velocity, W_R , is found from $W_R = M_R a_2 - u_p$ where $a_2 = \sqrt{\gamma R T_2}$. Using the ideal gas law the density in region 2 is found by $\rho_2 = \frac{P_2}{R T_2}$. The

pressure in region 5 behind the reflected shock is subsequently defined by equation B.6:

$$P_5 = [P_2 + \rho_2 (W_R + u_p)^2] - \rho_5 W_R^2 \quad (\text{B.6})$$

where ρ_5 is found by other known values, $\rho_5 = \rho_2 (W_R + u_p) / W_R$. Finally, the temperature behind the reflected shock is calculated using equation B.7:

$$T_5 = \frac{P_5}{P_2} \left(\frac{\frac{(\gamma+1)}{(\gamma-1)} + \frac{P_5}{P_2}}{1 + \frac{(\gamma+1)}{(\gamma-1)} \left(\frac{P_5}{P_2} \right)} \right) T_2 \quad (\text{B.7})$$

APPENDIX C: Test Section Secondary Flow Analysis

The vanes used in the cascade for the reflected shock heat transfer experiments all had a span of one inch (the middle instrumented vane was 2 in. long but was enclosed by the plexiglass end wall at 1 in.). Knowing the common axial chord lengths for both airfoil geometries studied experimentally, this gives a relatively low aspect ratio of 1.166. With such a small value, there is some cause for concern of leading edge horseshoe vortices and secondary flow growing inward from both endwalls, possibly having an adverse effect on heat transfer results at midspan measured by the heat flux gauges positioned there. A high enough magnitude growth of secondary flow could cause a reduction in effective flow area, giving unexpected flow properties towards the trailing edge (TE) of the vanes as well. Therefore, a study of the losses and growth of secondary flow over the vanes in the test section is necessary.

Benner et al. [63] recently derived a new loss breakdown scheme and the spanwise penetration depth correlation that can be used to characterize the growth of secondary flow as the TE is reached. This work was significant because the correlation for penetration depth of the passage vortex separation line at the TE is based on a very large database and statistically more meaningful than the previous correlations found by Sharma and Butler, which were derived from a rather small database. The new correlation for non-dimensional penetration depth defined by Benner is given by (C.1),

$$\frac{Z_{TE}}{h} = \frac{0.10(F_t)^{0.79}}{\sqrt{CR}\left(\frac{h}{C}\right)^{0.55}} + 32.70\left(\frac{\delta^*}{h}\right)^2 \quad (C.1)$$

where the terms that make up the correlation are defined as:

F_t = tangential loading coefficient, defined further in equation C.2

CR = convergence ratio, defined further is equation C.3

h/C = airfoil aspect ratio based on true chord

δ^*/h = non-dimensional inlet endwall boundary layer displacement thickness

From here, F_t and CR are defined in equations C.2 and C.3, respectively:

$$F_t = 2 \left(\frac{s}{b_x} \right) \cos^2 \alpha_m (\tan \alpha_1 - \tan \alpha_2) \quad (C.2)$$

$$CR = \frac{\cos \alpha_1}{\cos \alpha_2} \quad (C.3)$$

where $\tan \alpha_m = \frac{1}{2}(\tan \alpha_1 + \tan \alpha_2)$, s is vane pitch or circumferential spacing, b_x is axial chord, and α_1 and α_2 are inlet and exit flow angles measured from the axial flow direction. The variable values (in English units where applicable), which were the same for the VKI and LHL vanes, were the following: $s = 1.33$ in, $b_x = 0.8575$ in, $\alpha_1 = 0^\circ$, $\alpha_2 = -72.13^\circ$, $\alpha_m = -57.19^\circ$, $h = 1$ in, and $h/C = 0.72$ (where C was estimated from $C = \sqrt{H^2 + b_x^2}$ and H is estimated by the VKI airfoil height as H/L which is known to be 1.28). δ^* can be found based on the following relation from Schlichting [47]:

$$\delta^* = \int_0^\infty \left(1 - \frac{u}{U_\infty} \right) dy \approx \frac{1.721x}{\sqrt{\text{Re}_x}} \quad (C.4)$$

where x is the distance from the test section inlet to the vane leading edge (1 in.) which accounts for boundary layer growth on the endwall and Re_x is based on this distance. Re_x turns out to be about 10^6 making δ^*/h equal to 0.0017 in. Now, since all variables are known for the cascade vanes ($F_t = 2.825$ and $CR = 3.259$), the TE secondary flow penetration depth can be calculated. Plugging in all calculated variables into equation

A.1 gives a Z_{TE}/h of 0.1508. This means secondary flow has grown as it passes over the airfoil from the endwall to a maximum of 15% of the span on each side at the trailing edge. Therefore, midspan heat transfer measurements should be unaffected by any secondary flow in the low-aspect ratio vane cascade. Figure C.1 is a diagram showing the growth of secondary flow over a vane.

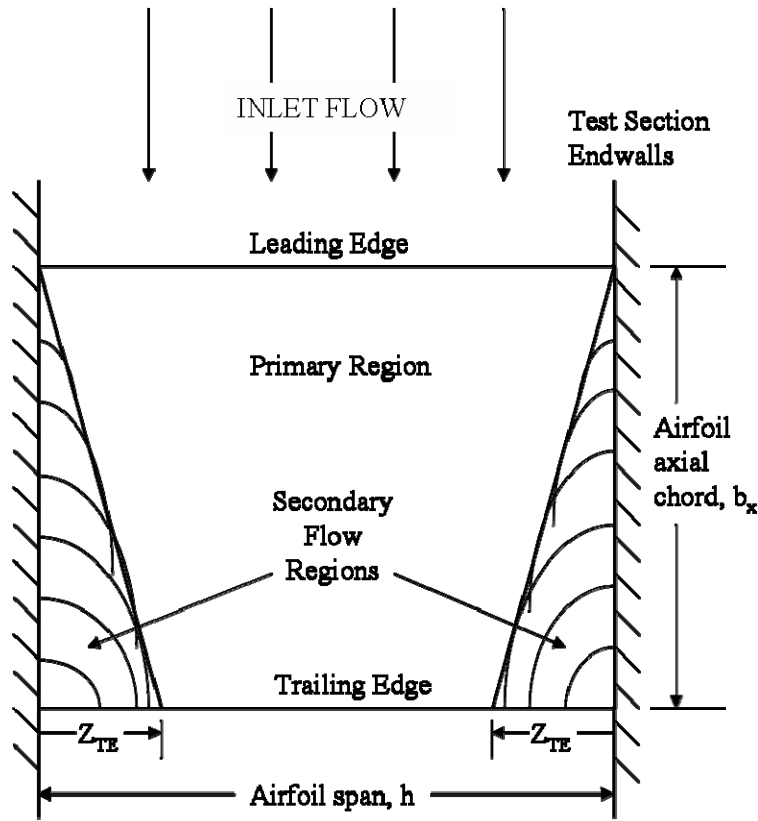


Figure C.1 Secondary flow over the surface of an airfoil.

As a supplement, the WILDCAT code and its 3-D counterpart by Dorney et al. [37] called CORSAIR were used to obtain decisive proof that secondary flow does not adversely affect midspan measurements. 2-D and 3-D simulations were run using the boundary conditions of the VKI run for which the LHL airfoil was optimized: run

MUR237. Figure C.2 shows a static pressure colormap for the cascade test section with the VKI vane geometry. Since the LHL vane has the same axial chord, number of airfoils, and turning (loading), the secondary flow characteristics are assumed the same when that vane set is installed in the test section. As it is a 3-D code, in order to simulate a linear cascade, the hub radius was increased to a very large level (≈ 99 in). Clearly, the plot shows no undesirable endwall gradients that would indicate secondary flow issues. The CORSAIR program is advantageous since it can be used to develop 3-D optimized airfoil geometries.

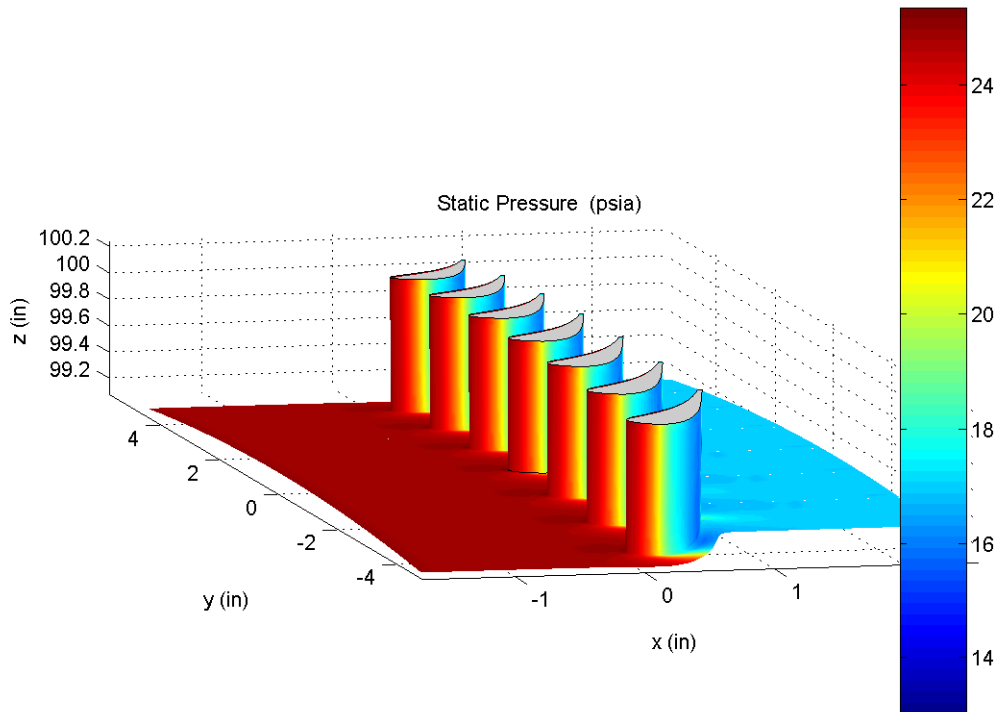


Figure C.2 Static pressure prediction of nominal cascade condition using 3-D CORSAIR code.

Figure C.3 is a loss profile plot for the specified boundary conditions showing that between 40% and 60%, the flow loss is stable and suitable for heat transfer measurements. Figure C.4 is a plot of pressure loading at six different spanwise locations

using the 3-D CORSAIR code with a comparison to the 2-D WILDCAT prediction at 50% span. This shows that the 2-D code predicts the same loading as the 3-D code for midspan calculations. Finally, figure C.5 is a total pressure color map obtained in the turbine design system, TDAAS, for a single flow passage looking upstream, where the left border represents the SS of the passage and the right border is the PS (x-axis is pitchwise). The major features seen are the vortices and secondary flow as developed by the time flow gets to 50% axial chord downstream of the trailing edge (the 50% chord downstream i-plane, using CFD terms). Clearly, even at 50% chord downstream of the TE, the secondary flow vortices have not penetrated midspan. Thus, the 2-D predictions obtained here are suitable for comparisons to the data measured in the linear cascade.

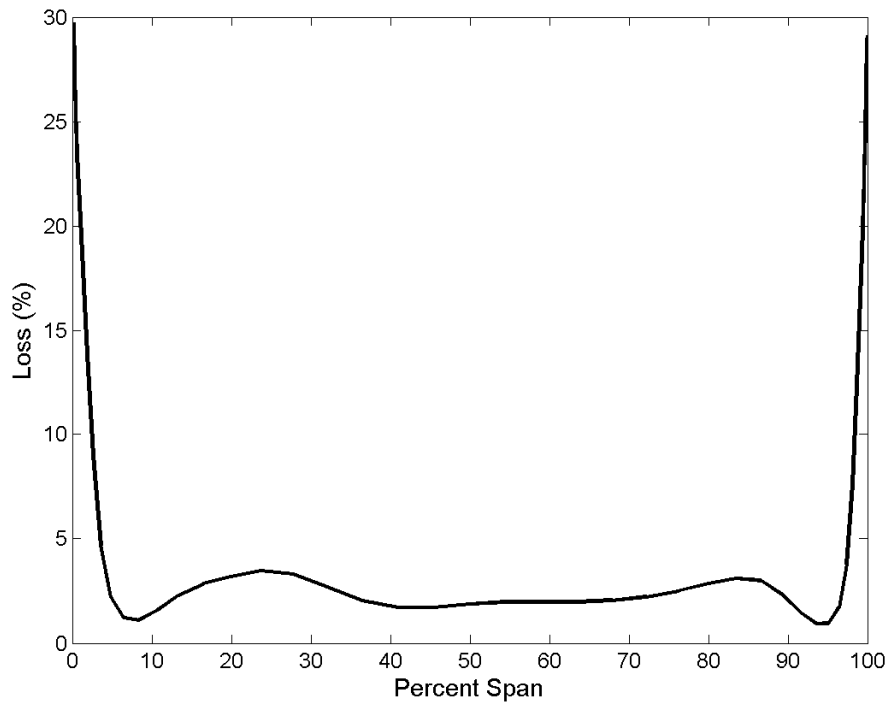


Figure C.3 Loss profile for test section vane aspect ratio showing stable midspan.

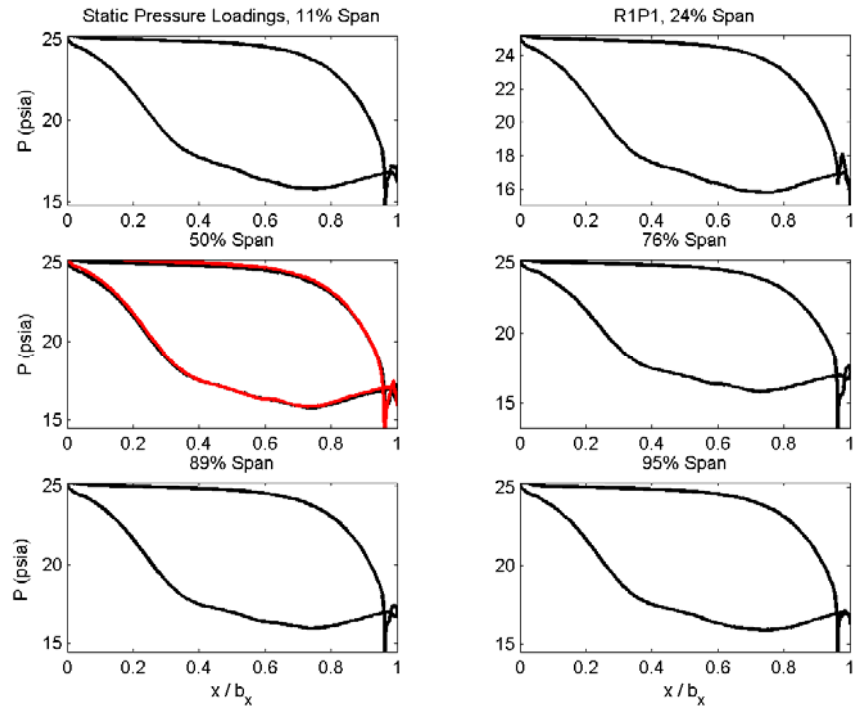


Figure C.4 Comparison of 2-D and 3-D code predictions at vane midspan.

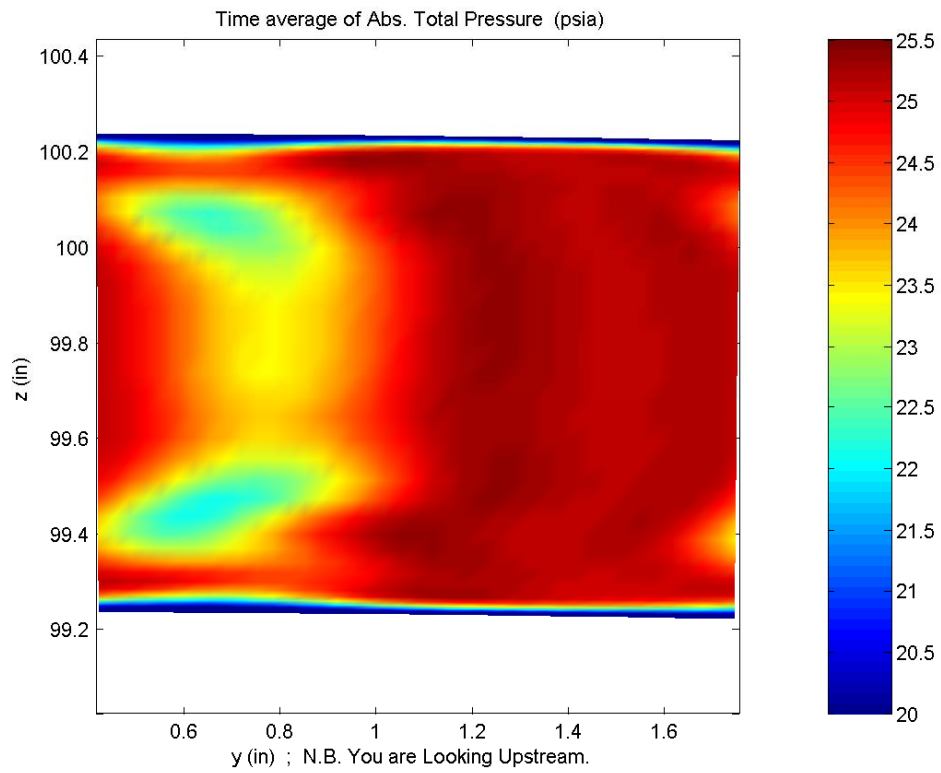


Figure C.5 Total pressure contour at the 50% chord downstream i-plane for 3-D flow prediction.

APPENDIX D: Fundamentals of Thin Film Heat Flux Gauge Operation

The thin-film heat flux gauge has been used in countless past applications for performing experimental heat transfer measurements in short duration high-temperature turbine-representative flows. It is a device consisting of a thin metal element having a very small heat capacity bonded to the surface of an insulating substrate. The insulator may have a thin film gauge placed on one side or both sides. One sided gauges were used here for the shock tube experiment, along with a Kapton substrate 50 microns thick and a Platinum metal layer 500-Å thick. When subjected to a change in heat flux like the one that occurs in the reflected shock tunnel, properly calibrated Platinum films can be used to determine the temperature history of the substrate surface to obtain the transient heat transfer characteristics. When basic theory concerning transient heat conduction is employed, the properties of the substrate are known (ρ , c , k), and a 1-D semi-infinite slab assumption concerning the insulating Kapton layer (Figure D.1), the heat flux to the insulator surface can be readily calculated.

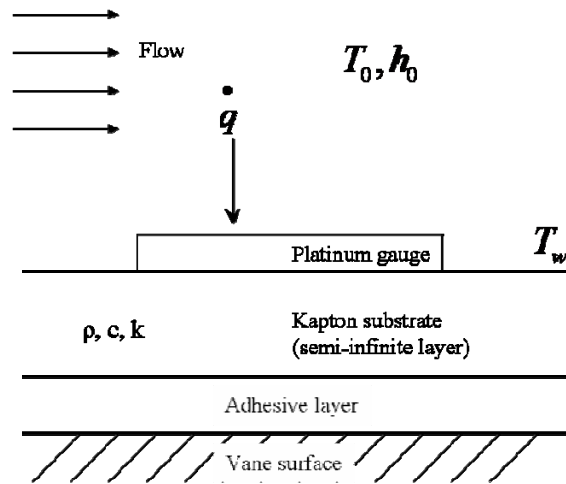


Figure D.1 Thin film gauge on semi-infinite layer.

According to Dunn [54], the available test time governs the substrate thickness onto which the gauge is painted (sputtered in this case), thus the relatively thin Kapton layer is appropriate for the unsteady, short-duration 5 ms tests created by the shock tube. The substrate was designed to be sufficiently thick so that the thermal wave does not penetrate to the backside of the Kapton over the length of the test time—otherwise a second gauge would have to be used to measure the temperatures there. Heat flux is deduced from the measured voltage vs. time history obtained by the gauges using either an analytical or numerical solution with specified boundary conditions.

The techniques and MATLAB codes for the impulse response method for semi-infinite substrate heat transfer gauges by Oldfield [50] were used to obtain heat flux from the raw voltage data. In that reference, Oldfield explains that heat flux can be calculated directly from a digitally recorded T signal, but that it is not always recommended because of the noise generated by the numerical error when digitizing the film voltage. This is not the case here, as the signal sampling resolution is significant and high frequency signals were pre-amplified prior to digitization [51]. The voltage was known by $V = I R$, where the constant current that was passed through the Platinum gauges is I and the temperature-dependent resistance of an individual gauge is $R = R(T)$. Thus, if $V = f(R)$, then $V = f(T)$. Temperature with respect to time, $T(t)$, can now be backed out from a digital signal knowing the voltage read and the proper resistance change for a given temperature which was provided by the temperature coefficient of resistance, α , calculated in the calibrations. Now that T is known, the 1-D heat conduction equation given by equation D.1 is used,

$$\frac{\partial^2 T}{\partial x^2} = \left(\frac{1}{\alpha} \right) \frac{\partial T}{\partial t} \quad (\text{D.1})$$

where α (different than the temperature coefficient of resistance) is the thermal diffusivity of the Kapton and equal to $k/(\rho c)$. Using the 1-D semi-infinite solid assumption, equation D.1 is solved numerically. To obtain the heat flux for an initially isothermal surface boundary condition (Dirichlet condition), Ref [57] gives D.2 for a step change in heat flux.

$$\frac{T(x,t) - T_i}{T_s - T_i} = \text{erf}\left(\frac{x}{2\sqrt{\alpha t}}\right) \quad (\text{D.2})$$

and now with $T(x)$ this can be differentiated to get temperature gradient at the surface and thus the heat flux by equation D.3:

$$q''_s(t) = \frac{k(T_s - T_i)}{\sqrt{\pi \alpha t}}. \quad (\text{D.3})$$

The technique of Oldfield uses these fundamental theories combined with an impulse response filter to obtain time-resolved heat flux. The time-resolved heat flux was in turn time-averaged to give the reflected shock data.

As an aside, assuming a constant heat flux, the penetration depth of the thermal wave going through the Kapton and adhesive (itself 50 μm thick) can be calculated and plotted. Figure D.2 below gives a plot the left side of equation D.2 plotted against depth, x , assuming a total insulator thickness of 100 microns and a time $t = 5$ ms. The plot shows that the percent rise in temperature at 100 μm is less than 0.1% of the surface temperature rise at 5 ms. That is, the substrate remained semi-infinite over the reflected-shock tunnel test time.

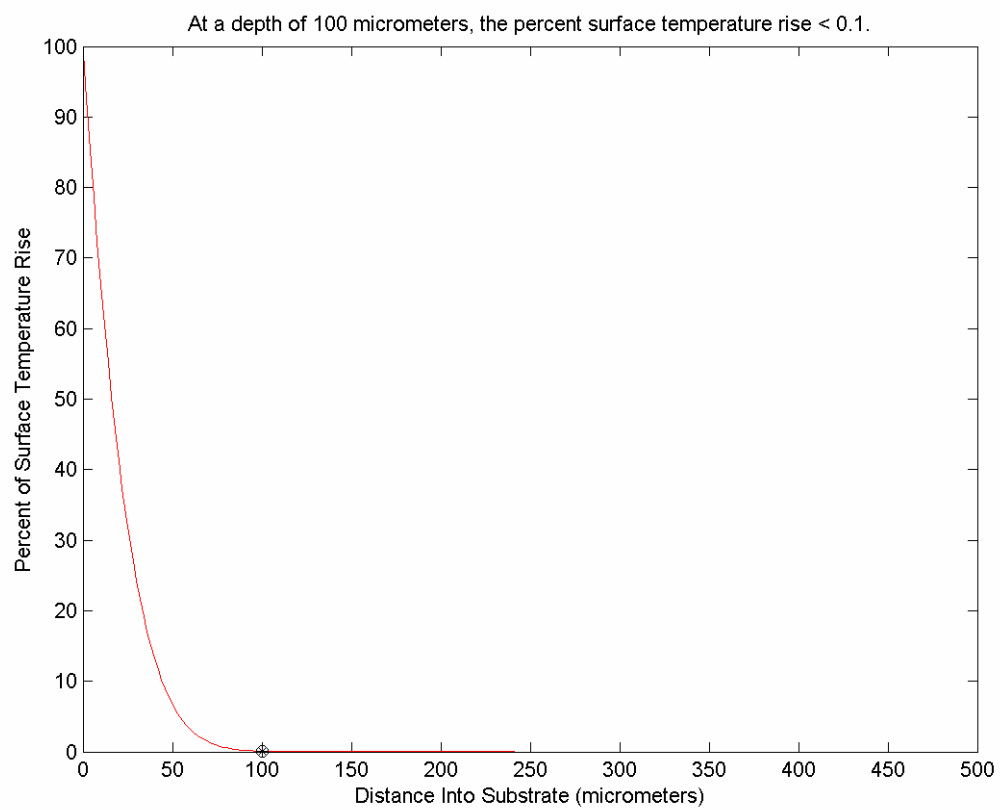


Figure D.2 Penetration depth of thermal wave for 100 micron insulator thickness.

Appendix E: Thin Film Heat Flux Gauge Production Process

The fabrication process for the thin film heat flux gauges used in the experiments of this thesis was defined by Dr. Richard Anthony and executed by Lt Ryan Lemaire, both of AFRL/PRTT. It is complex and careful in order to ensure the highest standard of heat transfer data collection. The following steps are followed to create the Kapton-platinum films:

- 1) The gauge pattern is drawn using drafting software in which the black lines will represent the conducting metal. Individual gauges or sensors should maintain at least a 10:1 ratio and all gauges on a film should have the same aspect ratio. Print the design using a high-resolution printer on to transparent film.
- 2) The 50 micron thick flexible Kapton substrate is cleaned and a 30 micron sheet of photoresist is adhered to one side of the Kapton under heat and pressure.
- 3) The printed gauge design is laid on top of the Kapton and photoresist with the photoresist side up in an air-evacuated 2000 W UV light exposure unit. The exposed photoresist (not blocked by the printed design) hardens.
- 4) A solution composed of 1% Na_2CO_3 by weight and distilled water heated to 100 °F is lightly sprayed on the unexposed photoresist, washing it away.
- 5) A 500-Å layer of platinum is sputtered over the entire Kapton sheet. Acetone is then used to wash away the hardened exposed photoresist and the platinum above it leaving platinum as it appeared in the printed design.

- 6) A 50 micron thick layer of adhesive with a release liner is applied to the back side of the film and left under pressure for 24 hrs.
- 7) The release liner may be removed and the film applied to the desired surface for which heat transfer data is to be collected.
- 8) JB Weld epoxy is used to connect lead wires to gauge leads on the film and to act as a strain release to increase the durability of the gauges.
- 9) In a final step, the platinum-Kapton thin film heat flux gauge is calibrated to ensure accurate heat transfer evaluation.

The work in the steps outlined above was performed in the AFRL/PRTT Heat Flux Instrumentation Laboratory (HFIL) except for the platinum sputtering which was done at AFRL/ML. Also, the extremely delicate application of the gauges to the models and subsequent soldering and securing of the lead wires was performed by Mr. Rob Free in AFRL/PRTE.

Appendix F: Calibration of Thin Film Heat Flux Gauges

The heat flux gauges used to measure midspan heat flux in a linear cascade for the VKI and LHL vanes were calibrated using a Omegalux model LMF-3550 oven to increase the air temperature and a Kaye Instruments model M2806/IRTD-500 RTD temperature probe to measure the temperature of the platinum surface of the gauges. This process was completed for both the VKI vane with 27 gauges and the LHL vane with 28 gauges. A +/- 12 V custom current source box similar to that used in the shock tube experiment was used to supply 4 amps (adjusted to real value using an exact resistor wired in series in the current line) of current to the gauges. Resistances of individual gauges were recorded at four different air temperatures and hence three even temperature steps (approximately 25, 50, 75, and 100 degrees Celsius) provided by the oven. Using equation F.1 below, the temperature coefficient of resistance, α , with units of $1/(^{\circ}\text{C})$ was calculated using a modified form of that defined by Holman [64].

$$\alpha = \frac{R_i - R_0}{R_0(T_i - T_0)} \quad (\text{F.1})$$

The subscript “i” denotes the properties of the specified temperature step in the calibration, while the subscript “0” is the value of the property at the initial temperature. An Excel spreadsheet was used to convert the recorded values of gauge resistances to corresponding values of α . Table F.1 gives the recorded resistances of the VKI vane calibration and Table F.2 gives that of the LHL vane heat flux gauges. Figures F.1 and F.2 are plots of R_0/R_i versus $T_i - T_0$ for the VKI and LHL vanes, respectively, from which the slope could be calculated to get α ’s for each gauge. From here, α was used to find time-varying temperature for each individual gauge from raw voltage signals.

Table F.1 VKI thin film heat flux gauge calibration data.

$R_m =$ $V_m =$		True current = 3.9974 mA		Room Temp = T1 =		21.94 °C 25 °C			
Temp step: RTD Temp [°C]:		1 25.00		2 45.19		3 67.05		4 89.28	
Gauge Label #	Gauge #	V_{gauge} [VDC]	R_{gauge} [Ω]	V_{gauge} [VDC]	R_{gauge} [Ω]	V_{gauge} [VDC]	R_{gauge} [Ω]	V_{gauge} [VDC]	R_{gauge} [Ω]
103-104	1	0.3395	84.9297	0.3489	87.2812	0.3597	89.9829	0.3729	93.2850
109-110	2	0.3197	79.9765	0.3283	82.1279	0.3384	84.6545	0.3504	87.6564
111-112	3	0.1830	45.7795	0.1878	46.9802	0.1937	48.4562	0.2005	50.1573
113-114	4	0.2035	50.9078	0.2087	52.2086	0.2154	53.8847	0.2230	55.7859
115-116	5	0.2024	50.6326	0.2078	51.9835	0.2143	53.6095	0.2218	55.4857
117-118	6	0.2006	50.1823	0.2057	51.4581	0.2124	53.1342	0.2198	54.9854
119-120	7	0.6099	152.5732	0.6259	156.5758	0.6461	161.6290	0.6683	167.1826
123-124	8	1.1000	275.1771	1.1284	282.2817	1.1638	291.1374	1.2001	300.2182
127-128	9	0.6935	173.4867	0.7111	177.8895	0.7342	183.6682	0.7576	189.5220
129-130	10	0.2055	51.4081	0.2106	52.6839	0.2177	54.4600	0.2249	56.2612
131-132	11	0.1934	48.3811	0.1983	49.5069	0.2052	51.3330	0.2122	53.0842
133-134	12	0.1857	46.4549	0.1904	47.5307	0.1970	49.2817	0.2036	50.9328
135-136	13	0.1795	44.9039	0.1840	46.0296	0.1905	47.6557	0.1967	49.2067
137-138	14	0.2029	50.7577	0.2079	52.0085	0.2151	53.8096	0.2220	55.5357
139-140	15	0.2004	50.1323	0.2058	51.4831	0.2126	53.1842	0.2193	54.8603
141-142	16	0.7008	175.3128	0.7202	180.1659	0.7441	186.1448	0.7678	192.0736
145-146	17	0.6933	173.4366	0.7123	178.1897	0.7361	184.1435	0.7593	189.9472
147-148	18	0.2001	50.0572	0.2054	51.3831	0.2122	53.0842	0.2186	54.6852
149-150	19	0.2030	50.7827	0.2084	52.1336	0.2153	53.8597	0.2218	55.4857
151-152	20	0.2039	51.0078	0.2092	52.3337	0.2162	54.0848	0.2226	55.6858
153-154	21	0.2358	58.9880	0.2419	60.5139	0.2501	62.5653	0.2575	64.4165
155-156	22	0.2675	66.9181	0.2744	68.5442	0.2837	70.9707	0.2920	73.0470
Time of day:		945		1100		1405		1458	

Table F.2 LHL vane thin film heat flux gauge calibration data.

$R_m =$ $V_m =$		True current =		Room Temp =	
68.369 Ω 0.2727 V DC		3.9886 mA		21.94 $^{\circ}\text{C}$ 25 $^{\circ}\text{C}$	
Temp step: RTD Temp [$^{\circ}\text{C}$]:		1		2	
Gauge Label #s		21.20		43.50	
Gauge #	V_{gauge} [VDC]	R_{gauge} [Ω]	V_{gauge} [VDC]	R_{gauge} [Ω]	V_{gauge} [VDC]
103-104	1	0.1887	47.3092	0.1942	0.2002
105-106	2	0.3065	76.8430	0.3155	0.3255
111-112	3	0.3142	78.7735	0.3231	0.3331
113-114	4	0.6446	161.6086	0.6631	0.6840
117-118	5	0.6800	170.4838	0.6991	0.7204
119-120	6	0.6898	172.9407	0.7092	0.7320
129-130	7	0.5815	145.7887	0.5974	0.6166
131-132	8	0.2069	51.8722	0.2124	0.2196
133-134	9	0.1969	49.3651	0.2022	0.2088
136-136	10	0.1842	46.1810	0.1892	0.1957
137-138	11	0.2030	50.8944	0.2092	0.2156
139-140	12	0.2062	51.6967	0.2125	0.2191
141-142	13	0.6853	171.8125	0.7068	0.7293
145-146	14	0.6591	165.2439	0.6798	0.7016
147-148	15	0.1920	48.1366	0.1978	0.2041
149-150	16	0.1928	48.3372	0.1985	0.2049
151-152	17	0.1936	48.5377	0.1993	0.2058
153-154	18	0.2523	63.2545	0.2597	0.2681
155-156	19	0.1895	47.5098	0.1950	0.2013
157-158	20	0.2455	61.5496	0.2526	0.2609
Time of day:		1430		1510	
				1610	
				1650	
				87.95	
				52.0226	
				84.8157	
				86.4202	
				177.4786	
				186.6045	
				189.5880	
				159.6781	
				56.8864	
				53.9782	
				50.7189	
				56.0841	
				56.8864	
				189.4877	
				182.2421	
				52.9753	
				53.1257	
				53.3263	
				69.4471	
				52.1229	
				67.5166	

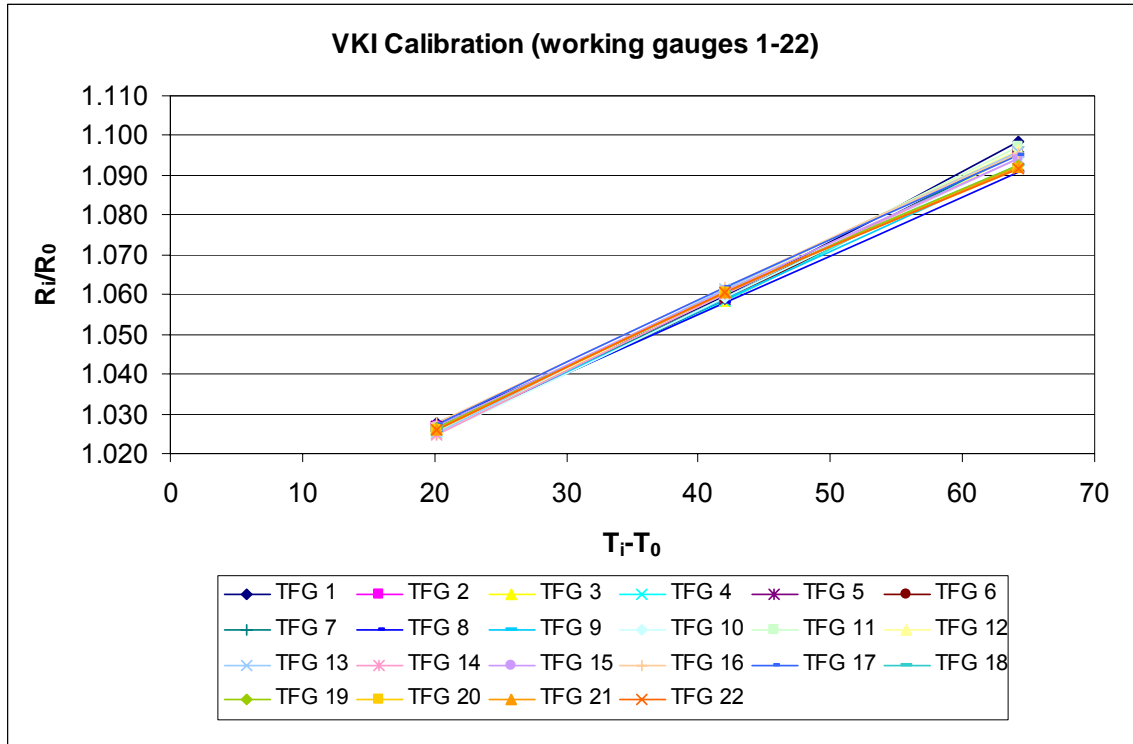


Figure F.1 Calibration curves to find α for VKI vane thin film gauges.

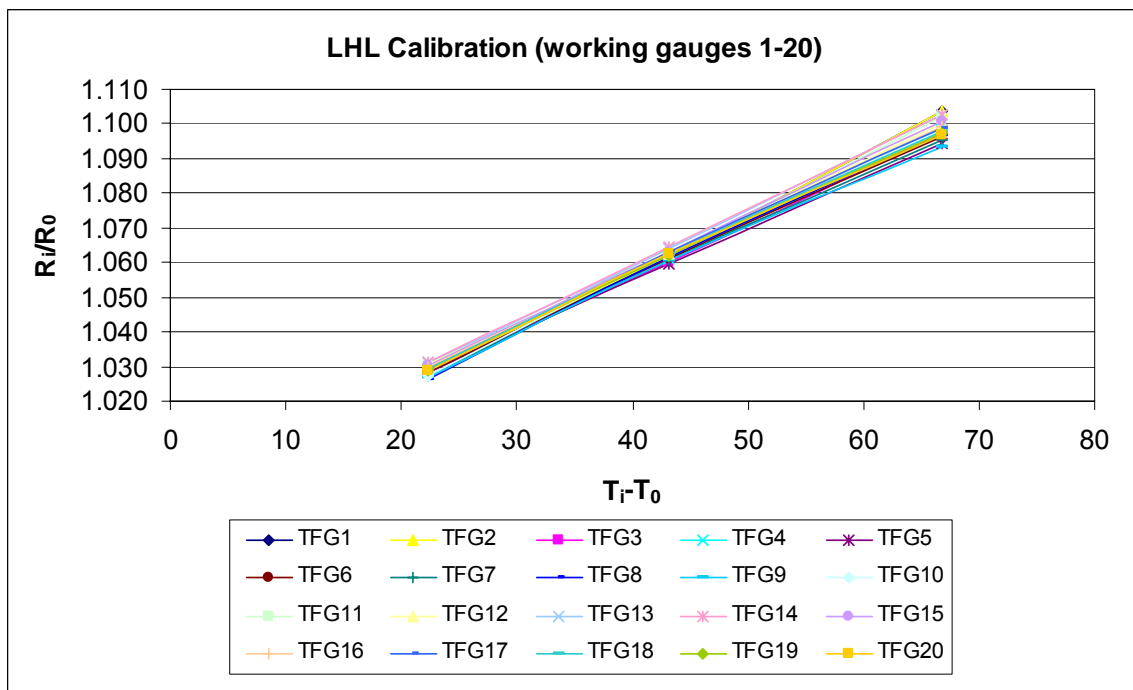


Figure F.2 Calibration curves to find α for LHL vane thin film gauges.

APPENDIX G: Heat Flux Gauge Coordinates for VKI and LHL Vanes

VKI Vane		
Gauge Number	Location of Gauge Center from LE [mm]	Fractional Surface Location, s/s_x
1	-31.00	-0.809
2	-26.40	-0.689
3	-21.80	-0.569
4	-17.20	-0.449
5	-12.60	-0.329
6	-9.20	-0.240
7	-6.90	-0.180
8	-4.60	-0.120
9	-2.30	-0.060
10	0.00	0.000
11	2.30	0.043
12	4.60	0.087
13	6.90	0.130
14	9.20	0.174
15	12.65	0.239
16	17.35	0.328
17	21.95	0.415
18	25.30	0.478
19	27.60	0.522
20	29.90	0.565
21	32.20	0.609
22	34.50	0.652
23	36.80	0.696
24	39.10	0.739
25	41.40	0.783
26	43.70	0.826
27	46.00	0.870

LHL Vane		
Gauge Number	Location of Gauge Center from LE [mm]	Fractional Surface Location, s/s_x
1	-31.91	-0.824
2	-27.31	-0.706
3	-22.71	-0.587
4	-18.11	-0.468
5	-13.51	-0.349
6	-10.11	-0.261
7	-7.81	-0.202
8	-5.51	-0.142
9	-3.21	-0.083
10	-0.91	-0.024
11	1.39	0.025
12	3.69	0.067
13	5.99	0.108
14	8.29	0.150
15	11.74	0.213
16	16.44	0.298
17	21.04	0.381
18	24.39	0.442
19	26.69	0.483
20	28.99	0.525
21	31.29	0.566
22	33.59	0.608
23	35.89	0.650
24	38.19	0.691
25	40.49	0.733
26	42.79	0.775
27	45.09	0.816
28	47.44	0.859

Appendix H: CAD Drawings of Designed Parts with Dimensions

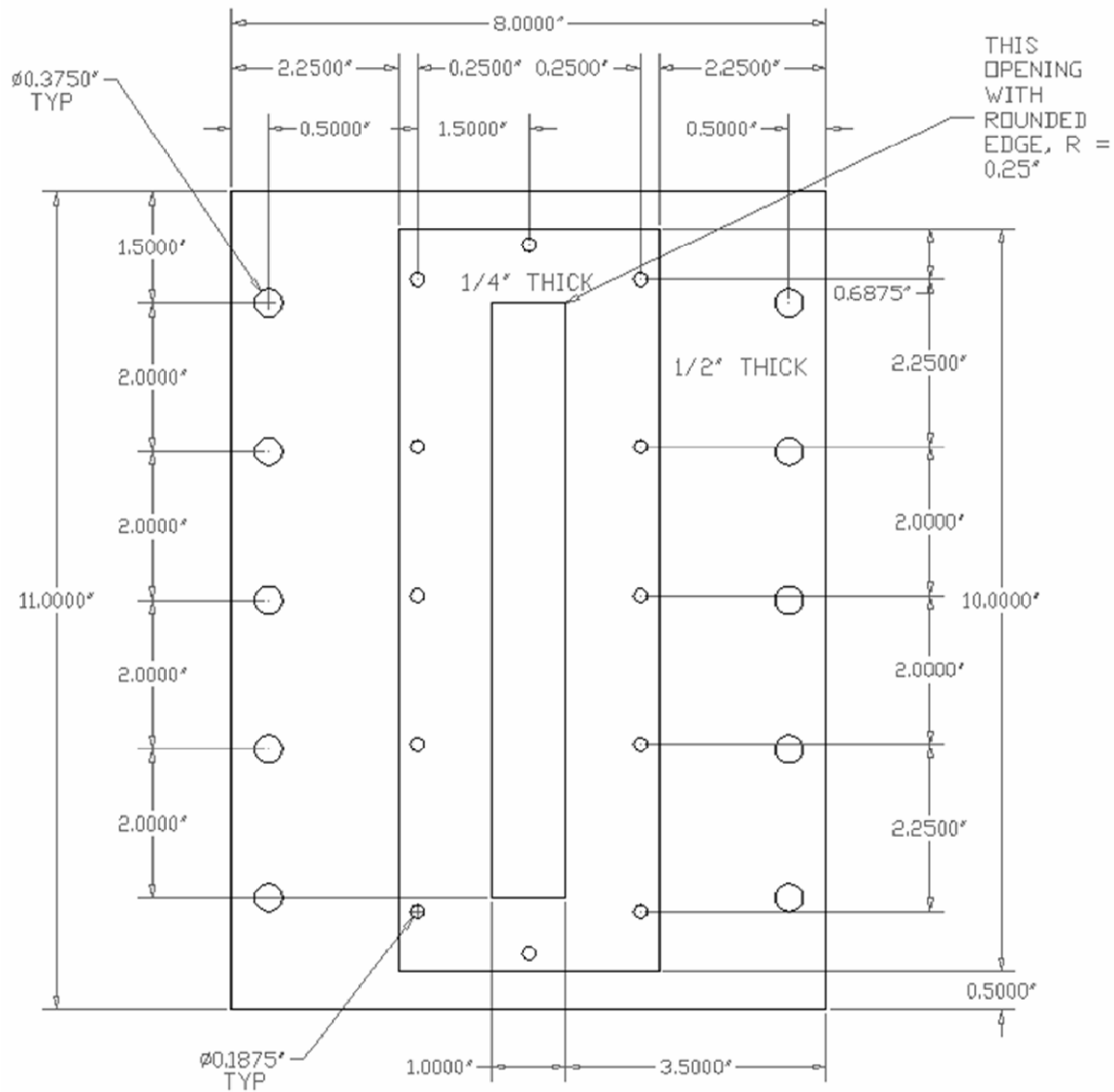


Figure H.1 Flange piece used to bolt cascade test section to shock tube, house the turbulence grid, and provide flow area reduction into cascade inlet.

GRID MESH (SQUARE),
0.035" DIA WIRE, 0.132"
APART

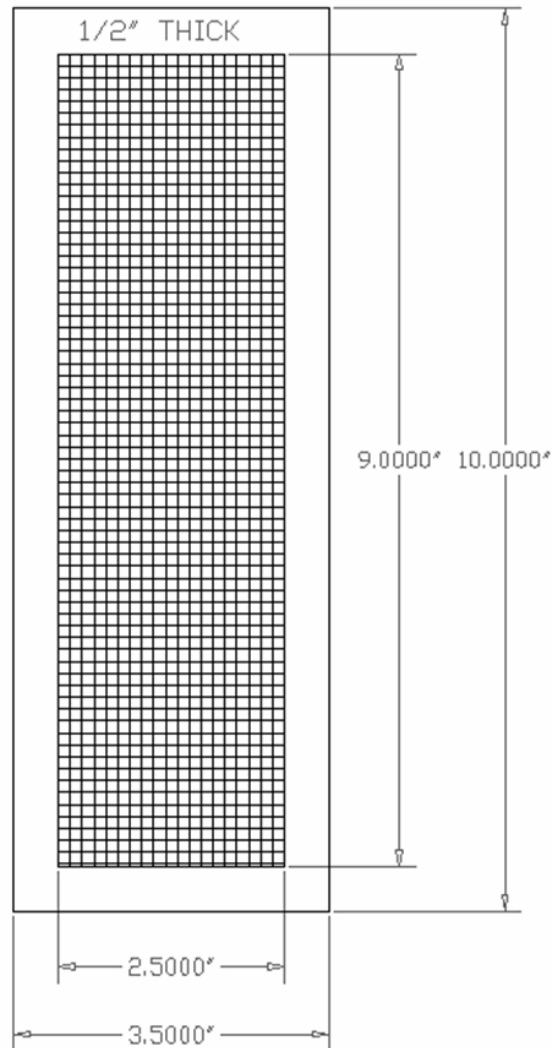


Figure H.2 Turbulence grid sandwiched between tow thin border plates for producing 6% theoretical freestream turbulence intensity.

PLEXIGLASS TEST SECTION WALL:
 3/4" THICK, ALL HOLES AROUND BORDER ARE DRILLED
 COMPLETELY THROUGH. AIRFOIL HOLES ARE DRILLED INTO
 'UNDER-SIDE' 1/2", THIS PIECE AS WELL AS A 'MIRROR' OF
 THIS PIECE IS REQUIRED.

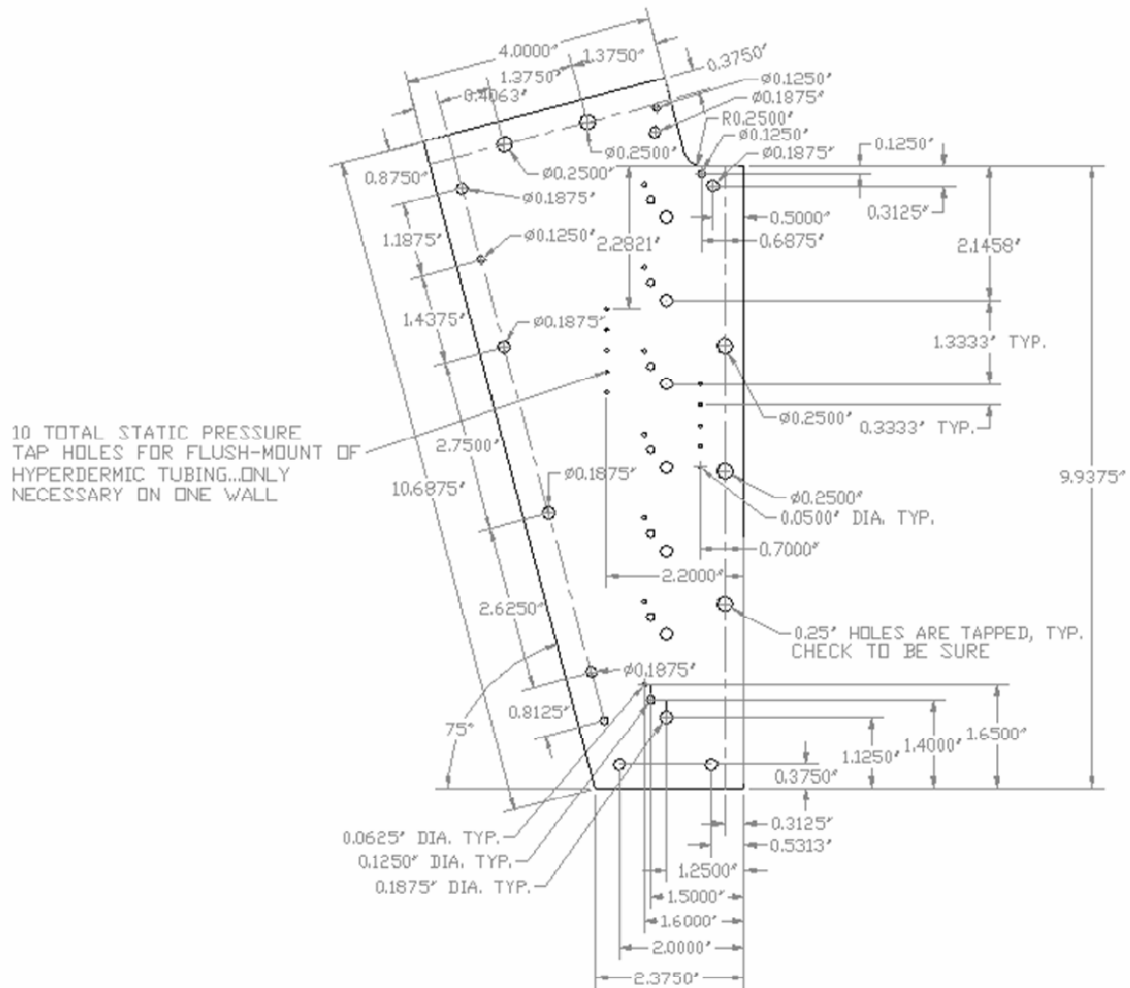


Figure H.3 Plexiglass side wall designed to interchangeably house both vane geometries in the 7-vane cascade test section using metal pins.

7-AIRFOIL CASCADE TEST SECTION:
SHOWS SIDE VIEW OF HOW AIRFOILS FIT WITHIN
METAL TEST SECTION WITH PLEXIGLASS WALLS.

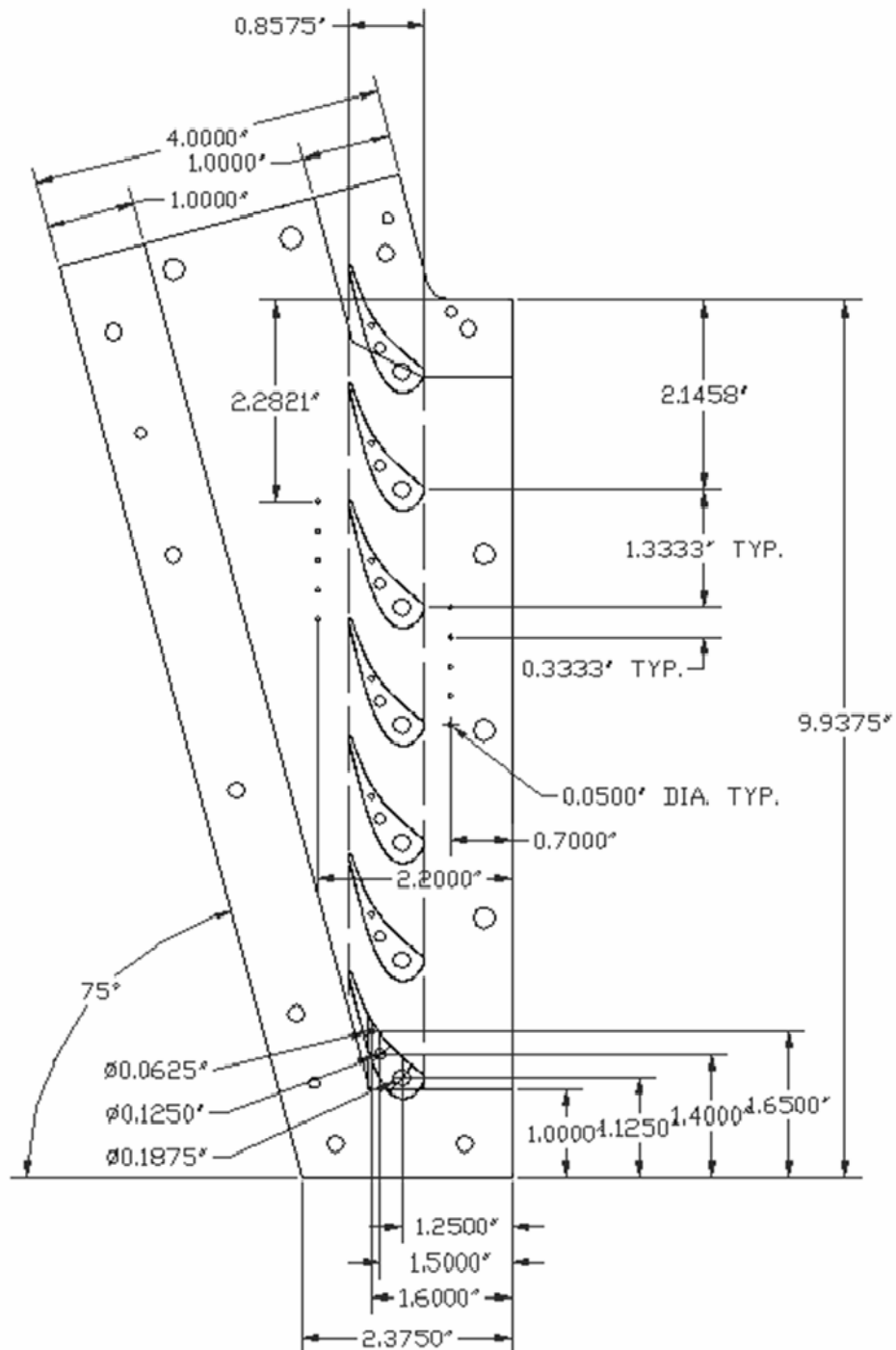


Figure H.4 Cascade test section with VKI vanes shown installed.

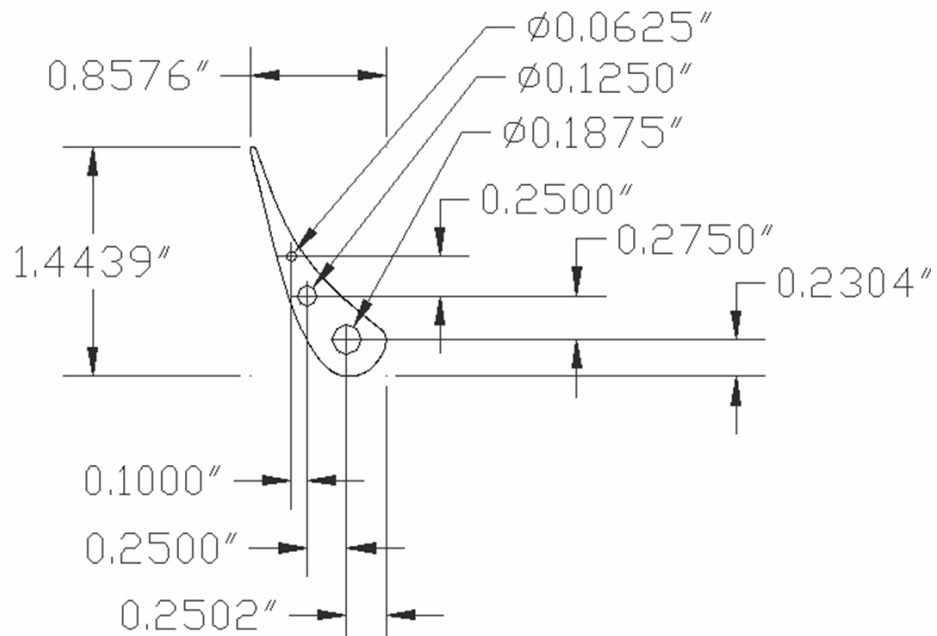


Figure H.5 VKI vane geometry with pin hole locations.

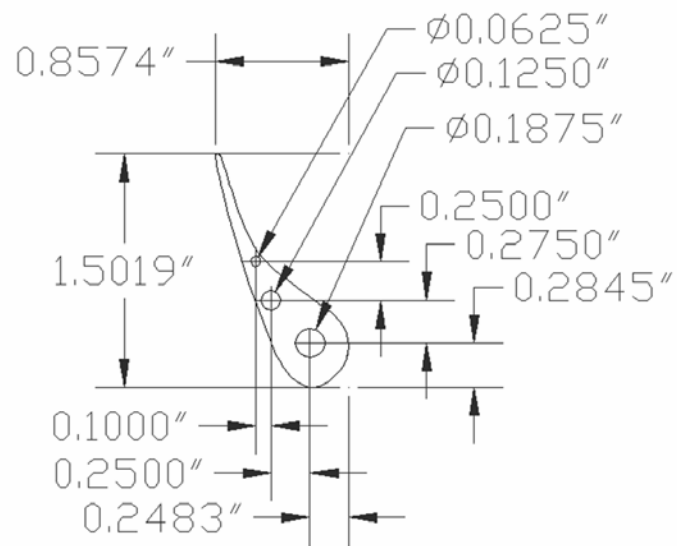


Figure H.6 LHL vane geometry with pin hole locations.

APPENDIX I: Additional Airfoil CFD Data

Presented in this appendix are airfoil data pertaining to the following subjects:

- Predicted boundary layer property comparisons using the AGS model for transition using WILDCAT for the MUR237 design conditions
- Area, suction side curvature, and thickness distributions for each vane geometry
- Heat transfer and pressure loading laminar and turbulent prediction comparisons of the VKI and LHL vanes for the MUR237 design conditions
- LHL vane manufacturing coordinates (normalized by axial chord)
- Velocity and temperature boundary layer profiles for laminar and turbulent predictions of the VKI and LHL vane at maximum height of the vanes on the suction side.

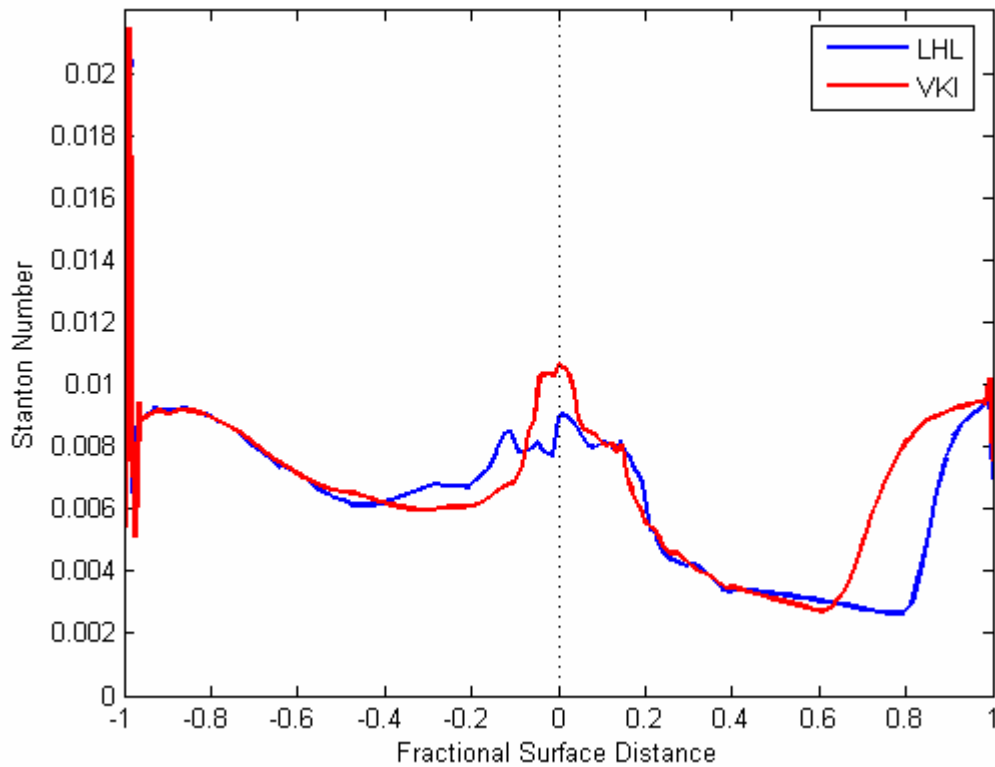


Figure I.1 Predicted Stanton number comparison for VKI and LHL vane geometries using the Abu-Ghannam and Shaw (AGS) transition model.

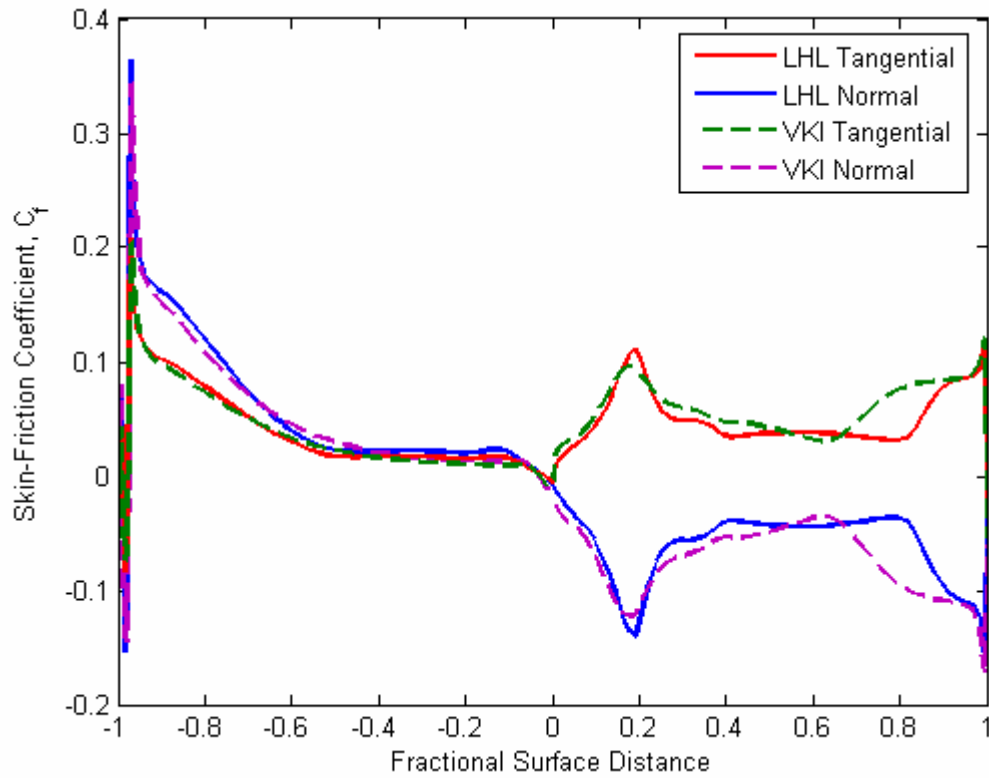


Figure I.2 Predicted skin friction coefficient comparison for VKI and LHL vane geometries using the AGS transition model.

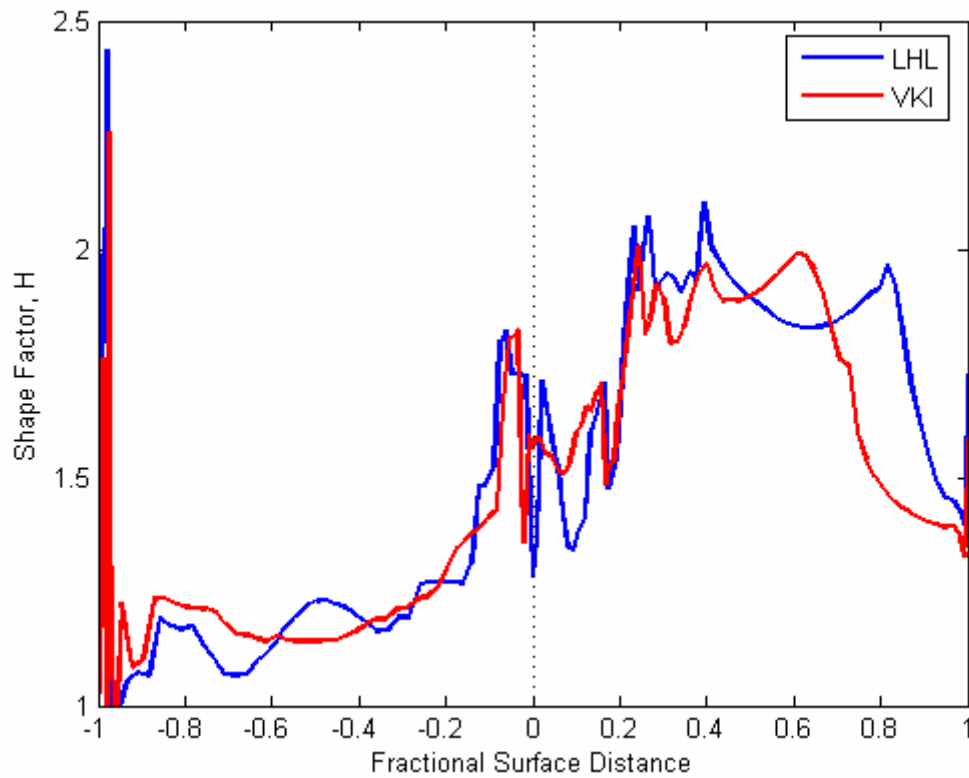


Figure I.3 Predicted shape factor comparison for VKI and LHL vane geometries using the AGS transition model.

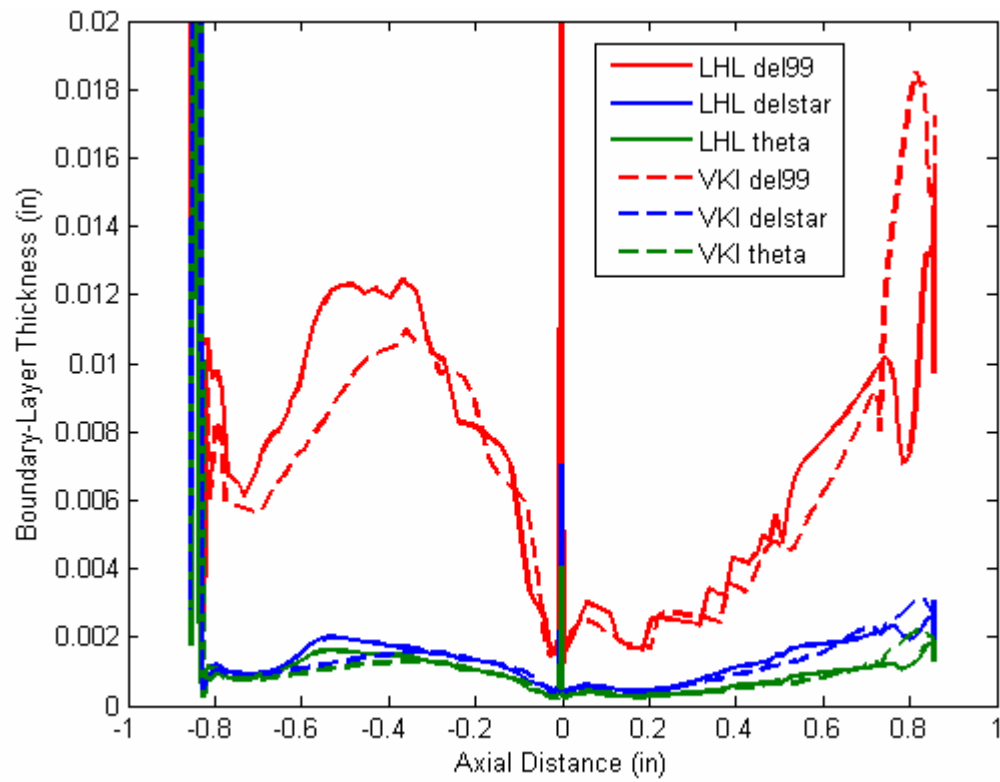


Figure I.4 Predicted boundary layer thickness comparison for VKI and LHL vane geometries using the AGS transition model.

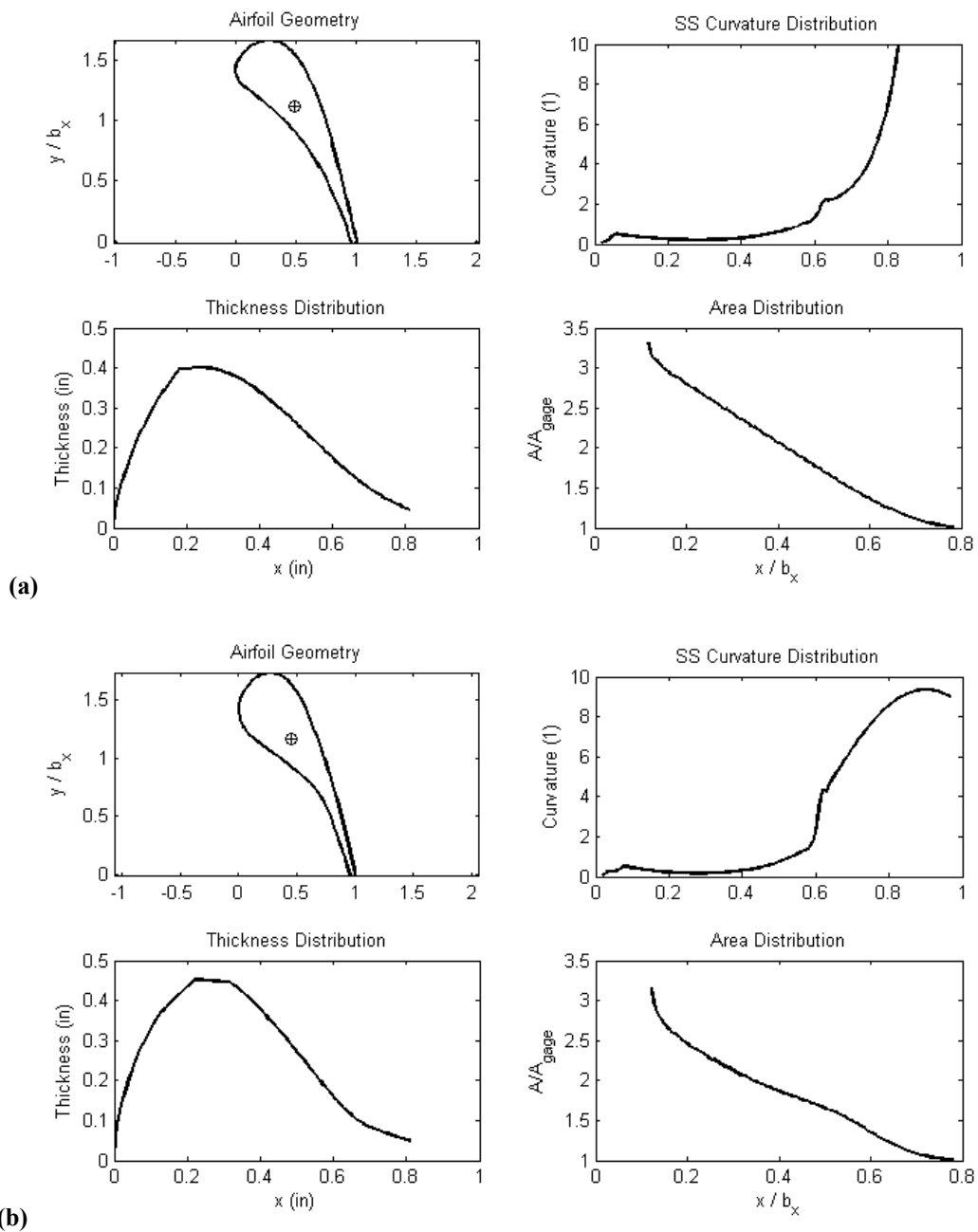


Figure I.5 Suction surface curvature, area, and thickness distributions for the VKI (a) and LHL (b) vanes.

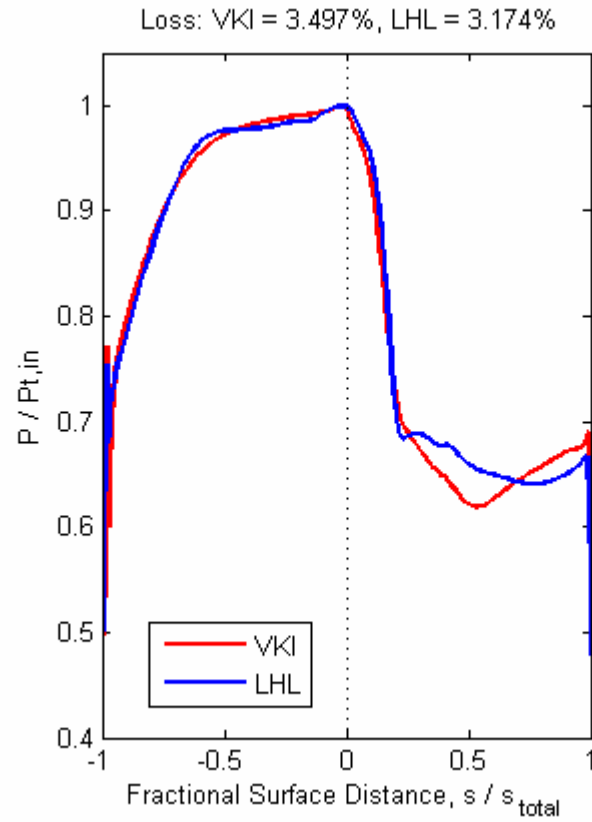


Figure I.6 Laminar prediction of pressure loading comparing the VKI and LHL vanes. The LHL geometry causes less loss than VKI.

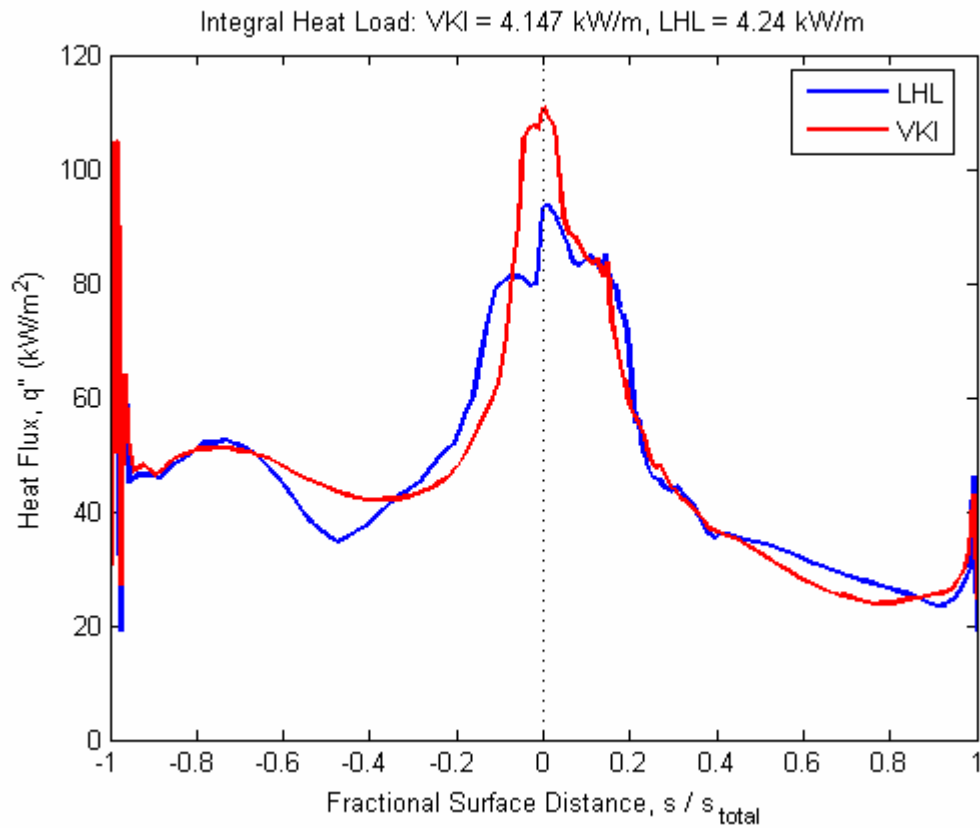


Figure 1.7 Laminar prediction of heat flux distribution comparison of VKI and LHL vanes. The LHL geometry clearly has lower LE heat flux.

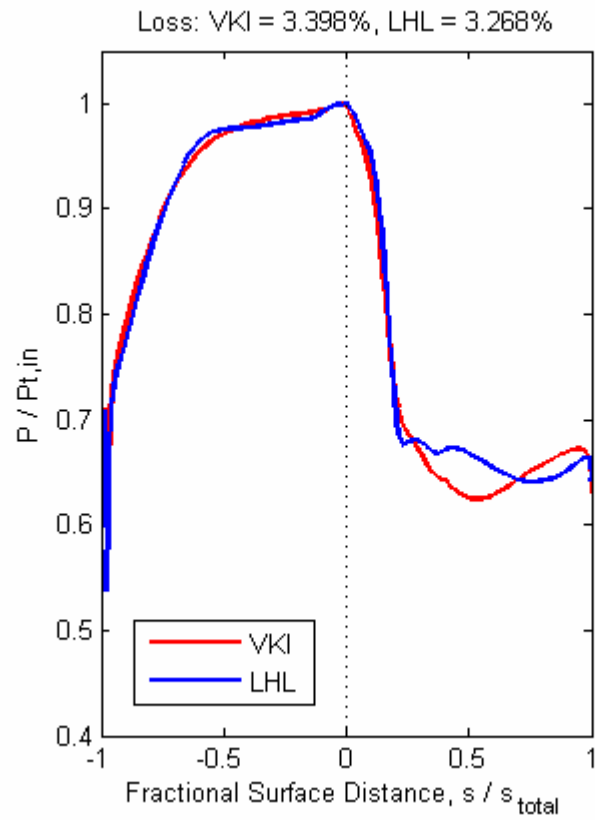


Figure I.8 Turbulent prediction of pressure loading comparing the VKI and LHL vanes. The LHL geometry causes less loss than VKI.

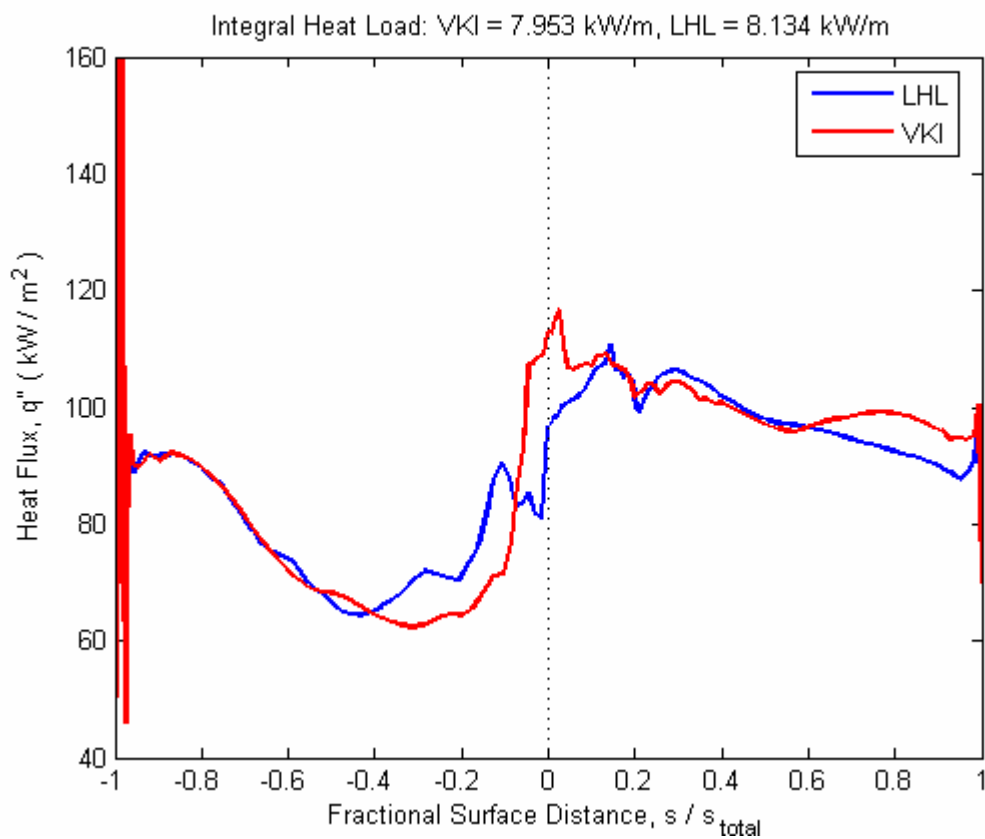


Figure I.9 Turbulent prediction of heat flux distribution comparing the VKI and LHL vanes. The LHL geometry exhibits lower LE heat flux.

Table I.1 LHL vane manufacturing coordinates.

x/b_x	y/b_x	x/b_x	y/b_x	x/b_x	y/b_x
0.000	1.421	0.642	1.262	0.964	-0.012
0.006	1.477	0.656	1.227	0.962	-0.009
0.012	1.500	0.669	1.190	0.961	-0.006
0.018	1.517	0.682	1.153	0.937	0.067
0.023	1.532	0.696	1.115	0.915	0.135
0.029	1.544	0.710	1.076	0.895	0.198
0.035	1.556	0.723	1.036	0.876	0.257
0.041	1.566	0.737	0.995	0.858	0.312
0.047	1.576	0.750	0.954	0.841	0.362
0.053	1.585	0.764	0.911	0.825	0.409
0.059	1.593	0.778	0.868	0.809	0.452
0.072	1.610	0.791	0.824	0.794	0.493
0.085	1.627	0.805	0.780	0.779	0.530
0.099	1.642	0.818	0.735	0.764	0.565
0.113	1.657	0.831	0.689	0.749	0.597
0.128	1.670	0.844	0.642	0.734	0.627
0.142	1.683	0.858	0.596	0.718	0.656
0.158	1.694	0.871	0.548	0.702	0.682
0.173	1.704	0.883	0.500	0.684	0.708
0.189	1.712	0.896	0.452	0.666	0.732
0.205	1.719	0.908	0.403	0.647	0.756
0.221	1.725	0.921	0.354	0.626	0.779
0.238	1.729	0.933	0.305	0.604	0.802
0.254	1.732	0.945	0.255	0.579	0.826
0.271	1.733	0.956	0.205	0.553	0.849
0.288	1.732	0.967	0.155	0.525	0.873
0.306	1.729	0.978	0.105	0.495	0.898
0.323	1.725	0.989	0.055	0.462	0.924
0.341	1.718	1.000	0.004	0.427	0.951
0.358	1.710	1.000	0.001	0.388	0.980
0.376	1.700	1.000	-0.002	0.347	1.011
0.394	1.687	0.999	-0.005	0.303	1.044
0.412	1.672	0.999	-0.008	0.255	1.079
0.430	1.656	0.997	-0.010	0.204	1.118
0.448	1.636	0.996	-0.013	0.149	1.159
0.466	1.615	0.994	-0.015	0.134	1.171
0.484	1.591	0.991	-0.016	0.119	1.183
0.502	1.564	0.989	-0.018	0.104	1.197
0.520	1.535	0.986	-0.019	0.089	1.212
0.538	1.503	0.983	-0.020	0.074	1.229
0.555	1.469	0.980	-0.020	0.059	1.248
0.573	1.431	0.977	-0.020	0.045	1.270
0.591	1.391	0.974	-0.019	0.030	1.297
0.603	1.360	0.971	-0.018	0.015	1.333
0.616	1.329	0.968	-0.016	0.000	1.421
0.629	1.296	0.966	-0.014		

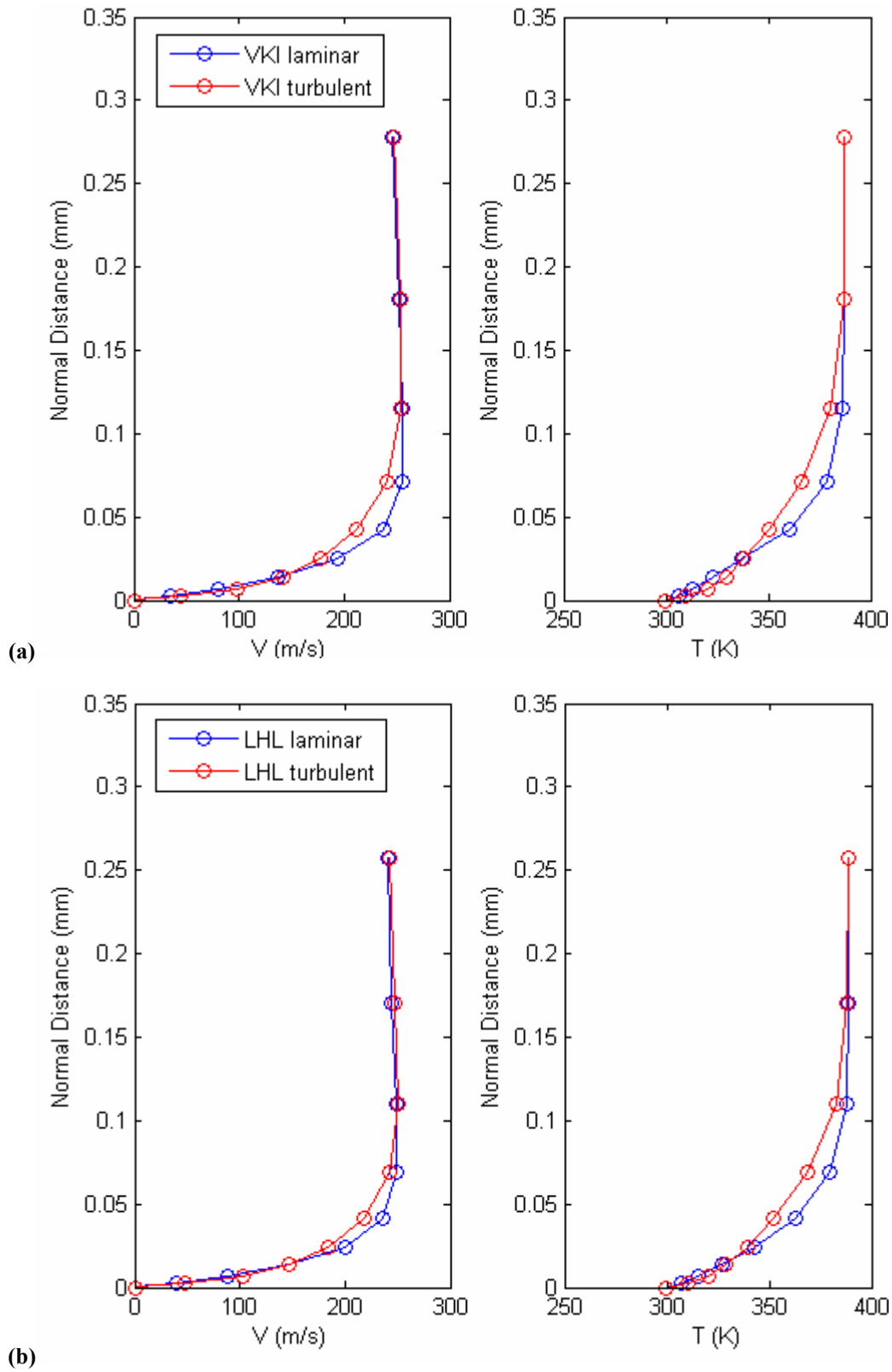


Figure I.10 Laminar and turbulent predictions of velocity and temperature profiles at maximum height of the vanes on the suction side for (a) the VKI vane and (b) the LHL vane using WILDCAT run at the MUR237 design conditions.

Appendix J: Determination of Turbulence Intensity from an Uncalibrated Hot-wire

The single film hot-wire and the two-component hot-wire (X-wire) used to find the turbulence intensity (Tu) in the cascade test section were not calibrated. To properly calculate Tu experimentally, King's Law [65] was considered valid. King's law is based on the assumption that Nusselt number, $Nu_D = f(Re_D)$. For a heated wire in constant-property flow, equation J.1 is

$$E^2 = A + BU^n \quad (J.1)$$

where $n = 0.5$, U is the flow velocity, and E is the hot-wire voltage. Differentiating King's law in equation J.1 gives

$$2EdE = nBU^{n-1}dU \quad (J.2)$$

where $B = (E^2 - A)/U^n$. Therefore, plugging B into equation J.2 gives

$$2EdE = [n(E^2 - A)U^{n-1}]/U^n \quad (J.3)$$

Rearranging gives the form:

$$\frac{2EdE}{n(E^2 - A)} = \frac{dU}{U} \quad (J.4)$$

Assuming $dE = (\overline{e'^2})^{1/2}$ and that $(\overline{u'^2})^{1/2} = dU$, equation J.5 gives the turbulence intensity,

$$Tu = \frac{\sqrt{\overline{u'^2}}}{U} = \frac{2E\sqrt{\overline{e'^2}}}{n(E^2 - A)} \quad (J.5)$$

where A is the no-flow voltage squared and E is the direct current (DC) component of the signal for a given U . Mee and Dickens [58] have shown this method yields Tu to within $\pm 18\%$ of the measured magnitude.

The autocorrelation function (ACF) is found by correlating a signal, $U(t_1)$, with a time-offset version of itself, $U(t_2)$. Thus, by definition the $ACF(t = 0) = 1$.

Finally, the turbulence length scale in the principal direction of the flow, Λ_x , can be found by equation J.6 from the ACF using the following formula:

$$\Lambda_x = U \int_0^{\infty} (ACF(t)) dt \quad (J.6)$$

This gives the largest turbulent eddy size expected in the flow.

APPENDIX K: Equipment Used

Item	Manufacturer	Part/Model #
DC Power Supply	Tektronix	PS280
High Frequency Processor	National Instruments	PXI-1045
Embedded Controller	“	PXI-8186
Simultaneous Sampling I/O	“	PXI-6120
Data Acquisition Card	“	SCXI-1140
“	“	SCXI-1121
“	“	SCXI-1321
BNC I/O and Timing Interface	“	BNC-2110
BNC I/O Data Card	“	SCXI-1305
15-Ch. Current Source/Amplifier	Custom AFRL Design (See Ref [51])	
Compressor	Craftsman	919.165310
Pressure Transducer	Druck	PDCR-22
Pressure Transducer	Kulite	XCS-062
Thermocouple	Omega	Type E
Two-sensor Hot-wire Probe	TSI	TSI-1250
Single-film Probe	“	1210-T1.5
Constant Temp. Anemometer	“	IFA-300
Powered Cold Junction	Omega	LXCJ-E
Oven	Omegalux	LMF-3550
RTD Temperature Probe	Kaye Instruments	M2806/IRTD-500
Square Mesh Round Wire Grid	McMaster-Carr	85385 T822

References

- [1] Mattingly, J. D. *Aircraft Engine Design, 2nd Edition*. American Institute of Aeronautics and Astronautics Education Series, AIAA, Reston, VA, 2002.
- [2] Nicholson, J.H, Forest, A. E., Oldfield, M. L. G., and Schultz, D. L. “Heat Transfer Optimized Turbine Rotor Blades—An Experimental Study Using Transient Techniques”, *ASME Journal of Engineering for Gas Turbines and Power*, Vol. 106, January 1984, pp. 173-182.
- [3] Clark, J. P., "An Integrated Design, Analysis, and Optimization System for Turbine Airfoils", AFRL Internal Report, 2004.
- [4] Dunn, M. G. and Stoddard F. J., “Studies of Heat Transfer to Gas Turbine Components”, Calspan Corporation, Buffalo, New York, 1977, pp. 1-48.
- [5] Dunn, M. G. and Hause, A., “Measurement of Heat Flux and Pressure in a Turbine Stage”, *ASME Journal of Engineering for Power*, Vol. 104, January 1982, pp. 215-223.
- [6] York, R. E., “Experimental Investigation of Endwall Heat Transfer and Aerodynamics in a Linear Vane Cascade”, *ASME Journal of Engineering for Gas Turbines and Power*, Vol. 106, January 1984, pp. 159-167.
- [7] Frye, John W. *Thin-Film Heat Transfer Gages*. Masters Thesis. School of Engineering, Air Force Institute of Technology (AU), Wright-Patterson AFB OH. March 1966.
- [8] Gochenaur, John E. *Investigation of Heat Transfer to a Turbine Blade Cascade Using Shock Tube*. Masters Thesis. School of Engineering, Air Force Institute of Technology (AU), Wright-Patterson AFB OH. December 1984.
- [9] Elrod W. C., Gochenaur, J. E., Hitchcock, J. E., and Rivir R. B., “Investigation of Transient Technique for Turbine Vane Heat Transfer Using A Shock Tube,” International Gas Turbine Symposium, September 1985.
- [10] Fillingim, Patrick K. *Flat Plate and Turbine Vane Cascade Heat Transfer Investigation Using A Shock Tube*. Masters Thesis. School of Engineering, Air Force Institute of Technology (AU), Wright-Patterson AFB OH. December 1985.
- [11] Dunn, M. G., “Current Studies at Calspan Utilizing Short-duration Flow Techniques”, Calspan Corporation, Buffalo, New York.

- [12] Graziani, R. A., Blair, M. F., Taylor, J. R., and Mayle, R. E., "An Experimental Study of Endwall and Airfoil Surface Heat Transfer in a Large Scale Turbine Blade Cascade", *ASME Journal of Engineering for Power*, Vol. 102, pp. 257-267, April 1980.
- [13] Wistanley, D. K., Booth, T. C., Dunn, M. G., "The Predictability of Turbine Vane Convection Heat Transfer", AIAA Paper No. 81-1435.
- [14] Consigny, H. and Richards, B. E., "Short Duration Measurements of Heat-Transfer Rate to a Gas Turbine Rotor Blade", *ASME Journal of Engineering for Power*, Vol 104, July 1982, pp. 542-551.
- [15] Simoneau, R. J. and Simon, F. F., "Progress towards understanding and predicting heat transfer in the turbine gas path", *International Journal of Heat and Fluid Flow*, Vol. 14, No. 2, June 1993, pp. 106-128.
- [16] Dunn, M. G., Rae, W. J., and Holt, J. L., "Measurement and Analysis of Heat Flux Data in a Turbine Stage: Part I – Description of Experimental Apparatus and Data Analysis", *ASME Journal of Engineering for Gas Turbines and Power*, Vol. 106, January 1984, pp. 229-233.
- [17] Dunn, M. G., Rae, W. J., and Holt, J. L., "Measurement and Analysis of Heat Flux Data in a Turbine Stage: Part II – Discussion of Results and Comparison with Predictions", *ASME Journal of Engineering for Gas Turbines and Power*, Vol. 106, January 1984, pp. 234-240.
- [18] Dunn, M. G., "Heat-Flux Measurements for the Rotor of a Full-Stage Turbine: Part I – Time-Averaged Results", *ASME Journal of Turbomachinery*, Vol. 108, July 1986, pp.90-97.
- [19] Blair, M. F., "Influence of Free-Stream Turbulence on Boundary Layer Transition in Favorable Pressure Gradients", *ASME Journal of Engineering for Power*, Vol. 104, October 1984, pp. 743-750.
- [20] Dunn, M. G., Martin, H. L., and Stanek, M. J., "Heat-Flux and Pressure Measurements and Comparison with Prediction for a Low-Aspect-Ratio Turbine Stage", *ASME Journal of Turbomachinery*, Vol. 108, July 1986, pp. 108-115.
- [21] Rae, W. J., Taulbee, K. C., and Dunn, M. G., "Turbine-Stage Heat Transfer: Comparison of Short-Duration Measurements with State of the Art Prediction", AIAA Paper No. 86-1465.
- [22] Haldemann, C. W., and Dunn, M. G., "Heat Transfer Measurements and Predictions for the Vane and Blade of a Rotating High-Pressure Turbine Stage", ASME Paper No. GT2003-38726.

- [23] Blair, M. F., Dring, R. P., and Joslyn, H. D., "The Effects of Turbulence and Stator/Rotor Interactions on Turbine Heat Transfer: Part II – Effects of Reynolds Number and Incidence", *ASME Journal of Turbomachinery*, Vol. 111, June 1988, pp. 97-103.
- [24] Galassi, L., King, P. I., Elrod, W. C., "Effects on Inlet Turbulence Scale on Blade Surface Heat Transfer", AIAA Paper No. 90-2264.
- [25] Kays, W. M. and Crawford, M. E., *Convective Heat and Mass Transfer*, McGraw-Hill Book Company, New York, 1993.
- [26] Giel, P. W., Van Fossen, G. J., Boyle, R. J., Thurman, D. R., and Civinskas, K. C., "Blade Heat Transfer Measurements and Predictions in a Transonic Turbine Cascade", NASA/TM Paper No. 1999-209296.
- [27] Radomsky, R. W., and Thole, K. A., "Detailed Boundary Layer Measurements on a Turbine Stator Vane at Elevated Freestream Turbulence Levels", ASME Paper No. 2001-GT-0169.
- [28] Demeulenaere, A., Ligout, A., Hirsch, C., "Application of Multipoint Optimization to the Design of Turbomachinery Blades", ASME Paper No. GT2004-53110.
- [29] Arts, T., Lambert de Rouvroit, L., and Rutherford, A. W., "Aero-Thermal Investigation of a Highly Loaded Transonic Linear Turbine Guide Vane Cascade", von Karman Institute for Fluid Dynamics, September 1990.
- [30] Nicholson, J. H., Forest, A. E., Oldfield, M. L. G., Schultz, D. L., "Heat Transfer Optimized Turbine Rotor Blades—An Experimental Study Using Transient Techniques", *ASME Journal of Engineering for Gas Turbines and Power*, Vol. 106, January 1984, pp. 173-182.
- [31] Durbin, P., Eaton, J., Laskowski, G., and Vicharelli, A., "Transonic Cascade Measurements to Support Turbulence Modeling", *Air Force Office of Scientific Research, Contractors Meeting in Turbulence and Rotating Flows*, 2004, pp. 57-62.
- [32] Obayashi, S. and Tsukhara, T., "Comparison of Optimization Algorithms for Aerodynamic Shape Design", *AIAA Journal*, Vol. 35, No. 8, August 1997, pp. 1413-1415.
- [33] Anguita, D., Cravero, C., Filz, C., Riviuccio, F., "An Innovative Technique for the Aerodynamic Design of Turbine Blade Profiles Using Artificial Intelligence", *Proceedings of the 33rd AIAA Fluid Dynamics Conference*, Orlando, FL, 2003.

- [34] Boyle, R. J., Ames, F. E., and Giel, P. W., "Predictions for the effects of Freestream Turbulence on Turbine Blade Heat Transfer", ASME Paper No. GT2004-54332.
- [35] Arnone, A., Bonaiuti, D., Focacci, A., Pacciani, R., and Del Greco, A. S., "Parametric Optimization of a High-Lift Turbine Vane", ASME Paper No. GT2004-54308.
- [36] Dorney, Daniel. J. and Sondak, Douglas. L. *WILDCAT: Program User's Manual*. April 2001.
- [37] Dorney, D. J. and Davis R. L., "Navier-Stokes Analysis of Turbine Blade Heat Transfer and Performance", *ASME Journal of Turbomachinery*, Vol. 114, October 1992, pp. 795-806.
- [38] Lee, D. and Knight, C. J., "Evaluation of an O-H Grid Formulation for Viscous Cascade Flows", AIAA Paper No. 89-0207.
- [39] Baldwin, B. S. and Lomax, H., "Thin Layer Approximation and Algebraic Model for Separated Turbulent Flows", AIAA Paper No. 78-257.
- [40] Abu-Ghannam, B. J. and Shaw, R., "Natural Transition of Boundary Layers—The Effects of Turbulence Pressure Gradient and Flow History," *Journal of Mechanical Engineering Science*, Vol. 12, No. 5, pp. 1-18, 1980.
- [41] Huber, F., personal communication.
- [42] Dagg, J. and Clark, J. P. "What Biological Evolution Teaches Us About Airfoil Design", presentation to AFRL/PRTT, August 2004.
- [43] Dagg, J., "Customizing the GA System", AFRL/PRTT internal report, August 2005.
- [44] Anderson, John D. *Modern Compressible Flow with Historical Perspective*, 3rd ed. Boston: McGraw-Hill, 2003.
- [45] Roach, P. E., "The Generation of Nearly Isotropic Turbulence by Means of Grids," Rolls Royce Ltd, 1986.
- [46] Johnson, P. D., personal communication.
- [47] Schlichting, H., *Boundary Layer Theory*, McGraw-Hill Book Company, New York, 1979.

- [48] Khalatov, A., Khalatov, S., Syred, N., and Bowen, P., "Effect of Secondary Flow on Heat Transfer Over A Guide Vane Suction Side", ASME Paper No. GT-2002-30197.
- [49] Dunn, M. G., "Phase and Time-Resolved Measurements of Unsteady Heat Transfer and Pressure in a Full-Stage Rotating Turbine", Calspan Corporation, 1989.
- [50] Oldfield, M. L. G., "Guide1 to Impulse Response Heat Transfer Signal Processing, Ver. 2", OUEL Report No. 2233/2000, Oxford, UK, 2000.
- [51] Anthony, R. J., Oldfield, M. L. G., Jones, T. V., and LaGraff, J. E., "Development of High Density Arrays of Thin Film Heat Transfer Gauges," *Proceedings of the 5th ASME/JSME Thermal Engineering Joint Conference*, San Diego, CA, 1999. Paper No. AJTE99-1659.
- [52] Doorly, J. E. and Oldfield, M. L. G., "The theory of multi-layer thin film heat flux gauges", *International Journal of Heat and Mass Transfer*, Vol. 30, No. 6, pp. 1159-1168, 1987.
- [53] Rees, W. G. *Physical Principles of Remote Sensing*. Cambridge University Press, Cambridge UK, 2001.
- [54] Dunn, M. G., "Convective Heat Transfer and Aerodynamics in Axial Flow Turbines", ASME Paper No. 2001-GT-0506.
- [55] Narasimha, R., "On the Distribution of Intermittency in the Transition Region of a Boundary Layer", *Readers' Forum, Journal of the Aeronautical Sciences*, pp. 711-712, 1957.
- [56] Clark, J. P. and Praisner, T. J., "Predicting Transition in Turbomachinery, Part I – A Review and New Model Development", ASME Paper No. GT2004-54108.
- [57] Incropera, F. P. and DeWitt, D. P. *Fundamentals of Heat and Mass Transfer*, 5th Ed. John Wiley & Sons, Hoboken, NJ, 2002.
- [58] Mee, D. and Dickens, T., "OUEL Blowdown Wind Tunnel Inlet Turbulence Measurement", Internal memorandum, Oxford University, July 1987.
- [59] Owen, F. K., "Transition Experiments on a Flat Plate at Subsonic and Supersonic Speeds", *AIAA Journal*, Vol. 8, No. 3, pp. 518-523.
- [60] Clark, J. P., Polanka, M. D., Meininger, M., and Praisner, T. J., "Validation of Heat-Flux Predictions on the Outer Air Seal of a Transonic Turbine Blade", *ASME Journal of Turbomachinery*, Vol. 128, July 2006.

- [61] Finke, A. K. and Sharma, O. P., “Low Cost, High-Temperature Blade. Appendix A – Aerodynamic and Heat Transfer Analysis of the Low Aspect Ratio Turbine (LART)”, Air Force Research Laboratory Paper No. AFWAL-TR-85-2053.
- [62] Polanka, M. D., Clark, J. P., White, A. L., and Meininger, M., “Turbine Tip and Shroud Heat Transfer and Loading Part B: Comparisons Between Prediction and Experiment Including Unsteady Effects”, ASME Paper GT-2003-38916.
- [63] Benner, M. W., Sjolander, S. A., and Moustapha, S. H., “An Empirical Prediction Method for Secondary Losses in Turbines: Part I – A New Loss Breakdown Scheme and Penetration Depth Correlation,” ASME Paper GT2005-68637.
- [64] Holman, J. P. *Experimental Methods for Engineers, 6th Ed.* McGraw-Hill, New York, 1994.
- [65] Bruun, H. H. *Hot-wire Anemometry, Principles and Signal Analysis.* Oxford University Press, Oxford, UK, 1995.
- [66] Clark, J. P., personal communication.

Vita

First Lieutenant Jamie J. Johnson was born in Doylestown, Pennsylvania. He attended Central Bucks High School West in Doylestown and graduated in 1998. Upon graduating high school he entered undergraduate studies at The Pennsylvania State University in University Park, Pennsylvania in the same year. In May of 2002, he graduated with a Bachelor of Science degree in Aerospace Engineering and by completing the Air Force R.O.T.C. program; he was commissioned a Second Lieutenant in the USAF.

His first assignment was for the Air Force Research Laboratory in the Turbine Division of the Propulsion Directorate as a turbine research engineer. In August 2004, he enrolled as a full time student at the Graduate School of Engineering and Management at the Air Force Institute of Technology (AFIT). Upon graduation from AFIT, he will receive a Master's Degree in Aeronautical and Astronautical Engineering. His next assignment will be for the Space and Missile Systems Center at Los Angeles AFB, California.

REPORT DOCUMENTATION PAGE				Form Approved OMB No. 074-0188	
<p>The public reporting burden for this collection of information is estimated to average 1 hour per response, including the time for reviewing instructions, searching existing data sources, gathering and maintaining the data needed, and completing and reviewing the collection of information. Send comments regarding this burden estimate or any other aspect of the collection of information, including suggestions for reducing this burden to Department of Defense, Washington Headquarters Services, Directorate for Information Operations and Reports (0704-0188), 1215 Jefferson Davis Highway, Suite 1204, Arlington, VA 22202-4302. Respondents should be aware that notwithstanding any other provision of law, no person shall be subject to a penalty for failing to comply with a collection of information if it does not display a currently valid OMB control number.</p> <p>PLEASE DO NOT RETURN YOUR FORM TO THE ABOVE ADDRESS.</p>					
1. REPORT DATE (DD-MM-YYYY) 03-2006		2. REPORT TYPE Master's Thesis		3. DATES COVERED (From – To) July 2004 – March 2006	
4. TITLE AND SUBTITLE Optimization Of A Low Heat Load Turbine Nozzle Guide Vane				5a. CONTRACT NUMBER	
				5b. GRANT NUMBER	
				5c. PROGRAM ELEMENT NUMBER	
6. AUTHOR(S) Johnson, Jamie J., First Lieutenant, USAF				5d. PROJECT NUMBER	
				5e. TASK NUMBER	
				5f. WORK UNIT NUMBER	
7. PERFORMING ORGANIZATION NAMES(S) AND ADDRESS(S) Air Force Institute of Technology Graduate School of Engineering and Management (AFIT/EN) 2950 Hobson Way, Building 640 WPAFB OH 45433-8865				8. PERFORMING ORGANIZATION REPORT NUMBER AFIT/GAE/ENY/06-M19	
9. SPONSORING/MONITORING AGENCY NAME(S) AND ADDRESS(ES) Air Force Research Laboratory, Propulsion Directorate, Turbine Division, Turbine Branch 1950 5 th St, WPAFB OH 45433				10. SPONSOR/MONITOR'S ACRONYM(S)	
				11. SPONSOR/MONITOR'S REPORT NUMBER(S)	
12. DISTRIBUTION/AVAILABILITY STATEMENT APPROVED FOR PUBLIC RELEASE; DISTRIBUTION UNLIMITED.					
13. SUPPLEMENTARY NOTES					
14. ABSTRACT Often turbomachinery airfoils are designed with aerodynamic performance foremost in mind rather than component durability. However, future aircraft systems require ever increasing levels of gas-turbine inlet temperature causing the durability and reliability of turbine components to be an ever more important design concern. As a result, the need to provide improved heat transfer prediction and optimization methods presents itself. Here, an effort to design an airfoil with minimized heat load is reported. First, a Reynolds-Averaged Navier-Stokes (RANS) flow solver was validated over different flow regimes as well as varying boundary conditions against extensive data available in literature published by the Von Karman Institute (VKI). Next, a nominal turbine inlet vane was tested experimentally for heat load measurements in a shock tube linear cascade with special attention paid to leading edge and suction side characteristics and used to validate the flow solver further at the experimental conditions. The nominal airfoil geometry was then redesigned for minimum heat load by means of both design practice and two types of optimization algorithms. Finally, the new airfoil was tested experimentally and heat load trends were compared to design levels as well as the nominal vane counterpart. Results indicate an appreciable reduction in heat load relative to the original vane computationally and experimentally providing credible evidence to further bolster the practice of preliminary design of turbine components solely with respect to heat transfer using computational models and methods traditionally employed purely by aerodynamicists.					
15. SUBJECT TERMS Turbine Vane, Heat Transfer, Optimization					
16. SECURITY CLASSIFICATION OF:			17. LIMITATION OF ABSTRACT UU	18. NUMBER OF PAGES 218	19a. NAME OF RESPONSIBLE PERSON DR. PAUL I. KING, AFIT/ENY
a. REPORT U	b. ABSTRACT U	c. THIS PAGE U			19b. TELEPHONE NUMBER (Include area code) (937) 255-3636 x4628

Standard Form 298 (Rev. 8-98)
Prescribed by ANSI Std. Z39-18